Carbon Cycling in a Glacier Ice Meltwater Impacted Freshwater System of the Canadian High Arctic

Biogeochemical Processes of the Lake Hazen Watershed

by

Paul Gerard Dainard

A thesis
presented to the University of Waterloo
in fulfillment of the
thesis requirement for the degree of
Doctor of Philosophy
in
Earth Sciences (Water)

Waterloo, Ontario, Canada, 2022

Examining Committee Membership

The following served on the Examining Committee for this thesis. The decision of the Examining Committee is by majority vote.

Supervisor(s)	Dr. Sherry Schiff Professor
External Examiner	Dr. Jemma Wadham Professor
Internal-External Examiner	Dr. Josh Neufeld Professor
Internal Member	Dr. Jenine McCutcheon Assistant Professor
Internal Member	Dr. Igor Lehnherr Adjunct Associate Professor

Author's Declaration

This thesis consists of material which I authored or co-authored: see Statement of Contributions included in this thesis. This is a true copy of the thesis, including any required final revisions, as accepted by my examiners.

I understand that my thesis may be made electronically available to the public.

Statement of Contributions

Research chapters comprising this thesis were designed by myself and Dr. Sherry Schiff. Over the course of this research, the thesis committee provided helpful feedback that supported the completion of each thesis chapter presented herein. Dr. Michael English also provided valuable mentorship during fieldwork and group discussions. This work was highly interdisciplinary and was part of collaborative projects that availed the sharing of resources, such as technical guidance, theoretical expertise, field sampling, laboratory analyses, and biogeochemical data. The remote and logistically challenging nature of my primarily field site (Lake Hazen) emphasized the importance of effective collaborations to best fulfill overarching project goals. The following thesis chapters were organized in the form publishable units, for which significant contributions are described:

Chapter 2 – "Carbon Chemistry, Isotopes (^{13}C, ^{14}C), DOC Characterization Techniques, and their use in Glacial Meltwater Impacted Freshwater Systems"

I originally conceptualized this review chapter while studying for my comprehensive exam. In order to best approach research questions posed in succeeding chapters (3 and 4), an in-depth literature review was required to synthesize what was known of carbon cycling in glacier ice meltwater impacted aquatic systems. I wrote this review chapter with feedback from Dr. Sherry Schiff.

Chapter 3 – "Quantification and Characterization of Dissolved Organic Carbon in Glacial Rivers of a Large High Arctic Watershed"

The writing and interpretation in this research chapter were my own, with support and guidance from Dr. Sherry Schiff and the thesis committee. I performed the majority of the field work, sample processing, and conducted several laboratory analyses for DOC quantification and characterization. Significant contributions were made by project collaborators, Dr. Pieter Aukes, Dr. Ryan Hutchins, and Richard Elgood (Environmental Isotopes Lab) for specialized laboratory analyses. Radiocarbon analyses were conducted at the Lalonde AMS Laboratory, Ottawa, Canada. Opportunistic supraglacial samples of glacier ice, snow, and a supraglacial stream were collected by Dr. Ashley Dubnick. Additional forms of support to this project are described in *Acknowledgements*.

Chapter 4 – "Impact of Mineral Weathering on Glacial River Biogeochemistries and Isotopes (^{13}C / ^{14}C) of Dissolved Inorganic Carbon (DIC)"

The writing and interpretation in this research chapter were my own, with support and guidance from Dr. Sherry Schiff and the thesis committee. Dr. Jason Venkiteswaran also provided mentorship and expertise pertaining to stable carbon isotopes of dissolved inorganic carbon (δ^{13}C-DIC) and isotopic fractionation. I performed the majority of the field work, in-field sample processing, and calculations pertaining to δ^{13}C and Δ^{14}C. Significant contributions were made from collaborators (Dr. Vincent St. Louis, Dr. Kyra St. Pierre, and Jessica Serbu) in the forms of sampling support, data availability, and technical guidance. General chemistry parameters were analyzed at the Biogeochemical Analytical Service Laboratory (BASL) of the University of Alberta. Stable carbon isotopes were analyzed at the Environmental Isotopes Laboratory (U. Waterloo), with significant contributions from Richard Elgood, Rhys Gwynne, and Philip Wright. Radiocarbon analyses were conducted at the Lalonde AMS Laboratory, Ottawa, Canada.

Chapter 5 – "Do Fe and pH affect Dissolved Organic Matter Fluorescence and Indices Derived from Excitation Emission Matrix Spectra?"

The writing and interpretation in this research chapter were my own, with support and guidance from Dr. Sherry Schiff, the thesis committee, and co-authors of the corresponding manuscript draft (Jennifer Mead, Dr. Pieter Aukes). The original experimental design belongs to Jenn Mead, who assessed the effects of Fe and pH on measures of DOM absorption and molecular size as part of her MSc thesis. I analyzed samples for their fluorescence character, PARAFAC modelled EEMS data, calculated fluorescence indices, and expanded this original project by writing a separate publishable unit pertaining specifically to the effects of Fe and pH on DOM fluorescence.

Abstract

Accelerated glacier ice mass loss and intensified meltwater fluxes are among principal vectors of change affecting northern latitudes in a warming climate. Aquatic systems impacted by glacier ice meltwater are vulnerable to hydrologic shifts in flow conditions that may render consequences to sources, and biogeochemical processes, controlling carbon cycling. Whereas the Canadian high Arctic is the third most extensively glacier covered region on Earth, it is relatively understudied with respect to carbon chemistry in glaciers, and meltwaters traversing proglacial freshwater systems (Chapter 2). To fill this knowledge gap, intensive multi-year (2015-19) sampling expeditions of the Lake Hazen watershed were completed, spanning various meltwater flow conditions. Lake Hazen is Canada's most northern large lake, located within the Quttinirpaaq National Park, on Northern Ellesmere Island, Nunavut, and is hydrologically dominated by seasonal pulses of glacier ice meltwaters that rapidly navigate the proglacial environment along glacial rivers. Overarching research objectives were to assess carbon chemistry in glacial runoff, whether proglacial river continua were simple pipelines for organic and inorganic carbon pools, and the sources and sinks of carbon in Lake Hazen.

Dissolved organic carbon (DOC) has a heterogeneous chemical composition in glacial headwaters that is a confluence of supraglacial meltwater sources (Chapter 3). However, abundant polycondensed aromatic "black carbon" molecules identified in a glacier snow sample were only sparingly detected in glacial headwaters, suggesting that this organic material is removed in the supraglacial environment either via adsorption to sinking particles (i.e., cryoconite), or long-term processing. DOC in glacial headwaters is ^{14}C-ancient, often pre-dating the most recent deglaciation (~ 5 ka BP), which provided compelling evidence that older sources of organic carbon must also be present. In fact, the δ^{13}C and Δ^{14}C of extremely low concentration DOC in glacial headwaters suggests that geogenic sedimentary rock organic carbon is an unprecedentedly important component of DOC. Downriver additions of DOC are increasingly humic-like, and shift towards more negative δ^{13}C and Δ^{14}C, which are in agreement with an OC source derived from terrigenous glacial till of the Wisconsin glaciation (< 75 ka BP). Downriver increases in ^{3}H concentrations suggest that mixing of meltwaters with loose sediment prompt the exfiltration of ^{14}C-ancient DOC from the riverbed. In fact, higher ^{3}H and more negative Δ^{14}C-DOC during high flow conditions support that the lateral expansion of the hyporheic zone releases DOC in ground ice thaw water to glacial rivers that is concentrated in ^{3}H from the warm post-bomb period (1960s).

By contrast, dissolved inorganic carbon (DIC) is controlled principally by carbonation weathering reactions of carbonate minerals along glacial river continua, but also the extent of atmospheric exchange (Chapter 4). Increased suspended sediment (TSS, PC), undersaturated CO_2, and isotopically negative $\delta^{13}C$-DIC and $\Delta^{14}C$-DIC are correlated across the dataset, and are typically associated with higher flow conditions. Greater availability of fine-grain particle surfaces for contact with meltwaters (i.e., suspended in solution, or in the riverbed/hyporheic zone) result in an increased prevalence of carbonate mineral weathering and CO_2 drawdown, and liberation of isotopically ($\delta^{13}C$, $\Delta^{14}C$) negative DIC to glacial rivers. Despite additions of DIC along glacial rivers, fast-flowing meltwaters during high flow conditions do not fully equilibrate with atmospheric CO_2, and remain isotopically negative along river transects. In fact, during higher flow conditions, the measured $\delta^{13}C$-DIC was much more negative than theoretical $\delta^{13}C$-DIC calculated assuming equilibrium conditions. The $\delta^{13}C$-PIC of suspended sediment is found to be more negative than conventional carbonates, suggesting that secondary carbonates are present, and/or that isotopic exchange mineral weathering reactions affects the $\delta^{13}C$-PIC. Whereas there is isotopic evidence of SO_4^{2-} derived from the weathering of pyrite based on sulphate isotopes ($\delta^{34}S$-SO_4, $\delta^{18}O$-SO_4), sulphide oxidation coupled to carbonate dissolution (SOC-CD) is only a minor source of DIC. Indeed, undersaturation in CO_2 (and fully saturated O_2), downriver increases in pH and decreases in sulphate mass fraction, low SO_4^{2-}, and alkalinity: DIC < 1 all pointed towards carbonation of carbonate minerals being the primary mineral weathering reaction and source of ^{14}C-ancient DIC to glacial rivers.

Legacy effects of ^{14}C-ancient DOC and DIC in glacial rivers are pervasive in Lake Hazen. Flow-weighted calculations of the seven major glacial river discharges reveal similar quantity and isotopic ($\Delta^{14}C$) character of DOC to that in Lake Hazen. Slightly less ^{14}C-ancient DOC in Lake Hazen is likely a result of in-lake mixing over many years (i.e., long lake residence time), but perhaps also small non-glacial inflows of comparatively ^{14}C-modern DOC, mineralization processes, autochthonous production, and/or adsorption of ^{14}C-ancient OC to sinking particles. By contrast, in-lake DIC has higher concentrations, and less negative isotopes ($\delta^{13}C$, $\Delta^{14}C$) compared to flow-weighted calculations of glacial river discharges. Carbonation weathering reactions of carbonate minerals persist over long periods of time in Lake Hazen, and an ingress of ^{14}C-modern atmospheric CO_2 only partially compensates for weathering induced CO_2 drawdown. The legacy of ^{14}C-ancient DOC and DIC will consequently be reflected in the Lake Hazen discharge (Ruggles River), and exported to coastal margins and marine environments.

One of the techniques used to assess dissolved organic matter (DOM) composition in this thesis was fluorescence spectroscopy and excitation emission matrix spectra (EEMS). Fluorescence of DOM using EEMS has been popularized over the last several decades as a fast, inexpensive, and non-destructive technique to characterize DOM in aquatic systems. Peak picking, derivation of fluorescence indices, and parallel factor analysis (PARAFAC) modelling are commonly applied to EEMS data to describe DOM fluorescence composition. However, iron (Fe) and pH influence DOM fluorescence and pose risks for misinterpretation of important DOM sources and biogeochemical processes when comparing freshwaters with different chemistries. As part of an ongoing collaborative project (Mead et al. unpublished), Fe (II), Fe (III), and pH titration experiments were performed on freshwater samples from diverse hydrological settings with inherent variability in DOM composition. In Chapter 5, the effects of Fe (II), Fe (III), and pH were assessed specifically based on their effects on DOM fluorescence EEMS, peaks, indices, and PARAFAC components. Non-uniform changes in DOM fluorescence intensity and spectral features were found that could not have been predicted *a priori* from concentrations of Fe or pH within the same sample or between samples. In particular, propagation of static fluorescence quenching, inner-filtering effects (IFEs), and co-precipitation of Fe-DOM complicated interpretations of changes of DOM fluorescence characteristics during Fe titration experiments. Effects on DOM fluorescence in freshwaters with Fe <0.5 mg L^{-1} and pH ~5 to 9 were found to be minimal, implying that comparison of DOM fluorescence data in aquatic systems with water chemistries within these ranges should yield robust characterization of fluorescing DOM.

Acknowledgements

I would like to start by recognizing key sources of funding and logistical support that helped make this research possible. Thank you to the Polar Continental Shelf Program, ArcticNet, NSERC, the Northern Scientific Training Program, Parks Canada, Environment and Climate Change Canada and Kenn Borek Air. Thank you to the Garfield Weston Foundation, the Government of Ontario (Queen Elizabeth II and Ontario Graduate Scholarships), and the University of Waterloo for awarding me with personal scholarships. I would like to acknowledge that my research was conducted on the traditional lands of the Inuit.

I owe a great deal of gratitude to my PhD supervisor Dr. Sherry Schiff. What a privilege it has been to learn from such an expert scientist these past several years. I am very grateful for all the amazing opportunities afforded to me as part of your lab group. Thank you to my Thesis Committee (Dr. Igor Lehnherr and Dr. Jenine McCutcheon) and Examining Committee (Dr. Josh Neufeld and Dr. Jemma Wadham) for all their valuable feedback. Your thoughtful questions and feedback during my defense truly made it a special day, and one that I will never forget. I would also like to thank Dr. Michael English for all your mentorship during our field work in the North; your ability to collaborate and bring the best out of people was a privilege to watch. Thank you to Richard Elgood for so much technical guidance and mentorship over the years; I always felt that you were in my corner, and I always appreciated it. Thank you to Dr. Pieter Aukes, Dr. Ryan Hutchins, and Jennifer Mead for your positive energy and our many chats about DOC, and Dr. Jason Venkiteswaran for being a great resource for carbon isotopes. Thank you to Jennifer Hickman, Sarah Sine, and Philip Wright all your help in the lab and preparing for field seasons, and to the rest of the group that made our HydroMicro lab meetings a great place to share ideas and learn over the years. Thank you to Dr. Vincent St. Louis, Dr. Kyra St. Pierre, Jessica Serbu, Maria Cavaco, Victoria Wisniewski, Danielle Lemire, Paul Sokoloff, Dr. Troy McMullin, Dr. Ashley Dubnick, and Dr. Brad Danielson for making field work at Lake Hazen such a great and memorable experience.

Outside of school, I have been lucky to have been surrounded by a wonderful group of people who have supported me during my studies. Thanks to my parents, family, and in-laws for all your encouragement (and for refraining from asking if I was ever going to graduate). Bronte, thanks for being there every step of the way. It's been quite the adventure exploring the world with you these past several years, and I can hardly wait to see what comes next!

Table of Contents

List of Figures

List of Tables

Chapter 1
General Introduction

1.1 The Earth and a Changing Climate

The pursuit of a better understanding of the planet Earth is at the core of natural sciences and elemental cycling amongst environmental compartments. Such studies have slowly removed the shroud that once obscured much of The Earth's long history (~4.54 billion years;[1]). Similarly to disciplines of the social sciences in which humans seek to evoke learnings from historical records or artifacts, reconstruction of past elemental cycling and biogeochemical processes can help depict how Earth's natural systems have been shaped over time, and how they may continue to be shaped in the future. Correspondingly, a key area of focus for environmental scientists at the advent of the twenty-first century has been to more completely understand how Earth's climate is changing, improve modelling of future projections, and implement mitigation strategies where possible.

Whereas natural environmental forcings such as solar and volcanic activity can influence global climate, since pre-industrial times (i.e. 1850s), this natural variability has been vastly overshadowed by anthropogenic forcings[2–4]. Driven by spikes in greenhouse gas concentrations, a widening temperature anomaly is a major impact of climate change[5–7]. The implications of different levels of global warming have been a keen focus when considering guidelines of policy instruments and the potential range in severity of impacts based on different future trajectories of warming trends[8–10]. For instance, the fifth synthesis report of the International Panel of Climate Change[11] provides representative pathway scenarios for greenhouse gas concentrations and projected feedbacks to global average surface temperature, precipitation, and sea level.

Global effects of climate change are expected to be complex and far-reaching. For example, sea level rise has received attention, not only from economic perspectives based on flooding, infrastructure, and tourism[12–15], but also in regards to habitat vulnerability and displacement of biota[16–19]. There is also evidence that the frequency and intensity of extreme weather events, such as flooding, droughts, heat waves, and storms, will respond to a changing climate[20,21]. Case studies have been conducted around the world to assess potential threats of extreme weather events in specific regions[22–26]. Increased lengths of frost-free time and growing seasons can affect naturally occurring flora and agriculture[27–30]; the latter has since prompted proposals of adaptation strategies for the

industry[31–33]. Indeed, ecosystems may be reshaped with a changing climate, including shifts in biodiversity[34,35] and the prevalence of invasive species[36,37].

On a global scale, the precise nature and extent of the impact of climate change are still being refined with continued research, but the potential severity is becoming increasingly clear. Humans have already rendered such significant influence on the Earth that scientists argue we have effectively created a new geological epoch, the "Anthropocene"[38,39]. Defining the Anthropocene, and what its official start date should be, are still matters of discussion[40,41]. It is still unclear whether history will one day reflect the Anthropocene as being among other officially recognized geological epochs. Perhaps more prudently we might ask ourselves: what will be the concerted global response to climate change via advances in research, engineering, and policy over the coming years, and how might these continued efforts shape Earth's future for the better or worse?

1.2 Sensitivity of Arctic Environments

Climate change does not affect all parts of Earth equally. Natural systems at latitudinal extremes experience heightened climate induced stresses via polar amplification[42,43]. Several mechanisms contribute to Arctic amplification, which results in surface temperature increases of Arctic regions being greater than those of mid-latitude regions[44,45]. In fact, there is an ongoing debate amongst researchers as to whether or not the effects of Arctic amplification in turn translate to mid-latitudes where additional weather and climate change impacts may be rendered[46,47].

Arctic sea ice extent and thickness are also responding to warming. Younger, thinner sea ice has become more prevalent as stocks of multi-year sea ice have been depleted[48,49], resulting in shallower snow depths on Arctic sea ice[50,51]. Reductions in September minima of Arctic sea ice have been reported since prior to 1953[52], a trend that has intensified in these past few decades with record lows observed during numerous years since 2007[53–55], including an all-time low during September 2012. A loss of Arctic sea ice is expected to influence global weather and climate, atmospheric circulation patterns[56,57], and may implicate marine primary productivity in Arctic seawater[58].

Other climate change induced effects on Arctic environments include increases in permafrost temperatures and changes in snow cover on land. Permafrost refers to perennially frozen soil or substrate and has been classified in various ways over the years based on its extent, or coverage[59]. In general, sparse permafrost extent ranges from 'isolated patches' to 'sporadic discontinuous', whereas more extensive coverage includes zones of 'widespread discontinuous' and 'continuous' permafrost.

In the northern hemisphere there is a general increase in permafrost continuity with increasing latitude, as referenced in maps of permafrost coverage in Alaska and northern Canada[60,61], although local features relating to geology and topography can also be a factor. To this point, there is ongoing research in regards to relationships between thermokarst landform formation and ice wedge degradation with permafrost thaw[62,63]. Central themes of studies involving permafrost thaw include hydrological impacts[64,65], release or retention of carbon dioxide and methane[66–68], and enhanced export of various biogeochemical parameters to proximal streams and rivers[69,70].

The IPCC released a *Special Report on the Ocean and Cryosphere in a Changing Climate*[71] with detailed discussion of these aforementioned impacts of climate change to Arctic environments. Another major observed physical change to the cryosphere detailed in this IPCC report was related to glacier and ice sheet mass loss. An important premise to research chapters of this thesis is that glacier retreat and changes to glacial ice meltwater flux regimes could implicate glacially fed aquatic systems as Arctic environments continue to warm.

1.3 Glacier Ice Mass Loss and Meltwater Fluxes to Aquatic Systems in a Warming North

Glacier ice mass loss has become a topic of increased scrutiny over the past several decades as researchers strive to best quantify ice mass loss on a global scale, as well as the extent to which this change can be attributed to anthropogenic causes[72,73]. In the northern hemisphere, the Greenland Ice Sheet and Canadian Arctic Archipelago are among major repositories of glacier ice, both of which have exhibited accelerated ice mass loss in recent years[74–76]. Different emission scenarios are important when estimating future trajectories of glacier ice mass loss[77,78], although short-term (21st century) recoveries are not expected under even the most stringent mitigation scenarios[79].

Glacier ice mass loss has been highlighted as an important driver of sea level rise[80,81] and will likely have hydrologic implications for glacier meltwater fed aquatic systems. However, a recent study reviewed variability in glacier ice mass and runoff changes and how regional responses can be quite divergent from what is observed globally[82]. For instance, Antarctica and the Canadian Arctic are the two major glaciated regions by area and volume, but the projected percent volume changes for these regions by 2100 are different[82]. There are also commonalities associated with anticipated trajectories of glacier ice mass loss and meltwater flux intensities. First of all, it stands to reason that, within earlier stages of progressive glacier ice mass loss, increased volumes of glacial runoff would also be

expected. However, it has been proposed that, once appreciable glacier ice mass loss has accrued, a 'tipping point' will be reached due to a volume response lag, after which annual and melt-season glacial runoff will be reduced[83,84]. This underscores the importance of considering net glacier ice mass loss when modeling long term hydrologic changes of glacial runoff in response to climate change and how this may implicate glacier-fed aquatic systems.

Not surprisingly, glacial meltwater impacted freshwater systems are amongst the most sparsely studied given the logistical challenges often associated with in-field sampling. In the high Arctic, short windows of opportunity during polar summers, limited infrastructure at field sites, inclement weather, and high costs can all be barriers to achieving indepth sampling during field seasons. Despite these challenges, researchers have increasingly directed studies towards better describing biogeochemistries and ecosystem structure of glacially-impacted freshwater systems, and potential implications of variable glacial meltwater fluxes. The primary goal of this thesis is to advance the understanding of the impacts of glacial meltwater on carbon cycling in freshwater systems of the Canadian high Arctic.

1.4 Summary of Thesis Chapters and the study site (Lake Hazen Watershed)

Studies of biogeochemistries of glaciated freshwater systems are emerging as a critical area of northern research based on the increased sensitivity of the Arctic to the many vectors of climate induced change. Following this general introduction (Chapter 1) is a review (Chapter 2) of the inherent importance of carbon cycling to climate change, inorganic and organic pools of carbon, and biogeochemical processes controlling their evolution in natural systems. Chapter 2 details analytical tools used to assess carbon cycling, including stable and radioactive isotopes, and DOC characterization techniques, and how these techniques have advanced our understanding of carbon cycling in glacial ice meltwater impacted freshwater systems. Chapter 2 provides fundamentals for 3 research-based manuscripts (Chapters 3, 4, 5), and the overall conclusions gleaned from this research (Chapter 6).

Chapters 3 and 4 assess carbon cycling in the heavily glaciated (i.e., glacier ice covered) Lake Hazen watershed. Lake Hazen is located in the Canadian high Arctic, on northern Ellesmere Island, within the Quttinirpaaq National Park, Nunavut (81.8ºN, 71.4 ºW). The surrounding landscape is reflective of a polar semidesert, with a mean annual temperature of ~ -20 ºC, and typically less than 150 mm annual precipitation[85,86]. To the northwest of Lake Hazen are the Great Land Mountains, and

to the southeast is the Hazen Plateau[85,87]. Together, these topographic features offer protection to the lower Lake Hazen watershed from cold coastal weather and create a 'thermal oasis', whereby summer temperatures can exceed 20 ºC[86,88]. As such, low-lying vegetation coverage is typical of valleys and protected areas of the lower Lake Hazen watershed, contrasted by the comparatively barren Hazen Plateau and glacier covered mountains. Lake Hazen is the world's largest high Arctic freshwater lake by volume, and is hydrologically dominated by seasonal glacier ice meltwater discharge that is delivered to the northwestern shore of the lake via ~11 glacial rivers[89]. Lake Hazen has a relatively large surface area ~542 km^2 and a maximum depth (~267 m) situated just to the southeast of John's Island[90]. Further southeast across the lake is the solitary outflow from Lake Hazen, the Ruggles River, which flows into the Nares Strait and the Lincoln Sea.

Lake Hazen has been found to be responding to a warming climate, with increased glacial meltwater fluxes and an likelihood of ice-free conditions, reducing lake residence time, and affecting the loading of various chemical species to the lake[89,91]. The water chemistry and extremely low biologic activity of Lake Hazen earn it ultra-oligotrophic status[92,93], although it is unclear how climatic induced changes Lake Hazen's biogeochemistry could affect aquatic ecosystem structure in the future[89]. Recent research of microbial diversity in the Lake Hazen watershed provided an important baseline of microbial community structure as related to various physicochemical parameters[94]. With respect to carbon cycling, evidence that proglacial aquatic systems may act as sinks for atmospheric CO_2 has also brought attention to Lake Hazen and its glacial river inflows[95]. A keen motivation of the research that comprises Chapters 3 and 4 was to add in-depth characterization to organic and inorganic carbon pools in glacial rivers of the Lake Hazen watershed to better understand biogeochemical processes along glacial river transects and their role in carbon cycling. Overarching research questions in Chapters 3 and 4 include: what is the carbon chemistry of glacial meltwaters, how are meltwaters transformed along glacial river transects, what biogeochemical processes are controlling downriver dynamics, and are other variables intrinsic to the physical character of the river, hydrology, general chemistry important factors? Finally, how do findings gleaned from this research inform us of future implications to carbon cycling in Lake Hazen watershed under stressors of a changing climate?

Chapter 3 contains a detailed assessment of DOC in glacial rivers of the Lake Hazen watershed. Water isotopes (δ^2H-H_2O, $\delta^{18}O$-H_2O) and tritium (^3H) concentrations are used to investigate supraglacial and proglacial water sources to glacial rivers flowing into Lake Hazen, and are coupled

with DOC quantification and characterization data (absorption, fluorescence, size exclusion, molecular characterization), stable (δ^{13}C-DOC) and radiocarbon (Δ^{14}C-DOC) isotopes. Goals are to assess DOC concentration and composition in glacial headwaters as well as the sources of OC and processes responsible for its transformation along glacial river transects. Glacial river watershed characteristics, interannual variability spanning sampling years, and seasonality are considered with respect to DOC and glacial meltwater flux characteristics. Analyses of opportunistic samples from the supraglacial environment (glacial ice, snow, and stream) are used to characterize DOC in these supraglacial compartments as well as to relate it to glacial headwater samples. This research is the first in-depth analysis of DOC in glacial rivers of the Lake Hazen watershed and adds to what is known of glaciated aquatic systems in the Arctic.

The focus of Chapter 4 is on the evolution of the carbonate system along glacial river transects in the Lake Hazen watershed. The carbonate system is defined using common chemistry measurements (DIC, pCO_2, pH, temperature), and coupled with isotopic measures of δ^{13}C-DIC and Δ^{14}C-DIC. As a baseline for comparison, theoretical δ^{13}C-DIC is calculated assuming atmospheric and chemical equilibrium conditions, using well-known physical and chemical fractionation factors pertaining to the carbonate system, and compared to actual measured δ^{13}C-DIC values. Sources of DIC to glacial rivers are also assessed using mass balance calculations that constrained the δ^{13}C and Δ^{14}C of DIC added to solution spanning glacial headwaters to downriver sites. These data are interpreted in conjunction with the availability of fine-grain suspended sediment in glacial rivers (TSS, PC), the stable carbon isotopes of the particulate inorganic carbon fraction (δ^{13}C-PIC), and the percent saturation of dissolved gases in solution (% sat. CO_2, and O_2), to resolve the role of mineral weathering reactions in shaping glacial river carbonate chemistry. Sources of DIC to glacial rivers will also be considered based on the physical characteristics of glacial rivers, and the meltwater flow conditions, and its eventual fate upon discharge to Lake Hazen surface waters.

Chapter 5 examines the impacts of Fe and pH on common fluorescence measures of DOC[96]. Climate-induced shifts towards brownification, or colouration, of natural waters has stressed the need to assess how variable water chemistries can impact analytical measures that are frequently relied upon when describing DOC quantity and quality. DOC fluorescence excitation emission matrix spectra (EEMS), fluorescence indices, and parallel factor analysis (PARAFAC) modelled fluorescence components are assessed spanning Fe (II), Fe (III), and pH titration experiments to determine how comparable these measures are across natural waters of variable chemistries. The

inner filter effect (IFE) is allowed to proceed to highlight inferred shifts in DOC fluorescence composition that proliferate without supplementary correction. Co-precipitation of Fe-DOC and Fe (oxy) hydroxide complexes, Fe oxidation state, static fluorescence quenching, the IFE, and protonation/deprotonation of organic fluorophores in acidic/basic conditions are among the mechanisms considered with respect to their potential effects to DOC fluorescence over the course of Fe (II), Fe (III), and pH titration experiments.

Finally, Chapter 6 provides a synthesis of contributions of research comprising this thesis. The overall role of glacial rivers in carbon cycling in high Arctic watersheds is detailed with respect to organic and inorganic carbon pools. The quantity and chemical composition of DOC is discussed based on supraglacial and proglacial sources of organic material, and its eventual fate in Lake Hazen, as are the roles of mineral weathering reactions and atmospheric exchange to supplying DIC. These findings will be used to speculate on future implications of climate induced change to carbon cycling in high Arctic glacial meltwater impacted aquatic systems. Future research directions will also be considered, followed by a concluding statement for the cumulative work contained herein.

Chapter 2
The use of Carbon Isotopes ($\delta^{13}C$, $\Delta^{14}C$) and DOC Characterization Techniques in Glacial Meltwater Impacted Freshwater Systems

2.1 Carbon Cycling

A central theme of climate change and global warming is the carbon cycle. Carbon dioxide (CO_2) emissions continue to increase, with an estimated ~72% share of total greenhouse gas (GHG) emissions, followed by methane (CH_4 ~19%) and nitrous oxide (N_2O; ~6%)[97]. Global emissions of all GHGs were estimated to be ~52 gigatonnes of CO_2 equivalents (eq) for the year of 2018, where 'eq' effectively normalizes greenhouse gases to CO_2 based on their global warming potentials (GWPs) over a certain time period. Estimates of fossil fuel reserves have been used to model what the long-term effects of 5 trillion tonnes of cumulative carbon emissions could mean for global warming and Earth's natural systems[98]. It certainly is not prescripted that fossil fuel stocks will continue to be used until they are exhausted as cleaner energy technologies and CO_2 emission mitigation strategies continue to be implemented around the globe. Even so, the introduction of geologic fossil fuel carbon to the atmosphere has created a longstanding imbalance between sources and sinks of atmospheric CO_2 between environmental compartments[99].

Atmospheric concentrations of CO_2 have increased steadily from pre-industrial (~278 ppm) to current (~414 ppm) levels[100]. While global oceans are important sinks for atmospheric CO_2, they are not impervious to climate induced stresses[101]. Elevated atmospheric CO_2 concentrations impact oceans by shifting the carbonate system and causing acidification that can impact the ability of coral reefs and marine calcifiers to thrive depending on their abilities to regulate pH[102–104]. Similarly, while forests play a role in the sequestration of atmospheric CO_2 via photosynthetic processes, their capacity as a sink has been impacted by deforestation and land use changes[99,105,106]. Macro-scale modeling of carbon sources, sinks, and fluxes between environmental compartments produces 'carbon balance sheets' that are often used in climate research to discuss overarching changes to the global carbon cycle. In order for such modeling to be effective, an appreciation for the environmental processes controlling the distribution and dynamics of carbon-containing species in natural systems is required. Carbon cycling can be broken down to that pertaining to inorganic and organic carbon pools, which will be discussed further as it pertains to the dissolved phase in aquatic ecosystems.

2.1.1 Dissolved Inorganic Carbon (DIC)

The carbonate system is a core component of how a waterbody regulates pH and is defined by well-known chemical equilibria, dissociation constants, and temperature specific relationships[107,108] that are summarized in Figure 2.1. Dissolved inorganic carbon (DIC) is the sum of carbonate species, namely CO_2^* ($H_2CO_3 + CO_2$), HCO_3^-, and CO_3^{2-}, and is influenced in natural waters by mineral interactions, biological activity, and atmospheric exchange. CO_2^* is a weak acid and, as long as the solution in question is above pH ~ 4.5, lends acid neutralizing capacity in the form of carbonate alkalinity. Physical and chemical parameters such as temperature, pressure, and ionic strength affect the solubility of CO_2 in solution. The partial pressure of CO_2 (pCO_2) reflects its solubility at equilibrium conditions, and percent saturation (CO_2 % sat.) is commonly used to evaluate the measured pCO_2 relative to its calculated equilibrium value.

The pH buffering strength of natural waters is largely controlled by local geology and the extent of carbonate mineralogy. Physical and chemical conditions of an aquatic system influence the solubility of carbonate minerals, carbonate speciation within the DIC pool, and are linked to the balance between bioerosion and biocalcification, the latter of which being a source of particulate inorganic carbon (PIC). On the other hand, carbonate mineral dissolution and chemical weathering liberate CO_3^{2-} and HCO_3^- and cause alkalinity and DIC concentrations to increase as calcite saturation is approached. Carbonate mineral weathering is driven by the availability of the reactants, namely CO_2, organic and mineral acids, and reactive mineral surfaces, and is shaped by thermodynamic conditions. Consumption of CO_2 would shift the carbonate equilibrium, prompting the drawdown of atmospheric CO_2 into solution. Silicate weathering also consumes CO_2, but is not a source of DIC to solution, and is thermodynamically less favourable than carbonation reactions of carbonate minerals[109]. By way of contrast, pyrite weathering and sulphide oxidation coupled to carbonate dissolution (SOC-CD), release inorganic carbon to the DIC pool and is a source of CO_2[110]. Reaction kinetics for atmospheric exchange of CO_2 and/or its weathering of carbonate mineral surfaces would also be different in an idealized well-mixed open system, versus a poorly mixed closed system. Indeed, carbonate mineralogy and reactions with CO_2 can have an important, albeit complex, effect on the DIC pool and atmospheric exchange of CO_2.

Biologic activity can also be heavily influential to the carbonate system in natural waters. Autotrophs produce organic molecules via photosynthetic processes (photoautotrophs) or chemosynthesis (chemoautotrophs), whereas heterotrophic microorganisms consume organic carbon

and respire CO_2. Photosynthetic and respiration processes are effectively in competition with one another, the balance of which determines whether aquatic biota and microbiota are net sources or sinks of CO_2. The trophic status of a freshwater body, local hydrologic conditions, sunlight availability, and supply of organic carbon are among many factors that could affect this balance between CO_2 fixation and respiration. Furthermore, mineralization of dissolved organic carbon (DOC) by solar radiation, or photolysis, can also be an important source of CO_2.

There is evidently a great deal of connectivity between pools of carbon from terrigenous, aquatic and atmospheric compartments, as well as amongst various carbon containing chemical species. The scope of many important research questions regarding carbon cycling are often tied to sources of carbon, how it transformed, and its eventual fate. Stable and radiocarbon isotopes have emerged as powerful techniques that can address this research goal.

2.1.2 Stable Carbon ($\delta^{12}C$, $\delta^{13}C$) and Radiocarbon ($\Delta^{14}C$) Isotopes

Environmental isotopes have received widespread application to better understand the cycling of several key elements (i.e., H, C, N, O, and S) in natural systems. Isotopes of a chemical element have different numbers of neutrons, and consequently different atomic masses. Consistent with principles of thermodynamics and kinetics, lighter or heavier isotopes of an element often exhibit different reactivities with respect to a range of physical, chemical, and biological processes. This selectivity results in isotopic fractionation, where isotopically lighter or heavier chemical species are either enriched or depleted in the products of a reaction. In fact, fractionation of environmental isotopes is the basis for the variability in their isotopic signatures observed throughout natural systems. Isotopic values (deltas; δ) express the difference in the isotopic ratios of a sample and a reference standard, divided by the isotopic ratio of the reference standard, and are commonly reported in parts per thousand (per mille; ‰)[111]. In physical, chemical, and biological processes that exhibit isotopic selectivity, fractionation factors (α) are useful measures of ratio of isotopic ratios of reactant relative to that of the product. Fractionation factors can be converted to enrichment factors (ε) to illustrate the approximate ‰ shift in the isotopic value associated with the isotopic fractionation process. As an example, $\delta^{13}C_{sample,}$ α, and ε for the chemical fractionation between carbon dioxide (CO_2) and bicarbonate (HCO_3^-)[111] are depicted in Table 2.1.

There is ambiguity in using the terms ‘enriched’ and ‘depleted’ in isotopic studies. Firstly, in the case of stable carbon isotopes, these terms are neither used to describe an amount of ^{12}C nor ^{13}C, but rather the change (δ) in their ratio ($^{13}C/^{12}C$) in a sample relative to a reference standard, divided by the

standard, and calibrated to the marine fossil 'Pee Dee Belemnite' (i.e., Vienna PDB). It is clear that in order to confidently compare isotopic values (i.e., $\delta^{13}C$) among studies, correct calibration to the universal reference standard is imperative. Historically, any 'enrichment' or 'depletion' of $\delta^{13}C$ has been reported respective of the heavier stable carbon isotope (^{13}C), unless otherwise specified. In an example scenario, a stable carbon isotope value ($\delta^{13}C$) of -4 ‰ may have been referred to as being 'depleted' relative to the VPDB reference standard used. At the same time, this hypothetical sample (-4 ‰) could have been referred to as being isotopically 'enriched' relative to another sample with $\delta^{13}C$ of -10 ‰. Furthermore, when a physical process or chemical reaction involved isotopic fractionation, the product may have been discussed as being either isotopically 'enriched' or 'depleted' relative to the parent material, or reactant(s). Indeed, 'enriched' and 'depleted' are only meaningful when expressed *relative* to something else, and often times the proper context has not been given for a reader to correctly interpret the isotopic data reported. Therefore, in the succeeding sections, isotopic values (δ) will be discussed as being 'lower', 'higher', or more (or less) 'negative' or 'positive' relative to reactants, end-members, or other samples, to limit ambiguity associated with their reporting and discussion.

Given numerous interplaying factors that influence the carbonate system and carbon cycling, stable carbon isotopes ($\delta^{13}C$, or $^{12}C/^{13}C$) have received widespread application for studies of various environmental systems. A major consideration of $\delta^{13}C$ cycling is the intense isotopic fractionation associated with CO_2 fixation to organic carbon in plants[112]. C3 plants dominate at mid-high latitudes of the northern hemisphere and exhibit lower $\delta^{13}C$ in organic carbon that generally range from -32 to -24 ‰, than atmospheric CO_2 (i.e., $\delta^{13}C\text{-}CO_2$ ~ -8 to -9 ‰). Plant organic carbon is respired by heterotrophic microbes as it is degraded in soils, and soil $\delta^{13}C\text{-}CO_2$ can become more positive by preferential diffusive loss of ^{12}C to the atmosphere. In other words, with progressive diffusion of soil CO_2 to the atmosphere, the CO_2 that remains in the soil will have more ^{13}C. Dissolution and mixing of soil CO_2, with comparatively more positive $\delta^{13}C$-DIC from either infiltrating surface water or groundwater, can further affect the $\delta^{13}C$-DIC of porewater. Isotopic fractionation exists amongst carbonate species that form DIC. Thus, the $\delta^{13}C$-DIC in aquatic systems can respond strongly to the range of physical and biogeochemical factors affecting carbonate speciation[111] detailed in section 2.1.1. Isotopic connectivity between dissolved inorganic and organic carbon pools extends to major loss mechanisms by which DOC becomes mineralized to CO_2, namely photochemical and microbial degradation. The balance between these sinks versus sources of DOC, such as soil-derived organic

carbon, autochthonous production, and sediment interactions contribute to shaping the δ^{13}C-DOC observed in natural waters.

Isotopic fractionation effects to carbon containing chemical species, as well as the intricate networks whereby different sources of carbon become mixed, create a complex schematic of δ^{13}C cycling in the environment. Such a depiction is presented in Figure 2.1 for a generic freshwater system at mid-high latitude within the northern hemisphere as a tool for interpreting δ^{13}C cycling. In this depiction, interactions with the particulate phase are also considered, including approximate δ^{13}C for marine and freshwater carbonate minerals and their role in the balance between carbonate dissolution and calcification. Particulate carbon has organic and inorganic fractions for which δ^{13}C-POC and δ^{13}C-PIC can be determined, respectively. More complex details, including kinetic isotopic fractionation associated with carbonate mineral dissolution and chemical weathering, as well as the extent of chemical and isotopic equilibration with atmospheric pCO_2, will be discussed in Chapter 4.

Radionuclides of an element have excess nuclear energy and are unstable, undergoing radioactive decay that results in the loss of that radionuclide and the eventual formation of a stable isotopic product. Radiocarbon (^{14}C) is naturally produced in the upper atmosphere by high energy cosmic ray spallation and is oxidized to $^{14}CO_2$, which is then integrated into the global carbon cycle. However, given its high energy and instability, ^{14}C undergoes beta negative decay over time, which involves the emission of an electron and an electron antineutrino while a ^{14}C neutron is converted to a proton in the formation of ^{14}N. This means that in environments where carbon is sequestered away from atmospheric exchange or mixing with other sources of carbon, there will be a gradual depletion in the remaining ^{14}C that can be equated to the time elapsed. The radioactive decay of ^{14}C takes place at a fixed rate, for which the real half-life, or Cambridge half-life, is 5730 ± 40 years. However, by convention, the archaeologic 'Libby' half-life ($t_{1/2}$ = -8033 ln (0.5) = 5568 years) is still used for radiocarbon dating, and is calibrated to calendar years based on the time elapsed for sample collection relative to pre-bomb conditions (1950s). Equations pertaining to the radioactive decay of ^{14}C are provided in Table 2.3.

In addition to radioactive decay, ^{14}C also partakes in isotopic fractionation for which the $\alpha_{C14:C12}$ is approximately the square of $\alpha_{C13:C12}$[113]. This fractionation was historically corrected for by using δ^{13}C of an oxalic acid (I) reference standard made from a sugar beet crop prior to thermonuclear testing in the 1950s and subsequent perturbations of atmospheric ^{14}C-CO_2 levels. Since supplies of oxalic I have since been exhausted, normalization to new reference standards, such as oxalic acid (II), is now

required when using $\delta^{13}C$ to correct for isotopic fractionation of ^{14}C in a sample[114]. The $\delta^{13}C$ normalized specific ^{14}C activity of the oxalic I reference standard is thus denoted 'A_{ON}', and that of the sample is 'A_{SN}'. The fraction of modern carbon ($F^{14}C$) in a sample is expressed as the ratio of these parameters ($F^{14}C = A_{SN}/A_{ON}$), and has been reviewed for correct usage and reporting notation in a recent study[115]. The per mille difference in ^{14}C, or '$D^{14}C$', can then be derived as $D^{14}C = (F^{14}C - 1) \bullet 1000$ ‰). Finally, '$\Delta^{14}C$' is common to geochemical studies, and requires an extra step of 'age correction' to pre-bomb (1950) conditions ($\Delta^{14}C = F^{14}C \bullet e^{((1950\text{-year})/8267)} - 1) \bullet 1000$ ‰[113,116]. Correspondingly, the radiocarbon age is reported in years before present (yBP), where 'present' and 'modern carbon' are relative to the year 1950. Calculation and reporting notation of $F^{14}C$, $\Delta^{14}C$, and ^{14}C age are summarized in Table 2.3.

The power of radiocarbon analyses for studies of carbon cycling emerges when *aged* sources of carbon are being considered. For instance, organic carbon in soils that has been sequestered away from exchange with *modern* atmospheric CO_2 undergoes progressive decay and isotopic depletion of ^{14}C towards the minimum detectable fraction modern carbon, or $F^{14}C$, that corresponds to ~55,000 yBP. In other words, the point where $F^{14}C$ falls below the detection limit is beyond the chronological limit of radiocarbon analyses for determining the age of carbon containing chemical species. To this point, ^{14}C in carbonate minerals and fossil organic carbon formed millions of years ago has long since decayed to a point where there is no detectable ^{14}C remaining, corresponding to a theoretical minimum of ~-999.99 ‰, and often being referred to, colloquially, as being '*^{14}C-dead*'. Geologic repositories can exhibit connectivity to other environmental compartments via erosional processes, thereby integrating this ancient material into the carbon cycle. Incomplete combustion products of fossil fuel burning can also introduce ^{14}C-dead particulate material to the atmosphere for supplemental transport and cycling.

Carbon cycling in natural systems can involve extensive mixing of ^{14}C *modern* and ^{14}C *aged* material. Firstly, photosynthetic processes using ^{14}C modern atmospheric CO_2 will result in that level of activity being reflected in the OC produced. This applies to plant OC and its degradation products in recently formed detritus and soil. However, as you descend a vertical soil profile, the accumulation of years of degradation, burial, and sequestration typically results in increasingly ^{14}C aged material. In aquatic systems, decomposition of recently produced organic matter is a source of ^{14}C modern material to the DIC pool, as is atmospheric exchange of CO_2. In fact, in absence of other major sources or sinks of C, atmospheric exchange and equilibration of modern ^{14}C-CO_2 is often a driving

force pushing the ^{14}C-DIC towards modern values in aquatic systems. Recalling the carbon cycling schematic (Figure 2.1), this is rarely the case in freshwater systems where intricate networks of hydrologic connectivity, sources of C, mixing, and biogeochemical processes are all factors. Measures of radiocarbon for key components of aquatic carbon cycling (Δ^{14}C-DOC, Δ^{14}C-DIC, ^{14}C ages in yBP) can be used to provide strongly complimentary isotopic information to that of stable carbon isotopes (δ^{13}C-DOC, δ^{13}C-DIC) and other chemical characterization techniques.

2.1.3 Dissolved Organic Carbon (DOC)

DOC is often defined as that which passes through a 0.45 μm filter, providing an operational separation from POC[117], although monitoring programs commonly use filter pore sizes ranging anywhere from 0.2 μm to 0.7 μm. DOC is an unusual analyte in that it has an undefined chemical structure, and is typically comprised of complex mixtures of organic molecules that include humic substances, proteins and amino acids, lignin, carbohydrates, and lipids, fatty acids, biomacromolecules, and polycyclic aromatic compounds[117,118]. The chemistry and relative proportions of these organic molecules in a DOC sample is often highly dependent on the environment from which that sample was taken and the *source* of DOC.

The terrigenous environment is a major source of organic material. Soils of different regions (i.e. tropical, temperate, tundra) or positions in soil profiles (i.e. age and extent and extent of degradation) can have highly variable organic carbon content[119]. Soil organic carbon (SOC) consists of the degradation products of vascular plants that have undergone a high degree of microbial processing in soils. SOC can serve as a source of DOC to porewaters and proximal freshwater systems[120,121] in which a chemical fingerprint of the soil parent material, often highly altered, is effectively inherited.

Progression along aquatic continua involves mixing of DOC from a confluence of sources as well as the accumulative effect of a number of important degradation and removal processes. Photolysis, microbial degradation, and sedimentation are major loss mechanisms for DOC in natural waters and can have variable removal rates and effects on the chemical composition of the remaining DOC[122–127]. As such, the evolution of DOC along aquatic continua has become a keen area of study where researchers look to constrain shifts in DOC characteristics based on overarching variables. Reproducible shifts in DOC composition and reactivity along aquatic continua have been investigated and related to the degradation extent of DOC as well as different types of natural waterbodies, water residence times, and land uses in the watershed[128–132]. Such research aids in interpretations as to whether aquatic systems act as ‘passive pipes’ or more ‘reactive conduits’ with respect to DOC[133,134].

DOC in natural waters has frequently been discussed as being of either allochthonous or autochthonous origin. Allochthony, or being 'terrigenous' in nature, refers to DOC that has originated from the terrestrial environment through interactions with soils, or organic substrates. Soil-derived DOC is typically rich in high molecular weight humic substances of elevated aromaticity, namely humic and fulvic acids, that originate largely from the OC-laden upper soil horizons. Autochthony, on the other hand, involves DOC that has been produced via photosynthetic processes in aquatic environments, such as those pertaining to algae and other photoautotrophs. DOC of autochthonous origin is regularly associated with organic material shifted towards comparatively lower molecular weight structures that can include amino acids, proteins, and simple aliphatic molecules. Degrees of allochthony and autochthony must be discussed in relative terms given that DOC in natural waters contains such a wide array of organic molecules from a variety of sources. This is especially the case since major biogeochemical processes such as sedimentation, biodegradation, and photolysis act selectively on DOC removal based on its chemical composition, thereby reshaping the remaining DOC pool accordingly.

2.1.4 DOC Characterization

A number of analytical techniques have been applied to advance the characterization of DOC in natural systems. Absorbance spectroscopy quantifies the light absorbing, or '*chromophoric*' portion of dissolved organic matter (CDOM). Indeed, many of the roles that DOC plays in aquatic systems have to do with its ability to absorb solar radiation at UV and visible wavelengths. An absorption coefficient ($\alpha_{CDOM}(\lambda)$, or more succinctly, α_λ), is quantitative with respect to the light absorbing properties of CDOM at a particular wavelength. However, CDOM absorption spectra are collected over a range of absorption wavelengths, and the ratios of absorption coefficients can give insight into CDOM compositional changes (e.g. α_{255}: α_{365}; [135]). Shifts in the shape of absorption spectra over a range of wavelengths can also be interpreted using regression analyses to determine spectral slopes (i.e., $S_{275\text{-}295}$) or the ratio of spectral slopes ($S_R = S_{275\text{-}295}$: $S_{350\text{-}400}$;[136]. Normalizing absorption coefficients to the concentration of DOC can also depict the proportion of chromophoric material per mg C L^{-1} (i.e., $SUVA_{255} = \alpha_{255}$ / [DOC];[137] Weishaar et al. 2003). Higher specific absorption coefficients are commonly discussed as being indicative of CDOM with elevated conjugation and aromaticity because of the inferred heightened density of delocalized pi electrons contributing to this absorption per mg C L^{-1}. Given that CDOM absorption spectra are typically collected from ~ 200 to 800 nm at 1 nm increments, there is a great deal of freedom with respect to potential CDOM

absorption parameters to calculate. Accordingly, the literature reflects a wide range of reported CDOM absorption parameters that target characteristics such as relative molecular weight, degree of aromaticity, and source of CDOM[126,138]. Details pertaining to the derivation of common measures of CDOM absorption are summarized in Table 2.4.

A fraction of light absorbed by a molecule can then be emitted at a longer wavelength, a phenomenon known as fluorescence. Fluorescence spectroscopy quantifies fluorophoric dissolved organic matter (FDOM) and is commonly quantified using excitation emission matrix spectra (EEMS). EEMS contain a series of 2-D emission spectra collected at regular increments of excitation wavelengths that, when combined, form 3-D arrays of fluorescence data. FDOM fluorescence characteristics can be inferred through the calculation of fluorescence peaks at fixed excitation-emission wavelength pairs, or across wavelength ranges. EEMS fluorescence peaks have been associated with different pools of FDOM, namely humic-like (A, C, and M peaks) and protein-like (T and B peaks) pools. For instance, the conventional UV humic-like 'A peak' is commonly calculated at ex260/em380-460 nm, whereas the tryptophan-like peak is calculated at ex275/em340 nm[139]. Similarly to CDOM absorption parameters, FDOM peaks ratios (i.e., C peak : A peak) and specific fluorescence coefficients for peaks normalized to DOC concentration (i.e. spA) have been used to classify FDOM composition[126,139,140]. Other indices, such as the humification index (HIX) and biological index (BIX), also exploit ratios of EEMS fluorescence measures to interpret FDOM composition. HIX is a proxy for the degree of humification (i.e., C: H content[141,142]), whereas BIX is used to infer the extent of biologically produced 'autochthonous' FDOM[143]. EEMS fluorescence parameters commonly used to describe FDOM composition are summarized in Table 2.5. In addition to these measures, there are also more advanced modeling procedures available to deconvolute complete EEMS datasets and the wealth of fluorescence data contained therein. Parallel factor (PARAFAC) analysis has become a prominent approach to modeling FDOM fluorescence data, identifying the underlying principal fluorescent components that best describe the variance in fluorescence data comprising an EEMS dataset[144–146].

CDOM and FDOM characterization techniques take advantage of fractions of the DOC pool that exhibit absorption and fluorescence responses upon irradiation with photons. Depending on the research questions of a particular study, supplementary analytical techniques may be helpful to either provide greater depths of chemical characterization within these optically active components, or to capture other fractions of the DOC pool that are not optically active. For instance, size exclusion

chromatography (SEC) can be used to separate DOC molecules based on their hydrodynamic radii, or molecular size. Larger organic molecules are eluted from the column first and are followed by smaller molecules at longer retention times. Peaks associated with retention time have been used to identify distinct fractions of the DOC pool including biopolymers (BP), humic substances (HS), building blocks (BB), as well as low molecular weight neutrals (LMW-N) and acids (LMW-A). Indepth discussion of this technique and DOC fractions identified is provided elsewhere[147–150].

Techniques for particularly advanced characterization of DOC at the molecular and structural level include Fourier transform ion cyclotron resonance mass spectrometry (FTICR-MS) and nuclear magnetic resonance (NMR) spectroscopy. FTICR-MS uses mass to charge (m/z) values of mass spectra peaks to assign molecular formulae to the thousands of organic molecules comprising a DOC sample[151]. Elemental ratios of molecular formulae are often depicted in van Krevelen diagrams along with the overarching chemical classes that groups of these molecules are expected to belong to, thereby giving unique insight into DOC composition[152]. As such, there has been an increasing application of FTICR-MS to environmental studies where sources, sinks, and reactivity of DOC are concerned[128,153–156]. Finally, one of the most powerful analytical techniques, NMR spectroscopy, is also an option when a highly detailed chemical description of molecular fractions of DOC is needed[157]. Under the application of a magnetic field, nuclei in the analyte can undergo chemical shifts relative to a reference that are influenced by the presence of surrounding chemical functionalities that affect the electronic environments of the nuclei. ^{1}H and ^{13}C-NMR spectroscopy, including 2-D ^{1}H-^{13}C heteronuclear multiple-quantum correlation (HMQC) spectra, have greatly advanced the chemical characterization of DOC[158], aquatically available organic carbon in green algae and cyanobacteria[159], and the photochemical degradation products of different sources of DOC[160].

There are often trade-offs with respect to the depth of chemical characterization of DOC achieved and the time, complexity, and cost of the analysis in question. Depending on the nature of the research questions of the study, different analytical techniques might be more or less appropriate. For instance, a macro-scale study of thousands of water samples might be advantaged by using a fast and inexpensive technique to capture compositional shifts in DOC across the wide range of samples. Perhaps more advanced chemical analyses would be applied to a subset of these samples if an additional level of chemical characterization were to be helpful in addressing the underlying research questions of the study. Furthermore, various techniques used to assess DOC composition not only have different depths of chemical characterization, but often also capture distinct analytical windows

of the DOC pool. Consequently, it can be advantageous to combine techniques when striving to create a more complete picture of DOC composition, which is frequently the case for studies of DOC in natural waters[161].

2.2 Carbon Cycling in Glacial Ice Meltwater Impacted Freshwater Systems

Carbon cycling in glacier-fed aquatic ecosystems can be dictated by a supraglacial and subglacial contributions to bulk meltwaters, as well as proglacial water sources, and downstream evolution. Depending on a myriad of properties pertaining to the glaciers and proglacial meltwater pathways, the relative importance of their overall roles in the cycling of carbon can be highly variable.

Glacier surfaces, or supraglacial environments, are largely covered by glacial ice, snow, firn, ponded meltwater, and supraglacial streams. Atmospheric deposition is an important pathway by which carbon is delivered to glacier surfaces and can include natural and anthropogenic sources of material. An important natural source of carbon is aeolian deposition, which involves geologically sourced mineral dust from the surrounding landscape[162–164]. Depending on particle size, this material can become airborne by local wind events and dust storms, making local geology important with respect to the constitution of particulate carbon delivered to the supraglacial environment. Aeolian material of particularly fine-grain size can be suspended in the atmosphere and transported even longer ranges prior to its eventual deposition. Naturally occurring forest fires and anthropogenic burning of biomass and fossil fuels are other well-known sources of incomplete combustion products and particulate carbon to the atmosphere, and potentially also to supraglacial environments.

Anthropogenic particulate carbon in the atmosphere exists across a particle size continuum that ranges from coarser charred biomass, to charcoal, to ultra-fine soot particles. These incomplete combustion products can also be referred to as ‘black carbon’ and have been assessed based on their susceptibilities to be atmospherically transported long distances[165,166]. Black carbon is a poorly understood fraction of the carbon pool for which recent research has focused on analytical techniques used for its quantification, its pyrogenic sources, and its chemical properties along the combustion continuum[167–169]. In fact, ramped pyrolysis experiments have not only exploited different thermal resistivities amongst black carbon components[170,171], but also non-petrogenic chemical species to answer questions regarding the cycling of these distinct carbon pools in natural systems[172]. Deposition of mineral dust and black carbon may not only accelerate ice melt via reductions in albedo of glacier surfaces[173,174], but can also play an important role in supraglacial carbon cycling.

Emerging research has shown certain supraglacial environments to be unprecedentedly dynamic with respect to the production, consumption, and processing of carbon by microbial communities[175–177]. Supraglacial primary producers actively fix atmospheric CO_2 in the production of highly biolabile OC[178]. There is also evidence that supraglacial fossil fuel derived carbon may be more biolabile than previously thought[179]. A recent study found that increased inorganic carbon availability enhanced productivity of glacial snow algae[180], further exemplifying the importance of constraining supraglacial carbon cycling in a changing climate.

Atmospheric deposition to glacier surfaces is of particular interest given that supraglacial deposits, also known as cryoconite, have been found to be hotspots of microbial activity[181,182]. Cryoconite is comprised of aeolian deposition of material from the surrounding landscape, such as minerals, organic carbon, and biomass, and can also include incomplete combustion products such as pyrogenic black carbon. The chemical composition of cryoconite has been linked to dissolved ion concentrations[183] as well as supraglacial microbial activity and carbon cycling[184,185]. Dissolution of salts in mineral dust can shape the geochemistries of different supraglacial compartments, as can mineral weathering reactions[186]. Furthermore, since cryoconite reduces glacier surface albedo, biogeochemically dynamic melt-filled depressions termed 'cryoconite holes' can form[187–189]. Cryoconite holes can impart an effect on supraglacial hydrology in that meltwaters can drain through porous ice comprising this surficial weathering crust[190].

Major aquatic systems on glacier surfaces include pooling of meltwaters in supraglacial ponds and lakes, as well as supraglacial streams that serve as the connective tissue between these systems. Studies have looked to better describe carbon cycling in supraglacial ponds, lakes, streams, cryoconite holes, glacial ice, and glacial snow as well as the biogeochemical processing taking place therein. Part of the impetus behind this research is that bulk supraglacial meltwater fluxes are a composite of meltwaters from these compartments, which has implications to receiving proglacial aquatic systems, especially with changes to glacial meltwater flux regimes.

The subglacial environment can also be influential with respect to the biogeochemistries of proglacial headwaters sampled at glacier termini, as well as downgradient proglacial aquatic systems. The level of importance of subglacial drainage to proglacial systems has to do with the thermal regime of the glacier in question. For instance, in warm-based glaciers, meltwaters infiltrate from supraglacial compartments through englacial drainage networks before they reach the glacier bed. Here, contact of subglacial waters with glacier bed sediment can yield hospitable conditions for

mineral weathering reactions, including those mediated by microorganisms[110,191,192]. Oxidation of organic carbon stores in the subglacial sediment and bedrock are therefore important, in addition to the drawdown of atmospheric gases in partially open system conditions[193]. In addition to microbially mediated chemical weathering in the subglacial environment[110,191,192], researchers have more recently turned their attention to better understanding the implications of chemical weathering and solute fluxes to proglacial systems[194–196]

The magnitude of subglacial flow to proglacial systems relative to that from the supraglacial environment is thus of consequence to glacial headwater biogeochemistries, including DOC concentration and composition, and can evolve over the course of melt seasons[197,198]. Polythermal glaciers have mixed thermal regimes that can have complex hydrologic characteristics, including the prevalence of subglacial drainage and flowpath routing[199–201]. On the other hand, subglacial inputs are heavily restricted, or non-existent, in cold-based glacier systems (i.e., frozen to the bedrock) where the supraglacial environment controls meltwater export to proglacial systems. In the case of cold-based systems, supraglacial meltwaters can flow directly over glacier tongues and into proglacial rivers or streams, but can also drain diverse flowpaths around glacier margins before eventually contributing to bulk meltwater flow[202]. The thermal regime and meltwater flowpaths to a glaciated system therefore garner importance with respect to biogeochemistries in receiving proglacial aquatic systems.

Carbon cycling in the proglacial environment not only relates to meltwater sources (i.e., supraglacial, subglacial, ice-marginal), but can also be heavily shaped by subsequent carbon sources and processes within proglacial meltwater conduits. The balance of carbon sources and sinks in glaciated aquatic systems is often very different than that observed at more temperate locales, where higher rates of organic carbon mineralization from photolysis and heterotrophy can be net sources of CO_2 to the atmosphere. In glaciated watersheds, atmospheric exchange and chemical weathering reactions become much more instrumental in determining DIC speciation and CO_2 flux. The roles of carbonate and silicate mineral weathering reactions have been highlighted recently in the context of glacial ice meltwater impacted aquatic systems behaving as sinks for atmospheric CO_2[203]. The source of protons for mineral dissolution (i.e., via carbonation or sulphide oxidation coupled reactions) is of consequence to the overall CO_2 balance[204] and is a key consideration during ion provenance modeling. Studies have looked to tease apart the relative importance of carbonation and sulfide oxidation coupled reactions to the CO_2 balance in different proglacial meltwaters, including

comparisons with non-glacial systems[205,206]. Evidence of a rapidly evolving carbonate system along glacial river transects has sparked an interest to best understand the sources of DIC, as well as the biogeochemical processes taking place in the proglacial environment.

DOC has also been a keen focus of research in glacial meltwater impacted watersheds, based on its quantification and measures of its chemical composition. The bioavailability of DOC mobilized from glaciers has been determined as the percent of DOC that is bioavailable (%BDOC) via microbial incubation experiments and discussed in the context of previously unrecognized bioavailable sources of DOC to proglacial systems[207–211]. High %BDOC in glacial-derived meltwaters could impact carbon cycling of receiving aquatic systems, in that biolabile OC has increased susceptibility to microbial processing and mineralization to CO_2. The radiocarbon age of the DOC (^{14}C-DOC) compared to %BDOC available at only a few sites suggests that ancient glacially derived DOC can have higher biolabilities than comparatively ^{14}C modern DOC[208,209,212]. Given the importance of DOC to glacial meltwater impacted aquatic systems, hydrologic controls and watershed characteristics have also been associated with DOC exported to proglacial systems[198,207,208,210,213,214].

Another important aspect is DOC quantification and characterization along proglacial conduits. Recent findings have highlighted that proglacial streams and rivers may not be simple pipelines with respect to DOC loading and can show shifts in chemical composition along proglacial continua[210,213–216]. The terrigenous environment can be a major source of OC in proglacial systems, although the exact mechanisms by which OC enters the DOC pool may be variable. For instance, soil-derived DOC could be delivered via inflowing surface waters and/or ground ice and permafrost thaw water sources. Groundwater inputs, and river infiltration and mixing within the hyporheic zone, can be sources of DOC. Freshly eroded stream/river banks and turbulent meltwater flows can yield high loads of suspended material, including POC, for which its fate (i.e. loading, transport, and bioavailability) can be of consequence to proglacial carbon cycling[198,211,217,218]. However, interactions between POC and DOC pools in the proglacial environment are perhaps less clear. A catalogue of far-reaching research projects of DOC in glaciated systems from Alaska, Antarctica, the Canadian Arctic, Greenland Ice Sheet, Tibetan Plateau and Himalayas, European Alps, and Iceland is provided in Table 2.6.

Several research questions regarding DOC in glacier covered systems are well-resolved, whereas many others are less clear. Firstly, many studies have reported chemically diverse DOC in compartments of the supraglacial environment (ice, snow, meltwater), and have provided evidence for

probable sources (atmospheric deposition, C fixation, microbial degradation) of compositionally distinct fractions of DOC. Atmospheric deposition of particulate carbon to glaciers can be variable in magnitude and composition based on the local geology, vegetation, prevailing wind strength and direction, and proximity to biomass and fossil fuel burning. Characterizing particulate sources to glaciers is of ongoing interest, and valuable next steps could involve revealing how factors controlling the nature of POC deposited to glacier surfaces vary globally, and how this impacts supraglacial DOC concentration and composition. This is especially relevant given the discrepancies in findings pertaining to the biolability of compositionally distinct fractions of DOC in supraglacial environments. Furthermore, supraglacial microbiologic regimes can be variable based on availability of light, water, nutrients, and organic substrates. As such, there is a clear opportunity to build a better understanding of DOC in supraglacial meltwaters of globally distributed glaciers based on the nature of atmospheric C deposition, C fixation, and microbial degradation on glacier surfaces. This would refine what is known of formation pathways, concentration, and chemical composition of DOC in bulk supraglacial meltwater flux to the proglacial environment.

In the proglacial environment, the general evolution of DOC character tends to follow a common downstream trajectory, although the underlying biogeochemical processes driving this change are less well-defined. For instance, glacial headwaters are often described as being primarily aliphatic (protein-like), although routing of meltwaters in ice-marginal channels, or subglacial discharge, in the case of in the case of warm or polythermal glaciers, can result in higher DOC concentrations, and a shift towards a more extensively conjugated, aromatic (humic-like), DOC composition in glacial headwaters. Higher meltwater flow conditions inevitably increase the total DOC flux to glacial headwaters, while at the same time tending to be associated with lower DOC concentrations that are more closely representative of bulk supraglacial meltwaters. As meltwaters proceed downstream in the proglacial environment, there is typically a shift towards higher DOC concentrations and higher proportions of soil-derived humic-like DOC originating from the surrounding landscape, or terrigenous environment. However, the precise source(s) and biogeochemical processes responsible for downstream changes in DOC are less clearly resolved, based largely on the variability in physical characteristics of watersheds for streams and rivers stemming from glaciers. For instance, surface water inputs can originate from thawing ground ice, wherein DOC is leached from low-lying vegetation and freshly degraded soil. Alternatively, meltwater interactions with the river-bed and hyporheic zone can accumulate downriver, adding microbially-derived DOC from the terrigenous environment. Finally, suspension of high concentrations of fine-grain (<0.45 μm) sediment in glacial

meltwaters may even be an important component of DOC. Therefore, while higher flow conditions typically result in lower concentrations in glacial headwaters, the opposite effect might be apparent further downstream, where increases in surface and groundwater inputs, lateral expansion of the hyporheic zone, and increased concentrations of suspended sediments, are all potential vehicles by which increased concentrations of humic-like DOC may arise.

The Canadian high Arctic is particularly understudied with respect to the DOC in glaciers and the proglacial environment, availing an opportunity to acquire novel data, while addressing the aforementioned knowledge gaps associated with DOC sources and sinks in glacial meltwater impacted aquatic systems worldwide. The handful of studies in the Canadian high Arctic where DOC data are reported for glaciers include: 1) DOC concentrations in glacier ice and basal ice (Devon Ice Cap)[219], 2) DOC concentrations in supraglacial snow, supraglacial meltwaters, subglacial drainage, and basal ice (John Evans Glacier)[220], 3) FDOM fluorescence (EEMS) for supraglacial snow, glacier ice, and basal ice (John Evans Glacier, Prince of Wales Glacier)[221], and 4) DOC concentrations, EEMS, and ^{1}H-NMR for glacial ice (White Glacier, John Evans Glacier)[222]. In fact, DOC concentrations were only reported recently for a proglacial aquatic system of the Canadian high Arctic. In this study, Canada's most northern glacier ice meltwater impacted lake (Lake Hazen), was found to be a sink for DOC[91]. Otherwise, sources of DOC to glacial headwaters and further along proglacial rivers and streams, the chemical composition of DOC, and the roles of meltwater flow conditions and watershed characteristics, have not been studied in the Canadian high Arctic.

Overall, carbon cycling in glaciated watersheds can be impacted by many factors, including variability in glacier thermal regimes (warm-based, polythermal, cold-based), supraglacial atmospheric deposition (aeolian, incomplete combustion products), meltwater routing (supraglacial, subglacial, ice-marginal), magnitude of flux (interannual, seasonal, diel), and contribution of diverse water sources (ground ice / permafrost thaw, ground water infiltration, hyporheic zone processes, surface streams). These factors affect the nature of organic and inorganic carbon stores, the mobilization of these stores, beyond which complex mixing, and a proliferation of various biogeochemical processes (atmospheric exchange, chemical weathering, respiration vs. C fixation) can further influence their cycling in proglacial systems. Based on the sensitivity of high Arctic environments to climate, and heavily understudied DOC in proglacial environments, it is crucial to assess the relative importance of these processes and how they impact carbon cycling in aquatic systems impacted by glacier ice meltwater.

Table 2.1: Carbonate system chemical equilibria, dissociation constants, and equations defining their relationships with temperature[107,108].

Carbonate System Equilibria

$$CO_{2(g)} \leftrightarrow CO_{2(aq)}$$

$$CO_{2(aq)} + H_2O_{(l)} \leftrightarrow H_2CO_{3(aq)}$$

$$H_2CO_{3(aq)} \leftrightarrow H^+{}_{(aq)} + HCO_3^-{}_{(aq)}$$

$$HCO_3^-{}_{(aq)} \leftrightarrow H^+{}_{(aq)} + CO_3^{2-}{}_{(aq)}$$

$$\boldsymbol{Note: CO_2^* = CO_{2(aq)} + H_2CO_{3(aq)}}$$

Dissociation Constants

$$K_H = \frac{[CO_2^*]}{pCO_2}$$

$$K_1 = \frac{[HCO_3^-][H^+]}{[CO_2^*]}$$

$$K_2 = \frac{[CO_3^{2-}][H^+]}{[HCO_3^-]}$$

Relationship with Temperature

$$pK_{CO_2} = -7 \cdot 10^{-5}T^2 + 0.016T + 1.11$$

$$pK_1 = 1.1 \cdot 10^{-4}T^2 - 0.012T + 6.58$$

$$pK_2 = 9 \cdot 10^{-5}T^2 - 0.0137T + 10.62$$

Table 2.2: Example depicting the isotopic value ($\delta^{13}C_{sample}$) as well as simplified expressions of the fractionation factor (α) and enrichment factor (ε) as they pertain to the chemical fractionation between gaseous carbon dioxide ($CO_{2(g)}$) and aqueous bicarbonate ($HCO_{3^{-}(aq)}$) in solution[111]:

Isotopic Signatures in per mille (‰)

$$\boldsymbol{\delta}^{13}C_{sample} = \left(\frac{\left(\frac{^{13}C}{^{12}C}\right)_{sample}}{\left(\frac{^{13}C}{^{12}C}\right)_{reference}^{VPDB}} - 1 \right) * 1000 \qquad (‰\, VPDB)$$

Note: international reference standard for carbon isotopes is Vienna Pee Dee Belemnite (VPDB)

Fractionation Factors (α)

$$\boldsymbol{\alpha}^{13}C_{CO_{2(g)}/HCO_{3(aq)}^{-}} = \left(\frac{\left(\frac{^{13}C}{^{12}C}\right)_{CO_{2(g)}}}{\left(\frac{^{13}C}{^{12}C}\right)_{HCO_{3(aq)}^{-}}} \right)$$

Enrichment Factors (ε)

$$\boldsymbol{\varepsilon}^{13}C_{CO_{2(g)}/HCO_{3(aq)}^{-}} = (\boldsymbol{\alpha} - 1) * 1000 \qquad (‰\, VPDB)$$

Table 2.3: Equations for radiocarbon decay (^{14}C; [111]), fraction modern carbon ($F^{14}C$;[113–116,223]), its derivation corrected for $\delta^{13}C$ fractionation and normalization to reference standards, as well as $\Delta^{14}C$ and ^{14}C age[113,116].

Radioactive decay of ^{14}C

$$^{14}_{6}C \rightarrow {}^{14}_{7}N + e^{-} + \bar{\nu}_e$$

- e^- = electron (or negative beta particle), $\bar{\nu}_e$= electron antineutrino

^{14}C decay equation

$$a_t = a_o * e^{-\lambda t}$$

- a_o = initial activity ($^{14}C/^{12}C$), a_t = activity after time elapsed ($^{14}C/^{12}C$)
- t = time elapsed since initial, where initial refers to pre-bomb conditions of 1950
- λ = Cambridge decay constant = $\ln(2)/t_{1/2}$ or 1/8267 yr^{-1}
- $t_{1/2}$ = half-life = 5730 years for ^{14}C

$$t = -8267 * \ln\frac{a_t{}^{14}C}{a_o{}^{14}C} \quad (yr)$$

Fraction Modern Carbon ($F^{14}C$)

$$\boldsymbol{F^{14}C} = \frac{A_{SN}}{A_{ON}}$$

$$A_{SN} = A_S * \left(\frac{\left(1-\frac{25}{1000}\right)}{\left(1+\frac{\delta^{13}C}{1000}\right)}\right)^2 \approx A_S * \left(1-\frac{2(25+\delta^{13}C)}{1000}\right)$$

$$A_{ON} = 0.95A_{OxI} * \left(\frac{\left(1-\frac{19}{1000}\right)}{\left(1+\frac{\delta^{13}C_{OxI}}{1000}\right)}\right)^2 \approx 0.7459A_{OxII} * \left(\frac{1-\frac{25}{1000}}{1+\frac{\delta^{13}C_{OxII}}{1000}}\right)^2$$

- A_S = specific activity of the sample
- A_{OxI} = specific activity of oxalic acid I reference standard
- A_{OxII} = specific activity of oxalic acid II reference standard
- A_{SN} = $\delta^{13}C$ normalized specific activity of the sample
- A_{ON} = $\delta^{13}C$ normalized specific activity of oxalic acid I reference standard
- $\delta^{13}C_{wood.}$ = -25‰, $\delta^{13}C_{ox.I.}$ = -19‰ (note: original reference standard oxalic acid (I) is no longer available, so further normalization to oxalic acid (II) is described above[114,116]
- $\delta^{13}C$ is the measured $\delta^{13}C$ of the sample

Table 2.3 continued:

Calculation of $D^{14}C$, $\Delta^{14}C$ and ^{14}C age

$$D^{14}C = (F^{14}C - 1) * 1000 \qquad (‰)$$

$$F^{14}C = \left(\frac{\Delta^{14}C}{1000} + 1\right) e^{(t-1950)/8267}$$

$$\boldsymbol{\Delta^{14}C} = \left[F^{14}C * e^{\lambda(1950-t)} - 1\right] * 1000 \qquad (‰)$$

$$\boldsymbol{Radiocarbon\ Age}\ (years\ before\ 'present';\ yBP) = -8033 \ln(F^{14}C)$$

- $D^{14}C$ = per mille isotopic value of ^{14}C
- $\Delta^{14}C$ = 'age corrected' per mille isotopic value of ^{14}C. The $\Delta^{14}C$ is commonly used in geochemical studies for a variety of analytes
- t = year sample was collected (note: additional correction would be required in situations when ^{14}C was measured in lab a different year than the sample was collected)

Table 2.4: Common measures of CDOM absorption, their calculation, and use in describing CDOM composition are provided below. There are referenced materials available for consultation for more extensive reviews of CDOM absorption parameters[126,138]

Parameter	Calculation	Description
Absorption coefficients (α_λ or $\alpha_{CDOM}(\lambda)$; m^{-1})	$\alpha_\lambda = \frac{\ln(10) * \text{Absorbance}}{\text{Pathlength (m)}}$	Quantification of CDOM absorption at specific wavelengths (α_{255}, α_{350}, α_{440})
Ratios of absorption coefficients	$\alpha_{255} : \alpha_{365}$ $\alpha_{465} : \alpha_{665}$	Inversely related to relative molecular weight of CDOM
Specific absorption coefficients (SAC_λ or $SUVA_\lambda$; L mg $C^{-1}m^{-1}$)	$SAC_\lambda = \frac{\alpha_\lambda}{[DOC]\ (mg\ C\ L^{-1})}$	Absorption per unit carbon positively correlated with CDOM aromaticity ($SUVA_{255}$, SAC_{350}, SAC_{440})
Spectral slopes (S; nm^{-1})	$\alpha_\lambda = \alpha_{\lambda_0} e^{-S(\lambda-\lambda_0)}$	$S_{275\text{-}295}$ and S_R have been inversely related to relative molecular weight of CDOM
Spectral slope ratio (S_R)	$S_R = \frac{S_{275-295}}{S_{350-400}}$	

Table 2.5: Common measures of FDOM fluorescence, their calculation, and use in describing FDOM composition are provided below. Slight discrepancies in the excitation and emission wavelengths used for these parameters can be found in the literature and care should be given when comparing calculated indices between studies.

Parameter	Calculation	Description
'Peak picking' of fluorescence intensity maxima (Raman units; r. u.) for excitation (Ex) and emission (Em) wavelength pairs or regions (nm)	A peak = Ex. 260 Em. 380-460 C peak = Ex. 350 Em. 420-480 M peak = Ex. 312 Em. 380-420 T peak = Ex. 275 Em. 340 B peak = Ex. 275 Em. 310	UV humic-like UV-vis humic-like UV humic like ('marine' humic-like, blue-shifted excitation via biogeochemical processing) Tryptophan-like Tyrosine-like (Coble, 1996) [139]
Peak Ratios	Capture shifts in FDOM fluorescence composition based on the characteristics of the peaks under consideration (C:A, C:M, A:T)	
Specific fluorescence peaks (r.u. L mg C^{-1})	$\mathrm{spA} = \frac{\text{A peak (r. u.)}}{[\mathrm{DOC}]\ (\mathrm{mg\ C\ L^{-1}})}$	Peak fluorescence intensity per unit carbon (spA, spC, spM, spT, spB)
Humification Index	$\mathrm{HIX} = \frac{\sum \text{Ex. 254 Em. 435} \rightarrow 480}{\sum \text{Ex. 254 Em. 300} \rightarrow 345}$	Proxy for degree of humification that can be normalized to decrease leverage of highly sensitive Em. 300-345 nm range (Zsolnay et al. 1999; Ohno, 2002) [141,142]
Normalized HIX	$HIX\ norm. = \frac{\sum \text{Ex. 254 Em. 435} \rightarrow 480}{\sum \text{Ex. 254 Em. 435} \rightarrow 480 + \sum \text{Ex. 254 Em. 300} \rightarrow 345}$	
Fluorescence Index	$\mathrm{FI} = \frac{\text{Ex. 370 Em. 450}}{\text{Ex. 370 Em. 500}}$	Proxy for shifts in microbial and terrestrial sources of FDOM (McKnight et al. 2001) [224]
Biological Index	$\mathrm{BIX} = \frac{\text{Ex. 310 Em. 380}}{\text{Ex. 310 Em. 430}}$	BIX and β:α exploit highly similar EEMS features and are both positively correlated with increased contribution of freshly produced, autochthonous FDOM (Parlanti et al. 2000; Wilson and Xenopoulos, 2009; Huguet et al. 2009) [143,225,226]
Freshness Index	$\beta{:}\alpha = \frac{\text{Ex. 310 Em. 380}}{\text{Ex. 310 Em. 420} - 435}$	

Table 2.6: Review of DOC concentration and/or composition analyses performed on samples taken from supraglacial and *proglacial* environments (note: among these studies, subglacial samples are also indicated where appropriate). List is not meant to be exhaustive, but rather a tool to direct the reader to studies of various glaciated systems and the DOC characterization techniques used therein.

Authorship	Sample Types	Location	Details	Analyses
(Aiken et al. 2014) [215]	Glacial ice, p*roglacial systems (creek, rivers, lake)*	Alaska, Canada	Yukon River and its tributaries (glacial vs non-glacial). Gulkana Glacier (ice).	[DOC], $SUVA_{254}$, EEMS, δ^{13}C-DOC, Δ^{14}C-DOC
(Antony et al. 2014) [227]	Snow	E. Antarctica	Surface snow	TOC, FTICR-MS
(Antony et al. 2017) [176]	Snow	E. Antarctica	Princess Elizabeth Land region (incubation experiment)	[DOC], FTICR-MS
(Antony et al. 2018) [228]	Snow	E. Antarctica	Princess Elizabeth Land region (photo-biochemical incubations)	[DOC], FTICR-MS
(Bagshaw et al. 2007) [229]	Glacial ice, cryowater	Antarctic Ice Sheet	Canada Glacier	[DOC]
(Bagshaw et al. 2013) [230]	Glacial ice, cryowater, *proglacial streams*	Antarctic Ice Sheet	Commonwealth, Canada, and Taylor Glacier	[DOC]
(Behnke et al. 2020) [214]	*Proglacial systems (rivers, creek)*	Alaska	Juneau Icefield, Herbert Glacier (glacial vs non-glacial)	[DOC], FTICR-MS, δ^{13}C-DOC, Δ^{14}C-DOC
(Barker et al. 2013) [231]	Glacial ice, snow, *proglacial streams*	Antarctic Ice Sheet	Wright, Commonwealth, Canada, Seuss, Taylor, and Howard Glacier	[DOC], EEMS
(Bhatia et al. 2006) [220]	Snow, supraglacial stream, subglacial, basal ice.	Canadian Arctic	Ellesmere Island, John Evans Glacier	[DOC]
(Bhatia et al. 2010) [197]	Supraglacial stream, snow, *proglacial tarn (lake),* subglacial	Greenland Ice Sheet	SW GIS, proximal to Jakobshavn, Nordensiold, JP Koch, and Polonia Glacier	[DOC], FTICR-MS
(Bhatia et al. 2013) [198]	Supraglacial stream, *glacial headwater, proglacial lake*	Greenland Ice Sheet	SW GIS, Qasigiatsigit Lake	[DOC], δ^{13}C-DOC, Δ^{14}C-DOC (+POC)
(Boix Canadell et al. 2019) [232]	*Proglacial streams*	Swiss Alps	%glacier coverage loss, %vegetated, %bare rocks, etc.	[DOC]
(Chliffard et al. 2019) [216]	*Proglacial streams*	Iceland	Vatnajökull, Langjökull, Hoffsjökull, Myrdalsjökull, Tungnafellsjökull Glacier	[DOC], $SUVA_{280,}$ EEMS
(Colombo et al. 2019) [233]	*Proglacial streams*	NW Italian Alps	Indren Glacier (modeled glacial discharge)	[DOC]
(Dubnick et al. 2010) [221]	Ice, snow, supraglacial stream, *proglacial (lake, stream)*, subglacial, basal ice	Antarctica, Canadian Arctic, Norway	AIS (Clark, Suess, Upper Victoria, Lower Wright), Ellesmere Island (John Evans, Prince of Wales), Norway (Engabreen)	EEMS
(Dubnick et al. 2017) [234]	Snow, ice, cryowater,	E. Antarctica	Garwood Valley in Southern Victoria	[DOC]

	supraglacial stream, *proglacial (stream, lake),* subglacial, basal ice.		Land, Joyce and Garwood Glacier	
(Dubnick et al. 2019) [219]	Glacial ice, basal ice	Canadian Arctic	Devon Ice Cap	[DOC], EEMS
(Fellman et al. 2010) [207]	*Nearshore marine*	Alaska	Juneau Icefield drainage area	[DOC], EEMS, %BDOC
(Fellman et al. 2014) [235]	*Glacial outflow, proglacial systems (river, creeks)*	Alaska	Juneau Icefield, Herbert Glacier	DOC], EEMS, δ^{13}C-DOC
(Fellman et al. 2015) [236]	Snow	Alaska	Juneau Icefield	[DOC], EEMS, δ^{13}C-DOC, Δ^{14}C-DOC
(Feng et al. 2016) [237]	Cryowater	Tibetan Plateau	Laohugou Glacier (N. TP) and Dongkemadi Glacier in Tanggula Mountains (central TP)	[DOC], absorption, EEMS, FTICR-MS
(Feng et al. 2018) [238]	Snow, Ice	N. Tibetan Plateau	N. Tibetan Plateau. - Laohugou Glacier	[DOC], absorption, EEMS, FTICR-MS
(Feng et al. 2021) [239]	Cryoconite leachate	N. Tibetan Plateau	Laohugou Glacier (N. TP)	[DOC], absorption, FTICR-MS
(Foreman et al. 2013) [240]	Supraglacial stream	Antarctica	Cotton Glacier	[DOC], EEMS
(Hagler et al. 2007) [241]	Snow	Greenland Ice Sheet	Summit GIS (highest point)	Water soluble organic carbon
(Hemingway et al. 2019) [210]	*Glacial rivers*	Western Himalayas	Upper Ganges Basin	[DOC], FTICR-MS. %BDOC
(Holt et al. 2021) [242]	*Proglacial streams*	Alaska	Juneau Icefield, Herbert Glacier	[DOC], absorption, EEMS, FTICR-MS, δ^{13}C-DOC, Δ^{14}C-DOC
(Hood et al. 2009) [208]	*Glacial runoff*	Alaska	11 watersheds sampled within the Gulf of Alaska drainage area	[DOC], EEMS, δ^{13}C-DOC, Δ^{14}C-DOC, Lignin, %BDOC
(Hood et al. 2015) [217]	Ice (englacial, surface, basal), cryowater, and *glacial meltwaters*	Various (review)	Antarctic Ice Sheet, Greenland Ice Sheet, and Mountain Glaciers	[DOC], *review*
(Hood et al. 2020) [243]	*Proglacial river and creeks*	Alaska	Juneau Icefield	DOC, POC, δ^{13}C-POC
(Hu et al. 2018) [244]	Glacial ice, snow	N. Tibetan Plateau	Laohugou Glacier	[DOC], *mini-review table*
(Kellerman et al. 2020) [245]	Glacial runoff	Greenland	Leverett Glacier	[DOC], EEMS
(Koziol et al. 2019) [246]	Supraglacial stream, snow, ice, *glacial runoff*	Norway	Foxfonna Glacier, Svalbard	[DOC], *large review table*
(Lawson et al. 2014) [211]	Stream, Snow, basal ice,	W. Greenland Ice	Leverett, Russell Glacier	[DOC], EEMS, free

	cryowater, *bulk runoff*	Sheet		carbohydrates and amino acids, %BDOC
(Legrand et al. 2013) [247]	Glacial ice, snow	Various (review)	Greenland Ice Sheet, Antarctic Ice Sheet, Alps	TOC, *large review table*
(Li et al. 2018) [248]	*Proglacial streams*	NW China	Urumqi and Dongkemadi Glaciers	[DOC], *large review table*
(Musilova et al. 2017) [177]	Glacial ice, snow, supraglacial stream, cryowater	Greenland Ice Sheet	Gross primary productivity, community respiration, etc.	[DOC], fluorescence, amino acids, carbohydrate, volatile fatty acids
(Paulter et al. 2012) [222]	Glacial ice	Arctic	White (Axel Heiberg), John Evans (Ellesmere), Joyce and Victoria (Antarctica) Glacier	[DOC], EEMS, ^{1}H NMR
(Preunkert et al. 2011) [249]	Glacial ice	Various	Greenland Ice Sheet, Antarctic Ice Sheet, Alps	TOC, *mini-review table*
(Singer et al. 2012) [212]	Glacial ice, *proglacial stream*	European Alps	Austrian Alps (26 Glaciers), % glacier cover of total drainage area	[DOC], % BDOC, EEMS, FTICR-MS, Δ^{14}C-DOC
(Smith et al. 2017) [178]	Supraglacial stream	Antarctic Ice Sheet	Cotton Glacier	EEMS, cellular analyses, ^{13}C labeling
(Smith et al. 2018*a*) [250]	Supraglacial stream	Incubation experiments	Cotton Glacier (note: Pony Lake, Suwannee River standards used for comparison)	[DOC], EEMS, FTICR-MS
(Smith et al. 2018*b*) [251]	Supraglacial stream, cryowater, glacial ice, supraglacial lake, sediment	Antarctica, and Greenland Ice Sheet	McMurdo Dry Valleys, Antarctica (Cotton and Canada Glacier). Western margin of Greenland Ice Sheet.	[DOC], EEMS
(Spencer et al. 2014*a*) [209]	Glacial ice, *proglacial streams and lakes*	Tibetan Plateau	Mount Nyainqentanglha and Karola Glacier	[DOC], $SUVA_{254}$, FTICR-MS, %BDOC, δ^{13}C-DOC, Δ^{14}C-DOC
(Spencer et al. 2014*b*) [213]	Glacial ice, snow, *glacial runoff*	Alaska	Mendenhall Glacier	[DOC], EEMS, δ^{13}C-DOC, Δ^{14}C-DOC
(Stubbins et al. 2012) [179]	Supraglacial stream, snow, cryowater, *glacial runoff*	Alaska	Mendenhall and Herbert Glacier	[DOC], $SUVA_{254}$, EEMS, lignin phenols, FTICR-MS, Δ^{14}C-DOC
(Yan et al. 2016) [252]	Glacial ice, snow, *proglacial stream*	Tibetan Plateau	Northern T.P. - Laohugou Glacier	[DOC], *mini-review table*
(Zhang et al. 2018) [253]	Glacial ice, snow	Tibetan Plateau	Southeastern T.P. - Yarlong, Dongga, Renlongba, Demula Glacier	[DOC], *large review table*

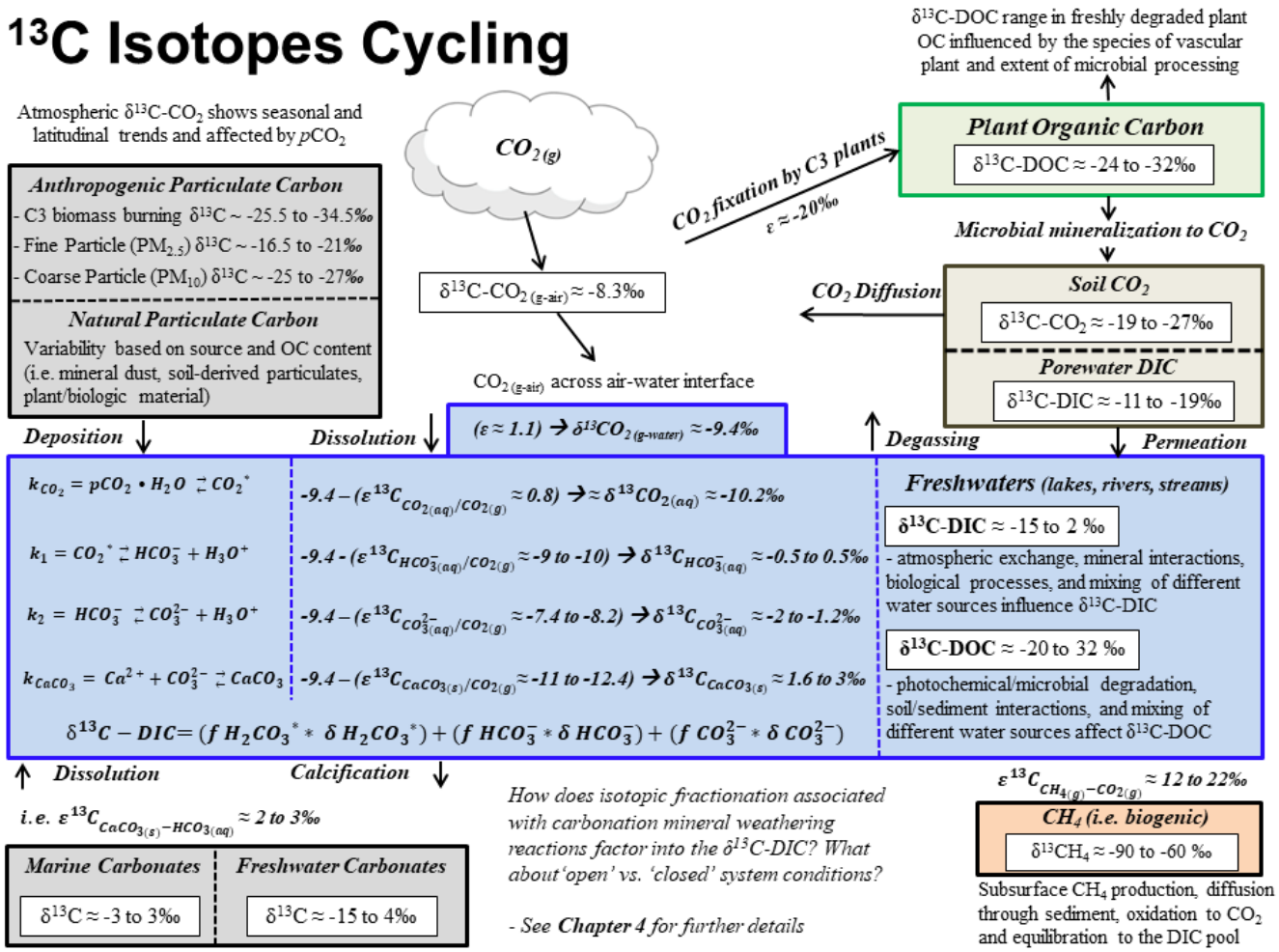

Figure 2.1: Schematic of stable carbon isotopes cycling in a generic freshwater system of the northern hemisphere that is dominated by C3 plants (i.e., no C4 fixation), and that is open to the atmosphere. **Please note** that this schematic is a guide, and that there are many scenarios in which unique environmental conditions result in isotopic fractionation and delta values that fall outside the ranges proposed above.

Chapter 3
Quantification and Characterization of Dissolved Organic Carbon in Glacial Rivers of a Large High Arctic Watershed

3.1 Introduction

The high Arctic contains heavily glaciated (i.e. glacier covered) terrain[254] that exhibits dynamic responses during summer melt, flushing glacial ice melt waters that are both physically and chemically unique to receiving aquatic systems[255]. The timing, magnitude, and biogeochemical characteristics of glacial melt waters can show intense spatial and temporal variability[199,234,256–258]. Climate change further complicates the predictability of melt water fluxes from glaciers[84,259] based on global trending directionality towards glacier ice mass loss and receding extents[72,260,261]. These phenomena are prevalent in the Canadian high Arctic with extreme melt and ice mass loss reported for the Canadian Arctic Archipelago[74,262,263]. The sensitivity of the Arctic to climate change has been well documented[264–266], and there is a growing impetus to assess how future changes in glacial ice regimes could impact biogeochemistries and ecologies of glacial meltwater impacted aquatic systems[267–269]. In particular, the export of carbon-containing species to proglacial environments has become a keen focus because it is integral to predicting future trajectories of the global carbon cycle[268,270,271].

Carbon in glaciers originates primarily from atmospheric deposition of fine-grain particulate material, such as aeolian deposition of mineral dust from the surrounding landscape[162–164]. Incomplete combustion byproducts of forest fires[173,272,273] and more highly graphitized soot from fossil fuel burning[168,274,275] can also be important sources of atmospheric black carbon. The ultra-fine particle fraction, in particular, is highly susceptible to long range transport[165,166,276,277]. Mineral dust and black carbon deposition to glaciers have received attention based on their potential to reduce albedo and accelerate glacier ice melt[173,174,278,279]. Black carbon ranges in size, solubility, and chemical structure along the combustion continuum[168,169,280] and can be a component of supraglacial dissolved organic carbon (DOC) pools[179,209,212].

Diverse microbial communities actively produce and consume DOC on glacier surfaces[175–177], wherein the dynamic balance of biologic C sources and sinks is instrumental when interpreting carbon fluxes[251,281–283]. Supraglacial hotspots for microbial abundance and diversity can coincide with

cryoconite, a composite of solid impurities and biomass that can accumulate on glaciers[181,182,284]. These areas of darkening on glacier surfaces reduce albedo and can form water-filled depressions with sinking sediment termed cryoconite holes[187,188,285]. The chemical composition of cryoconite and its organic carbon fraction have been highlighted as important in fostering the activity of microbiota and carbon cycling on glaciers[184,185,286]. Previous research has quantified and characterized DOC in supraglacial ponds and streams, glacial ice, and snow, to better understand this ubiquitous and ecologically important component of the carbon cycle in cryogenic systems[179,197,221,227].

The nature of DOC exported in glacial runoff is a confluence of aforementioned fluvio-glacial sources, as well as meltwater flow from the subglacial environment in the cases of polythermal and warm-based glaciers[198,219,287]. Subglacial flow is heavily restricted in cold-based glaciers, although there is physical evidence of subglacial influence constricted to the margins of glacier termini in a few cases[288–290]. Hydrologic routing along ice-marginal channels may also influence meltwater hydrochemistry[291] and the nature of DOC[231], although factors such as the local geology, extent of vegetation cover, and length of ice-marginal channels, could render variable effects. Accordingly, DOC in glacial headwaters of cold-based glacial streams and rivers may not be entirely representative of supraglacial meltwaters.

There have been several advances to the quantification and characterization of DOC in glacial runoff in recent decades, and the seasonal hydrological effects of variable meltwater flow conditions. Higher meltwater flux conditions typically result in DOC that is more similar to supraglacial environment, whereas 'terrigenous' inputs from the subglacial environment, or overridden soils, can be more impactful to DOC during lower flow conditions[198,213,245]. DOC in glacial runoff is often described as being comprised primarily of aliphatic organic molecules (protein-like), that are ^{14}C-ancient and highly biolabile[179,207–209].

Proglacial rivers and streams are not necessarily simple conduits for glacial runoff to be mobilized to receiving aquatic systems. In addition to overarching differences in DOC for 'non-glacial' versus 'glacial meltwater impacted' aquatic systems[215,232,292], there are also changes in DOC along proglacial continua. Often, this involves the downstream addition of soil-derived 'terrigenous' DOC[210,214,215], although one study has reported increasingly 'autochthonous' DOC composition along proglacial continua[216]. Depending on the physical characteristics of the proglacial environment, it is unclear whether warmer conditions and elevated meltwater flux will result in downstream DOC that more closely resembles glacial runoff, or if the hydrologic importance of laterally expanding hyporheic

zones and increased ground ice thaw water inputs will be increasingly significant sources of compositionally distinct DOC. The extent of terrigenous landscape development following glacier retreat may also be linked to DOC composition in stream water[242]. Consequently, there is a need to better understand sources of organic carbon, and processes, that control the evolution of DOC along proglacial continua.

The quantity and chemical composition of DOC in glacial runoff, and further downstream, are therefore important to understanding and predicting climate-induced changes to carbon fluxes in glacial meltwater impacted aquatic systems. Advances in this area have been achieved in studies of the Yukon River Basin[215,293], Juneau Ice Field[179,213,214,242], Greenland Ice Sheet[198,211,245,292], Tibetan Plateau[209,252,294], Iceland[216], and Antarctica[231,295]. However, despite the susceptibility of the Canada's North to climate change, and its heavily glacier covered landscape, little is known of processes dictating sources and sinks of DOC in proglacial streams and rivers of the Canadian high Arctic. To fill this knowledge gap, the heavily glaciated (~38%; [296]) Lake Hazen watershed, located within the Quttinirpaaq National Park of northern Ellesmere Island, Nunavut, Canada, is studied herein. For the first time, a detailed multi-year (2015, 2016, 2017, and 2018) dataset of DOC characteristics is presented for seven glacial river systems stemming from glaciers of the Northern Ellesmere Icefield and flowing into the northernmost large lake of Canada, Lake Hazen. Stable water (δ^2H-H_2O, δ^{18}O-H_2O) and tritium (^{3}H) isotopes are used to build an understanding of supraglacial and proglacial water sources to glacial rivers, from which DOC concentration and composition are described in opportunistic samples of the supraglacial environment (snow, ice, stream) and comprehensive surveys along glacial river transects. DOC is quantified and characterized using absorption and fluorescence spectroscopy, size exclusion chromatography (SEC), stable carbon (δ^{13}C) and radiocarbon (Δ^{14}C) isotopes, and Fourier transform ion cyclotron resonance mass spectrometry (FTICR-MS).

The goal of this research is to constrain the relative importance of sources of DOC to glacial rivers, as well as biogeochemical processes, hydrologic conditions (meltwater flux), and riverine features that control DOC dynamics along glacial river transects. Research questions will be addressed that include: 1) what are the sources of OC to DOC in the supraglacial environment? 2) are supraglacial meltwaters the same as glacial headwaters? 3) what sources and processes control DOC in glacial headwaters? 4) given the rapid transit times of meltwaters along glacial rivers (i.e., hours), are they simply conduits for DOC? 5) what are the sources of water (and DOC) along glacial river transects, and how do flow conditions and riverine features affect DOC quantity and composition? 6) is Lake

Hazen a mix of glacial meltwater inputs, or are there unique in-lake sources or sinks of DOC? 7) how might future projections of climate change and glacier ice meltwater flux regimes affect DOC cycling in receiving freshwater systems?

3.2 Methods

3.2.1 Sampling Sites

Lake Hazen base camp is located on northern Ellesmere Island within Quttinirpaaq National Park, Nunavut, Canada (81.8ºN, 71.4 ºW). Field work was conducted during polar summers spanning June 29th to August 1st 2015, July 10th to August 4th 2016, July 6th to 28th 2017, and July 21st to 28th 2018. Lake Hazen is ultra-oligotrophic, with a surface area of ~542 km^2 and a maximum depth of ~267 m. During 2015 and 2016, surface (~ 0 m) and deep (~ 250 m) water samples were collected near the centre of Lake Hazen 'centre buoy', far removed from sediment-laden glacial river plumes. Detailed bathymetry and sediment geochemistry of Lake Hazen can be found elsewhere[90].

Lake Hazen receives seasonal discharge from glacial rivers, the major seven (7) of which draining from the Northern Ellesmere Icefield on the northwestern reach of Lake Hazen. Glacier ice meltwaters were sample from glacial rivers during 2015-18 surveys. The Henrietta-Nesmith River was short (4.6 km), but drained the largest glaciated surface area (1041 km^2) and was sampled beneath the glacier within a broad river valley. The Gilman River drained the second largest glaciated area (704 km^2) and offered a 21.5 km river transect for sampling. The remaining rivers had variable lengths and drained comparatively smaller glaciated areas, namely Abbe (21.0 km; 204 km^2), Blister (10.5 km; 6 km^2), Snowgoose (16.6 km; 89 km^2), Turnabout (41.9 km; 259 km^2), and Very (39.0km; 269 km^2) rivers (Table 3.1). Glacial river transects consisted of samples taken just below the glacier termini, downriver (mid-river), and towards the river deltas (Figure 3.1). Opportunistic samples of the supraglacial environment taken from Henrietta-Nesmith Glacier (glacial ice) and from Gilman Glacier (glacial ice, snow, and supraglacial stream water) were also collected and analyzed as part of this study. Minor non-glacial surface water inputs also exist to Lake Hazen, the most prominent being Salor Creek, stemming from Craig Lake, on the northeastern side of Lake Hazen. The Ruggles River is the solitary outflow to the east, and discharges to the Nares Strait, followed by eventual circulation in the Arctic Ocean.

Glacier ice meltwater flow conditions spanning sampling years (i.e., 2015 to 2018) were an important consideration when assessing various chemical parameters in glacial rivers. Modelled

runoff data was available for glacial rivers during 2015 and 2016 in a recent study[95], and was used for flow-weighted calculations herein. In order to place these flow conditions in context with the remaining sampling years, we used in field observations and dialogue with Water Survey Canada (i.e., stage data of Ruggles River discharge). Flow conditions were high (2015), medium-high (2016), low (2017), and very low (2018), as summarized in *Appendix A – S3.1*.

The extent of glacier cover of each river system was expected to be important based on water sources and meltwater biogeochemistry. The % glaciated can be expressed as the ratio of the glacier cover area to that of the total area of the watershed. The highest % glaciated was for the Henrietta-Nesmith (~82%), followed by Gilman (~71%), Abbe (~52%), Snowgoose (~39%), Turnabout (~38%), and Very (~26%) (Table 3.1). The Blister River % glaciated was not reported as the watershed area was too small to resolve as part of modeling in a recent study of the Lake Hazen watershed, wherein supplementary catchment details can be referenced[203]. Turnabout River was unique from other glacial rivers in this study in that it drained through multiple small lakes prior to its eventual discharge to Lake Hazen. The Blister River transect was accessible by hiking from Lake Hazen base camp, and a number of small streams and overland seepage sites flowing into Blister River were also sampled along the transect during 2016 (not many flowing during 2017).

The geology of the Lake Hazen watershed is comprised of rocks that range in ages spanning the Early Paleozoic to the Cenozoic, for which there are metamorphic (slate, quartzite, schist, soapstone) and sedimentary (limestone, sandstone, siltstone, mudstone, shale, coal, siliciclastic) components, as well as evaporites[203,297–299]. Whereas the mineral composition of different basins were not assessed as part of this study, sedimentary rocks were observed to dominate the local geology. The most recent major glaciation of Northern Ellesmere Island was the Wisconsin glaciation, wherein Laurentide and Innuitian ice sheets advanced and covered most of the Lake Hazen watershed ~75 ka BP. Glaciers covered the majority of the Lake Hazen watershed until ~5.3 ka, followed by a rapid retreat to stabilize near present margins by ~5 ka[85]. During the expansion and retreat of glaciers, erosional processes resulted in the extensive mixing of glacial till, such that well-defined vertical profiles of historic soil/mineral composition were rarely apparent along the banks of glacial rivers. The intense grinding and pulverization of geologic material via erosional processes resulted in geologic material ranging from large boulders to fine-grain particles along glacial river continua.

3.2.2 DOC Concentration

DOC samples were filtered in the field using 0.45 µm polycarbonate filters into 40 mL glass amber vials. Samples were stored in the dark at ~ 4ºC prior to laboratory analysis. DOC concentration was measured using a Shimadzu Total Organic Carbon (TOC-L) analyzer with a detection limit of 0.1 mg C L^{-1} and a standard deviation typically less than 5% of the average concentration.

3.2.3 DOM Absorption

Samples were loaded in a 10 cm quartz cuvette and measured for spectral absorption spanning 200 to 800 nm at 1 nm increments using a Cary 100 UV-vis spectrophotometer. The instrument slit width was set to 0.5 nm and samples were blank corrected using NANOpure (≥ 18.2 mΩ-cm) water as a reference. Absorbance (A) was related to the absorption coefficient (α_λ; m^{-1}) following the relationship: $\alpha_\lambda = 2.303A / l$, where l = the cell pathlength (m). Whereas a number of absorption coefficients are commonly used for chromophoric DOM (CDOM) quantification, α_{255}, α_{350}, and α_{420} were monitored in this study to capture UV, UV/vis, and visible regions of CDOM absorption spectra, respectively. Specific absorption coefficients were calculated as the absorption coefficient normalized to DOC concentration (i.e. $SUVA_{255} = \alpha_{255}$ / [DOC]). Spectral slopes were determined across wavelength ranges spanning 275 to 295 nm ($S_{275\text{-}295}$) and 350 to 400 nm ($S_{350\text{-}400}$) using a non-linear fit[300,301] to capture subtle shifts in the shapes of absorbance spectra. The spectral slope ratio (S_R) was calculated from these values, where: $S_R = S_{275\text{-}295}$: $S_{350\text{-}400}$[136]. Given the extremely low absorption of glacial river samples, shorter excitation wavelengths associated with stronger signals (α_{255}, $SUVA_{255}$, and $S_{275\text{-}295}$) were relied upon when interpreting CDOM quantity and quality. Additional details regarding CDOM absorption parameters are available in Table 2.4.

3.2.4 DOM Fluorescence and EEMS

DOM fluorescence measurements were made using a Cary Eclipse Fluorescence Spectrophotometer. Excitation-emission matrix spectra (EEMS) were acquired in signal to noise ratio using a 1-cm quartz cuvette with excitation and emission slit widths set at 5 nm. EEMS scans for each sample were obtained by collecting fluorescence intensity measurements at 5 nm intervals for emission wavelengths ranging from 300 to 600 nm at excitation wavelengths ranging from 250 to 500 nm. Fluorescence spectra were normalized to Raman units by integrating the area under the Raman scatter peak for deionized water (NANOpure) blanks acquired daily[302].

EEMS data were used to determine intensities of major peaks commonly associated with DOC fluorescence. The humic-like peaks were identified as the fluorescence maxima within emission bands at fixed excitations, with A peak (ex260/em380-460 nm), C peak (ex350/em420-480 nm), and M peak (ex310/em380-420 nm;[139]). Protein-like T (tryptophan-like) and B (tyrosine-like) peaks are conventionally calculated at the wavelength pairs of ex275/em340 nm and ex275/em310, respectively[139]. However, given the extremely low protein-like fluorescence signals in this study, peaks were calculated as fluorescence maxima within narrow emission bands to reduce bias of spectral noise (T peak = ex275/em335-345 nm; B peak = ex275/em305-315 nm). Humic-like (A+C+M) and protein-like (T+B) peak fluorescence intensities were calculated in Raman units (r.u.) and used to infer the relative proportions of humic-like and protein-like fluorescence (i.e., humic% = (A+C+M) / (A+C+M+B+T) * 100. These indices are proxies of fluorescence character, and cannot be directly compared to studies where EEMS data arrays are modelled (i.e., PARAFAC) to distinguish between humic-like and protein-like fluorescence components. Parameters commonly used to describe fluorophoric DOM (FDOM) are summarized in Table 2.5.

3.2.5 Size Exclusion Chromatography

Samples were run on a Toyopearl HW-50S (Tosoh, Japan) size exclusion column paired with a thin film UV reactor used for organic carbon detection[303], and analyzed for organic carbon fractions following experimental design outlined elsewhere[150]. Briefly, samples were injected into a phosphate buffer (pH ~ 6.85) mobile phase, re-filtered in-line to 0.45 μm, and oxidized to CO_2 on a UV lamp at the column terminus, which was quantified by an infrared detector over a range of elution times. Raw output data was deconvoluted using ChromCALC and DOC-LABOR software, where the net organic material eluted from the column, or the hydrophilic fraction, was subclassified into five distinct groups based on molecular size, or hydrodynamic radii, and consequently retention time[303–305]. Peaks associated with elution time were applied to identify distinct fractions of organic material that have been used to advance its characterization in natural waterbodies[147–149]. The peak with the shortest retention time, or the group associated with the largest organic molecules, was biopolymers (BP), which included long chain polysaccharides, carbohydrates, proteins, and lipids. Humic substances (HS; complex humic and fulvic acids) were next to elute, followed by building blocks (BB; degraded forms of humic substances). The last two groups to elute were low molecular weight acids (LMW-A) and neutrals (LMW-N), comprised by small organic compounds such as amino acids, as well as

simple aldehydes and ketones. Resources are available for a more detailed description of these organic fractions and techniques used for peak identification and integration[149,150].

3.2.6 Water stable (δ^2H-H_2O and $\delta^{18}O$-H_2O) and Tritium (^3H) Isotopes

Stable and tritium isotope water samples were filtered to 0.45 µm and collected in 30 mL HDPE and 500mL Nalgene bottles, respectively. Bottles were allowed to overflow during filling in the field followed by sealing tightly, eliminating headspace and the potential for evaporative losses during storage (4ºC). Samples were analyzed at the Environmental Isotope Laboratory at the University of Waterloo. Briefly, water stable isotopes were measured on a Liquid Water Isotope Analyzer (model T-LWIA-45-EP) for which $\delta^2H = \pm 0.8‰$ and $\delta^{18}O = \pm 0.2‰$. Tritium samples were enriched 15X by electrolysis such that the detection limit was 0.8 ± 0.8 Tritium Units (TU) and analyzed using the Liquid Scintillation Counting (LSC) technique.

3.2.7 Fourier Transform Ion Cyclotron Resonance Mass Spectrometry

Acidified samples were captured on Bond Elut PPL cartridges (Agilent Technologies), followed by elution with methanol and storage in a freezer (-20ºC) until FTICR-MS analysis was conducted at the University of Alberta. Mass spectra were acquired using an Apex-Qe mass spectrometer (Bruker Daltonics), from which molecular formulae were determined and used to calculate elemental ratios (O:C, H:C), and the modified aromatic index (AI). These indices of chemical composition were then used to allocate organic compounds comprising each sample to compound classes that included highly unsaturated aromatic, unsaturated aliphatic, polyphenolic, and condensed aromatic molecular structures, the latter of which resembled dissolved black carbon components. Other compound classes were only sparingly identified in the samples analyzed as part of this study, including saturated fulvic acids, sugars, and peptides. Further information regarding the solid-phase extraction, FTICR-MS analysis, and calculation of chemical indices and proportional contributions of organic carbon compound classes can be found elsewhere[155].

3.2.8 Stable Carbon ($\delta^{13}C$-DOC and $\delta^{13}C$-POC) and Radiocarbon ($\Delta^{14}C$-DOC) Isotopes

DOC samples were collected in the field in 1 L Nalgene bottles and filtered within 24 hours to 0.45 µm. Stepwise filtration involved first using an in-line assembly and pushing water over a pre-combusted 0.8 to 1.2 µm Whatman quartz microfiber filter (QM-A). Particulate organic matter (POM) retained on the QM-A filters was frozen and retained for $\delta^{13}C$-POC analysis. The filtrate was then vacuum filtered over pre-combusted 0.7 µm glass fiber filters (GF/Fs) followed by 0.45 µm

polycarbonate membrane filters and stored in acid-washed polycarbonate bottles in the cold (4ºC) and dark. Each new filter used was primed with ~ 50 mL of sample water, which was discarded prior to final sample collection.

Stable carbon isotopes ($\delta^{13}C$) were analyzed at the Environmental Isotope Laboratory of the University of Waterloo with a precision determined from replicate samples of ± 0.2 ‰. $\delta^{13}C$-DOC samples were treated with ortho-phosphoric acid and potassium persulfate, the former serving to first remove inorganic carbonates to the headspace that were then flushed via bubbling with helium gas. Persulfate digestion at 100ºC oxidized any organic carbon remaining in the sample to CO_2, which was subsampled from the headspace using a syringe and injected to a MicroGas-IsoPrime Mass Spectrometer for analysis. A similar approach was used for material scraped from POM sample QM-A filters to analyze for $\delta^{13}C$-POC.

Radiocarbon ($\Delta^{14}C$) was measured using a 3 MV tandem accelerator mass spectrometer (Lalonde AMS Laboratory, Ottawa, Canada). Sample pretreatment involved CO_2 purification and graphitization that was conducted using equipment[306] and techniques described elsewhere[307]. The fraction of modern carbon ($F^{14}C$) was calculated as the $^{14}C/^{12}C_{sample}$: $^{14}C/^{12}C_{standard}$ using the oxalic acid II (Ox-II) standard[115], corrected for sample and machine fractionation using measured $\delta^{13}C$ in the AMS[113]. The $F^{14}C$ was then used to derive the radiocarbon age in years before present (BP = 1950 AD), as well as the per mille value relative to the standard normalized for isotopic fractionation ($\Delta^{14}C$-DOC), as detailed in Table 2.3, and the referenced materials therein. The average standard deviation among $F^{14}C$ values was 0.0046 ± 0.0022, which translated to $\Delta^{14}C$ ~ 4.6 ± 2.2 ‰, and ^{14}C ages ~ 76 ± 33 yBP.

3.3 Results

3.3.1 Supraglacial and Proglacial Water Sources

Proglacial water sources and their hydrologic importance to glacial rivers were assessed using water (δ^2H-H_2O, $\delta^{18}O$-H_2O, ^3H) isotopes. Glacial headwaters had stable water isotope values that plotted closely to the global meteoric water line (GMWL), which was also the case for the glacier snow, supraglacial stream, and glacial ice samples (Figure 3.2A). Glacial headwaters and downriver sites showed similar relationships with δ^2H-H_2O and $\delta^{18}O$-H_2O based on comparable linear regression equations and goodness of fit results (Table 3.2). The residuals of a best-fit line were not found to be significantly ($p < 0.05$) different for glacial headwaters when compared to those of downriver sites.

When considered cumulatively, glacial river transects, ice, snow, and supraglacial stream water isotopes data followed a linear distribution ($\delta^2H = 6.3 * \delta^{18}O - 39.9$ ‰; $R^2 = 0.91$) that was plotted as the local glacier ice melt water line (LGIMWL). Although complete glacial river transects adhered closely to the LGIMWL, downriver shifts towards less negative stable water isotopic values were typical for all years. Downriver changes in $\delta^{18}O$-H_2O were small during 2016 (+ 0.4 ± 0.2 ‰) and 2017 (+ 0.3 ± 0.4 ‰), and slightly more pronounced during 2018 (+ 1.2 ± 0.4 ‰), suggesting minor proglacial water sources to glacial rivers.

Stable water isotopes data also showed distinct behavior based on the glacial river watershed characteristics, and between sampling years. For instance, there was isotopic separation of glacial rivers along the LGIMWL that appeared to be associated with the glaciated area of the catchment, with the most negative δ^2H-H_2O and $\delta^{18}O$-H_2O values corresponding to the largest glaciated areas for the Henrietta-Nesmith (1041 km^2) and Gilman (704 km^2) river catchments (Figure 3.2A). These findings could suggest more intense isotopic fractionation associated with precipitation to higher altitude (colder temperature) glacier surfaces. Interannual variability in stable water isotopes for glacial rivers was depicted for years spanning 2015 to 2018, with linear regression analyses of data distributions for each sampling year (Figure 3.2B). Linear regressions were found to fit the data arrays well ($R^2 > 0.92$) and yielded equations with similar slopes (Table 3.2). However, regression results were significantly ($p < 0.05$) different from year to year in all cases, except when a comparison of 2016 and 2018 arrays was considered. The warm, high flow year (2015) plotted well below the GMWL, whereas the cold, low flow year (2017) plotted above the GMWL (Figure 3.2B). Accordingly, differences in ambient conditions on a yearly basis and the extent of glacier ablation and meltwater flux appear to have been reflected in stable water isotopes data.

Glacial river headwaters had ^3H concentrations ranging from 1.7 to 6.5 Tritium Units (T.U.) (Table 3.3), which were lower than average baseline ^3H in precipitation expected for the Canadian North (~10 to 20 T.U.;[308–310]). Opportunistic precipitation samples collected near Lake Hazen base camp during mid-July of 2017 (14.8 ± 0.9 T.U.; n = 3), and snowpack samples from the surface of Lake Hazen earlier that year (May 2017; 10.0 ± 0.8 T.U.; n = 3), were both within this expected range of ^3H concentrations. These precipitation samples were strongly contrasted by an extremely low ^3H concentration in supraglacial snow from the surface of Gilman Glacier (1.4 T.U.), that suggested either an effect of intense fractionation associated with temperature and altitude, or a longer residence time of supraglacial snow. The ^3H concentration of Gilman River glacial headwaters (1.7 T.U.) was

very similar to that of the glacial snow, as expected for a cold-based glacier dominated by supraglacial meltwater runoff.

On the other hand, ^{3}H concentrations were affected by proglacial water sources further along glacial river transects, and varied among rivers, and sampling years. During both higher and lower flow years (2016 and 2017), Blister, Gilman, and Snowgoose rivers transects all had downriver increases in ^{3}H concentrations that amounted to between 1.1 and 4.4 T.U., or ~1.7X, higher than their respective glacial headwaters (Figure 3.3A). The one instance where this downriver dynamic was not observed was for the Abbe River (2017), which remained relatively unchanged (-0.4 T.U.). ^{3}H concentrations appeared to be inversely related to the extent of glacier covered area, whereby the most sparingly glaciated Blister and Snowgoose River catchments had the highest ^{3}H concentrations in almost all cases. There was interannual variability in ^{3}H concentration measurements for the seven major glacial river discharges to Lake Hazen, yielding higher values during 2015 (6.5 to 11.5 T.U.) compared to 2016 (4.0 to 8.9 T.U.) and 2017 (2.8 to 10.0 T.U.) (Figure 3.3B). On a river-by-river basis, samples from 2016 and 2017 were between 0.8 to 3.8 and 1.2 to 6.3 T.U. lower than their 2015 counterparts, respectively. Assuming that ^{3}H concentrations in supraglacial meltwater were extremely low in each sampling year, this finding suggested that proglacial water sources were of greater hydrologic importance to glacial rivers during the high flow year (2015), compared to medium-high (2016), and low (2017) flow years.

Overland seepage sites, characterized by discharging groundwater trickling over low-lying vegetation and organic-rich soil, and small streams, were identified flowing into Blister River along the river continuum (10.5 km) and sampled during hikes. For this glacial river system, meltwaters originated from two minor glaciers (Arrow and Bridge) that accounted for a glaciated surface area of only ~ 6 km^2, and that did not originate from the greater ice cap (Figure 3.1). Overland seepage had less isotopically negative $\delta^{18}O\text{-}H_2O$ compared to samples taken along the Blister River transect, as was an opportunistic sample of ground ice from along the Lake Hazen shoreline near the Blister River delta (-25.8, -207.2 ‰; Figure 3.2A). In fact, the ^{3}H concentration for an overland seepage site sampled flowing into Blister River during 2017 (12.5 T.U.) was more representative of what would be expected for precipitation in the Canadian North, and was likely suggestive of a recent ground ice thaw water source. Even so, there could be a good deal of heterogeneity in ^{3}H concentrations in overland seepage sites or streams inflowing to glacial rivers, and additional sampling would be required to refine this interpretation. For instance, the $\delta^{2}H\text{-}H_2O$ and $\delta^{18}O\text{-}H_2O$ characteristics of small

streams inflowing to Blister River generally coincided with overland seepage sites, apart from a cluster of four stream samples that adhered much more closely to the LGIWL (~ -26.5, -204 ‰). Headwaters of these four small streams near the top of the catchment were not identified, but could have originated from glacier ice melt higher up in the icefield. Excluding these four samples, a ground ice thaw water line (GITWL) was calculated ($\delta^2H = 4.9 * \delta^{18}O - 83.2$ ‰; $R^2 = 0.92$) for overland seepage, streams, and the ground ice sample (Figure 3.2A). This further exemplified variable source waters to Blister River, as well as to inflowing streams of Blister River, and highlighted the importance of delineating glacier ice meltwaters and ground ice thaw waters. However, since the majority of Blister River transect stable water isotopes samples plotted closely along the LGIWL, ground ice thaw water inputs were hydrologically dwarfed by glacier ice meltwater.

3.3.2 DOC in Glacial River Headwaters and Supraglacial Environment

Freshwater samples taken just below glacier termini had low DOC concentrations and absorption coefficients (α_{255}) (0.22 ± 0.12 mg C L^{-1}; 0.86 ± 0.40 m^{-1}), translating to $SUVA_{255}$ of 4.75 ± 2.07 (Table 3.4A). Average humic-like peak (A+C+M) fluorescence (0.06 ± 0.02 r.u.) was higher than that of protein-like peaks (T+B; 0.04 ± 0.02 r.u.). On average, this ~ 63 % humic vs. 37 % protein fluorescence was in line with size exclusion chromatography (SEC) results that showed a dominant contribution of humic substances (HS = 38 ± 8 %) when compared to biopolymers (BP = 21 ± 7 %), building blocks, (BB = 11 ± 4 %), and low molecular weight neutrals (LMW-N = 30 ± 10 %). Low molecular weight acids (LMW-A) were almost ubiquitously below the detection limit and were only quantified in one glacial river headwater sample (Table 3.4A). Molecular characterization of glacial headwaters yielded H:C (1.36 ± 0.07) and O:C (0.39 ± 0.01), with the majority of DOC classified as either highly unsaturated aromatic (62 ± 9 %), unsaturated aliphatic (25 ± 9 %), or polyphenolic (7 ± 1) material (Table 3.4B). By comparison, only trace amounts of organic material (<3 % each) belonging to saturated fulvic acids, peptides, sugars, and polycondensed aromatic, or black carbon, compound classes. These results show that DOC in glacial headwaters was compositionally heterogenous, with major contributions of both aromatic, humic-like material, and unsaturated aliphatic compound classes, such as LMW-N and fluorescent amino acids (free or bound in proteins).

Even at such low amounts of DOC in glacial headwaters, there was agreement between DOC concentration and UV absorption (α_{255}), as well as between compositional measures using complimentary techniques (Figure 3.4A-D). For instance, %HS was positively correlated with

%humic fluorescence, as was %LMW-N with protein-like fluorescence ($p < 0.05$). Although DOC eluted from the SEC column did not necessarily fluoresce, there was likely considerable overlap between these pools of organic material. Glacial headwaters sampled during 2017 had among the lowest DOC concentrations (< 0.2 mg C L^{-1}), and 2018 samples had among the highest contributions of humic-like material (% HS, % humic fluor.; Figure 3.4A-D). However, given the narrow range of low DOC concentrations in glacial headwaters, changes in DOC quantity were not strongly related to shifts in its chemical composition, and glacial headwaters were relatively similar overall.

DOC quantity and composition were variable amongst supraglacial compartments. Glacial ice taken from Henrietta-Nesmith and Gilman glaciers had low DOC concentrations (0.22 and 0.29 mg C L^{-1}) and absorption coefficients (α_{255}; 0.94 and 1.67 m^{-1}), respectively. The SEC results for these glacial ice samples showed a deficit in larger organic molecule groups given that humic substances (HS) were below the detection limit and biopolymers (BP) had a very minor contribution to DOC (< 5%). Glacial ice samples had much higher proportions of low molecular weight SEC components and protein-like fluorescence (Table 3.4A; Figure 3.4D). A supraglacial stream sampled on Gilman Glacier had an even lower DOC concentration (0.18 mg C L^{-1}), α_{255} (0.57 m^{-1}), weak fluorescence peaks, and was primarily composed of BP (33.1 %), LMW-N (32.3 %), and HS (27.8 %). The presence of humic substances in the supraglacial stream implied that meltwaters were not derived exclusively from glacier ice, and likely included DOC from melting snow and firn, and solubilizing of aeolian deposition of POC on glacier surfaces.

The snow sample taken on Gilman Glacier had a high DOC concentration (0.42 mg C L^{-1}) and α_{255} (4.43 m^{-1}), an intense protein-like peak and humic-like fluorescence bands, and SEC data belonging to HS (48.3 %), BB (23.1 %), and LMW-N (21.7 %). Molecular characterization of this glacier snow sample yielded low H:C (1.20) and O:C (0.33), with molecular formulae resembling unsaturated aliphatic (33.1 %) and highly unsaturated aromatic (25.4 %) chemical structures. Notably, this glacier snow sample had a much higher proportional contribution of organic molecules belonging to the polycondensed aromatic black carbon compound class (27.6 %) than any other sample analyzed via FTICR-MS as part of this study (Table 3.4B). This is suggestive not only of anthropogenic aerosol deposition to the glacier surface, but also that the black carbon class molecules were removed prior to being discharged to glacial headwaters. Given that the supraglacial stream had such low measures of DOC quantity, it is possible that microbial processing had already mineralized the majority of black carbon organic molecules on the glacier surface, or that they had been adsorbed to sinking particles in

supraglacial meltwater (i.e., cryoconite). In this fashion, the remaining humic-like organic molecules in melting glacier snow likely mixed with smaller organic molecules in melting glacier ice to form bulk supraglacial meltwaters, prior to being flushed to the proglacial environment. EEMS spectra for glacial ice, supraglacial stream, glacial snow samples are presented alongside those for the Gilman River transect for comparison in Supplementary Materials (*Appendix A – S3.2A-F*).

Stable carbon isotopes of DOC in glacial headwaters collected during 2016 spanned a narrow range (~ -23.9 to -24.8 ‰; n = 5). These δ^{13}C-DOC values are strongly contrasted by the terrigenous δ^{13}C-DOC signal in active layer thaw water impacted subsurface samples collected from the nearby Skeleton catchment (-29.4 to -29.8 ‰; n = 2) and terrestrial overland seepage (-28.8 to -29.4 ‰; n = 3). The δ^{13}C-DOC of glacial headwaters may have been indicative of higher contributions of geogenic organic carbon from sedimentary rock, that was either delivered to the supraglacial environment via aeolian deposition, or added to meltwaters along ice-marginal channels, or immediately upgradient of glacial headwater sampling sites. Alternatively, the δ^{13}C-DOC in glacial headwaters could be explained by autochthonous production or long-term microbial processing of POC in the supraglacial environment. The δ^{13}C-POC of suspended sediment in glacial headwaters (-24.0 to -27.0 ‰; n = 5) were more variable than δ^{13}C-DOC, but also much less negative than terrestrial organic material. Similarities in δ^{13}C-DOC and δ^{13}C-POC could arise from common sources of dissolved and particulate organic phases, such as aeolian deposition of POC to glacier surfaces, sorption of DOC in meltwaters to suspended particles, and/or <0.45 µm particles comprising part of DOC. On the other hand, the one glacial headwater sample analyzed for δ^{13}C-DOC taken from Henrietta-Nesmith during the high flow year (2015) was much more negative (-28.1 ‰) than the 2016 samples (- 24.2 ± 0.4 ‰), which implies that terrestrially-derived organic material may be more important in the δ^{13}C-DOC of this singular 2015 sample.

Isotopic values of radiocarbon (^{14}C) identified that DOC in glacial headwaters was not ^{14}C-modern, but rather ^{14}C-ancient (~2900 to 7800 yBP; n = 9), in all cases. In fact, many of these samples (n = 5) pre-date the most recent glacial retreat of the Lake Hazen watershed (~5 ka yBP). In order for >5 ka BP samples to be possible, any ^{14}C produced since deglaciation must have been diluted with ^{14}C-dead organic material, which could have originated from microbial re-working of fossil fuel derived black carbon particles, glacial till predating the last deglaciation, or OC-poor geogenic sedimentary rock particles on glacier surfaces, along glacier margins, or immediately upgradient of glacial headwaters. Alternatively, ^{14}C ancient POC could be processed by microorganisms in porewaters of the riverbed

and hyporheic zone and released to the DOC pool. Ultra-fine particles <0.45 µm that comprised suspended sediment may also have been quantified as DOC. During the medium flow year (2016), Δ^{14}C-DOC spanned -438 to -623 ‰ (avg. = -535 ± 69 ‰; n = 7), translating to ^{14}C ages ranging from 4570 to 7762 yBP (Figure 3.5A-D; Table 3.4B). Two ^{14}C samples taken during the lower flow year (2017), from Gilman and Abbe glacial river headwaters, were found to have less negative Δ^{14}C-DOC values (-308 and -355 ‰), and younger ^{14}C ages (2892 and 3451 yBP), respectively. Gilman River glacial headwaters were sampled twice during 2016 (July 11th; –557 ‰ and August 1st; -623 ‰) and once during 2017 (July 20th; -355 ‰). Although ^{14}C differed, these Gilman River headwater samples were highly similar with respect to DOC concentration and composition data (Table 3.4A-B). In fact, the entire array of Δ^{14}C-DOC values did not respond strongly to quantitative measures of DOC, nor its composition, among glacial headwaters samples (Figure 3.5A-D). These findings suggest that increased ablation during the higher melt year (2016) either mobilized increasingly ^{14}C ancient DOC from the supraglacial environment, from the riverbed and laterally expanded hyporheic zone of the proglacial environment, ice-marginal channels, or ultra-fine <0.45 µm particles suspended in glacial meltwaters.

3.3.3 Downriver changes in DOC quantity and composition

DOC sampled at downriver sites were rarely representative of glacial headwaters. DOC concentrations in river deltas increased in almost all cases relative to respective glacial headwaters, although the extent of this increase was variable amongst the glacial rivers and between years. Only the Abbé River remained relatively unchanged in downriver DOC concentrations, whereas increases were observed for Blister (+0.1 ± 0.1), Gilman (+0.2 ± 0.2), and Snowgoose (+0.2 ± 0.1) in mg C L^{-1}. Given the extremely low concentrations of DOC in glacial river headwaters, this translated to ~1.6 to ~3X downriver increases. Detailed monitoring of the Blister and Snowgoose River deltas during 2015 and 2016 yielded an unresponsive distribution of DOC concentrations during the progressive ramp-up of glacial meltwater pulses, for which peak flow generally took place mid-July (*Appendix A – S3.3A-B*). The Turnabout River was anomalous as it flowed through a small lake and had a particularly high suspended sediment load. A complete transect of the Turnabout River in 2018 showed that while glacial headwaters had a DOC concentration of 0.29 mg C L^{-1} there was a 6-fold increase to 1.80 mg C L^{-1} in Turnabout Lake, which remained relatively stable (~1.89 mg C L^{-1}) towards the river delta. (Table 3.6A). Therefore, glacial rivers are not simple pipelines for DOC in glacial runoff, and there are sources of DOC in the proglacial environment.

Downriver changes in DOC concentration and composition were unidirectional for almost all rivers, suggesting common sources and/or processes influencing DOC along glacial river transects. A Pearson's correlation principal component analysis (PCA) was conducted in which DOC absorption, fluorescence, and SEC were used to illustrate separation of DOC characteristics in glacial river headwater samples compared to those taken from downriver sites (Figure 3.6A). Primary (F1) and secondary (F2) principal components accounted for 57.8 % of the total variance for data constituting 37 discreet observations and 9 descriptive variables, or measures of DOC composition. The % humic fluorescence and %HS were strongly correlated ($R^2 = 0.73$), whereas degraded humics, or building blocks (BB), were less strongly correlated with these parameters ($R^2 = 0.43$ and 0.34, respectively). Protein fluorescence % was correlated with %LMWN ($R^2 = 0.58$) and %BP ($R^2 = 0.44$). Bins of samples taken from glacial headwaters were generally observed to group within the upper left quadrant of the biplot where the composition of DOC was moreso controlled by BP% and protein-like fluorescence. DOC sampled from downriver sites showed a compositional shift towards the lower right quadrant based on the addition of humic-like organic material along glacial river transects. Binning these same observations based on year (2015-18) also served to provide spatial separation in DOC composition (Figure 3.6B). Samples taken during 2018 were higher in %HS and lower in %LMWN when compared to 2016 and 2017 for bins of both glacial headwater and downriver samples ($p < 0.05$). The %BB and % humic fluorescence also tended to be higher in 2018, although not achieving the same level of significance. DOC concentrations during 2018 were towards the higher end of the distribution for Blister, Snowgoose, and Turnabout Rivers, which could have influenced a shift towards larger organic molecules of increasingly humic character. Extremely low glacial river flow conditions were observed during 2018, such that small proglacial sources of humic-like DOC may have been more important than other years. The sparse observations for 2015 ($n = 4$) fell within the distributions of data for the other years. Therefore, downriver additions of DOC were almost exclusively linked to an increase in humic-like character increasingly associated with organic material derived from the terrigenous environment.

Several proglacial surface water inputs have the potential to influence DOC quantity and composition in glacial rivers. Several small overland seepage sites, characterized by water trickling over low-lying vegetation and organic-rich soil, were found flowing into Blister River along the glacier to delta transect and sampled opportunistically during hikes. Blister River was short (~ 10.5 km) and had comparatively low flow originating from two minor glaciers (Arrow and Bridge) that were isolated at lower elevation and not part of the ice cap. The overland seepage sites sampled

ranged in DOC concentration from 0.61 to 3.73 mg C L^{-1} with $SUVA_{255}$ (7.83 ± 1.43), spectral slope ($S_{275-295}$ = 0.015 ± 0.002), and dominant humic-like (A+C+M) (95.4 ± 1.3 %) fluorescence character relative to that of protein-like (T+B) peaks (4.6 ± 1.3 %). Overland seepage sample EEMS showed compositional similarities spanning 2015-2017 with excitation/emission maxima centered on Ex. <250 (~330) / Em. ~450 nm (*Appendix A – S3.4*). SEC data further described the chemical nature of DOC in overland seepage sites as having dominant contributions of humic substances (HS; 77 ± 4 %) and building blocks, or degraded humics (BB; 13 ± 1 %), that accounted for ~ 90% of the DOC. Stable carbon isotopes of DOC (δ^{13}C-DOC) had highly negative values for the overland seepage sites (-29.1 ± 0.3 ‰) that were congruent with that of soil-derived OC in subsurface samples of the nearby Skeleton catchment (SK sub ~ 29.6 ± 0.3 ‰). Streams flowing over OC-poor sedimentary rocks were also observed to be flowing into Blister River, and had DOC concentrations ranging from <0.1 to 1.16 mg C L^{-1}. Stream samples associated with the higher end of this DOC concentration gradient were expected to have greater contributions of OC either leached from streambeds, banks, and/or added via upgradient ground ice thaw water inputs.

Downriver increases in DOC concentration were commensurate with changes in other measures of DOC quantity, and increases in humic-like character. For instance, Gilman River had a downriver increase in DOC concentration (0.16 ± 0.09 to 0.40 ± 0.16 mg C L^{-1}) that was accompanied by an increase in α_{255} (0.74 ± 0.31 to 2.6 ± 1.0 m^{-1}). This addition of DOC was not reflected in significant changes in absorption characteristics, with $SUVA_{255}$ (6.4 ± 2.8) and $S_{275-295}$ (0.015 ± 0.003) remaining relatively stable spanning the transect. In general, humic-like fluorescence (A+C+M) increased from 56 ± 11% to 77 ± 3% along the Gilman River transect, accompanied by a significant ($p < 0.05$) increase in humic substances (%HS) and decrease in biopolymers (%BP), whereas LMWN remained low (26 ± 11 %). In contrast, one anomalous sample collected from the Gilman delta during 2016 (Aug 1st) had much higher protein-like fluorescence (T+B; ~74%), and low molecular weight neutrals (LMWN; ~73%), than the remainder of samples taken at this site. Together, these findings indicate that the downriver addition of DOC to the Gilman River was typically composed of humic-rich organic material (Table 3.6A), and were supported by FTICR-MS molecular characterization for the Gilman River. Downriver decreases in H:C from 1.41 to 1.27 during 2016, and from 1.39 to 1.30 during 2017, translated to higher proportional contributions of polyphenolic and highly unsaturated aromatic material for Gilman River delta samples (Table 3.6B). There were also downriver changes in δ^{13}C-DOC and δ^{13}C-POC. The Gilman River glacial headwaters had less negative δ^{13}C-DOC and δ^{13}C-POC (-23.9 and -24.1 ± 0.1 ‰) compared to the delta (-25.7 ± 0.5 and -25.7 ± 0.3 ‰),

respectively. This downriver shift was consistent with a downriver addition of terrigenous organic matter. Furthermore, ^{14}C-ancient glacial river headwaters (Δ^{14}C = -496 ± 166 ‰) became even lower downriver (-635 ± 69 ‰), the latter of which corresponding to ^{14}C ages of 8127 ± 1620 yBP. This downriver decrease in Δ^{14}C-DOC was observed in July and August of 2016, as well in July 2017, where Δ^{14}C became ~40, 92, and 285 ‰ lower, respectively. Therefore, downriver additions of DOC were humic-like, and terrigenous (δ^{13}C-DOC), but also increasingly ^{14}C-ancient. This DOC must have been derived from old soil organic carbon (i.e., glacial till) that was formed prior to the last deglaciation (> 5ka BP).

Stable (δ^{13}C) and radiocarbon (Δ^{14}C) isotopes revealed proglacial sources of DOC that varied along glacial river continua, and were influenced by meltwater flow conditions. For instance, during the medium flow year (2016), δ^{13}C-DOC was found to be less negative in glacial headwaters (-24.3 ± 0.4 ‰) compared to downriver sites (-25.7 ± 0.5 ‰; p <0.05). On the other hand, the δ^{13}C-POC spanned very similar ranges in glacial headwaters (-24.0 to -27.0 ‰) and downriver sites (-24.4 to -27.0 ‰), and had an overall average value of -25.7 ± 1.2 ‰. Although δ^{13}C-DOC and δ^{13}C-POC were not strongly correlated, the δ^{13}C-DOC typically became more similar to the δ^{13}C-POC downriver, suggesting that POC in the riverbed and suspended sediment could be a source of humic-like material to the DOC pool. Glacial river deltas sampled during the high flow year (2015) had much more negative δ^{13}C-DOC (-29.7 ± 1.7 ‰), less negative δ^{18}O-H_2O (-28.2 ± 0.8 ‰), and higher measures of humic-like DOC chemical composition compared to 2016 (p <0.05; Figure 3.7A-D). In the case of these 2015 samples, the δ^{13}C-DOC and δ^{18}O-H_2O values were similar to subsurface samples (SK catchment) and overland seepage sites that flowed into Blister River. On one hand, Blister River was associated with the least significant modelled runoff stemmed from sparingly glacier covered terrain (~ 6 km^2)[95], so proglacial surface water inputs would presumably be of greatest hydrologic significance. However, the Blister River delta had much older Δ^{14}C-DOC during 2015 (-441 ‰; 4615 yBP) compared to that of an overland seepage site (-190 ‰; 1624 yBP). Furthermore, Blister River glacial headwaters (-441 ‰; 4615 yBP) actually became slightly older downriver (-563 ‰; 6593 yBP) during 2016, despite a concomitant downriver increase in DOC concentration and humic-like composition. Overall, strong relationships of DOC concentration, composition, and δ^{18}O-H_2O data with Δ^{14}C-DOC were not found across the entire dataset, although preliminary evidence of inter-river and interannual differences between samples was apparent (Figure 3.8A-D). Although DOC composition and δ^{13}C became more similar to that of overland seepage sites as meltwaters evolved downriver, the Δ^{14}C indicated an older DOC source than that in the singular surface water inputs that

was sampled, such as the POC in the riverbed and suspended sediment. In fact, Δ^{14}C-DOC remained ^{14}C-ancient along glacial river transects, or even became slightly older, coinciding with increasingly negative δ^{13}C-DOC downriver. This relationship of δ^{13}C-DOC and Δ^{14}C-DOC was a striking finding, given that increasingly negative δ^{13}C-DOC almost always coincides with comparatively ^{14}C-modern DOC. This finding confirmed the importance of DOC additions along glacial river transects that was indicative of terrigenous, humic-like organic material derived from ^{14}C-ancient glacial till.

Inter-river variability in DOC quantity, composition, and isotopes could be related to physical riverine features, and watershed characteristics. The most extensively glaciated rivers (Henrietta-Nesmith and Gilman) generally had lower humic characteristics (% humic fluor. and %HS), higher % BP, and more negative Δ^{14}C-DOC (*Appendix A – S3.5A-B*). However, Snowgoose and Turnabout Rivers had very similar %glaciated (~38 to 39 %), but had distinct ranges in DOC concentrations (Snowgoose <0.10 to 0.68 mg C L^{-1}; Turnabout 0.74 to 1.89 mg C L^{-1}). Apart from one anomalous sample (August 2016), the Turnabout River also had higher measures of humic-like DOC. Snowgoose River was much shorter (~16.6 km) than the Turnabout River (~41.9 km), which could have influenced the relative availability of DOC sources along these glacial river continua. The Turnabout River flowed through a small lake during its transit towards Lake Hazen, which likely also contributed to the particularly high DOC concentrations and humic-like character detected for the Turnabout River delta. On the other hand, despite having comparable lengths, the Turnabout and Very (~39 to 42 km), and the Abbe and the Gilman (~21 to 22 km) also had differences in DOC concentration and composition. There were also similarities between the longest rivers (Turnabout and Very), in that they had Δ^{14}C-DOC values that were among the least negative at downriver sites, -400 and -477 ‰, respectively. Molecular characterization data identified that Turnabout and Very River had low H:C (~1:13) and high O:C (~0.47), selecting for high proportional contributions of organic fractions of highly unsaturated aromatics (76.5 ± 2.8 %) and polyphenolic structures (14.5 ± 0.6 %; Table 3.6). Thus, although the Very River had much lower DOC concentrations (0.25 to 0.40 mg C L^{-1}) the chemical character of DOC was similar when compared to the Turnabout River. Anomalously, DOC concentrations for the Snowgoose transect sampled August 1st 2016 (glacial headwaters) and July 30th 2016 (delta) showed a slight decrease from 0.20 to 0.10 mg C L^{-1}. This was confirmed with quantitative measures of absorption (α_{255}) that showed a decrease of similar magnitude (0.98 to 0.51 m^{-1}; ~2X decrease) for these samples. This transect for Snowgoose River showed ^{14}C-ancient organic material in glacial river headwaters (-569 ‰) that was very similar to that sampled downriver (-607 ‰), corresponding to ^{14}C ages of ~6704 and 7448 yBP, respectively. Δ^{14}C-

DOC was comparatively less depleted in Abbe (-355 ‰) and Blister (-441 ‰) glacial headwaters, which became markedly more ^{14}C-ancient (-449 and -563 ‰, respectively) for downriver sites, along with increased DOC concentration, α_{255} and humic-like character. Inter-river and interannual variability underscore the importance of considering transects individually when assessing the transformation of DOC along glacial river continua. However, downriver shifts towards more negative δ^{13}C and Δ^{14}C coincided almost exclusively with increases in DOC concentration, α_{255}, humic fluorescence %, and decreases in proportional contributions of biopolymers (%BP) (Figure 3.10A-G; *Appendix A – S3.6A-H*). This suggests that, although downriver sources of DOC are similar among most glacial rivers, the extent to which they act to supply OC to the DOC pool are variable, and are likely based on a combination of factors, such as the extent of glacier coverage, length of the river, and meltwater flow conditions.

The source of DOC along glacial river transects is most likely the riverbed. The hyporheic zone becomes laterally expanded downriver, especially in braided river deltas, wherein DOC produced from the microbial processing of POC in riverbed sediment may enter the DOC pool in porewaters, and subsequently the bulk glacial river meltwaters. This process becomes more important during high flow conditions, as do the concentrations of suspended material (TSS, PC) in meltwaters. Although these variables were not strongly correlated with Δ^{14}C-DOC, samples with the highest TSS and PC concentrations coincided with some of the most negative Δ^{14}C-DOC values (*Appendix A – S3.7*). Furthermore, less negative Δ^{14}C-DOC values for Abbe and Gilman River during the lower flow year (2017) were typically associated with lower TSS and PC. Measures of TSS and PC were likely not directly responsible for Δ^{14}C-DOC, but rather correlated with the effects of increased meltwater flux. However, there is also the possibility that ultra-fine grain <0.45 μm suspended particles could be quantified as 'DOC', and may have contributed to the quantification of Δ^{14}C-DOC. These mechanisms by which ^{14}C-ancient, humic-like DOC enters glacial rivers are not mutually exclusive, although exfiltration of porewaters also explains downriver increases in stable water isotopes and tritium. Therefore, exfiltration of hyporheic zone porewaters was found to be the principal mechanism controlling DOC concentration and composition along glacial river continua.

3.3.4 Characteristics of DOC in Lake Hazen

DOC concentrations for surface layer (0 m) and deep (250 m) samples of Lake Hazen (2015-16; ~ 0.3 to 0.4 mg C L^{-1}) were within the range of glacial river discharges (<0.1 to 1.1 mg C L^{-1}) for these years (Table 3.6A). During the highest flow year (2015), Lake Hazen surface water had δ^{13}C-DOC (-

30.6 ‰) and Δ^{14}C-DOC (-327 ‰, or ~ 3112 yBP; Table 3.6B). This was comparable to glacial river discharges during 2015 (-28.1 to -31.9 ‰), of which the only sample analyzed for Δ^{14}C-DOC (Blister River) was also similar (-441 ‰, or ~ 4615 yBP). Furthermore, during the medium-high flow year (2016), Lake Hazen surface water had a similar Δ^{14}C-DOC (-415 ‰, or 4247 yBP), that was at the upper end of the range of glacial river discharges sampled that same year (-400 to -714 ‰, or 4038 to 9997 yBP). A flow and DOC weighted input of δ^{13}C-DOC and Δ^{14}C-DOC was calculated for the seven major glacial river discharges to Lake Hazen during 2016, using modelled runoff from a recent study[95]. Average DOC concentrations, δ^{13}C-DOC, and Δ^{14}C-DOC values for glacial river discharges (mid-July, early August) were incorporated into this calculation. The mass weighted DOC concentration for the glacial rivers (~0.5 mg C L^{-1}) and Δ^{14}C-DOC (-501.9 ‰, or 5535 yBP) were older than those of the Lake Hazen surface water (~ 0.4 mg C L^{-1}; -415 ‰, or 4247 yBP). Whereas the δ^{13}C-DOC was not measured for this Lake Hazen surface water sample, it was likely also comparable to the mass weighted δ^{13}C-DOC (-25.8 ‰). These results point towards DOC in Lake Hazen surface water being a confluence of glacial river discharges, and that slight discrepancies in Δ^{14}C-DOC likely had to with mixing of lake water from previous years (i.e., long lake residence time). However, there are several potential mechanisms by which small amounts of comparatively ^{14}C-modern DOC may have entered Lake Hazen, such as small non-glacial inputs (Salor Creek, Skeleton Creek). Assuming that non-glacial surface water inputs were ^{14}C-modern (~0 ‰), and had DOC concentrations of ~ 2 mg C L^{-1}, they would need to account for ~5% of the hydrologic budget to Lake Hazen to match surface water Δ^{14}C-DOC. This is an extreme overestimation, and it is expected that non-glacial inputs are both hydrologically and chemically insignificant to Lake Hazen. Another potential source of less ^{14}C-ancient DOC to Lake Hazen surface waters could include in-situ primary production. Lake Hazen Δ^{14}C-DIC (Chapter 4) was less negative than Δ^{14}C-DOC, so C fixation and autochthonous production of DOC from DIC could have resulted in less negative in-lake Δ^{14}C-DOC than in bulk glacial river discharges. Adsorption of DOC to sinking particles may have also been a sink of ^{14}C-ancient DOC to the lake sediment, whereby any comparatively ^{14}C-modern DOC additions would become more important. Similar logic could apply if <0.45 μm suspended sediment particles contributed to Δ^{14}C-DOC that was quantified in turbulent glacial rivers, that then settled out of solution once in Lake Hazen. Given that surface water samples were taken at the centre of Lake Hazen far removed from glacial river plumes, and that the lake has a long residence time and is generally well-mixed, this surface water sample should be an unbiased representation of in-lake DOC and Δ^{14}C-DOC. In order to better constrain the vertical distribution and temporal variability of DOC

in Lake Hazen, more extensive sampling and analyses for DOC composition and isotopic character could be conducted spanning a range of depths and sampling years. The legacy of ^{14}C-ancient DOC in glacial rivers is largely retained in Lake Hazen, and mixing of lake waters from previous years is likely the cause of slight differences in Lake Hazen DOC versus flow-weighted calculations. Although less probable, inputs of comparatively ^{14}C-modern DOC to Lake Hazen surface waters, or preferential removal of ^{14}C-ancient organic carbon to the sediment could have been contributing factors to this apparent discrepancy.

3.4 Discussion

3.4.1 Relative importance of water sources to glacial river headwaters and along the river length

Differing supraglacial and proglacial water sources affect the extent of DOC loading and its chemical characteristics along river continua. The supraglacial environment is expected to contain material (snow, ice, meltwater) that is isotopically representative of precipitation to glacier surfaces, where evaporation and/or sublimation, and successive freezing, melting, and re-freezing events take place over time, and can impart fractionation to water isotopes[311–313]. Stable water isotopes of snow, supraglacial stream, and glacial ice samples from Gilman and Henrietta-Nesmith glaciers plotted closely to both the global meteoric water line (GMWL) and the local glacier ice melt water line (LGIMWL). The glacial river headwater samples also coincided with the GMWL and LGIMWL, confirming a dominant meteoric signature that was shaped by atmospheric deposition to the supraglacial environment, and any subsequent isotopic fractionation associated with evaporation and selective freezing. Isotopic separation of glacial rivers along the LGIMWL was explained by unique glacier and river catchment features. The most isotopically negative δ^2H-H_2O and δ^{18}O-H_2O signatures corresponded to the largest glaciated areas for the Henrietta-Nesmith (1041 km^2) and Gilman (704 km^2) river catchments, whereas more sparingly glaciated river catchments such as Snowgoose (89 km^2) and Blister (6 km^2) were less negative. Larger glacier expanses were generally correlated with higher altitudes in the Lake Hazen watershed, which would be associated with colder temperatures and consequently more intense fractionation during, and prior to, the condensation of water vapour and snowfall. Precipitation to high altitude supraglacial environments would thus be expected to be more depleted in water isotopes, which would be reflected in meltwaters sampled from receiving glacial rivers.

Glacial river headwaters are a confluence of melting snow and ice from various supraglacial flowpaths that primarily were observed to flow over glacier tongues, but also around glacier ice margins (i.e., the edges of glacier termini). In the proglacial environment, small braided channels would often coalesce within <500 m of the glacier termini at which point they were sampled, although for the Henrietta-Nesmith Glacier proglacial meltwater flowpaths maintained some heterogeneity along the extent (4.6 km) of the river. Glaciers of the Lake Hazen watershed have been reported to be cold-based[85], which, coupled with in-field observations, implied that subglacial contributions to bulk meltwater were likely heavily restricted to areas of close proximity to glacier termini. This rationale, coupled with extremely low concentrations of dissolved ionic species in the glacial headwaters[203], are in line with these glaciers being cold-based with minimal sub-glacial contributions.

Interannual variability in water isotopic data for glacial river transects showed the most extreme differences between data distributions between the warm, high flow year (2015) and the cold, low flow year (2017) that had numerous precipitation events. Water isotopic data for all sampling years followed relatively similar linear regression slopes given that glacier ice meltwater was by far the dominant water source to glacial rivers. However, a major difference observed was a shift along the y-axis where 2015 data plotted below the GMWL and LGIMWL, and 2017 data plotted above these linear equations. Meltwaters originating from glacier ice with unique formation chronologies can reflect historic climate artefacts (temperature, precipitation) in glacial ice core water isotope data[314,315]. To this effect, the depth of glacial ablation during different melt seasons could be an important consideration when interpreting unique water isotope data distributions. For instance, intense meltwater fluxes in 2015 implied that greater glacier ablation depths, and likely also higher elevation ablation zones, were reached over the course of the season. Greater ablation depths would access ‘older’, perennially frozen glacial ice and firn that could have different water isotopic signatures compared to surficial material. Conversely, not only were ablation depths expected to have been much less extensive during 2017, but numerous precipitation events could have supplied ‘fresh’ locally derived precipitation to supraglacial environments that was then flushed to glacial rivers on more rapid time scales (i.e., same melt season). The Lake Hazen watershed is located within an arid Arctic desert landscape, from which excessive evaporation could have resulted in isotopically lighter, locally derived precipitation being delivered to supraglacial systems. Given the extensive precipitation during 2017, this could have resulted in the shift in the water isotopic data above the LGIMWL for glacial river transect samples during this year.

In the Canadian high Arctic and Greenland Ice Sheet, the legacy of bomb ^{3}H in fresh deposition has been progressively removed over the past several decades as natural background atmospheric ^{3}H concentrations are approached[309,310]. However, higher ^{3}H concentrations were present in precipitation in the 1950s to 1980s and can be preserved at depth in glacial ice cores. We can assume that if meltwaters were derived from ice formed *before* thermonuclear testing began in the 1950s the natural pre-bomb ^{3}H concentrations would have decayed below the detection limit (< 1.0 T.U.) while sequestered in glacial ice preceding our sampling seasons (2015-18). Ice cores of the Canadian high Arctic[316] and elsewhere[317–319] have identified ^{3}H bomb peak concentrations in ice sampled at least several meters below the glacier surface. The depth of ^{3}H bomb peaks in glacial ice can be variable based on the extent of precipitation, rates of compaction and accumulation of material of glacial surface, and the extent of ablation. For instance, a recent study of the Canadian Arctic Archipelago showed highly negative modelled glacier ice mass balances near glacier tongues, whereas neutral and positive mass balances existed at higher altitudes in regions more centralized within glacial expanses[74]. Depth of ablation zones and the magnitude of meltwater fluxes thereby derived could thus relate to ^{3}H concentrations measured in supraglacial meltwater flux. Furthermore, the source of precipitation to the supraglacial environment, and potentially even altitudinal isotopic fractionation effects, could also shape supraglacial ^{3}H concentrations. Although a reconstruction of proportional contributions of water from specific supraglacial compartments was not approached as part of this study, it is unlikely that either pre-bomb ^{3}H, or peak-bomb ^{3}H, were significant components of bulk supraglacial meltwater discharge.

Glacial rivers had lower ^{3}H concentrations than opportunistic precipitation and snowpack samples of the Lake Hazen watershed, and the average baseline ^{3}H in precipitation expected for the Canadian North[310,320]. Low ^{3}H concentrations in glacial headwaters (1.7 to 6.5 T.U.) could be explained by an inclusion of older glacial meltwaters to bulk meltwaters, which has been proposed previously for glacial runoff in the Wind River Range, Wyoming (2.6 to 10.8 T.U. [321]). For instance, based on modern ^{3}H concentrations in precipitation (~10 to 20 T.U.), and the half-life of ^{3}H (~12.4 years), sequestration of frozen material on glacier surfaces for at least a couple decades would be required in order to reach $^{3}H < 3$ T.U. Alternatively, modern precipitation to high altitude glacier surfaces may have undergone intense isotopic fractionation during successive condensation events, such that the heaviest isotope of water (^{3}H) may have already been considerably depleted upon atmospheric deposition. Direct comparisons of ^{3}H concentrations between studies are often unrealistic based on changing bomb-test ^{3}H in the atmosphere over time, global variability in atmospheric ^{3}H (i.e. lower in

the Southern hemisphere), and strong latitudinal dependence of ^{3}H in precipitation[309,322]. Even so, ^{3}H concentrations in glacial headwaters of the Lake Hazen watershed were similarly low to a glacial stream of the Lake Fryxell watershed, Antarctica (3.1 ± 0.3 T.U. [313]). By way of contrast, the Bhagirathi River, draining the Gangotri Glacier, was found to have higher average ^{3}H concentration (8.8 T.U.), which was attributed to meltwater inputs from relatively modern glacial snow, rather than older glacial ice[323]. In our study of the Lake Hazen watershed, given that only one supraglacial snow sample was collected and measured for ^{3}H concentration, the variability in ^{3}H amongst glaciers (altitudes) and their respective supraglacial compartments (glacial ice, firn, and snow) remains unclear. However, what can be concluded, is that bulk supraglacial meltwaters stemming from glaciers of the Lake Hazen watershed were a composite of meltwaters derived from recent precipitation to glacier surfaces, as well as aged meltwaters from deeper ablation zones.

Further into the proglacial environment, glacial river discharges to Lake Hazen ranged in ^{3}H concentrations from 2.3 to 11.5 T.U. spanning 2015-17, and were quite similar to ^{3}H reported for the Yukon River (3.0 to 12.9 T.U. [324]). Low ^{3}H concentrations in the Yukon River were attributed to glacial meltwater being a much more important water source compared to the remaining five major rivers draining the pan-Arctic watershed (8.6 to 34.9 T.U. [324]).

At a particularly high latitude (~82ºN), the Lake Hazen watershed is underlain by continuous permafrost that generally remains unperturbed and stable over long periods of time. Elevated ^{3}H concentrations have been associated with permafrost thaw influenced waters in the Canadian sub-Arctic[325] and Qinghai-Tibet Plateau[326], particularly for sporadic discontinuous and extensive discontinuous permafrost regions. In the Lake Hazen watershed, ground ice thaw water inputs to glacial rivers could have resulted in the slight enrichment of ^{3}H observed along Blister, Gilman, and Snowgoose River transects sampled during 2016 and 2017. Ground ice thaw water inputs may have entered glacial rivers either by surficial inflows of small streams or overland seepage, infiltration along the river banks, or thawing of the riverbed and mixing in the hyporheic zone. Ground ice thaw water was likely comprised of spring snow melt water, or summer rain. Likely of less significance, ground ice thaw water could have also originated from the lower active layer or permafrost in the case of exposed ground ice seams along glacial river banks, for which vertical profiles can span a range of ^{3}H concentrations[327]. Smaller amounts of peak-bomb ^{3}H from the 1960s could have potentially also contributed to downriver increases in ^{3}H concentrations.

Higher ^{3}H concentrations for glacial river samples collected during the 2015 appeared to support the increased hydrologic importance of ground ice thaw waters, or modern precipitation, during this warm, high flow year. While water isotopic values for 2015 did not coincide with the ground ice thaw water line (GITWL), the 2015 data array did plot closer to the GITWL when compared to other sampling years. This could also explain the highest downriver ^{3}H concentrations belonging to the most sparingly glaciated rivers (Blister and Snowgoose), where proglacial water sources would have been of greater bearing.

Riverine features were likely related to the hydrologic importance of ground ice thaw water sources to glacial rivers. For instance, the lateral expansion of the hyporheic zone during high flow conditions would increase the surface area of meltwater contact with the riverbed and riverbanks, potentially accelerating ground ice thaw. Particularly in the case of braided channels of river deltas, widening of meltwater flowpaths could contact subsurface thaws that would be otherwise inaccessible. Alternatively, greater densities of overland seepages sites and inflowing streams could also increase ground ice thaw water contributions to glacial rivers.

In summation, tritium and stable water isotopes provide insight into the likely sources of DOC to glacial rivers. Low ^{3}H in glacial headwaters indicated that bulk meltwaters were a mix of recent precipitation to glacier surfaces, and older ice melt from deeper ablation zones. Atmospheric deposition of organic carbon to glacier surfaces may have therefore been sequestered for several decades prior to being flushed to the proglacial environment, during which time biogeochemical processes likely changed its chemical composition. Lower ^{3}H and more negative $\delta^{18}O\text{-}H_2O$ in glacial headwaters of more extensively glacier covered river catchments also suggest that DOC might be mobilized from older glacier ice. Alternatively, larger glaciers might simply have lower ^{3}H and more negative $\delta^{18}O\text{-}H_2O$ based on more intense isotopic fractionation associated with colder temperatures, and higher altitudes. In either case, it is likely that larger glaciers, associated with higher glacial meltwater fluxes, would have DOC in glacial headwaters that was more representative of DOC in bulk supraglacial meltwaters. This rationale was in line with the most ^{14}C-ancient glacial headwaters (i.e., $\Delta^{14}C$-DOC) belonging to extensively glacier covered catchments (Henrietta-Nesmith, Gilman).

Downriver, high ^{3}H and $\delta^{18}O$ during the highest flow year (2015) were contrasted by lower values during low flow conditions (2017), indicating that proglacial water sources were of greater importance during higher flow conditions. Proglacial water sources are likely derived from the thawing of ground ice, and could be delivered to glacial rivers via surface water inputs (overland

seepages, small streams), or by porewater infiltration through the riverbed. Indeed, higher flow conditions could cause the lateral expansion of the hyporheic zone at downriver sites, and access biogeochemically unique water sources. For instance, overland seepage sites flow over organic-rich active layer soils, whereas older organic material from lower soil horizons, in abundance of OC-poor sedimentary rock, composes the riverbeds of glacial rivers. Surface water inputs would be diluted ~1000X in glacial rivers, so it is extremely unlikely that thaw waters with ^{3}H concentrations of recent precipitation could account for downriver increases in ^{3}H. On the other hand, incorporation of bomb-peak ^{3}H from ground ice thaw infiltration through the hyporheic zone and river bed would require smaller additions to water to elicit this change in ^{3}H, and is a much more likely explanation. Furthermore, given that $\Delta^{14}C$-DOC remained ^{14}C-ancient, and even decreased slightly along several river transects, the riverbed must have been the principal source of ground ice thaw water and DOC.

3.4.2 Supraglacial DOC sources are similar to other glaciers worldwide, and a contributor of humic-poor DOC to glacial runoff

Glacial ice of the two glaciers sampled in the Lake Hazen watershed (Gilman, Henrietta-Nesmith) had very low concentrations of DOC with low humic content, similar to other glaciers sampled worldwide. For instance, DOC concentrations in glacier ice were typically <0.5 mg C L^{-1} for studies ranging from the Tibetan Plateau[209,244,252,253], the Greenland Ice Sheet[177,247,249], the Antarctic Ice Sheet[217,230,231], the European Alps[212], and the high Arctic[213,219,246]. However, higher DOC concentrations have also been reported, such as those for glacial ice cores sampled from White Glacier and John Evans Glacier of the Canadian high Arctic[222]. Specific absorption coefficients ($SUVA_{254}$) for our Lake Hazen watershed glacial ice samples were extremely low and fell within the same range as those previously identified for glacial ice sampled from Mount Nyainqentanglha and Karola glaciers of the Tibetan Plateau[209]. Further, low humic-like fluorescence and non-detect humic substances in SEC results for Henrietta-Nesmith and Gilman glacial ice were in line with results from a recent study[219] where glacial ice sampled from the Devon Ice Cap of the Canadian high Arctic was found to have EEMS dominated by protein-like fluorescence. The comparatively weak humic-like fluorescence that prevailed was restricted to shorter excitation and emission wavelengths, similarly to glacial ice EEMS in this study (*Appendix A - S3.1A-F*). The low concentrations of humic-poor DOC in glacial ice were not surprising, as terrigenous sources of organic material to the supraglacial environment would be minor, and years of slow acting degradation processes may have further reduced the humic nature of DOC in glacial ice.

The supraglacial stream sample (Gilman Glacier) had low DOC concentration (~ 0.2 mg C L^{-1}) and humic-poor composition that was similar when compared to those in the glacial ice samples. This was also within the range of DOC concentrations identified for supraglacial stream samples in studies conducted elsewhere[177,179,197,198,211,240]. $SUVA_{254}$ for supraglacial streams of the Mendenhall Glacier[179] were also comparable to that determined for the Gilman Glacier. Whereas supraglacial stream DOC has been reported to primarily exhibit protein-like fluorescence characteristics[178,179,240], the presence of mineral particles, such as those found in supraglacial stream sediment and cryoconite holes, has been associated with a shift to favour humic-like fluorescence[251]. Although SEC data indicated slightly higher proportional contributions of biopolymers (%BP) and humic substances (%HS) in the supraglacial stream when compared to glacial ice, this may have been a product of the extremely low DOC concentration of the sample rather than a significant compositional change. Soil-derived humic-like DOC would be heavily restricted from the supraglacial environment, with aeolian deposition of terrigenous POC being only a minor precursor to the introduction of this material.

Snow sampled from the Gilman Glacier revealed compositionally distinct DOC when compared to the supraglacial stream and glacial ice. The Gilman Glacier snow DOC concentration (0.42 mg C L^{-1}) was within the range of reported values for glacier snow in recent studies (~ 0.1 to 0.6 mg C L^{-1}; [179,197,211,213,231,236,241,244,252]). SEC data supported the presence of both larger humic substances, and smaller organic structures such as amino acids found free or bound in proteins. Indeed, EEMS fluorescence had an intense protein-like fluorescent peak as well as a comparatively fainter humic-like signal, both of which have been shown to contribute to DOC fluorescence in glacier snow[179,221,231,238]. The intensity of the protein-like excitation at ~270 nm was reflected in the absorption spectrum as well, with the corresponding absorption peak distorting the spectral slope ($S_{275\text{-}295}$) calculated from what is typically a relatively featureless exponentially decay in absorption. The H:C (1.20) and O:C (0.33) were low, and molecular characterization highlighted contributions of condensed aromatic black carbon, unsaturated aliphatic, and highly unsaturated terrigenous organic molecules to the DOC pool. These compound classes have also been found to control TOC composition in glacier snow sampled from the Antarctic Ice Sheet[227], whereas a recent study of the Tibetan Plateau found higher lipids and aliphatics, and only sparingly detectable condensed aromatics in glacier snow[238]. Evidence of DOC derived from atmospheric black carbon, or soot, deposition to glacier snow of the Greenland Ice Sheet has been reported where H:C and O:C were 1.22 and 0.41, respectively[197]. Atmospheric deposition of fine-grain particulate material containing incomplete combustion byproducts and black carbon has also been suggested to be a source of radiocarbon (^{14}C)

ancient carbon to supraglacial environments[179,208,209,212]. In summation, the Gilman Glacier snow sample showed evidence of DOC from multiple sources based on the prevalence of not only polycondensed aromatic constituents resembling black carbon, but also highly unsaturated terrigenous organic molecules and unsaturated aliphatics with intense protein-like character.

Sources of organic material to the supraglacial environment have often been studied with respect to their biolabilities. Several studies highlight the increased biolability of ^{14}C-DOC ancient material in glaciated catchments, although supplementary DOC compositional characterization data amongst these biolabile samples has been diverse[208,209,211,212]. Anthropogenic polycondensed aromatic particulate material deposited to glacier surfaces[179] could be part of this ^{14}C-ancient DOC[209,213]. However, terrigenous material from the surrounding landscape would be the principal source of ^{14}C-aged POC in aeolian deposition, including OC from petrified soils, or OC-rich sedimentary rock. Microbial oxidation of particulate carbon could then incorporate its degradation products into the dissolved phase for supplementary processing and recycling. ^{14}C dead material from carbonate minerals could also be incorporated into the supraglacial DOC pool via interplaying chemical weathering and microbial processing pathways. For instance, carbonation reactions of ^{14}C-modern atmospheric CO_2 and ^{14}C-dead carbonate minerals would yield negative Δ^{14}C in the dissolved inorganic carbon pool (Δ^{14}C-DIC) for incorporation in the microbial loop. The resultant Δ^{14}C-DIC of carbonation reactions could be even more negative Δ^{14}C in the case of closed systems (i.e., cryoconite holes) where internal sources of CO_2 are pre-aged. Recent research has highlighted unprecedentedly dynamic supraglacial microbial assemblages, and that DOC produced by photoautotrophs was highly biolabile and rapidly processed by heterotrophic microorganisms[176,178]. Organic material derived from degrading supraglacial microorganisms via cellular lysis and release of their exudates could therefore be a potential source of bioavailable DOC that was either ^{14}C-modern or ^{14}C-old. Similarly, local precipitation derived from the surrounding landscape could be a source of either ^{14}C-modern or ^{14}C-old DOC to glacier surfaces, especially given the intensely evaporative, arid, polar desert landscape conditions and the sparingly concentrated supraglacial DOC.

DOC concentrations in glacial river headwaters of the Lake Hazen watershed are within the ranges reported for glacial runoff, but are typically lower than those stemming from warm and polythermal glaciers[198,210,213,216,217]. Furthermore, DOC concentrations in glacial headwaters encompassed those measured in supraglacial samples (ice, snow, stream), which was expected as bulk discharge is a confluence of supraglacial meltwater sources. Meltwater routing along ice-marginal channels, or

between glacier termini and headwater sites, may have been more been more impactful to glacial headwater samples comprising the higher end of the DOC concentration distribution. However, based on the limited sampling of the supraglacial environment in this study, the variability of DOC in bulk supraglacial meltwaters remains unclear, as are the roles of ice-marginal channels and upstream proglacial environments.

DOC composition in glacial headwaters appeared most similar to that of the supraglacial stream sample as opposed to the glacier ice and snow samples. The supraglacial stream had modest contributions of both smaller (LMW-N, BB) and larger (BP, HS) size classes of organic materials, whereas humic substances (HS) were not detected in glacial ice samples. Furthermore, the high proportion of black carbon components in glacier snow (~28%) was not reflected in the glacial headwater samples (<3%), suggesting that this fraction of organic material was either rapidly processed in the supraglacial environment, or removed from solution via adsorption to sinking particles (i.e., cryoconite). Given the chemical recalcitrance of polycondensed aromatic black carbon, it is unlikely that this compound class exhibited such a high lability relative to the remainder of the DOC pool, and it is much more probable that black carbon was incorporated into the cryoconite. Supraglacial stream water would include melt products of ice, firn, and snow, prior to discharge via supraglacial meltwater channels to the proglacial environment, which could explain the quantitative and compositional similarities of DOC sampled from the supraglacial stream to that in the majority of glacial headwater samples.

Glacial headwater δ^{13}C-DOC values (-24.2 ± 0.4 ‰) were similar to those of the Herbert Glacier outflow glacial end-member determined as part of a recent study of the Juneau Icefield[214], as well as previous research projects that assessed δ^{13}C-DOC in glacial runoff[198,209,213]. Supraglacial productivity, or extensive processing of OC by heterotrophic microorganisms, could explain these δ^{13}C-DOC values, and contributions of smaller organic molecules types (LMW-N ~ 30%, BB ~ 11%), and protein-like fluorescence, to DOC in glacial headwaters. However, DOC character was primarily humic-like, suggesting that terrigenous organic carbon was the main source of DOC to glacial headwaters. Although the δ^{13}C-DOC was starkly contrasted by 'fresh' plant-derived δ^{13}C-DOC in subsurface and overland seepage samples (~ -29 to -30 ‰), old soil-derived OC mixed with geogenic OC from sedimentary rocks could account for less negative δ^{13}C values (> -25 ‰). Aeolian deposition of soil particles and mineral dust to glacier surfaces may have supplied an energy source for supraglacial microbes and affected the δ^{13}C-DOC in glacial runoff. These soils and minerals also

compose the river bed of glacial headwaters, where porewaters infiltrating the hyporheic zone, or <0.45 μm particles in suspended sediment, could also supply this humic-like organic material to the DOC pool in glacial headwaters.

There was interannual variability in Δ^{14}C-DOC in glacial headwaters measured in the medium-high flow year (2016) compared to the lower flow year (2017), which appeared to suggest that either different sources of DOC were mobilized from the supraglacial environment to glacial headwaters, or that the meltwater flux intensity may have been an influential factor. During 2017 (lower flow), Gilman and Abbe glacial headwaters had extremely low DOC concentrations (~0.1 mg C L^{-1}) and Δ^{14}C-DOC of -308 and -355 ‰, respectively. By way of contrast, although the entire array of Δ^{14}C-DOC for glacial meltwater samples (n = 7) taken during 2016 (medium-high flow) also had extremely low DOC concentrations (~0.1 to 0.3 mg C L^{-1}), these samples had a much lower range in Δ^{14}C-DOC (-438 to -623 ‰). This was similar to meltwaters draining the Greenland Ice Sheet, where higher DOC concentrations (0.5 to 4.1 mg C L^{1}) and Δ^{14}C-DOC (~ -250 ‰) were found during low flow, compared to higher flow conditions (0.1 to 0.6 mg C L^{-1}; ~ -400 ‰)[198]. Whereas subglacial contributions were heavily restricted in cold-based glaciers of the Lake Hazen watershed, similar logic could apply in that higher flow conditions resulted in glacial headwaters that were more representative of bulk supraglacial meltwaters. However, there were a couple other major differences in physical and chemical characteristics of glacial headwater sampling sites during these contrasting meltwater flow conditions that may have impacted DOC. In higher flow conditions, lateral expansion of the riverbed and hyporheic zone may have resulted in the exfiltration of DOC in porewaters with older ^{14}C ages. Furthermore, more intense flows typically corresponded to higher concentrations of suspended solids (TSS, PC) in meltwaters, for which concentrations of < 0.45 μm particles would also be higher. It is possible that < 0.45 μm particles (soils, geogenic) were quantified as Δ^{14}C-DOC, and resulted in older ^{14}C ages during high flow conditions. DOC concentrations in glacial headwaters remained extremely low in both 2016 and 2017, suggesting that the importance of terrigenous sources of DOC from ice-marginal channels, river banks, or the river bed, were not significantly different based on meltwater flow conditions between these years.

3.4.3 The ^{14}C of DOC in glacial rivers was controlled by terrigenous OC, including ^{14}C-old soils, ^{14}C-ancient glacial till, and ^{14}C-ancient geogenic material

The expected ^{14}C ages in local soils helped constrain the measured ^{14}C-DOC in glacial river samples. Glaciers covered most of the Lake Hazen basin until ~5.3 ka BP, followed by a rapid retreat to stabilize near present margins by ~5 ka BP[85], reflected in part by a peat sample from Skeleton Creek on the northwest side of Lake Hazen having ^{14}C age ~5 ka BP[328]. However, glacial rivers reached even more ^{14}C-DOC ancient ages in our study, ranging from ~2.9 to 10.0 ka BP. To get older than ~5 ka BP, there would need to be a contribution of organic material to the DOC pool that had even lower ^{14}C content than soil formed since the last deglaciation. For instance, ancient soils formed prior to being covered by the Laurentide and Innuitian ice sheets during the Wisconsin glaciation (~75 ka BP) are ^{14}C-dead (i.e., no detectable ^{14}C), given that they have less than the minimum detectable fraction of modern carbon in a sample (~ 55 ka). In fact, extensively eroded river banks can mobilize soil organic material from isotopically distinct soil horizons, illustrated in a study where Arctic tundra soils were aged only several hundred years near the surface (0 to 20 cm), but were much older (~7.2 ka BP) in deeper (90 to 100 cm) layers[329]. For this same soil profile, Guo et al.[329] reported $\delta^{13}C$ for soil organic carbon within a narrow range (-26 to -27 ‰) compared to that of ^{14}C-modern tundra plant samples ($\delta^{13}C$ ~ -29 ‰). In the Lake Hazen watershed, intense erosion and mixing of glacial till during historic advance and retreat of glaciers, likely prevented the formation of well-defined soil layers, and resulted in heterogeneous soils of mixed geologic provenance and age exposed along glacial river continua. As such, one possible explanation for the ^{14}C ages in glacial rivers (~2.9 to 10.0 ka BP) could be the mixing of old soils (< ~5 ka BP) with older ^{14}C-dead OC in glacial till (> 75 ka BP).

Soil organic carbon could be an important precursor to POC in suspended sediment of glacial rivers, for which the $\delta^{13}C$-POC was found to span -24.0 to -27.0 ‰. These $\delta^{13}C$-POC values were similar to those in outflow waters from glaciers of the Greenland Ice Sheet (-26.1 to -26.4 ‰)[198], and Duvannyi Yar thaw streams from Yedoma permafrost of the Siberian Arctic (-24.8 to -25.7 ‰), the latter of which being among the most ^{14}C ancient POC and DOC ever reported (> 19,000 yBP)[330]. Extremely low organic carbon content in POC sampled from Taiwanese mountain rivers were dominated by geogenic rock material with $\delta^{13}C$-POC spanning ~ -20.2 to -25.2 ‰[331]. These are strongly contrasted by $\delta^{13}C$-POC in rivers of the northeastern United States (-25.6 to -33.7 ‰[332]), and

the six largest rivers of the pan-Arctic watershed (-28.4 to -33.0 ‰)[333], where biospheric OC would be expected to be a more important component of POC.

Geogenic organic carbon from sedimentary rocks can be a source of ^{14}C-dead organic material in subsoils, that varies in importance based on bedrock type and organic carbon content[334,335]. In the Lake Hazen watershed, sedimentary rocks ages range from the early Paleozoic to Cenozoic, and include carbonates, slate, sandstone, siltstone, mudstone, shale, and coal[297,298]. Hydrocarbon-rich coal, or petrogenic rock material, is unique in that it has a much higher organic carbon content than other sedimentary rocks, and more negative δ^{13}C-POC[331]. In fact, a study of the Mackenzie River in the Canadian Arctic assessed how the mixing of biospheric and petrogenic sources to POC can complicate interpretations of Δ^{14}C-POC, and implemented correction procedures for in the calculation of ^{14}C ages[336]. In our study, the δ^{13}C-POC and δ^{13}C-DOC in glacial rivers, together with extremely low contributions of polycondensed aromatic black carbon molecules, suggested that coal-derived petrogenic organic carbon contributions to the POC in suspended sediment were minor compared to other geogenic sedimentary rock types. Therefore, despite the much lower OC contents in carbonates, slate, sandstone, siltstone, mudstone, and shale, the abundance of mineral surfaces to interact with meltwaters in suspended sediment made them a likely source of ^{14}C-dead POC to glacial rivers.

Given the extremely low DOC concentrations of glacial rivers, only a small contribution of ^{14}C-dead OC from glacial till or geogenic material would be required to push Δ^{14}C-DOC towards more negative values, and older ^{14}C ages. Even for a glacial river sample that already had ^{14}C-ancient DOC (e.g., -500 ‰), inclusion of only 10 to 20% of ^{14}C-dead OC (e.g., -1000 ‰) to the DOC sample would be required to make that sample 50 to 100 ‰ more negative. This is a significant difference in ^{14}C ages corresponding to Δ^{14}C-DOC values of -500 and -600 ‰, which are ~5.5 to 7.3 ka BP, respectively. Variable proportions of ^{14}C-dead OC in glacial river DOC samples could help explain differences in ^{14}C ages of DOC between river catchments. Furthermore, slight downriver shifts towards more isotopically negative Δ^{14}C-DOC values could indicate increased contributions of ^{14}C-dead OC to the DOC pool. In the case of glacial river DOC concentrations that were < 0.5 mg C L^{-1}, a 10 to 20% contribution of ^{14}C-dead OC would correspond to < 0.1 mg C L^{-1}, which is an especially viable hypothesis based on extensive contact and mixing of meltwaters with fine-grain particles of ancient soils and geogenic material.

Therefore, there are several different sources of organic material that contributed to DOC in glacial rivers. Minor contributions of smaller organic molecules, and protein-like fluorescence character, are

likely linked to supraglacial primary productivity and heterotrophy. However, DOC character was primarily comprised of larger, humic-like organic structures, highlighting the importance of terrestrially derived organic carbon sources. For instance, aeolian deposition of fine-grain soil and geogenic sedimentary rock particles were all probable sources of POC to glacier surfaces, and were common to the riverbed and hyporheic zone, suspended sediment, and riverbanks of glacial rivers. This terrigenous material was likely composed of variable degrees of mixing of soils formed since the last deglaciation (< ~ 5 ka BP), prior to the Wisconsin glaciation (< ~ 75 ka BP), and geogenic sedimentary rock from the early Paleozoic to Cenozoic, which could explain the range of ^{14}C ages in glacial headwaters. The high black carbon content in supraglacial snow must have either been processed in the supraglacial environment, or settled out of solution to cryoconite, given that the polycondensed aromatic compound class was only sparingly detected along glacial river continua.

3.4.4 DOC concentration and composition changes along the length of glacial rivers with the addition of ^{14}C ancient soil-derived DOC

Glacial rivers are not simple pipelines with respect to DOC concentration and composition, even during the rapid time scales that encompassed their complete transit from glacier termini to river deltas. These downriver changes take place on the order of hours given the river lengths (~ 4.6 to 41.9 km), and rapid river velocity, except for the Turnabout River that flowed through a small lake with an unknown residence time. Downriver DOC concentrations were higher for most glacial rivers, and spanned a wider range in values when compared to glacial headwater samples. A downriver shift in DOC composition to favour humic-like characteristics and more negative $\delta^{13}C$-DOC values was suggestive of the chemical nature of DOC being added along river continua. This was similar to findings of a recent study of the Upper Ganges Basin in which downstream increases in DOC concentrations were accompanied by a shift in molecular composition from primarily aliphatic and peptide-like structures to favour soil-derived compound classes[210]. Given the nutrient starved, dilute nature of glacial meltwaters in the Lake Hazen watershed, and the brief transit times accrued along river transects, processes such as photolysis, microbial degradation, and autochthonous production were not expected to have had an appreciable influence on DOC in glacial rivers. Sources of humic-like DOC along glacial river transects were therefore expected to be terrigenous, such as soil and sediment-derived material, although the exact mechanism by which this organic carbon entered solution was less clear.

One hypothesis of a DOC source to glacial rivers is runoff from proximal terrain. Flushing of soil-derived DOC in runoff to glacial meltwaters has been reported before for a vegetated hillslope upgradient of glacial headwaters[213], as well as further into the proglacial environment[337]. Glacial headwaters often had low ^{3}H concentrations (1.7 to 6.5 T.U.) such that the addition of recent precipitation and/or ground ice thaw water to glacial rivers via overland seepage runoff could explain downriver increases in ^{3}H concentrations that were almost ubiquitously observed along glacial river transects. For instance, ^{3}H concentrations in an overland seepage site sampled along Blister River (12.5 T.U.), Lake Hazen snowpack (10.0 ± 0.8 T.U.), and local precipitation (14.8 ± 0.9 T.U.) samples were higher than those in glacial headwaters and could have elicited downriver increases in ^{3}H concentrations. The hydrologic importance of overland seepage inflows was generally expected to be minimal based on water isotope ($\delta^{18}O$-H_2O, $\delta^{2}H$-H_2O) data. Despite downriver shifts to favour higher $\delta^{18}O$-H_2O, similar linear equations and goodness of fit were found when considering glacial headwaters vs. downriver sites, and glacial river transects data distributions strongly adhered to annual local water lines. During the high flow year (2015) glacial rivers had higher ^{3}H concentrations and the local water line shifted slightly towards the ground ice thaw water line (GITWL), which may suggest an increased contribution of DOC delivered via runoff to glacial rivers during this year. This could also explain the accentuated humic character of DOC and particularly negative $\delta^{13}C$-DOC for glacial river samples collected during 2015. Indeed, water isotopes, ^{3}H, and the *majority* of DOC data are in agreement with rationale surrounding addition of DOC to glacial rivers from precipitation washing over vegetated terrain, or from surficial ground ice thaw water. However, overland seepage would supply DOC to glacial rivers that was comparatively ^{14}C-modern relative to glacial headwaters, which was contrary to the evolution of $\Delta^{14}C$-DOC along glacial river transects.

The downriver addition of humic like DOC did not result in a shift towards more ^{14}C modern values as expected. Instead, while $\Delta^{14}C$-DOC spanned similar ranges for glacial headwaters (-308 to -623 ‰, or 2892 to 7762 yBP) compared to downriver sites (-400 to -714 ‰, or 4038 to 9997 yBP), each of the 6 glacial river transects assessed showed downriver shifts (~ 40 to 285 ‰) towards increasingly negative $\Delta^{14}C$-DOC values. Therefore, ^{14}C-ancient soil-derived organic material must have controlled DOC not only in glacial headwaters, but also downriver. The addition of DOC along glacial river transects was likely derived from local soils formed since the last deglaciation (~5 ka BP), mixed with older OC sources. Coal seams (black carbon) could have been a geologic source of ^{14}C-dead material, but were expected to be a minor component of the local geology and a minimal source of DOC to glacial rives. This was supported by molecular characterization results, that showed

polycondensed aromatic black carbon molecules as a very minor (< 4 %) component of DOC. Similarly, although geogenic OC derived from sedimentary rock (early Paleozoic to Cenozoic) is ^{14}C-dead and could explain the Δ^{14}C-DOC becoming more negative downriver, it contradicts the downriver shift towards increasingly negative δ^{13}C-DOC values. Therefore, the source of DOC along glacial river transects must have been a mix of old soil OC formed since the last deglaciation < 5 ka BP) and ancient soil OC (i.e., glacial till) from lower soil horizons formed prior to the Wisconsin glaciation (> 75 ka BP).

It is well known that thawing ground ice and permafrost can mobilize stocks of soil organic carbon to proximal freshwater networks. DOC in thawing Arctic soils has garnered attention based on its biodegradability and propensity for mineralization to CO_2[338,339], as has the fate of POC in receiving aquatic systems[329,340]. In recent years, the POC pool has been scrutinized more closely, revealing relationships between the chemical composition of POC and DOC, their isotopic character (^{13}C, ^{14}C), and other biogeochemical parameters in thaw water impacted Arctic freshwater systems[341–343]. Downriver decreases in Δ^{14}C-DOC are highly irregular amongst river systems because ^{14}C modern sources typically overshadow those that are ^{14}C ancient. Instead, extreme glacial river characteristics of the Lake Hazen watershed (low DOC and highly variable suspended sediment concentrations), may have contributed to this unique finding of the proglacial evolution of Δ^{14}C-DOC.

Downriver sites often had eroding lower soil horizons exposed along the banks of glacial rivers, which could have been a conduit by which ^{14}C ancient OC was added to solution. In fact, there were much wider ranges in concentrations of suspended material (TSS, PC) at downriver sites, which were among the most Δ^{14}C-DOC negative samples. Suspended material in glacial rivers (*arctic flour*) would have included both freshly eroded soils from river banks, and resuspended material from the sediment. The particularly fine-grain (<0.45 μm) fraction of this suspended material (i.e., colloidal sized particles) likely had an organic carbon component that was quantified as DOC. Whereas the δ^{13}C-POC of different size fractions of suspended sediment was not assessed as part of this study, the range of δ^{13}C-POC at downriver sites (-24.4 to -27.0 ‰) was very similar to that of δ^{13}C-DOC (-24.6 to -26.3 ‰) for samples collected during 2016. These findings corroborate a linkage between ^{14}C-ancient dissolved and particulate organic carbon phases.

Fine-grain particles (< 0.45 μm) in suspended sediment may have affected measures of DOC quantity, composition, and isotopes. For instance, the TOC analyzer applied a combustion temperature of ~680ºC, which would capture nearly all <0.45 μm organic molecules present, except

for the particularly thermally resistive fraction of the black carbon pool. Particulate matter can also scatter light within the pathlength of a cuvette and impact DOC absorption and fluorescence measurements, especially when there are low amounts of CDOM and FDOM. Finally, <0.45 µm particles likely had variable susceptibilities to UV oxidation and infrared detection (SEC), solid phase extraction and electrospray ionization (FT-ICRMS), and acidification, persulfate digestion, and ionization ($\delta^{13}C$, $\Delta^{14}C$). It is expected only the most refractory organic material would have evaded detection using these techniques. Whereas the recalcitrance of different organic molecules to sample preparation, treatment, and detection techniques was beyond the scope of this study, these points deserve further investigation based on interpretations of DOC in extreme aquatic systems such as glacial rivers of the Lake Hazen watershed.

Porewater exfiltration of ^{14}C-ancient DOC through the riverbed is the most likely mechanism to explain downriver DOC evolution, given that it is also in agreement with downriver increases in ^{3}H and $\delta^{18}O$-H_2O. For instance, expansion of the hyporheic zone during higher flow conditions could have accessed ^{14}C-ancient, microbially processed, soil-derived OC in ground ice thaw water. Although the isotopic composition of OC in riverbed porewaters was primarily expected to be reflective of the local soils and geology, another possibility had to do with OC in glacial meltwater towards the end of previous melt seasons. For instance, as glacial rivers dry towards the end of each polar summer, standing water along glacial river continua either evaporates, or infiltrates into the riverbed. Therefore, as meltwaters ramp-up during succeeding melt seasons, this frozen water in the river bed may be mobilized along glacial river transects. Prior to becoming frozen, or after melting, this water could interact with ancient soils and/or geogenic OC to become even more ^{14}C-ancient than glacial headwaters. Based on more negative $\Delta^{14}C$-DOC in medium flow (2016) compared to lower flow (2017), this suggested that the importance of thaw water exfiltrating through the riverbed was greater than that of comparatively ^{14}C-modern surface water inputs to DOC. Less is known about extremely low flow year (2018) in absence of isotopic data (^{3}H, $\delta^{13}C$, $\Delta^{14}C$), although higher concentrations of humic-like DOC were found. It is possible that a) lateral expansion and exfiltration of porewaters would have been much less significant, b) there would have been limited riverbank erosion and gravel bed mixing with such weak meltwater flow conditions, and c) other proglacial sources of DOC would have been less extensively diluted by glacier ice meltwater. Thus, it is hypothesized that during 2018 glacial rivers likely had low ^{3}H concentrations that were similar to the other low flow year (2017) and DOC that was comparatively ^{14}C-modern to other sampling years. It should be noted that these preceding rationales are not mutually exclusive from the potential effects

of <0.45 μm particles in suspended sediment on Δ^{14}C-DOC along glacial river transects. However, only porewater exfiltration through the hyporheic zone explains the downriver additions of humic-like DOC, more negative carbon isotopes (δ^{13}C, Δ^{14}C), and increases in ^{3}H and stable water isotopes.

3.4.5 DOC in Lake Hazen is a composite of meltwaters from glacial rivers with little in-lake modification

Climatic changes to high Arctic environments could impact organic carbon cycling in aquatic ecosystems. Recent research has identified that warming and increased meltwater fluxes to Lake Hazen has significantly increased the delivery of organic carbon and sediment, while decreasing the lake residence time by >70%[89]. Glacial rivers funnel high loads of suspended solids into Lake Hazen that settle out and give rise to elevated turbidity and particulate carbon at depths >200m[203]. This particulate material may be entrained in the sediment, partially resuspended by microbial processes during diagenesis, or incorporated into the food web via benthic feeding organisms. A recent study of Lake Hazen illustrated full depth profiles of DOC concentrations for ice covered vs open water conditions (2013 to 2017[91]) for which data points followed similar and narrow vertical distributions that were almost exclusively <0.4 mg C L^{-1}. Lake Hazen has been shifting to favor ice-off conditions during the polar summer[89], which could also affect whether the lake is a source or sink for DOC.

The fate of DOC in Lake Hazen was assessed using mass flow and DOC weighted calculations for the seven major glacial river discharges sampled during 2016. These calculations predicted in-lake DOC concentrations (~ 0.5 mg C L^{-1}), δ^{13}C-DOC (-25.8 ‰), and Δ^{14}C-DOC (~ -502 ‰, or 5535 yBP). Lake Hazen is hydrologically dominated by glacial rivers, and receives only minor inflows from a few seasonally flowing non-glacial sources, so it was not surprising that surface waters appeared to represent a confluence of glacially derived meltwaters. For instance, the Lake Hazen surface water sample had a similar DOC concentration (~ 0.4 mg C L^{-1}), and Δ^{14}C-DOC (~ -415 ‰, or 4247 yBP) that was only slightly younger than the mass weighted value. Comparatively ^{14}C-modern DOC could be added to Lake Hazen via in-lake primary production, in small non-glacial surface water inputs, or precipitation falling directly on the lake. Alternatively, ^{14}C-ancient DOC in glacial river discharges could be partially offset in Lake Hazen if it were to adsorb to sinking particles, rendering the lake sediment a potential sink for DOC. Finally, the Lake Hazen centre buoy sampling site was far removed from sinking, sediment-laden glacial river plumes, implying that potential effects of <0.45 μm ^{14}C-ancient particles to DOC quantification in the Lake surface water

would be largely limited. A combination of these in-lake processes could explain the slight discrepancy between mass balanced and measured Δ^{14}C-DOC in Lake Hazen surface water.

Warming summers in the high Arctic could intensify meltwater fluxes and contributions of ground ice thaw waters along glacial rivers, further lessening the hydrologic importance of non-glacial inflows to Lake Hazen. In the long term, unmitigated climate change and continued warming could result in glacier ice mass loss such that surface areas of glaciers available for ablation become reduced and meltwater fluxes actually decrease. Alternatively, lower flow conditions could limit the lateral expansion of glacial river hyporheic zones, and result in ^{14}C-ancient OC remaining sequestered in the landscape, rather than mobilized downriver. In these scenarios, there would be a heightened importance of terrigenous, non-glacial source waters to Lake Hazen, comparatively ^{14}C-modern DOC, and perhaps a shift away from ultra-oligotrophy. Continued research of glacial meltwater impacted aquatic systems of high Arctic environments promises to further resolve their biogeochemical responses to change, sources/sinks and chemical composition of organic carbon, and how these findings fit into the global carbon cycle.

3.5 Conclusions

This study delivered an assessment of DOC concentration, composition, and isotopic (δ^{13}C, Δ^{14}C) data for glacial rivers of the Lake Hazen watershed in the Canadian high Arctic, as well as opportunistic samples of the supraglacial environment. Based on low ^{3}H concentrations in glacial headwaters, bulk supraglacial meltwaters were expected to be derived primarily from older glacier ice, but also recent precipitation. Colder temperatures associated with higher altitude glaciers may have also resulted in more intense isotopic fractionation associated with precipitation (i.e., low ^{3}H) to glacier surfaces. In fact, glacial headwaters stemming from the largest glaciers (i.e., Gilman, and Henrietta-Nesmith Glaciers) had the most isotopically negative stable water isotopes (δ^{2}H-H_2O and δ^{18}O-H_2O). Contributions of DOC to bulk meltwater discharge included terrigenous organic material (i.e., aeolian deposition), supraglacial productivity, and long-term microbial reprocessing on glacier surfaces. Particularly high proportions of polycondensed aromatic (black carbon) organic material in Gilman Glacier snow were not retained in any of the glacial river samples, suggesting that this chemically distinct fraction of supraglacial DOC had a different fate (i.e., rapidly processed, or adsorbed to sinking particles in supraglacial meltwaters). Supraglacial stream waters are a composite of melting ice and snow, and are expected to be most representative of DOC exported in glacial runoff. Glacial headwaters were indicative of ^{14}C-ancient DOC that had a heterogeneous composition

primarily comprised of humic-like substances, but also lower molecular weight aliphatic molecules. The δ^{13}C-DOC (> -25 ‰) coupled with extremely low DOC concentrations appeared to suggest that geogenic organic carbon may have also been a minor component of DOC in glacial headwaters. The range of DOC quantity and composition in glacial headwater samples, albeit narrow, indicates that the extent of meltwater contact with the terrigenous environment along ice-marginal channels or immediately upgradient of glacial headwaters may have had variable effects on DOC.

Downriver increases in DOC concentration, humic-like character, and more negative δ^{13}C-DOC and Δ^{14}C-DOC showed that DOC evolution along glacial rivers was strongly linked to the ^{14}C-ancient terrestrially derived organic carbon. Given that ^{14}C ages of DOC in glacial rivers often exceeded maximum ages of soils formed since the most recent deglaciation (~ 5 ka BP), there must have been older OC sources, such as glacial till formed prior to the Wisconsin glaciation (<75 ka BP), or geogenic sedimentary rock OC from the early Paleozoic to Cenozoic. Increasingly negative δ^{13}C-DOC downriver refined this interpretation, highlighting that glacial till must have been the primary source of OC along glacial river continua. Comparatively ^{14}C-modern surface water inputs (overland seepage, small streams) could not explain the downriver transformation of Δ^{14}C-DOC. Instead, downriver sources of ^{14}C-ancient DOC likely included porewater exfiltration of ground ice thaw water through the riverbed. In addition to perennially frozen ground ice below the riverbed, thaw waters were probably also composed of glacial river meltwaters that soaked into the riverbed during annual melt seasons, and underwent subsequent freeze/melt cycles. The lateral expansion of the hyporheic zone during high flow conditions could access more ground ice surface area in soils, thereby mobilizing more ^{14}C-ancient soil-derived OC along glacial river continua. Stable water isotopes generally adhered to annual local water lines with similar slopes, although the highest flow year (2015) was associated with less negative values than the low flow year (2017). The distribution of ^{3}H concentrations for glacial river discharges were also highest during 2015, suggesting that proglacial ground ice thaw water sources became more important during high flow conditions. High DOC concentrations and humic composition during the extremely low flow year (2018) might suggest that there is a ‘tipping point’ with respect to the effect of flow conditions on DOC. For instance, with increasing flow DOC in rivers may be progressively diluted by glacier ice meltwater until sufficient flow is achieved (i.e., high flow conditions) for riverbank erosion, gravel bed mixing, and lateral expansion of the hyporheic zone. Downriver evolution of meltwaters, and higher flow conditions, also tended to coincide with higher concentrations of suspended sediments (TSS, PC) from previously frozen, eroding riverbanks. Ultra-fine (<0.45 μm) organic particles from ancient soils

or geogenic material may have also contributed to DOC quantification and characterization, especially in the case of samples with low DOC concentrations and high suspended sediment loads.

Together, these findings show that glacial rivers were not simple pipelines connecting the cryosphere to receiving aquatic systems, that DOC was transformed on rapid timescales within these dynamic meltwater conduits, and that climate induced changes to meltwater flux conditions will impact the loading of relict soil derived organic carbon to Lake Hazen. Flow-weighted calculations of the seven major glacial river discharges identified similar DOC quantity and isotopic ($\Delta^{14}C$) character to that in Lake Hazen. Small discrepancies may be accounted for by mixing of lake waters from previous melt seasons, but perhaps also by minor sources of comparatively ^{14}C-modern DOC (i.e., small non-glacial inflows, autochthonous production), or sinks preferentially acting on ^{14}C-ancient DOC (i.e., degradation processes, adsorption to sinking particles). Increased glacier ablation and meltwater fluxes will likely result in seasonal pulses of ^{14}C-ancient POC in sediment delivered to Lake Hazen from river bank erosion and glacial margins, but also ^{14}C-ancient DOC in porewaters exfiltrating through the riverbed via expanded hyporheic zones and leached from this ancient material. We find that the similarities in flow-weighted calculations of and lake waters indicates that the legacy of ^{14}C-ancient DOC discharged by glacial rivers will be passed through Lake Hazen to coastal margins via the Ruggles River.

Table 3.1: Major glacial rivers inflowing to Lake Hazen and their watershed characteristics

Glacial Rivers	River Length (km)	Watershed Surface Area (km^2)	Glaciated Surface Area (km^2)	Glaciated (%)
Abbe	21.0	390	204	52
Blister	10.5	---	6	---
Gilman	21.5	992	708	71
Henrietta-Nesmith	4.6	1270	1041	82
Snowgoose	16.6	222	87	39
Turnabout	41.9	678	259	38
Very	39.0	1035	269	26

Table 3.2: Linear regressions of water isotope (δ^2H-H_2O, $\delta^{18}O$-H_2O) data for glacial rivers of the Lake Hazen watershed.

Dataset	Linear Equation	R^2
Glacial river headwaters	$\delta^2H = 6.4 * \delta^{18}O - 36.1$ ‰	0.89
Glacial river downriver sites (i.e., deltas + mid)	$\delta^2H = 6.1 * \delta^{18}O - 45.9$ ‰	0.90
Local glacier ice melt water line (**LGIMWL** = glacial river transects, glacial ice, snow, and supraglacial stream)	$\delta^2H = 6.3 * \delta^{18}O - 38.9$ ‰	0.91
2015	$\delta^2H = 7.4 * \delta^{18}O - 12.4$ ‰	0.95
2016	$\delta^2H = 7.3 * \delta^{18}O - 10.7$ ‰	0.99
2017	$\delta^2H = 6.8 * \delta^{18}O - 23.9$ ‰	0.92
2018	$\delta^2H = 6.8 * \delta^{18}O - 25.5$ ‰	0.98
Ground ice thaw water line (**GITWL** = overland seepage and streams inflowing to Blister River) ***Note**: excluding four samples identified in Results to coincide more closely to LGIMWL*	$\delta^2H = 4.9 * \delta^{18}O - 83.$ 2‰	0.92
Global Meteoric Water Line (**GMWL**)	$\delta^2H = 8 * \delta^{18}O + 10$ ‰ VSMOW	

Table 3.3: Tritium (^3H) concentrations (Tritium Units; T.U.) for glacial rivers of the Lake Hazen watershed, precipitation, and snowpack samples

River	Type	Date	Tritium (± 0.8 T.U.)
Blister	Delta	10-Jul-15	11.2
Snowgoose	Delta	03-Jul-15	11.5
Henrietta-Nesmith	Headwater	15-Jul-15	6.5
Very	Delta	15-Jul-15	6.9
Abbé	Delta	15-Jul-15	7.0
Turnabout	Delta	15-Jul-15	8.3
Blister	Headwater	29-Jul-16	4.6
Blister	Delta	29-Jul-16	7.4
Snowgoose	Delta	30-Jul-16	8.9
Gilman	Headwater	01-Aug-16	2.8
Abbe	Delta	01-Aug-16	4.0
Gilman	Delta	01-Aug-16	4.1
Snowgoose	Headwater	01-Aug-16	5.8
Turnabout	Delta	01-Aug-16	7.5
Very	Delta	02-Aug-16	4.9
Henrietta-Nesmith	Headwater	02-Aug-16	5.1
Gilman	**Supraglacial Snow**	20-07-2017	**1.4**
Base Camp	**Precipitation**	12-07-2017	**14.6**
Base Camp	**Precipitation (AM)**	13-07-2017	**14.1**
Base Camp	**Precipitation (PM)**	13-07-2017	**15.8**
Lake Hazen	**Snowpack 5**	21-05-2017	**9.1**
Lake Hazen	**Snowpack 6**	21-05-2017	**10.5**
Lake Hazen	**Snowpack 8**	21-05-2017	**10.5**
Gilman	Headwater	20-07-2017	1.7
Gilman	Mid-River	20-07-2017	2.5
Gilman	Delta	20-07-2017	2.8
Abbe	Headwater	20-07-2017	3.3
Abbe	Delta	20-07-2017	2.9
Snowgoose	Headwater	21-07-2017	2.5
Snowgoose	Mid-River	21-07-2017	4.6
Snowgoose	Delta	21-07-2017	5.2
Henrietta-Nesmith	Headwater	21-07-2017	2.3
Very	Delta	21-07-2017	5.6
Turnabout	Delta	22-07-2017	7.0
Blister	Headwater	22-07-2017	4.8
Blister	Mid-River	22-07-2017	6.8
Blister	Delta	22-07-2017	10.0
Blister	Overland Seepage	22-07-2017	12.5
Salor Creek	Non-glacial	26-07-2018	10.3

Table 3.4: DOC concentration and composition using **(A)** absorption, fluorescence, size exclusion, **(B)** molecular characterization, and $\delta^{13}C$ and $\Delta^{14}C$ for samples of glacial river headwaters as well as opportunistic glacier snow, stream, and ice samples

A) Glacial Headwater Sites

River	Date	[DOC] mg C L^{-1}	Absorption			Fluorescence		Size Exclusion Chromatography Components (%)				
			a_{255} (m^{-1})	$SUVA_{255}$ (L mg C^{-1} m^{-1})	$S_{275-295}$ (nm^{-1})	Humic % (A+C+M)	Protein % (T+B)	BP	HS	BB	LMW-N	LMW-A
Blister	16-07-2015	0.25	---	---	---	---	---	---	---	---	---	---
Gilman	11-07-2016	<0.10	0.39	4.26	0.012	50.7	49.3	---	---	---	---	---
Henrietta-N.	11-07-2016	0.23	0.83	3.62	0.018	55.1	44.9	---	---	---	---	---
Snowgoose	11-07-2016	0.30	0.53	1.76	0.012	50.7	49.3	---	---	---	---	---
Blister	15-07-2016	<0.10	0.28	6.06	0.008	20.9	79.1	23.1	22.1	9.9	44.9	n.d.
Blister	19-07-2016	0.48	1.60	3.36	0.013	74.3	25.7	---	---	---	---	---
Blister	29-07-2016	0.21	0.37	1.76	0.016	62.0	38.0	28.6	41.5	7.7	22.2	n.d.
Gilman	01-08-2016	0.14	1.13	7.82	0.016	70.9	29.1	31.0	37.6	7.0	24.5	n.d.
Snowgoose	01-08-2016	0.20	0.98	4.97	0.012	64.0	36.0	24.4	28.9	5.8	41.0	n.d.
Henrietta-N.	01-08-2016	0.24	0.87	3.58	0.015	62.5	37.5	12.8	27.7	4.7	50.9	3.9
Abbe	20-07-2017	<0.10	0.66	8.13	0.020	70.4	29.6	18.8	37.1	10.4	33.7	n.d.
Gilman	20-07-2017	0.11	0.65	5.97	0.017	72.2	27.8	26.0	39.2	6.9	27.8	n.d.
Henrietta-N.	21-07-2017	<0.10	0.66	8.88	0.015	76.4	23.6	18.0	35.0	16.9	30.1	n.d.
Snowgoose	21-07-2017	0.15	0.86	5.65	0.016	77.0	23.0	20.2	38.7	6.5	34.7	n.d.
Blister	22-07-2017	0.16	0.62	3.97	0.016	71.9	28.1	19.5	35.3	11.2	34.0	n.d.
Henrietta-N.	23-07-2018	0.14	0.85	6.13	0.018	64.3	35.7	23.6	39.4	13.6	23.4	n.d.
Abbe	23-07-2018	0.20	0.85	4.29	0.017	54.8	45.2	21.4	37.6	18.5	22.5	n.d.
Gilman	24-07-2018	0.29	0.81	2.85	0.018	65.9	34.1	20.8	42.9	13.3	23.0	n.d.
Snowgoose	24-07-2018	0.39	1.54	3.92	0.014	74.3	25.7	16.9	46.5	14.4	22.2	n.d.
Turnabout	25-07-2018	0.29	1.79	6.20	0.014	65.8	34.2	32.4	42.3	11.0	14.4	n.d.
Gilman (*glacier snow*)	21-07-2017	0.42	4.43	10.47	0.006	44.1	55.9	4.3	48.3	23.1	21.7	2.6
Gilman (*supra. stream*)	21-07-2017	0.18	0.57	0.68	0.019	42.0	58.0	33.1	27.8	6.9	32.3	n.d.
Henrietta-N. (*glacial ice*)	21-07-2017	0.22	0.94	0.56	0.017	31.9	68.1	4.7	n.d.	17.3	61.9	16.1
Gilman (*glacial ice*)	21-07-2017	0.29	1.67	0.69	0.024	43.7	56.3	4.3	n.d.	22.0	63.5	10.1

B) Glacial Headwater Sites

River	Date	[DOC]	H:C	O:C	FTICR-MS compound classes (%)							Carbon Isotopes			
					BC	Poly.	↑ Unsat. Arom.	Unsat. Aliph.	Sat. FA	Sug.	Pept.	δ^{13}C-POC (‰)	δ^{13}C-DOC (‰)	Δ^{14}C-DOC (‰)	^{14}C age (yBP)
Henrietta-N.	15-07-2015	0.46	---	---	---	---	---	---	---	---	---	---	-28.1	---	---
Gilman	11-07-2016	<0.10	---	---	---	---	---	---	---	---	---	-24.0	---	-557.4	6483
Henrietta-N.	11-07-2016	0.23	---	---	---	---	---	---	---	---	---	---	-23.9	-566.1	6643
Snowgoose	11-07-2016	0.30	---	---	---	---	---	---	---	---	---	-26.9	-24.0	-438.4	4570
Blister	15-07-2016	<0.10	---	---	---	---	---	---	---	---	---	---	---	-441.5	4615
Blister	29-07-2016	0.21	---	---	---	---	---	---	---	---	---	---	-24.4	---	---
Gilman	01-08-2016	0.14	1.39	0.38	1.1	5.1	62.6	23.3	4.0	0.5	3.5	-24.2	-23.9	-622.5	7762
Snowgoose	01-08-2016	0.20	---	---	---	---	---	---	---	---	---	-26.8	---	-569.4	6704
Henrietta-N.	02-08-2016	0.24	---	---	---	---	---	---	---	---	---	-27.0	-24.8	-552.7	7243
Abbe	20-07-2017	<0.10	---	---	---	---	---	---	---	---	---	---	---	-354.5	3451
Gilman	20-07-2017	0.11	1.41	0.39	2.2	6.6	52.9	33.9	2.6	0.4	1.5	---	---	-307.9	2892
Henrietta-N.	21-07-2017	<0.10	1.28	0.41	1.9	8.0	71.6	16.8	1.1	0.3	0.4	---	---	---	---
Gilman (*glacier snow*)	21-07-2017	0.42	1.20	0.33	27.6	8.8	25.4	33.1	3.9	0.8	0.5	---	---	---	---

Note: Abbreviated FTICR-MS compound classes presented above for condensed aromatics or 'black carbon' (**BC**), polyphenolics (**Poly.**) highly unsaturated aromatics (**↑ Unsat. Arom.**), unsaturated aliphatics **(Unsat. Aliph.**), saturated fulvic acids (**Sat. FA**), sugars (**Sug.**), and peptides (**Pept.**).

Table 3.5: DOC concentration and composition using absorption, fluorescence, size exclusion, and $\delta^{13}C$ for overland seepage sites and glacial streams flowing into Blister River, as well as subsurface samples from the nearby Skeleton (SK) catchment

Sample ID	Date	[DOC] mg C L^{-1}	Absorption			Fluorescence		SEC components (%)					Isotopes
			a_{255}	$SUVA_{255}$	$S_{275-295}$	Humic %	Protein %	Biop.	HS	BB	LMW-N	LMW-A	$\delta^{13}C$-DOC (‰)
SEEP 2	09-07-2015	1.0	7.8	7.7	0.015	93.3	6.7	---	---	---	---	---	
SEEP	04-07-2015	3.7	28.9	7.8	0.015	96.6	3.4	---	---	---	---	---	-29.2
SEEP	06-07-2015	3.4	26.9	7.9	0.015	96.3	3.7	---	---	---	---	---	---
SEEP	09-07-2015	3.2	27.4	8.5	0.015	96.3	3.7	1.2	79.6	13.1	6.1	n.d.	---
SEEP	01-08-2015	2.4	18.3	7.6	0.015	---	---	---	---	---	---	---	-29.4
SEEP 11	29-07-2016	0.8	3.5	4.5	0.017	---	---	---	---	---	---	---	---
SEEP 2	15-07-2016	0.9	7.1	8.3	0.015	---	---	---	---	---	---	---	---
SEEP 2	19-07-2016	0.7	---	---	---	---	---	---	---	---	---	---	---
SEEP 6	15-07-2016	0.8	7.8	10.0	0.016	---	---	---	---	---	---	---	---
SEEP	15-07-2016	3.3	26.4	8.0	0.014	95.3	4.7	1.8	78.7	13.1	6.4	n.d.	---
SEEP	19-07-2016	2.7	24.8	9.1	0.008	96.7	3.3	---	---	---	---	---	---
SEEP	29-07-2016	2.3	19.6	8.5	0.015	95.1	4.9	1.4	79.2	13.1	6.3	n.d.	-28.8
SEEP X	22-07-2017	0.6	3.7	6.0	0.016	94.0	6.0	0.5	71.1	13.8	13.0	1.6	---
Stream 10	16-07-2015	0.3	---	---	---	---	---	---	---	---	---	---	---
Stream 4	16-07-2015	0.8	---	---	---	---	---	---	---	---	---	---	---
Stream 5	16-07-2015	0.7	---	---	---	---	---	---	---	---	---	---	---
Stream 6	16-07-2015	1.2	---	---	---	---	---	---	---	---	---	---	---
Stream 7	16-07-2015	0.8	---	---	---	---	---	---	---	---	---	---	---
Stream 8	16-07-2015	0.9	---	---	---	---	---	---	---	---	---	---	---
Stream 9	16-07-2015	0.4	---	---	---	---	---	---	---	---	---	---	---
Stream 6	19-07-2016	0.9	3.5	4.1	0.007	---	---	---	---	---	---	---	-27.7
Stream 7	15-07-2016	<0.1	0.9	28.1	0.021	---	---	---	---	---	---	---	---
Stream 7	19-07-2016	0.2	---	---	---	---	---	---	---	---	---	---	-25.3
Stream 7	29-07-2016	0.2	0.7	2.8	0.015	88.2	11.8	---	---	---	---	---	---
Stream 8	15-07-2016	0.5	1.0	2.3	0.022	---	---	---	---	---	---	---	---
SK Sub 1	17-07-2015	7.6	106.9	14.0	0.008	95.8	4.2	---	---	---	---	---	-29.8
SK Sub 1	01-08-2015	7.2	79.0	11.0	0.006	95.5	4.5	3.8	71.1	20.1	9.8	n.d.	-29.4

SK SEEP (17/07/2016) [DOC] = 0.9 mg C L^{-1}, **$\Delta^{14}C$-DOC = -189.6 ‰, or ~1624 yBP**.

Table 3.6: DOC concentration and composition using **(A)** absorption, fluorescence, size exclusion, **(B)** molecular characterization, and $\delta^{13}C$ and $\Delta^{14}C$ isotopes for glacial river delta samples taken during, or within a couple days of, helicopter surveys. Non-glacial inflow to Lake Hazen, Salor Creek, is also presented

A) Glacial River Deltas

River	Date	[DOC]	Absorption			Fluorescence			SEC components (%)			
		mg C L^{-1}	a_{255}	$SUVA_{255}$	$S_{275-295}$	Humic %	Protein %	Biop.	HS	BB	LMW-N	LMW-A
Snowgoose	14-07-2015	0.25	---	---	---	85.5	14.5	0.7	55.5	14.7	29.2	n.d.
Abbe	15-07-2015	0.25	1.90	7.73	0.010	80.8	19.2	---	---	---	---	---
Blister	15-07-2015	0.24	---	---	---	---	---	2.8	59.5	13.8	23.8	n.d.
Turnabout	15-07-2015	0.74	5.62	7.56	0.015	91.4	8.6	2.6	67.7	13.7	15.9	n.d.
Very	15-07-2015	0.26	1.89	7.36	0.010	86.1	13.9	---	---	---	---	---
Gilman	11-07-2016	0.48	2.50	5.21	0.011	80.1	19.9	---	---	---	---	---
Turnabout	11-07-2016	1.03	7.97	7.74	0.016	91.8	8.2	---	---	---	---	---
Very	11-07-2016	0.40	2.38	5.90	0.016	77.2	22.8	---	---	---	---	---
Abbe	13-07-2016	0.79	4.43	5.58	0.011	78.0	22.0	---	---	---	---	---
Snowgoose	13-07-2016	<0.10	1.22	12.21	0.014	82.5	17.5	---	---	---	---	---
Blister	15-07-2016	0.28	1.49	5.24	0.011	68.6	31.4	9.4	50.2	10.8	29.6	n.d.
Blister	29-07-2016	0.25	0.92	3.69	0.017	81.7	18.3	5.5	58.3	10.8	25.4	n.d.
Snowgoose	27-07-2016	0.44	1.02	2.32	0.014	79.2	20.8	---	---	---	---	---
Snowgoose	30-07-2016	0.10	0.51	5.35	0.021	90.9	9.1	---	---	---	---	---
Abbe	01-08-2016	0.25	0.99	3.93	0.012	73.9	26.1	4.0	57.9	10.4	27.8	n.d.
Gilman	01-08-2016	0.58	4.02	6.89	0.024	25.5	74.5	1.5	20.9	5.0	72.6	n.d.
Turnabout	01-08-2016	1.06	7.86	7.42	0.019	39.4	60.6	1.6	37.5	6.6	50.0	4.3
Very	02-08-2016	0.27	1.90	6.95	0.013	83.9	16.1	4.2	28.8	6.5	58.7	1.9
Abbe	20-07-2017	0.13	0.89	6.87	0.017	71.3	28.7	10.0	45.6	9.4	35.0	n.d.
Gilman	20-07-2017	0.24	2.46	10.37	0.017	74.2	25.8	5.5	41.6	9.9	43.0	n.d.
Snowgoose	21-07-2017	0.25	0.94	3.78	0.017	87.3	12.7	4.6	46.6	13.5	35.3	n.d.
Very	21-07-2017	0.25	1.92	7.73	0.015	89.2	10.8	2.4	52.0	11.9	32.3	1.4
Blister	22-07-2017	0.32	1.57	4.95	0.016	78.3	21.7	3.5	62.7	11.7	21.9	n.d.
Turnabout	22-07-2017	0.93	6.42	6.90	0.016	92.9	7.1	2.3	74.0	10.6	12.1	1.0

Abbe	23-07-2018	0.20	1.23	5.99	0.018	66.5	33.5	23.0	50.7	11.8	14.5	n.d.
Very	23-07-2018	0.27	1.78	6.57	0.019	77.2	22.8	7.5	58.7	17.4	16.5	n.d.
Gilman	24-07-2018	0.31	1.55	4.95	0.016	76.6	23.4	7.1	70.9	10.1	11.8	n.d.
Snowgoose	24-07-2018	0.64	3.11	4.88	0.018	86.1	13.9	6.2	61.6	17.5	8.7	6.1
Turnabout	25-07-2018	1.89	12.91	6.82	0.017	90.5	9.5	5.5	80.2	4.8	7.4	2.0
Blister	26-07-2018	0.43	2.59	5.99	0.018	80.9	19.1	5.3	65.2	19.6	9.9	n.d.
Salor Creek	26-07-2018	2.35	9.62	4.10	0.024	83.7	16.31	10.8	75.3	3.8	7.1	3.0
Lake Hazen (surface)	29-07-2015	0.35	---	---	---	---	---	---	---	---	---	---
Lake Hazen (250 m)	29-07-2015	0.29	---	---	---	---	---	---	---	---	---	---
Lake Hazen (surface)	08-08-2016	0.4	0.30	0.75	0.019	---	---	---	---	---	---	---
Lake Hazen (250 m)	08-08-2016	0.3	0.37	1.24	0.011	---	---	---	---	---	---	---

B) Glacial River Deltas

					FTICR-MS compound classes (%)							Carbon Isotopes			
River	**Date**	**[DOC]**	**H:C**	**O:C**	**BC**	**Poly.**	**↑ Unsat. Arom.**	**Unsat. Aliph.**	**Sat. FA**	**Sug.**	**Pept.**	**δ^{13}C-POC (‰)**	**δ^{13}C-DOC (‰)**	**Δ^{14}C-DOC (‰)**	**^{14}C age (yBP)**
Blister	29-06-2015	0.23	---	---	---	---	---	---	---	---	---	---	-31.5	---	---
Blister	13-07-2015	0.29	---	---	---	---	---	---	---	---	---	---	-31.9	---	---
Blister	18-07-2015	---	---	---	---	---	---	---	---	---	---	---	---	-441.4	4615
Abbe	15-07-2015	0.25	---	---	---	---	---	---	---	---	---	---	-28.4	---	---
Turnabout	15-07-2015	0.74	---	---	---	---	---	---	---	---	---	---	-28.2	---	---
Very	15-07-2015	0.26	---	---	---	---	---	---	---	---	---	---	-29.9	---	---
Gilman	11-07-2016	0.48	---	---	---	---	---	---	---	---	---	-25.5	-25.3	-596.9	7234

Turnabout	11-07-2016	1.03	---	---	---	---	---	---	---	---	---	-25.7	-26.3	-399.9	4038
Very	11-07-2016	0.40	---	---	---	---	---	---	---	---	---	-27.0	-25.4	-476.5	5135
Abbe	13-07-2016	0.79	---	---	---	---	---	---	---	---	---	-24.4	---	-586.4	7029
Blister	15-07-2016	0.28	---	---	---	---	---	---	---	---	---	---	-25.1	-563.4	6593
Snowgoose	27-07-2016	0.44	---	---	---	---	---	---	---	---	---	---	-24.6	---	---
Snowgoose	30-07-2016	0.10	---	---	---	---	---	---	---	---	---	---	---	-607.5	7448
Gilman	01-08-2016	0.58	1.30	0.45	1.1	7.8	67.9	20.4	0.5	0.3	2.2	-25.9	-26.1	-714.2	9997
Abbe	20-07-2017	0.13	---	---	---	---	---	---	---	---	---	---	---	-449.0	4723
Gilman	20-07-2017	0.24	1.27	0.38	3.8	14.6	57.8	21.8	1.4	0.4	0.3	---	---	-592.6	7149
Very	21-07-2017	0.25	1.14	0.47	3.7	14.9	74.4	6.5	0.2	0.2	0.1	---	---	---	---
Turnabout	22-07-2017	0.93	1.13	0.47	2.9	14.1	78.5	4.2	0.2	0.2	0.1	---	---	---	---
Salor Creek	26-07-2018	2.35	1.18	0.53	2.61	3.41	89.35	4.40	<0.1	0.1	0.1	---	---	---	---
Lake Hazen (surface)	29-07-2015	0.35	---	---	---	---	---	---	---	---	---	---	-30.6	-326.5	3112
Lake Hazen (surface)	08-08-2016	0.4	---	---	---	---	---	---	---	---	---	---	---	-415.4	4247

Note: Abbreviated FTICR-MS compound classes presented above for condensed aromatics or 'black carbon' (**BC**), polyphenolics (**Poly.**) highly unsaturated aromatics (↑ **Unsat. Arom.**), unsaturated aliphatics **(Unsat. Aliph.**), saturated fulvic acids (**Sat. FA**), sugars (**Sug.**), and peptides (**Pept.**)

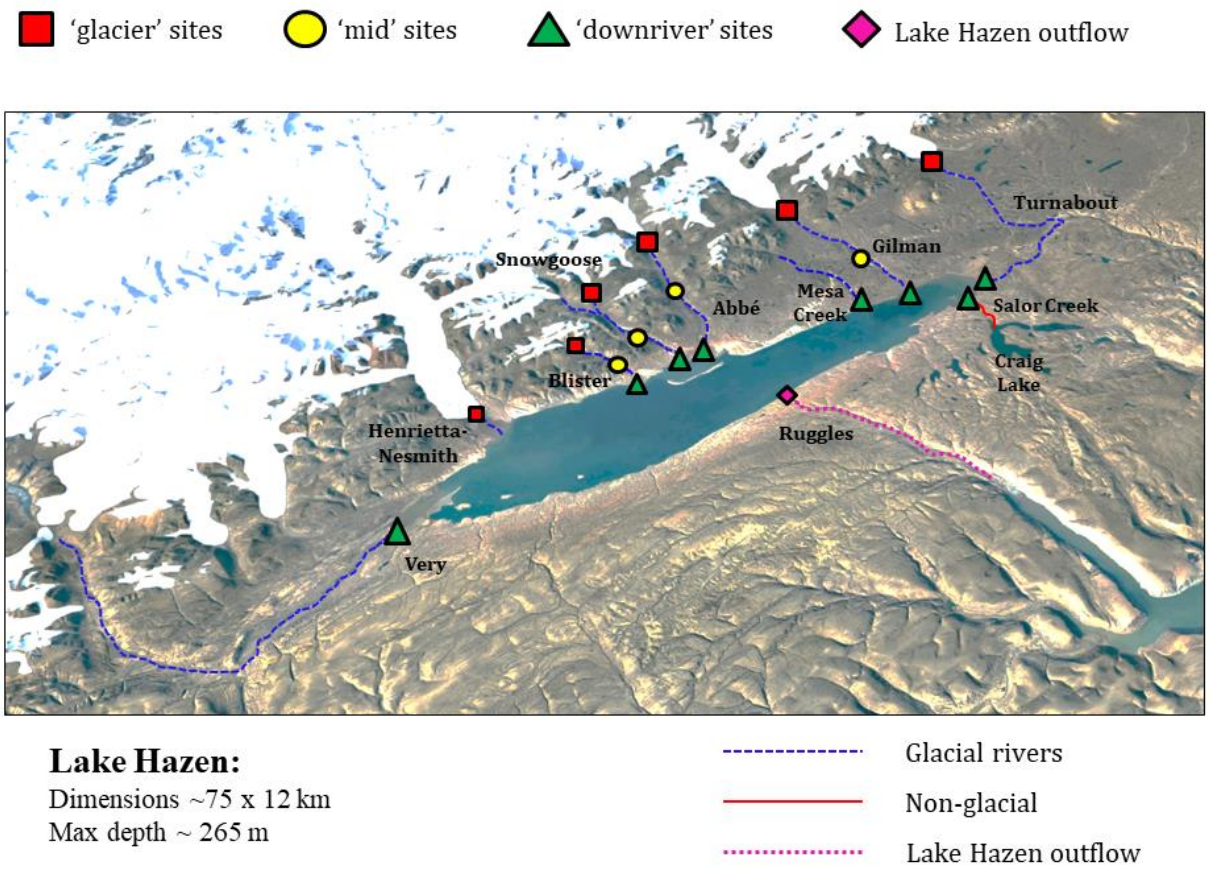

Figure 3.1: Sampling sites located along major glacial river systems draining glaciers in the Lake Hazen watershed (Abbe, Blister, Gilman, Henrietta-Nesmith, Snowgoose, and Turnabout), a minor glacial creek (Mesa), a non-glacial lake (Craig Lake) and its discharge (Salor Creek), and the outflow from Lake Hazen (Ruggles River) towards Chandler Fjord and eventually the Nares Strait.

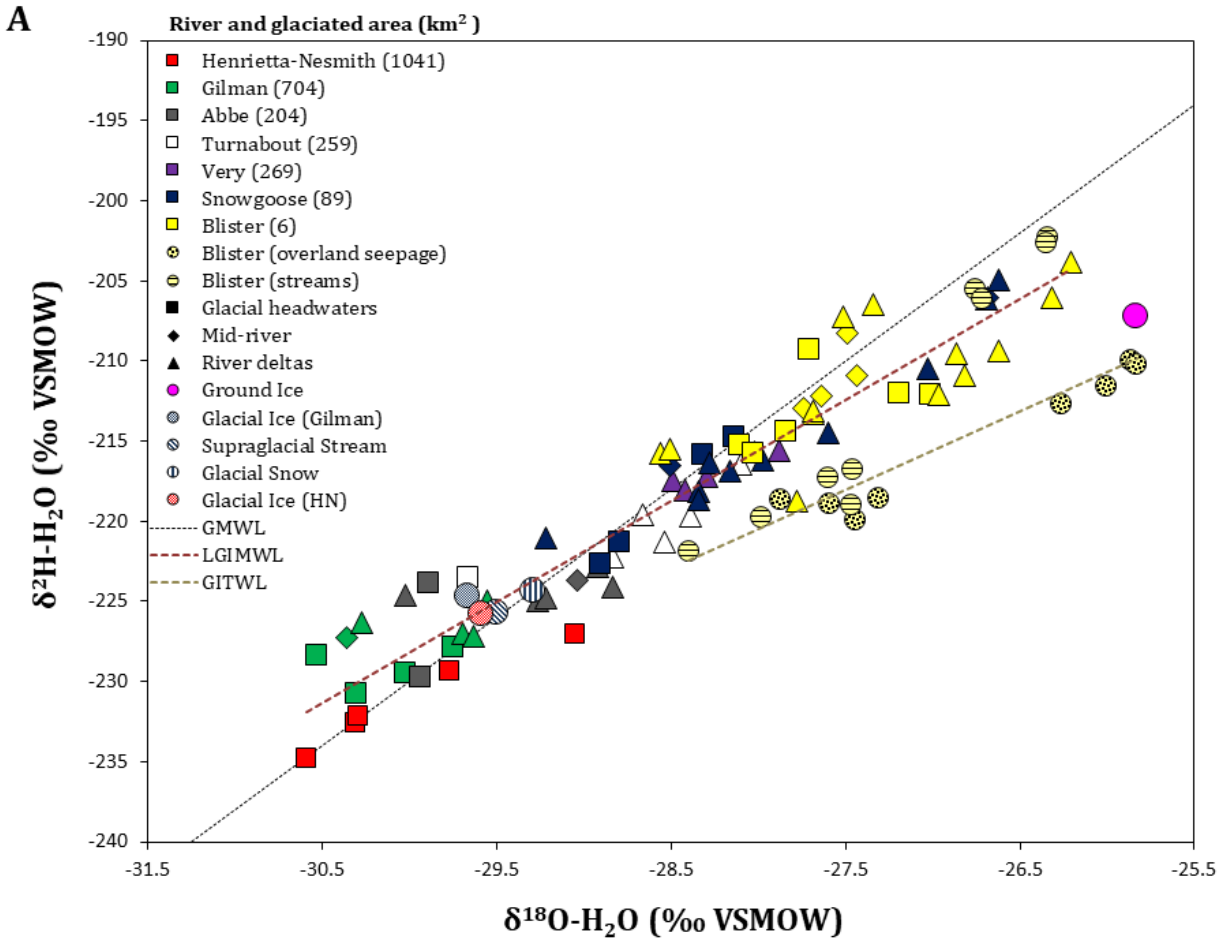

Figure 3.2A: Water isotopes (δ^2H-H_2O and δ^{18}O-H_2O) data for glacial river continua including glacial headwaters (*squares*), mid-river (*diamonds*), and river delta (*triangles*) sites. Streams and overland seepage sites taken along the Blister River continuum were plotted (*circles*) to show decoupling of glacier ice melt from other water sources. Supraglacial stream, glacial snow and glacial ice samples taken from Gilman and Henrietta-Nesmith glaciers (2017) were plotted as well as a ground ice sample taken near the Blister River delta (2016). The global meteoric water line (GMWL; $\delta^2H = 8 * \delta^{18}O + 10$‰ VSMOW), local glacier ice melt water line (LGIMWL; $\delta^2H = 6.3 * \delta^{18}O$ -39.9 ‰; $R^2 = 0.91$) and the ground ice thaw water line (GITWL; $\delta^2H = 4.9 * \delta^{18}O$ -83.2 ‰; $R^2 = 0.92$). The glaciated areas (km^2) pertaining to each glacial river catchment are listed in the legend.

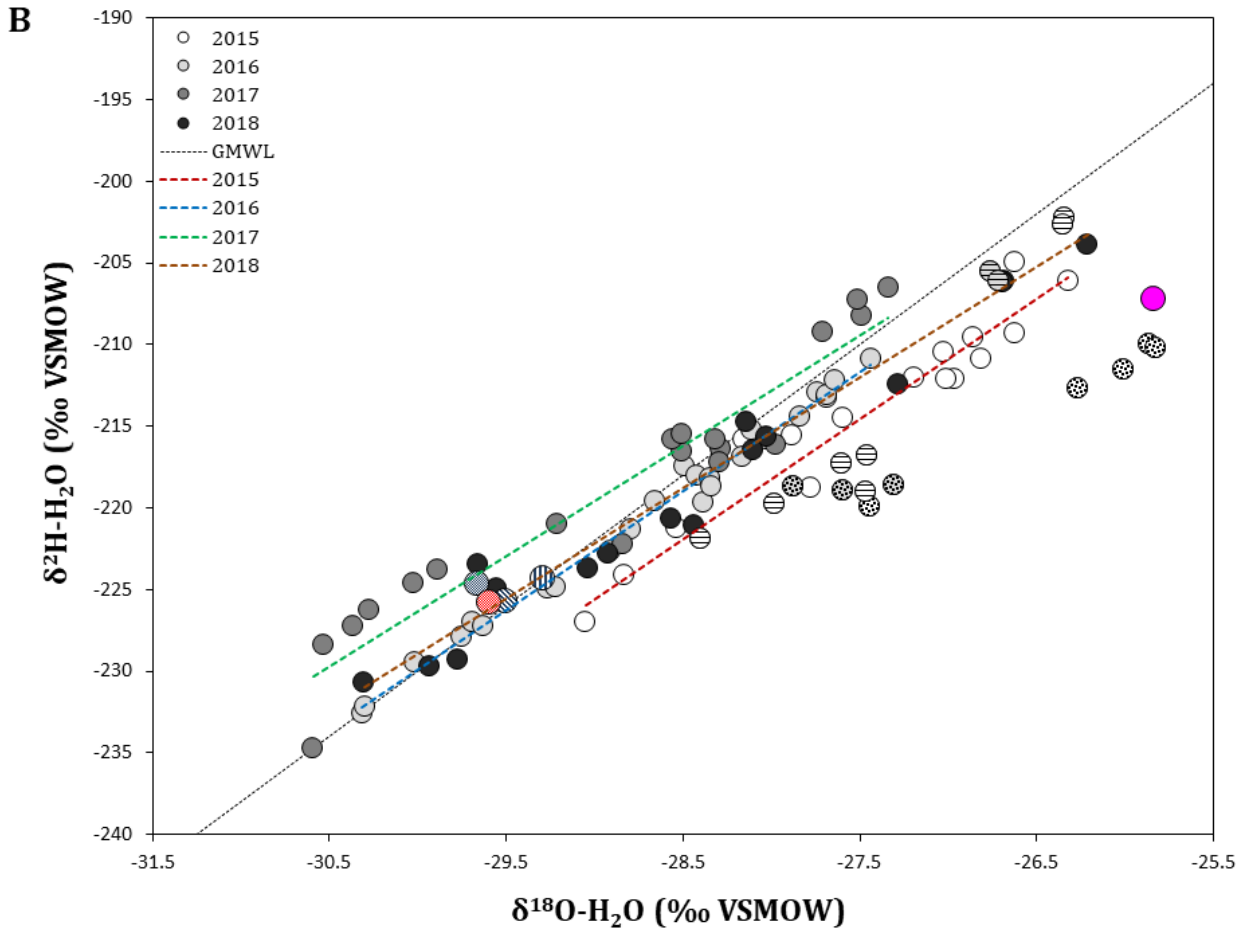

Figure 3.2: B) Interannual variability in water isotope data and linear regression results for glacial river samples taken during 2015 ($\delta^2H = 7.4 * \delta^{18}O$ -12.4 ‰; $R^2 = 0.95$), 2016 ($\delta^2H = 7.3 * \delta^{18}O$ -10.7 ‰; $R^2 = 0.99$), 2017 ($\delta^2H = 6.8 * \delta^{18}O$ -23.9 ‰; $R^2 = 0.92$), and 2018 ($\delta^2H = 6.8 * \delta^{18}O$ -28.5 ‰; $R^2 = 0.98$).

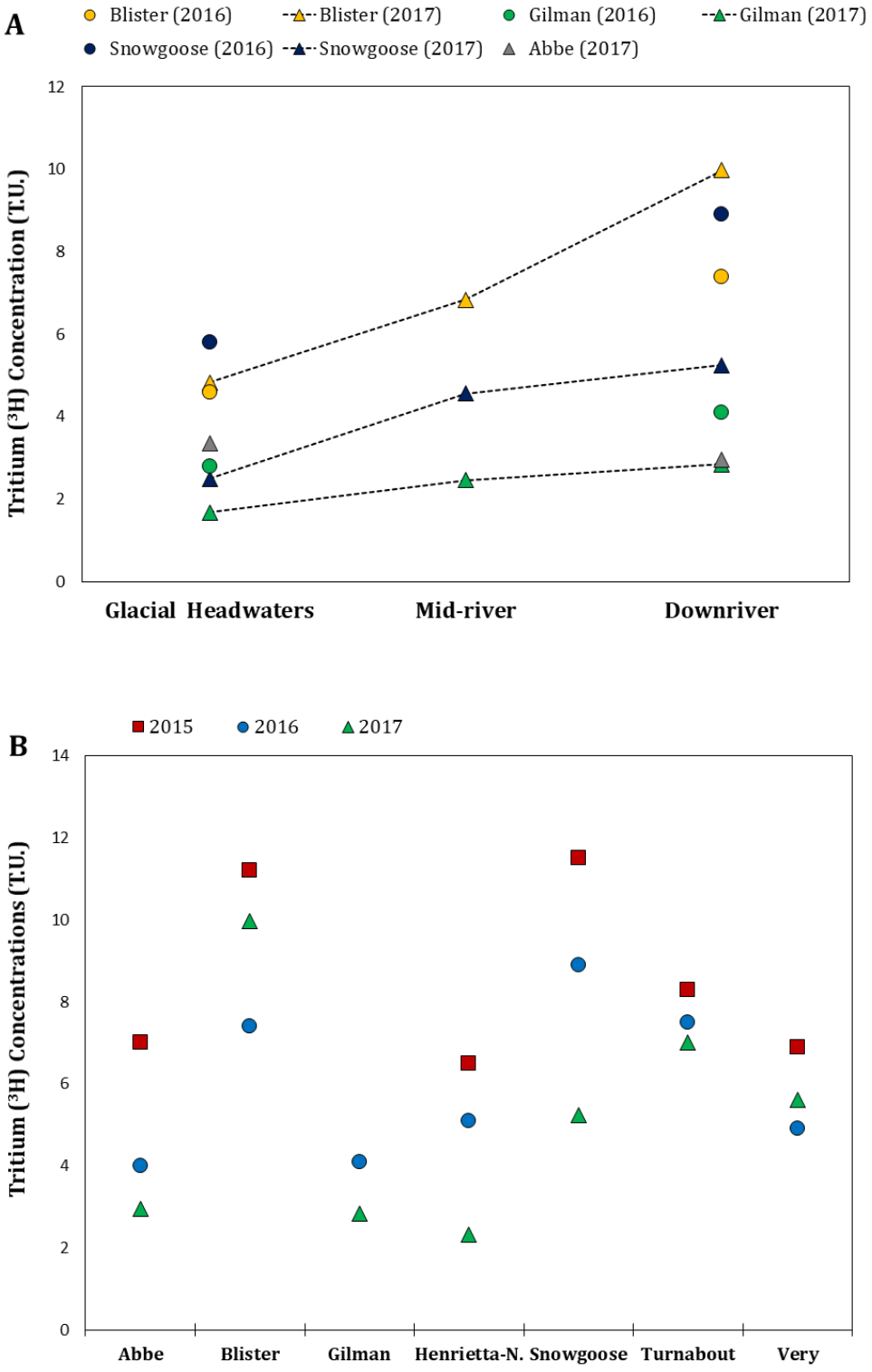

Figure 3.3: **(A)** Tritium (^{3}H) in Tritium Units (T. U.) for glacial river transects and **(B)** compared at downriver sites for high (2015), medium (2016), and low (2017) flow years.

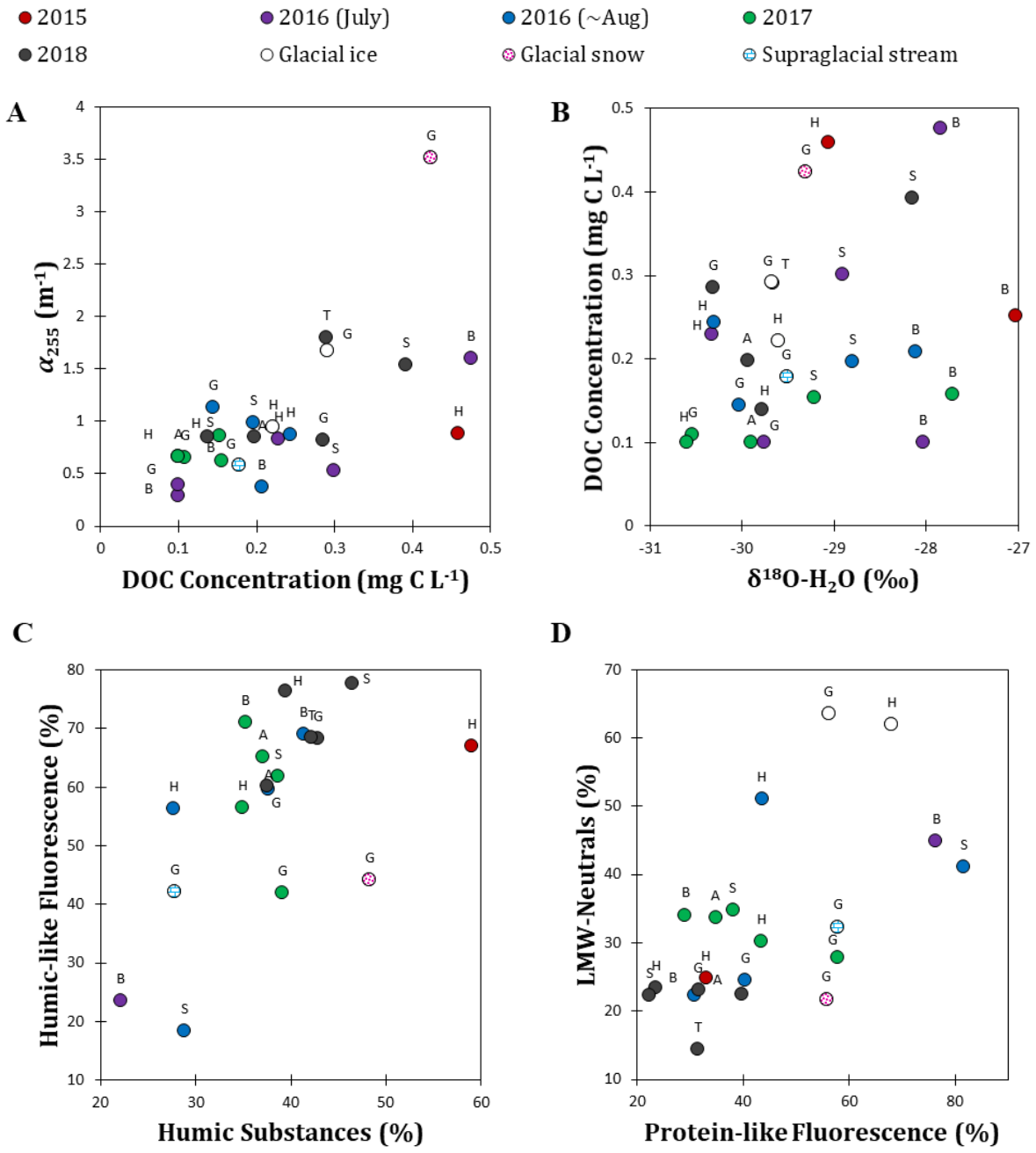

Figure 3.4A-D: (A) DOC concentration, absorption (α_{255}), water isotopes ($\delta^{18}O$-H_2O), **(B-C)** fluorescence and size exclusion (humic substances and low molecular weight neutrals; LMW-N%) data for glacial headwater samples taken during 2015, 2016, 2017, and 2018. Glacial ice, glacial snow, and supraglacial stream samples are illustrated here as well for comparison. Note: during 2016 samples were subcategorized based on major helicopter surveys, where "~Aug" = July 27th to August 5. Glacial river samples are labeled: A = Abbe, B = Blister, G = Gilman, H = Henrietta-Nesmith, S = Snowgoose, T = Turnabout, and V = Very).

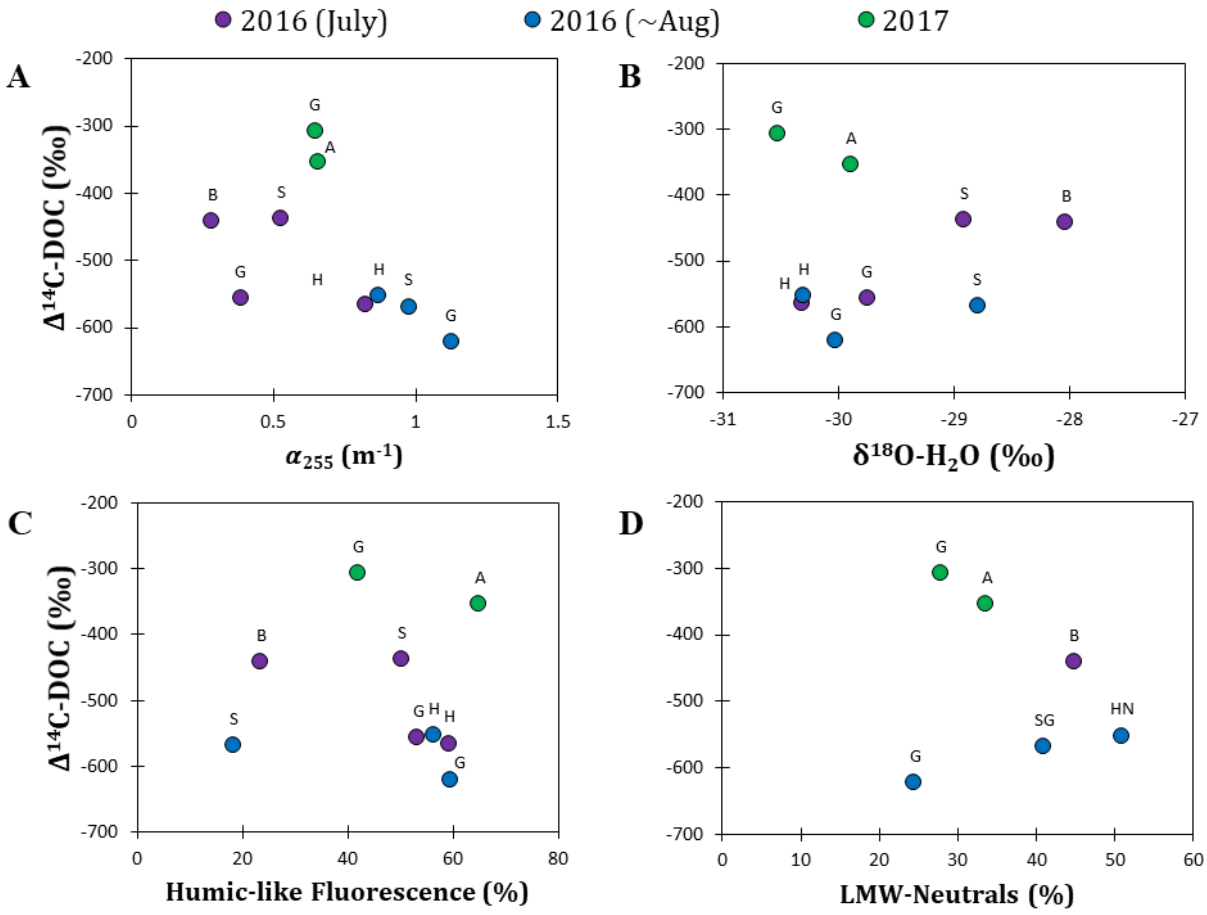

Figure 3.5A-D: Δ^{14}C-DOC for glacial river headwater samples taken during 2016 and 2017 plotted against **(A)** the absorption coefficient of calculated at 255 nm (α_{255}), **(B)** water isotopes ($\delta^{18}O$-H_2O), **(C)** the proportion of humic-like (A + C + M peaks) fluorescence relative to protein-like (T + B peaks) fluorescence, and **(D)** and low molecular weight neutrals (%LMW-N) derived from size exclusion data as available (i.e. full suite of analyses not conducted for all samples).

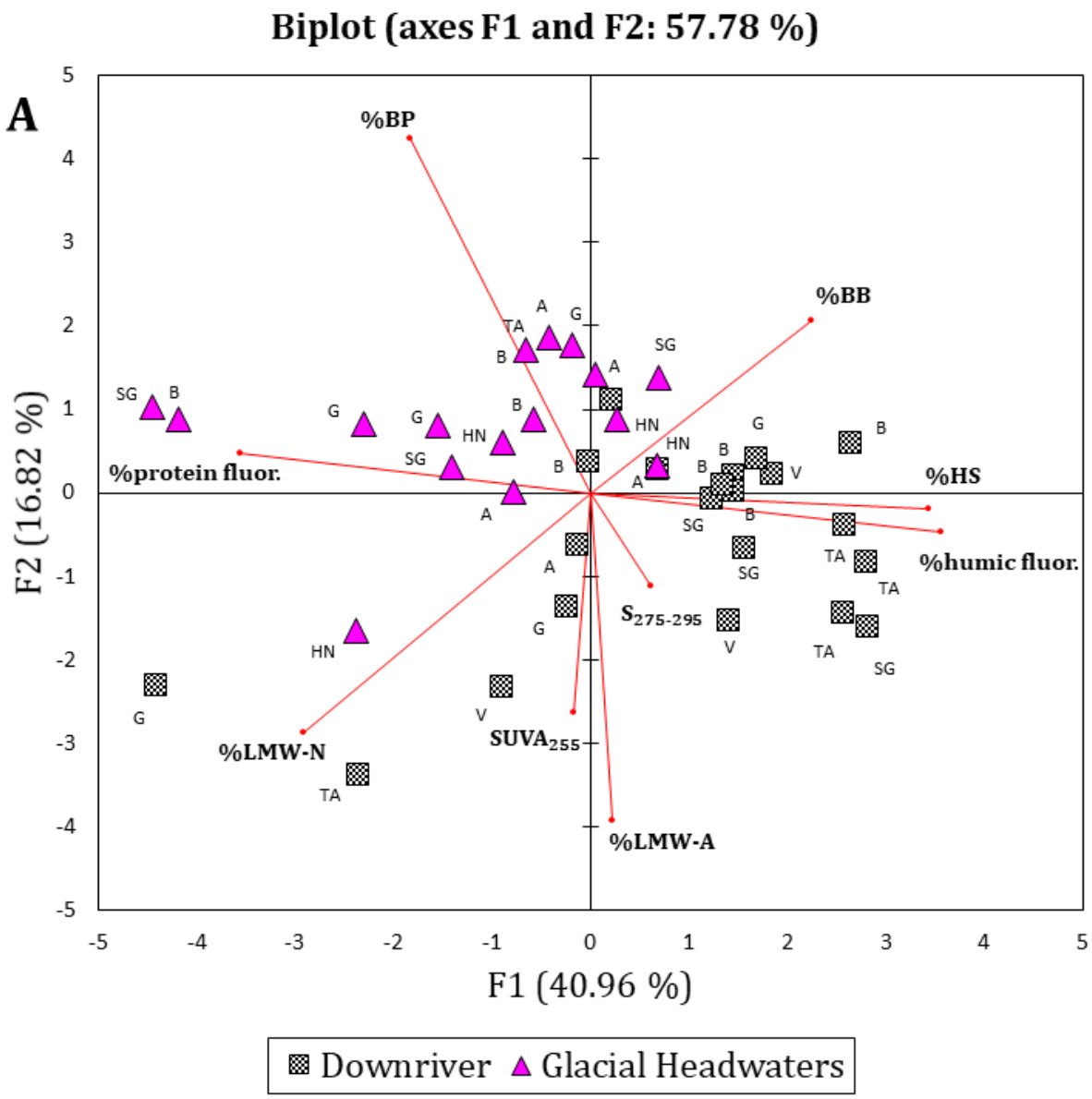

Figure 3.6 (A-B): Principal component analysis for DOC absorption ($SUVA_{255}$, $S_{275-295}$), fluorescence (% humic, % protein fluor.), and size exclusion chromatography (%BP, %BB, %HS, %LMWN, %LMWA) data for **(A)** glacial headwaters versus downriver sites and for **(B)** sites spanning 2015-18 (A = Abbe, B = Blister, G = Gilman, HN = Henrietta-Nesmith, SG = Snowgoose, TA = Turnabout, and V = Very).

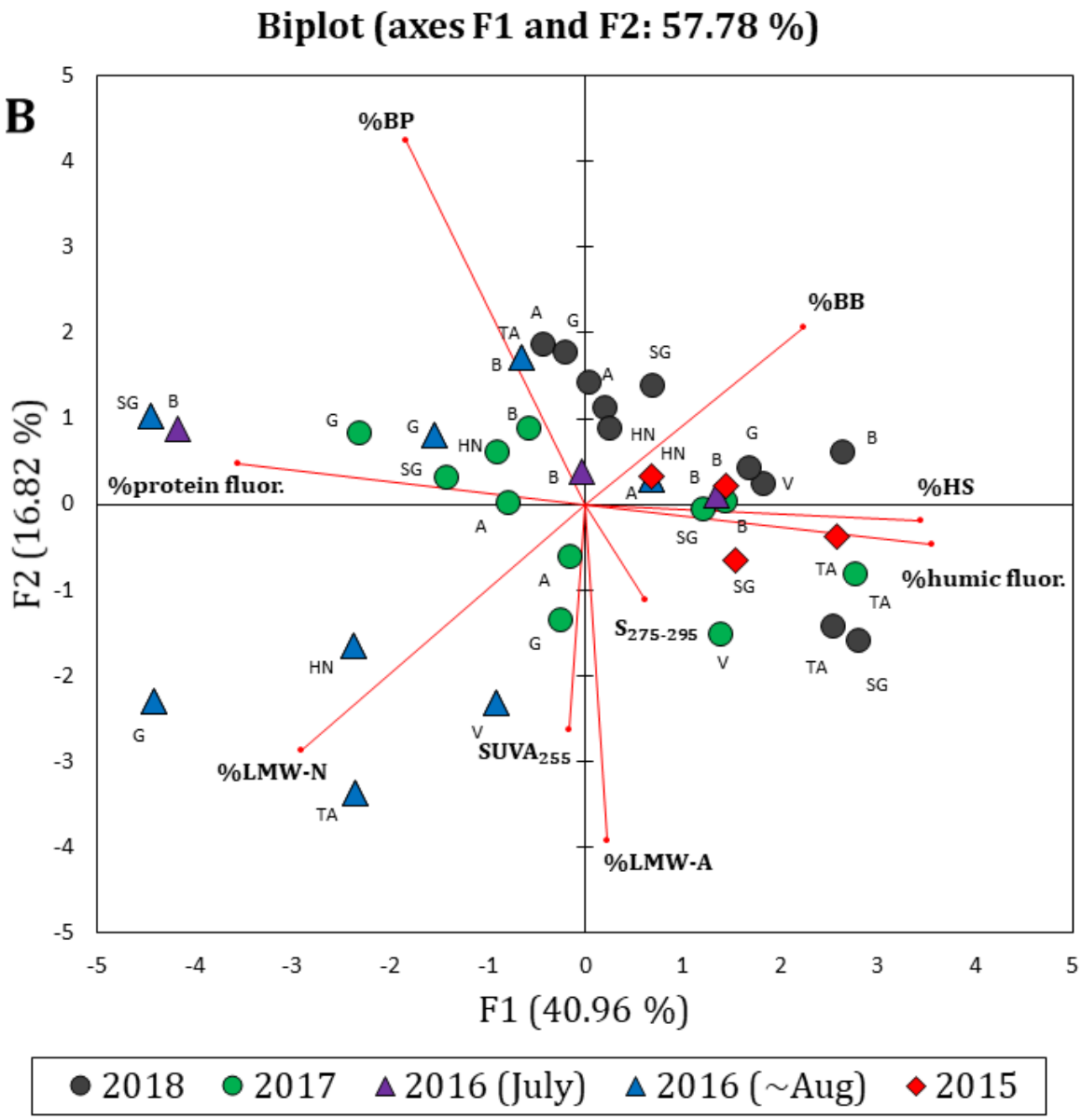

Figure 3.6 (*continued*): Principal component analysis for DOC absorption ($SUVA_{255}$, $S_{275-295}$), fluorescence (% humic, % protein fluor.), and size exclusion chromatography (%BP, %BB, %HS, %LMWN, %LMWA) data for **(A)** glacial headwaters versus downriver sites and for **(B)** sites spanning 2015-18 (A = Abbe, B = Blister, G = Gilman, HN = Henrietta-Nesmith, SG = Snowgoose, TA = Turnabout, and V = Very).

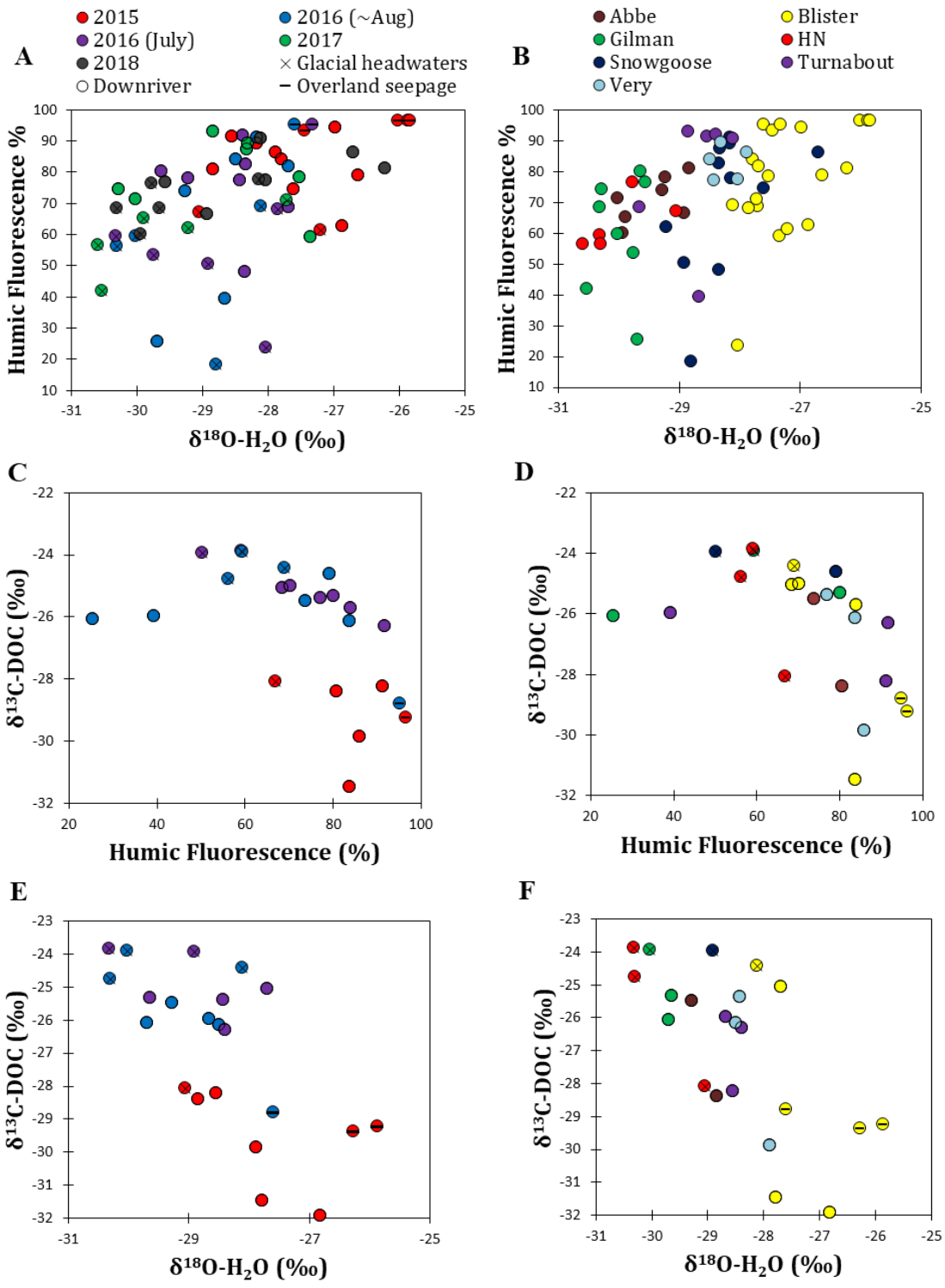

Figure 3.7A-F: Water isotope ($\delta^{18}O$-H_2O), humic-like fluorescence, and stable carbon isotopes ($\delta^{13}C$-DOC) for glacial headwater and downriver samples for years spanning 2015, 2016, 2017, and 2018. Data for overland seepage sites flowing into Blister River was included here for comparison.

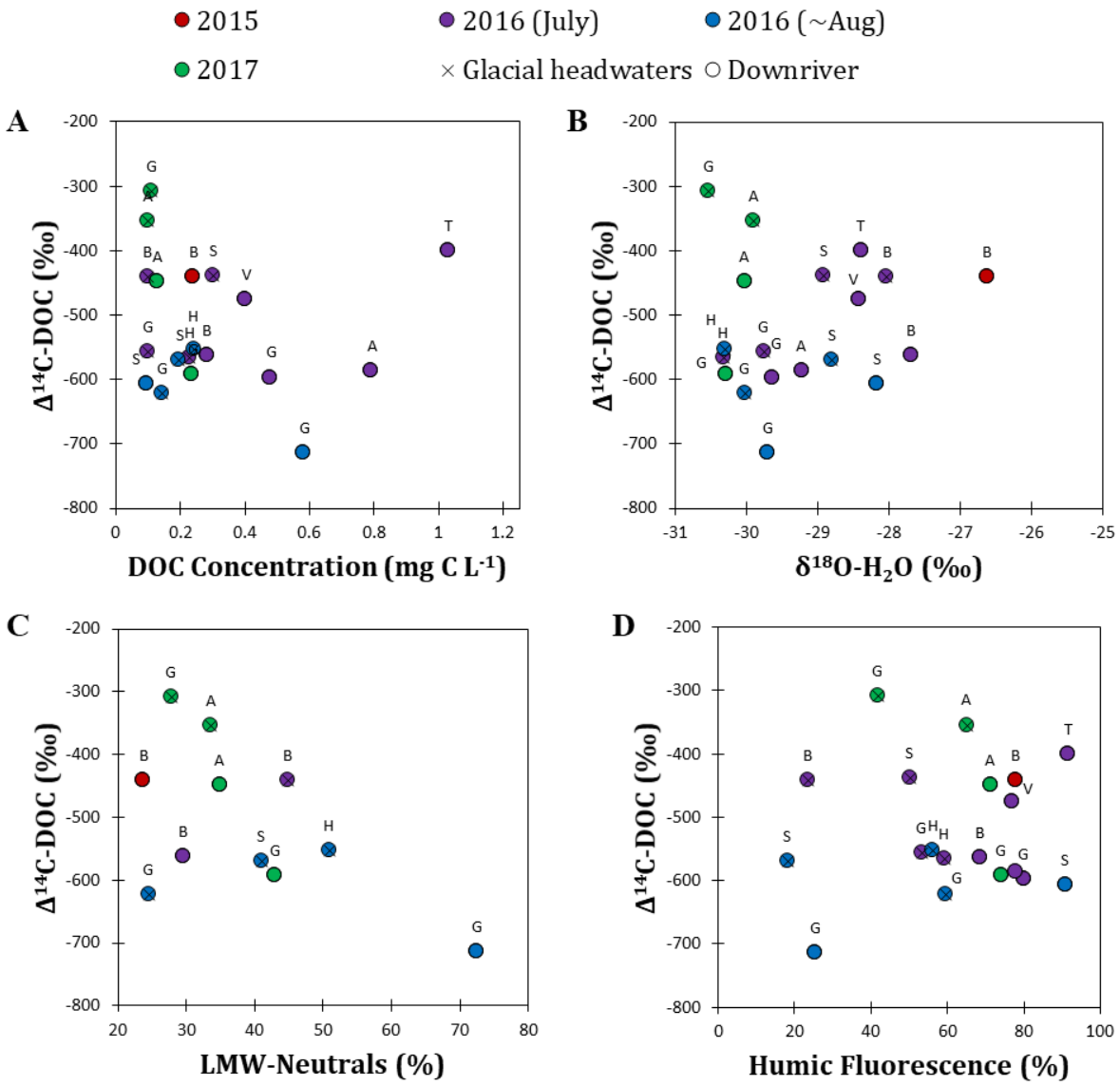

Figure 3.8A-D: Relationship of Δ^{14}C-DOC with DOC concentration, δ^{18}O-H_2O (‰), and measures of DOC composition for glacial river headwater and downriver samples spanning sampling years of 2015, 2016, and 2017. Glacial river data points are labeled: A = Abbe, B = Blister, G = Gilman, H = Henrietta-Nesmith, S = Snowgoose, T = Turnabout, and V = Very).

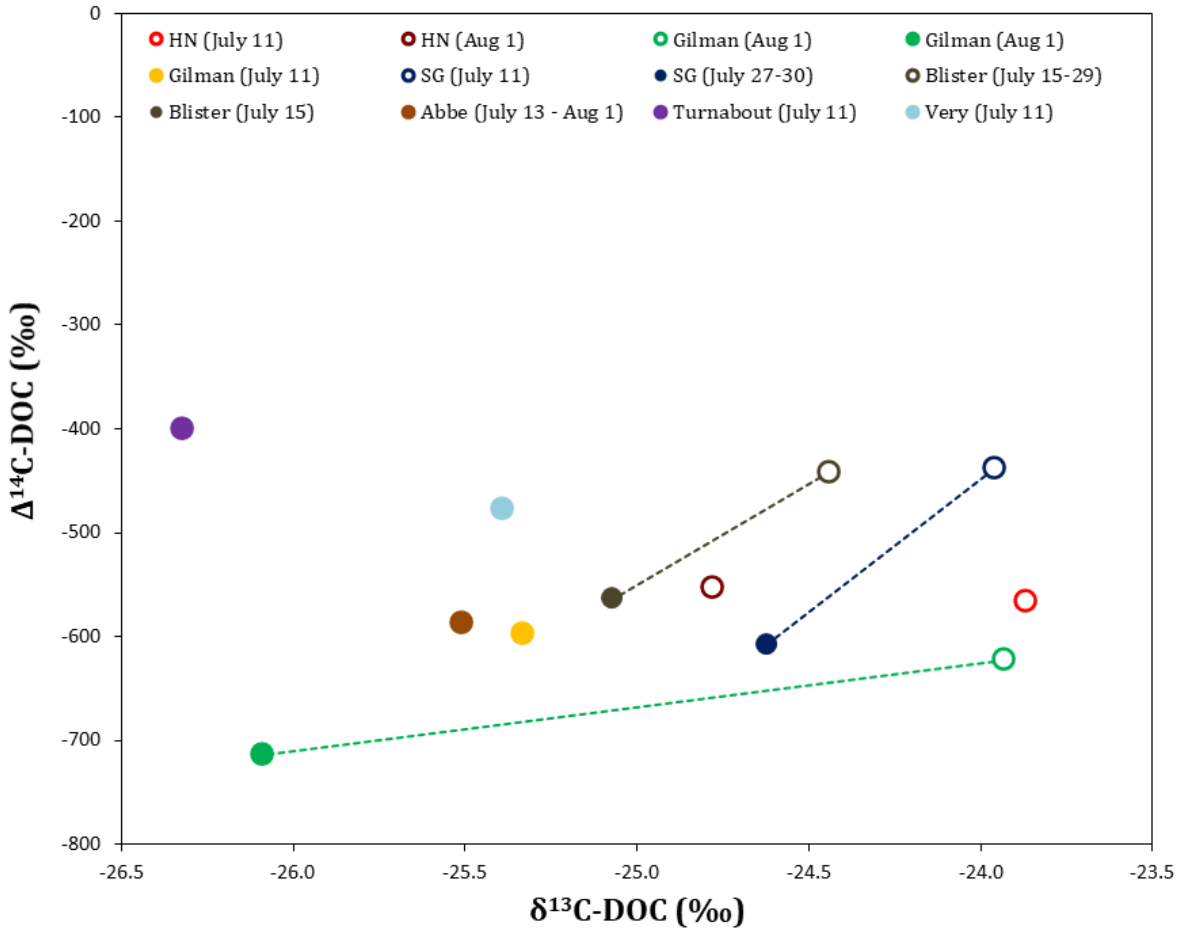

Figure 3.9: Stable ($\delta^{13}C$) and radiocarbon ($\Delta^{14}C$) isotopes of dissolved organic carbon (DOC) for glacial headwaters (*open circles*) and downriver sites (*filled circles*) for glacial rivers sampled during summer 2016. (Note: samples for which $\delta^{13}C$ and $\Delta^{14}C$ were not collected on the same sampling day are identified in the legend.)

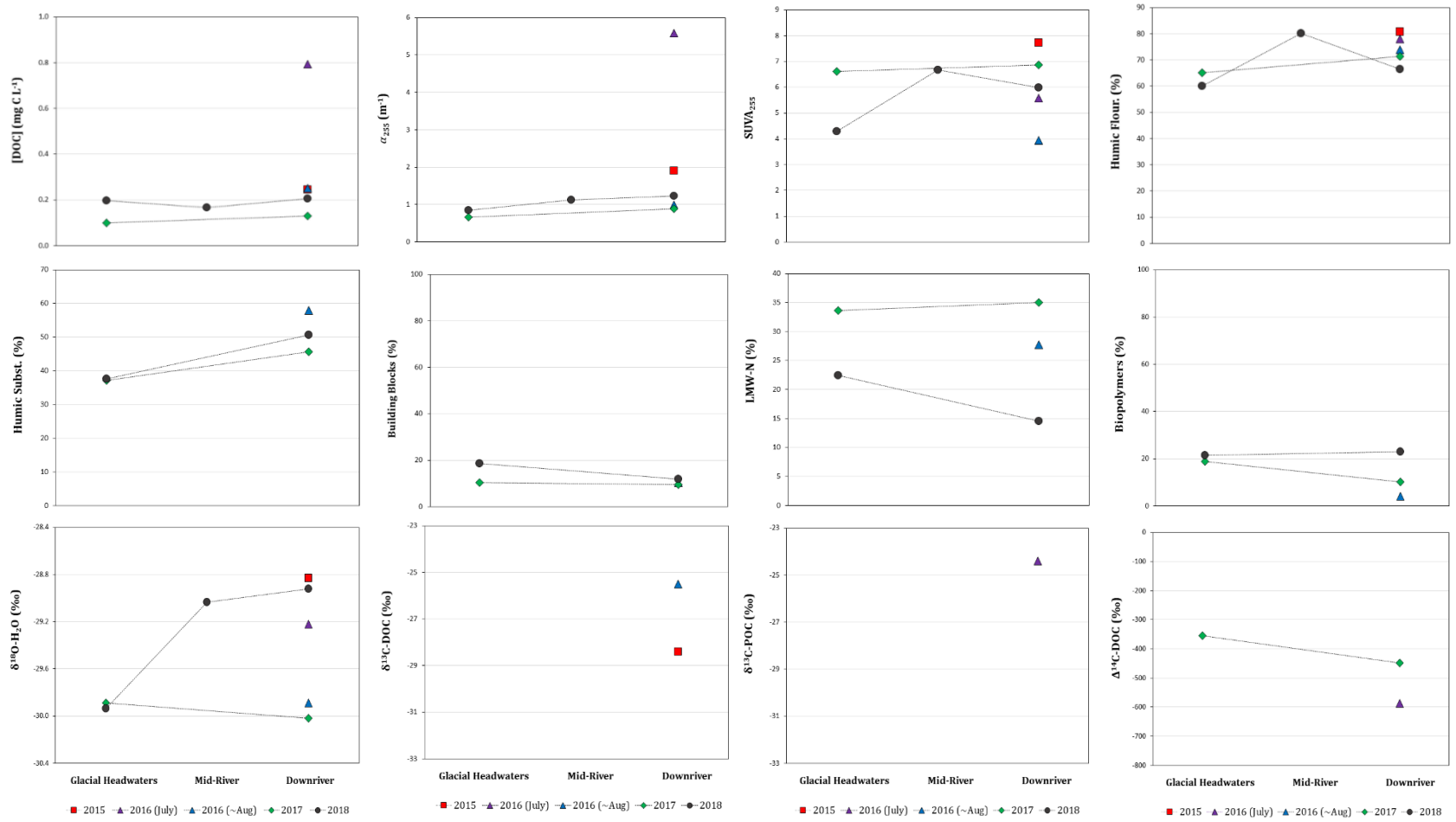

Figure 3.10A-G: DOC along glacial river transects (glacial headwaters, mid-river, downriver) for **A)** Abbe River, **B)** Blister River, **C)** Gilman River, **D)** Henrietta-Nesmith, **E)** Snowgoose, **F)** Turnabout, and **G)** Very River spanning sampling years 2015 to 2018.

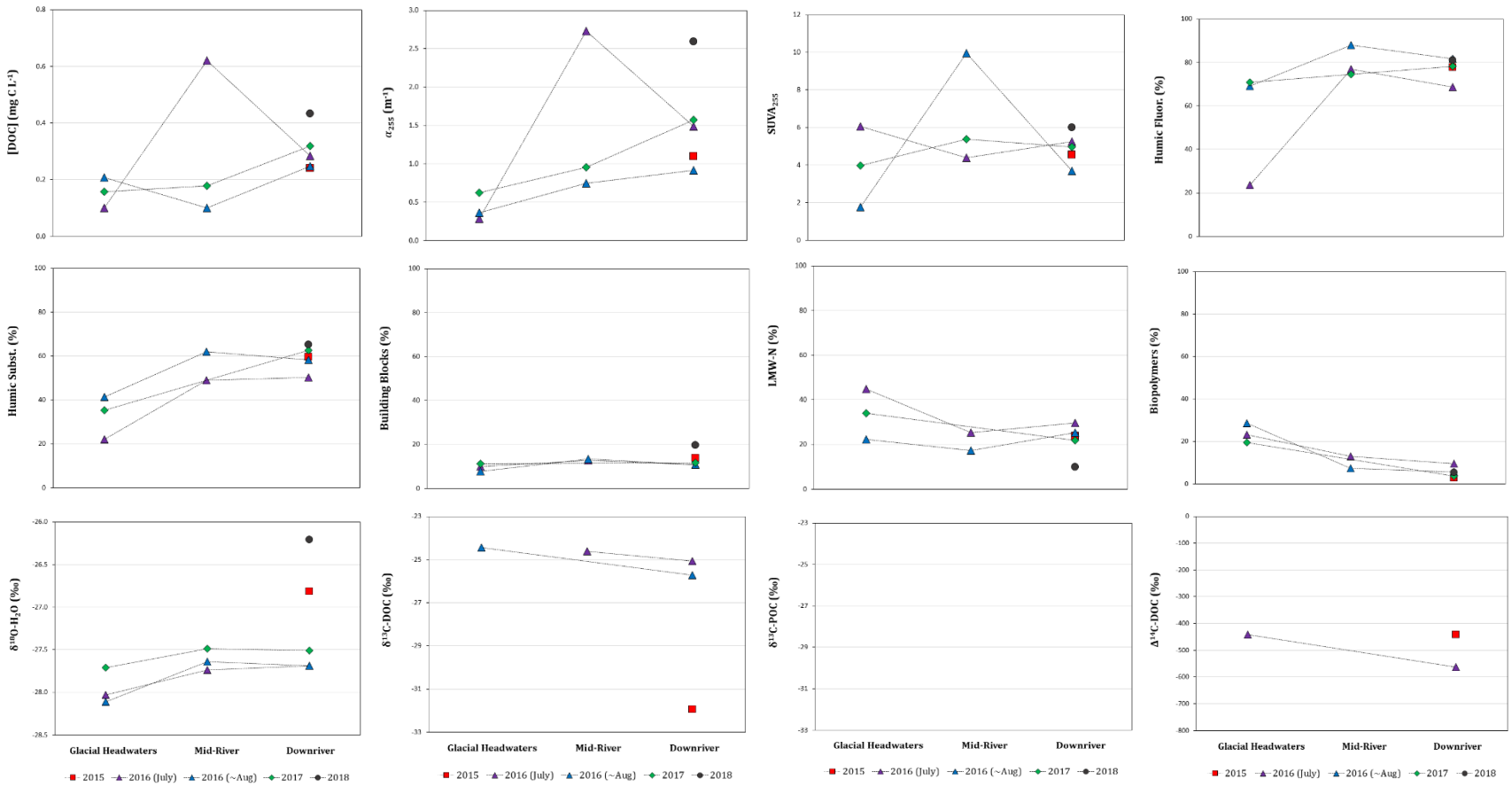

Figure 3.10A-G: DOC along glacial river transects (glacial headwaters, mid-river, downriver) for **A)** Abbe River, **B)** Blister River, **C)** Gilman River, **D)** Henrietta-Nesmith, **E)** Snowgoose, **F)** Turnabout, and **G)** Very River spanning sampling years 2015 to 2018.

C) **Gilman River** (21.5 km, ~71% glaciated)

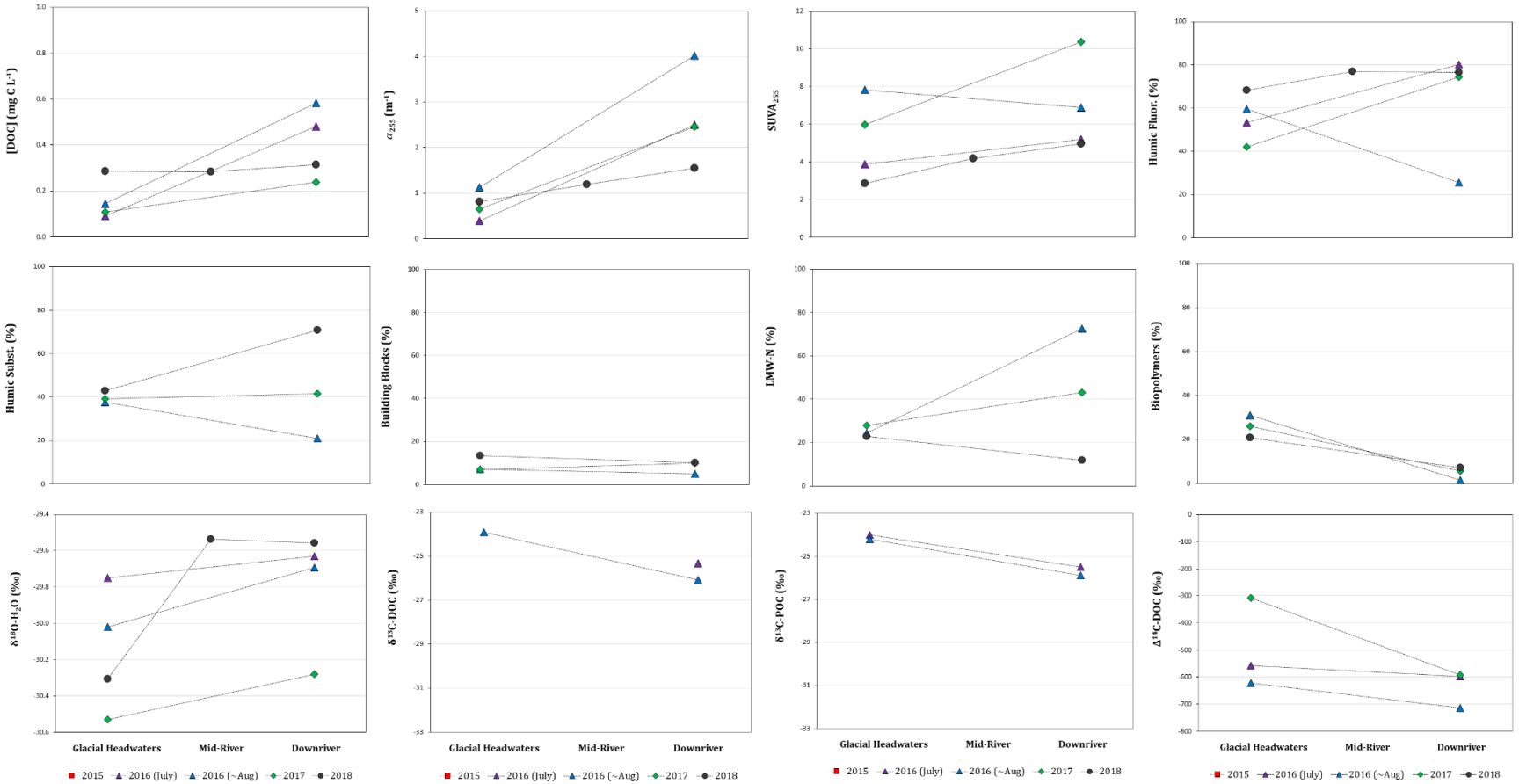

Figure 3.10A-G: DOC along glacial river transects (glacial headwaters, mid-river, downriver) for **A)** Abbe River, **B)** Blister River, **C)** Gilman River, **D)** Henrietta-Nesmith, **E)** Snowgoose, **F)** Turnabout, and **G)** Very River spanning sampling years 2015 to 2018.

D) **Henrietta-Nesmith River** (4.6 km, ~82% glaciated)

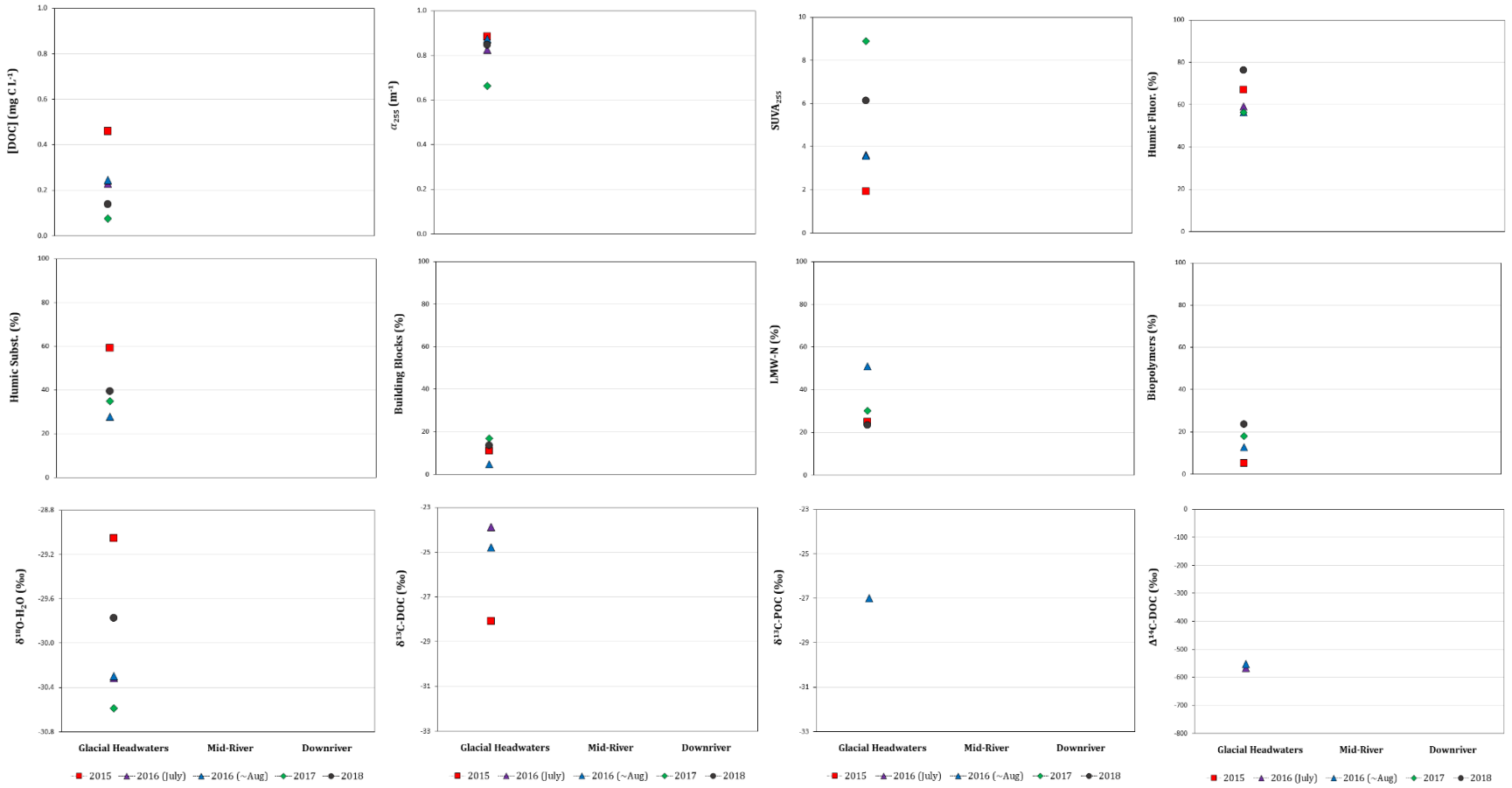

Figure 3.10A-G: DOC along glacial river transects (glacial headwaters, mid-river, downriver) for **A)** Abbe River, **B)** Blister River, **C)** Gilman River, **D)** Henrietta-Nesmith, **E)** Snowgoose, **F)** Turnabout, and **G)** Very River spanning sampling years 2015 to 2018.

E) **Snowgoose River** (16.6 km, ~39% glaciated)

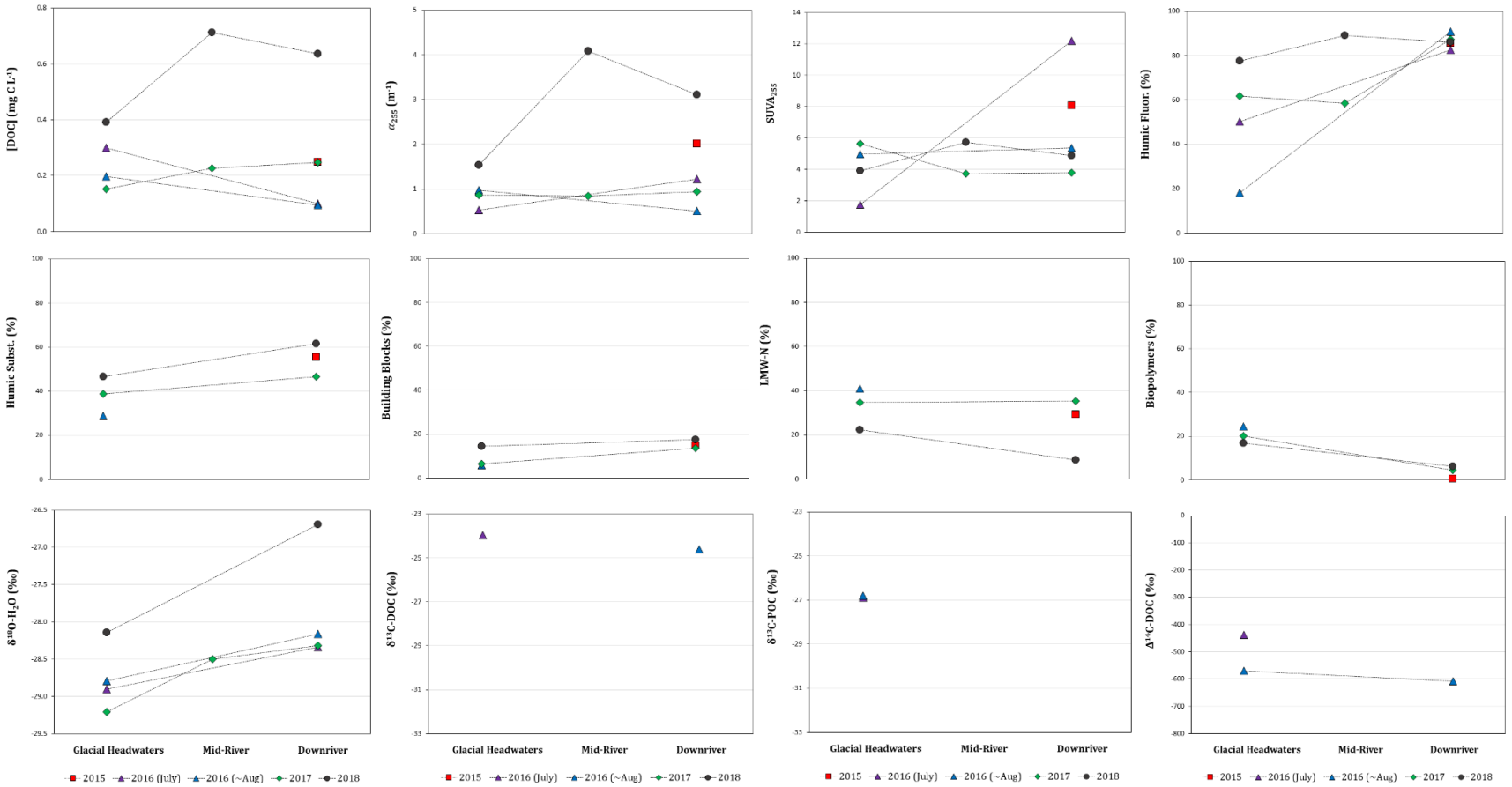

Figure 3.10A-G: DOC along glacial river transects (glacial headwaters, mid-river, downriver) for **A)** Abbe River, **B)** Blister River, **C)** Gilman River, **D)** Henrietta-Nesmith, **E)** Snowgoose, **F)** Turnabout, and **G)** Very River spanning sampling years 2015 to 2018.

F) **Turnabout River** (41.9 km, ~38% glaciated)

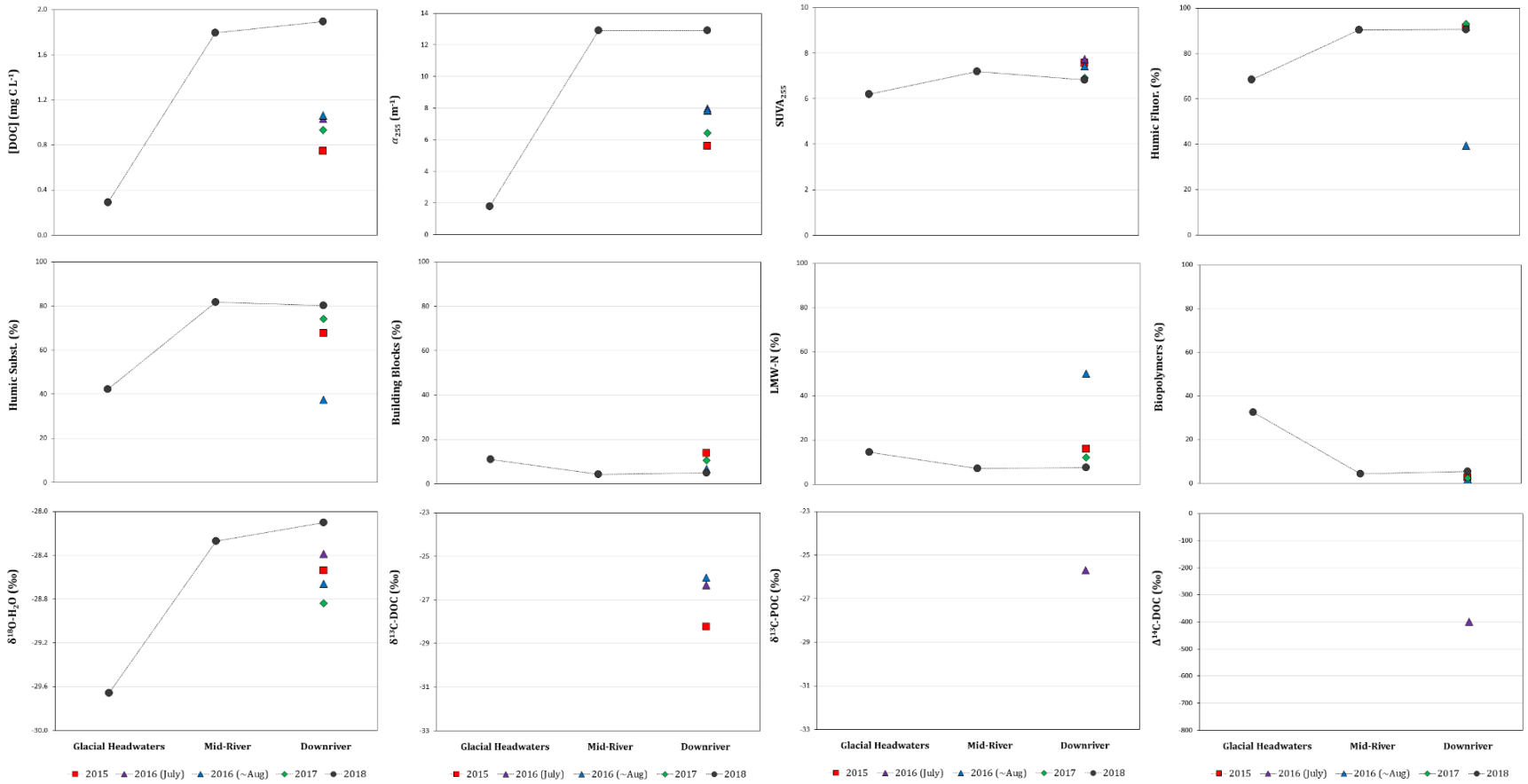

Figure 3.10A-G: DOC along glacial river transects (glacial headwaters, mid-river, downriver) for **A)** Abbe River, **B)** Blister River, **C)** Gilman River, **D)** Henrietta-Nesmith, **E)** Snowgoose, **F)** Turnabout, and **G)** Very River spanning sampling years 2015 to 2018.

G) **Very River** (39.0 km, ~26% glaciated)

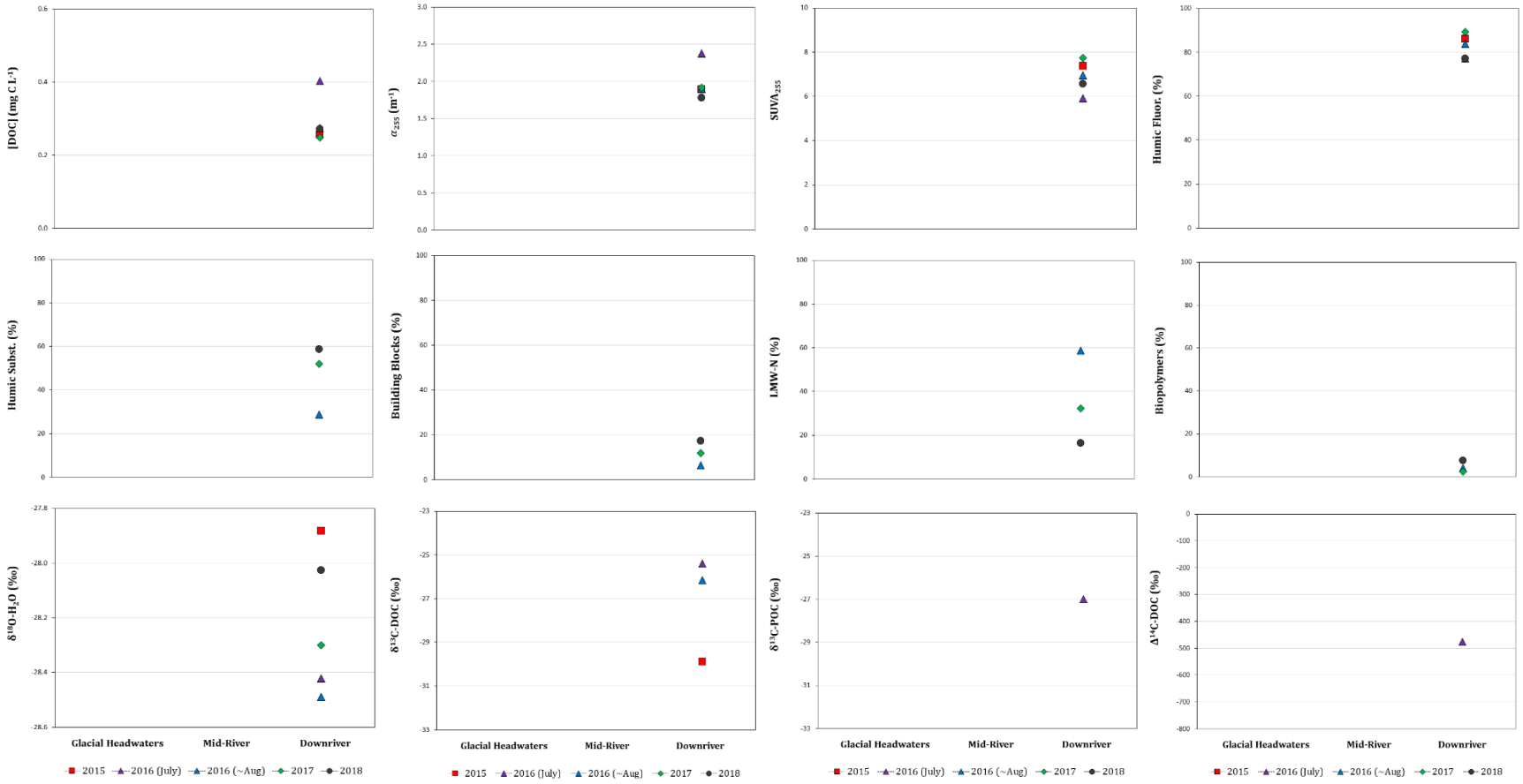

Figure 3.10A-G: DOC along glacial river transects (glacial headwaters, mid-river, downriver) for **A)** Abbe River, **B)** Blister River, **C)** Gilman River, **D)** Henrietta-Nesmith, **E)** Snowgoose, **F)** Turnabout, and **G)** Very River spanning sampling years 2015 to 2018.

Chapter 4
Impact of Mineral Weathering on Glacial River Biogeochemistries and Isotopes ($\delta^{13}C$, $\Delta^{14}C$) of Dissolved Inorganic Carbon (DIC)

4.1 Introduction

The Canadian Arctic holds one of the Earth's largest stocks of land ice, wherein there have been changes to the areas of ice caps and glaciers in these past several decades[344,345]. Future glacier ice mass loss can be variable under different climate change scenarios[77], and can cause long-term hydrologic shifts in glacier ice meltwater fluxes[82,84]. Studies have looked to better understand meltwater flux intensity and routing in glaciated (i.e. glacier covered) systems[346,347], as well as the implications of these hydrologic changes to the structure of receiving aquatic ecosystems[255,348]. Biogeochemistries of glacial runoff are also of pivotal consequence to meltwater-impacted aquatic systems, and have been investigated based on measures of microbiota[349,350], nutrients, and solutes[351–354]. Furthermore, climate induced changes to processes controlling carbon chemistry in ice sheets and glaciers may impact carbon cycling on local to global scales[355].

Biogeochemical processes can influence the cycling of carbon in various environmental compartments in glaciated systems. For instance, carbon cycling in supraglacial systems can be linked to activity of microbe assemblages, particularly in the presence of mineral depositions known as cryoconite[182,356]. Carbon sources fueling supraglacial primary productivity and heterotrophy are thus an ongoing interest[178,357], as are their relation to glacier surface darkening, reduced albedo, and accelerated melt[285,358,359]. In subglacial systems, geochemical reactions are of importance to carbon chemistry, including microbially mediated mineral weathering reactions[191,360,361]. The carbonate system and the balance between net CO_2 release versus carbon sequestration can depend on the prevalence of subglacial mineral weathering reactions vs sulphide-coupled mineral dissolution and organic carbon oxidation[110,193,205,362]. Recent research has looked beyond glacier termini to proglacial aquatic systems where mineral weathering can persist[194–196,363], result in the proglacial consumption of CO_2[206], and even transform glacial meltwater impacted freshwater systems into significant sinks of atmospheric CO_2[95]. With the advent of identifying this unprecedented sink of CO_2, there is a need to better understand mechanisms of mineral weathering reactions and CO_2 drawdown in proglacial aquatic systems, and how they control carbonate speciation and dissolved inorganic carbon (DIC) chemistry along proglacial continua (rivers, streams) under variable meltwater flow conditions.

Rapid evolution of carbon chemistry in proglacial meltwaters is a complex interplay between atmospheric exchange, weathering reactions, biological processes, abiotic OC mineralization, and mixing water sources that requires greater understanding in glacier-fed aquatic systems in order to predict their role in carbon cycling with a changing climate. Stable ($\delta^{13}C$) and radioactive carbon ($\Delta^{14}C$) isotopes can serve as tracers of carbon sources and also provide insight as to the prevalence of biogeochemical processes affecting carbon cycling in natural systems. In this study, measures of general chemistry, dissolved gases, and isotopic analyses ($\delta^{13}C$-DIC, $\Delta^{14}C$-DIC) are assessed for glacial rivers stemming from cold-based glaciers of the Lake Hazen watershed, over four sampling seasons (2016 to 2019) with variable meltwater flow conditions. Objectives are to 1) constrain sources of inorganic carbon to the DIC pool in glacial river headwaters, 2) evaluate processes controlling changes to DIC further downstream into the proglacial environment along glacial river continua, 3) assess the effects of variable meltwater flow conditions on these processes during polar summers spanning higher and lower flow years, 4) determine the fate of DIC in Lake Hazen, and 5) infer how climate change and hydrologic shifts in glacier ice meltwater flux may affect inorganic carbon cycling in high Arctic glacier ice meltwater impacted aquatic systems in the future.

4.2 Methods

4.2.1 Sampling

Samples were taken from glacial rivers of the Lake Hazen watershed during 2016 to 2019 (Figure 3.1). Complete glacial river transects spanning glacial headwaters, to mid-river, and downriver (i.e., river deltas) were sampled whenever possible. In several cases, where this was not logically feasible, only downriver sites were sampled in order to capture the carbon chemistry of meltwaters discharging to Lake Hazen. Surface layer (~ 0 m, 15 m) and deep (~ 250 m) water samples were collected near the centre of Lake Hazen 'centre buoy', far removed from sediment-laden glacial river plumes. Detailed descriptions of the Lake Hazen watershed can be found in Chapter 2 and elsewhere[89,95], including its glacial history[85], the extent of glacier cover in river catchments, the lengths and physical features of rivers, as well as the bathymetry and sediment geochemistry of Lake Hazen[90]. The geology of the Lake Hazen watershed is comprised of rocks that range in ages spanning the Early Paleozoic to the Cenozoic, for which there are metamorphic (slate, quartzite, schist, soapstone) and sedimentary (limestone, sandstone, siltstone, mudstone, shale, coal, siliciclastic) components, as well as evaporites[203,297–299]. Whereas the mineral composition of different basins was not assessed as part of

this study, sedimentary rocks (i.e., primary marine carbonates) were observed to dominate the local geology. During the expansion and retreat of glaciers, erosional processes resulted in the extensive mixing of glacial till, such that well-defined vertical profiles of historic soil/mineral composition were rarely apparent along the banks of glacial rivers. The intense grinding and pulverization of geologic material via erosional processes resulted in geologic material ranging from large boulders to fine-grain particles along glacial river continua. Sampling years spanned a variety of meltwater flow conditions, ranging from medium-high (2016), low (2017), very low (2018), and high (2019), and are summarized in *Appendix A – S3.1*.

At each glacial river sampling site, either a calibrated portable Hach meter (HQ40d) or sonde (EXO2) was used to measure temperature, pH, conductivity, and dissolved oxygen. Dissolved CO_2 concentrations were then determined using a Vaisala GM222 CO_2 probe with input parameters of *in-situ* temperature and pressure. Atmospheric pCO_2 was estimated based on the location of the Lake Hazen watershed, sampling year, and time of year[364], and used to calculate the percent saturation of CO_2 in solution.

For general chemical parameters, unfiltered water was collected in 1L Nalgene bottles and brought back to the field lab for processing (< 24 hours). Pre-weighed cellulose-acetate filters (0.45 µm) were used to sample for suspended (TSS, PC) and dissolved (TDS) parameters. General chemistry filtered samples were then stored in the cold and dark prior to analysis at the Biogeochemical Analytical Service Laboratory (BASL) of the University of Alberta. Particulate matter was also collected using an in-line filtration setup where sample water was passed over pre-combusted Whatman quartz microfiber filters (0.8 to 1.2 µm; QM-A). This particulate material was frozen and retained for stable carbon isotopic analysis of the particulate inorganic fraction (δ^{13}C-PIC) at the Environmental Isotope Laboratory of the University of Waterloo.

Samples for DIC concentrations, stable (δ^{13}C-DIC) and radiocarbon (Δ^{14}C-DIC) isotopes were filtered (0.45 µm, Whatman) in the field. Filtered water was used to wash sampling vials prior to sample collection. DIC concentration and δ^{13}C-DIC samples were taken in 12 mL exetainers with septa caps, whereas Δ^{14}C-DIC samples were collected in 60 mL glass serum bottles with rubber stoppers. Filtered water was allowed to overflow the rinsed sampling containers to eliminate headspace. In the case of the Δ^{14}C-DIC samples, 21G1.5 needle tips were used to pierce the rubber stoppers prior to sealing in order to purge any air from the samples. Needles were then removed, and

the stoppered vials were inverted to check for air bubbles. Sampling containers were secured with tape and prepared for fixation with $ZnCl_2$ shortly following sample collection (< 24 hours).

The $ZnCl_2$ solution was prepared using anhydrous (>98%) $ZnCl_2$ salt (Alfa Aesar) dissolved in NANOpure (≥18.2 mΩ-cm) water to a concentration of ~3.6 M. The $ZnCl_2$ solution was added to 12 mL exetainer samples (0.05 mL) using a 1 mL syringe equipped with a 25G needle, with a second 'waste' syringe and 25G needle used to simultaneously collect sample water displaced from the exetainer. A similar approach was applied when spiking 60 mL serum bottle samples with the $ZnCl_2$ solution. In this case, the volume of $ZnCl_2$ used was increased proportionally to the sample volume (0.25 mL) using 5 mL syringes equipped with 21G1.5 needles. Afterwards, sealed sampling vials were inverted several times to ensure that the $ZnCl_2$ was fully mixed in solution, prior to storage in cold and dark conditions.

4.2.2 DIC concentrations, Stable Carbon (δ^{13}C-DIC), and Radiocarbon (Δ^{14}C-DIC) Isotopic Analyses

Samples were analyzed for DIC concentrations following different approaches depending on the sampling season. During 2016 and 2017, samples were prepared by injecting a He headspace (3 mL) into the exetainer, followed by acidification to a pH <2 with 85% H_3PO_4. Samples were then mixed on an orbital elliptical shaker for ~ 2 hours, which allowed equilibration between the headspace and liquid phase. Finally, the equilibrated headspace was injected into a Varian 3800 gas chromatograph to measure the DIC concentration. Samples collected during 2018 and 2019 field seasons were injected directly into a Dohrmann DC-190 TOC analyzer (in DIC mode) for quantification of DIC concentrations. The liquid injection was acidified with H_3PO_4 to purge DIC from solution as CO_2, which was measured on an infra-red detector. A number of samples from 2016 and 2017 were re-run on the Dohrmann DC-190 to ensure high reproducibility and agreement in DIC concentrations with both methods.

Stable carbon isotopes of DIC (δ^{13}C-DIC, δ^{13}C-PIC) were analyzed at the Environmental Isotope Laboratory (University of Waterloo) using a GasBench II system interfaced to a MAT 253 IRMS (Thermo Scientific, Bremen, Germany). Water samples (1-4 mL) were injected into helium-filled 12 mL septum capped vials (Exetainers, Labco, High Wycombe, UK) containing 1 mL 85% phosphoric acid, and shaken for 90 minutes to force equilibration between the liquid phase and gaseous CO_2. A similar approach was used for the particulate phase, for which baked (to remove organics) solid material was scraped off QM-A filters into the exetainer for acidification. In both cases, the evolved

CO_2 was purged from vials through a double-needle sampler into a helium carrier stream (20 mL/min). The gas was sampled using a six-port rotary valve (Valco, Houston TX) with a 100 µL loop programmed to switch at the maximum CO_2 concentration in the helium carrier. The CO_2 was passed to the IRMS through a Poroplot Q GC column (25 m x 0.32 mm ID, 45°C, 2.5 mL/min). A reference CO_2 peak was used to calculate provisional delta values of the sample CO_2 peak. Each sample value obtained was the average of three injections. Furthermore, duplicate samples were run a minimum of every five samples to ensure reproducibility. Final $\delta^{13}C$ values were obtained after adjusting the provisional values for changes in linearity and instrumental drift such that known $\delta^{13}C$ values for laboratory reference materials were obtained. At least three laboratory reference materials were analyzed for every 10-12 samples. Laboratory reference materials ranged between -2 and -43 ‰. Final $\delta^{13}C$ values were expressed relative to the international standard V-PDB (Vienna PeeDee Belemnite) with a precision determined from replicate samples of ± 0.2 ‰.

Radiocarbon (^{14}C) was measured using a 3MV tandem accelerator mass spectrometer (Lalonde AMS Laboratory, Ottawa, Canada) following protocols outlined elsewhere[306-307]. Briefly, DIC was purged from the liquid sample to a He-sparged headspace via acidification (85% H_3PO_4) and heating (60ºC), followed by cryogenic purification and graphitization of CO_2 for ^{14}C analysis (Lalonde AMS Laboratory). The fraction of modern carbon ($F^{14}C$) was calculated as $^{14}C/^{12}C$sample: $^{14}C/^{12}C$standard using the oxalic acid II (Ox-II) standard[115]. Isotopic fractionation was then corrected via normalization to $\delta^{13}C$ of Pee Dee Belemnite (PDB)[113]. Radiocarbon age in years before present (BP = 1950 AD) and the corrected per mill depletion or enrichment ($\Delta^{14}C$-DIC) were then calculated using the fraction modern carbon ($F^{14}C$; Table 2.3). The average standard deviation among $F^{14}C$ values was 0.0038 ± 0.0035, which translates to $\Delta^{14}C$ ~ 3.8 ± 3.5 ‰, and ^{14}C ages ~ 40 ± 30 yBP.

4.2.3 Defining the carbonate system

DIC is the sum of carbonate species:

$$DIC = CO_{2(aq)}^{*} + HCO_{3\ (aq)}^{-} + CO_{3\ (aq)}^{2-}$$

The carbonate system is defined by the following equilibria[107]:

$$CO_{2(g)} \leftrightarrow CO_{2(aq)}$$

$$CO_{2(aq)} + H_2O_{(l)} \leftrightarrow H_2CO_{3(aq)}$$

$$H_2CO_{3(aq)} \leftrightarrow H^+{}_{(aq)} + HCO_3^-{}_{(aq)}$$

$$HCO_3^-{}_{(aq)} \leftrightarrow H^+{}_{(aq)} + CO_3^{2-}{}_{(aq)}$$

$$\boldsymbol{Note: CO_2^* = CO_{2(aq)} + H_2CO_{3(aq)}}$$

Temperature (T) specific equilibrium constants were calculated for the carbonate system using the following equations[108]:

$$pK_{CO_2} = -7 \cdot 10^{-5}T^2 + 0.016T + 1.11$$

$$pK_1 = 1.1 \cdot 10^{-4}T^2 - 0.012T + 6.58$$

$$pK_2 = 9 \cdot 10^{-5}T^2 - 0.0137T + 10.62$$

Equilibrium constants for the carbonate system were applied to supplementary calculations in the determination of concentrations of carbonate species. Fractional (f) contributions of carbonate species to bulk DIC (with a sum of 1) were also calculated. For example:

$$fHCO_3^- = \frac{[HCO_3^-]}{[DIC]}$$

$$fCO_2^* + fHCO_3^- + fCO_3^{2-} = 1$$

To fully define the carbonate system at equilibrium conditions only two of the six variables are required (H^+, $[CO_2]$, $[HCO_3^-]$, $[CO_3^{2-}]$, carbonate alkalinity, and [DIC])[365]. Accordingly, there are a number of different calculation approaches that could be employed for different combinations of variables. Since supplementary calculations of theoretical δ^{13}C-DIC are linked to the fractional

contributions of carbonate species, it was important to evaluate different approaches to defining the carbonate system (*Appendix B*).

4.2.4 Theoretical Equilibrium δ^{13}C-DIC

The following isotopic calculations of δ^{13}C-DIC require temperature specific isotopic fractionation factors, an end-member for $\delta^{13}C\text{-}CO_{2\,(g\text{-}air)}$, and fractional contributions of carbonate species. Firstly, physical isotopic fractionation occurs when $CO_{2\,(g)}$ crosses the gas-water interface, in accordance with the following relationship, where $\boldsymbol{\alpha}$ is the equilibrium fractionation factor[366,367]:

$$CO_{2(g-air)} - CO_{2(g-water)} \rightarrow 1000 \ln \alpha = -\left(0.373 * \frac{10^3}{T}\right) + 0.19$$

The $\delta^{13}C\text{-}CO_{2\,(g\text{-}water)}$ at equilibrium can then be calculated:

$$\delta^{13}C - CO_{2(g-water)} = \alpha * \left(\delta^{13}C - CO_{2(g-air)} + 1000\right) - 1000$$

The $\delta^{13}C\text{-}CO_{2\,(g\text{-}air)}$ was assumed to be -8.3‰ based on the years sampled (2016-19), seasonality (July-August), and the geographic location of the Lake Hazen watershed[368]. Fractionation factors for chemical isotopic fractionation of carbonate species could then be calculated at specific temperatures relative to the equilibrium $CO_{2\,(g\text{-}water)}$[369]:

$$CO_2 - CO_{2(g-water)} \rightarrow 1000 \ln \alpha = -0.91 + 0.0063 * \frac{10^6}{T^2}$$

$$HCO_3^- - CO_{2(g-water)} \rightarrow 1000 \ln \alpha = -4.54 + 1.099 * \frac{10^6}{T^2}$$

$$CO_3^{2-} - CO_{2(g-water)} \rightarrow 1000 \ln \alpha = -3.4 + 0.87 * \frac{10^6}{T^2}$$

Similarly, isotopic signatures for each carbonate species were calculated using $\delta^{13}CO_{2\,(g\text{-}water)}$). As an example, for $\delta^{13}C\text{-}HCO_3^-$:

$$\delta^{13}C - HCO_3^- = \alpha * \left(\delta^{13}C - CO_{2(g-water)} + 1000\right) - 1000$$

Fractional contributions of carbonate species were applied to resolve the bulk theoretical equilibrium δ^{13}C-DIC:

$$\delta^{13}C - DIC_{theoretical} = (fCO_2 * \delta CO_2) + (f\,HCO_3^- * \delta\,HCO_3^-) + (f\,CO_3^{2-} * \delta\,CO_3^{2-})$$

In this fashion, theoretical equilibrium δ^{13}C-DIC could be determined based on the fractional contributions of carbonate species calculated from measured [DIC], pH, and pCO_2.

4.3 Results

4.3.1 Glacial headwater geochemistry and inorganic carbon isotopes

Glacial river headwaters samples taken < 500 m from glacier termini were cold (1.8 ± 1.5 ºC) and dilute, with low measures of specific electrical conductance (SEC < 111 µS cm^{-1}) and total dissolved solids (TDS < 70 mg L^{-1}; Figure 4.1A-B). These meltwaters were typically observed to have a milky appearance based on the presence of suspended fine-grain powder 'rock flour' derived from glacial till, and had total suspended solids (TSS) concentrations spanning <5 to 670 mg L^{-1}. Particulate carbon (PC) concentrations were largely < 2 mg C L^{-1}, apart from two samples with much higher values of 5.9 and 10.7 mg C L^{-1}, from Snowgoose (2018) and Henrietta-Nesmith (2016) rivers, respectively (Figure 4.1C-D).

Glacial headwater samples spanned a narrow range of slightly basic pH values (~ 6.9 to 8.2), with only a few others having higher measures of pH (8.4, 9.2; n = 2). Carbonate speciation was dominated by HCO_3^- for these samples, given their close proximity to the theoretical maximum HCO_3^- at pH ~8.3. Increased DIC concentrations were typically accompanied by a shift towards more alkaline conditions and lower dissolved [CO_2] (Figure 4.2A-D). In fact, the most extensively glacier covered systems (Henrietta-Nesmith, Gilman), with the most negative δ^{18}O-H_2O (< -29.4 ‰), had high DIC concentrations (250 ± 114 µM) and were undersaturated in CO_2 (~61 ± 16 sat. %). In contrast, glacial headwaters originating from smaller glaciers (Blister, Snowgoose) had comparatively positive δ^{18}O-H_2O (> -29.2 ‰), lower DIC concentrations (69 ± 28 µM), and were less undersaturated in CO_2 (~88 ± 9 %) (Figure 4.2E-H). Whereas glacial headwaters were almost ubiquitously

undersaturated with respect to CO_2, they were nearly fully saturated with respect to dissolved O_2 (100 ± 5 sat. %).

Stable carbon isotopes of DIC (δ^{13}C-DIC) indicated that glacial headwaters were rarely in isotopic equilibrium with atmospheric CO_2. Within the range of pH and temperature measurements for glacial river headwaters, the theoretical equilibrium δ^{13}C-DIC would be expected to be within -2.5 to 0.5 ‰ (*Appendix B*). On the other hand, many of the actual measured δ^{13}C-DIC values for glacial river headwaters were found to be more negative, reaching a minimum of -6.5 ‰ (Table 4.1A; Figure 4.3A-F). In particular, samples taken during the high flow year (2019) had δ^{13}C-DIC that was more negative ($p < 0.05$; -4.5 ± 1.3 ‰) than those of the low flow year (2017; -0.7 ± 1.8 ‰). The δ^{13}C-PIC of suspended sediment particulate material in glacial headwaters were also negative during 2019 and covered a wide range of values (-0.9 to -6.9 ‰; Table 4.2). These δ^{13}C-PIC values were more negative than what would be expected solely for primary marine carbonate minerals (~ 0 ‰)[111], and indicated the presence of secondary freshwater carbonates as well. Although both δ^{13}C-PIC and δ^{13}C-DIC were negative in glacial headwaters, and spanned similar ranges, they were not significantly related (Figure 4.4).

DIC of glacial headwaters was not ^{14}C modern, but rather was comprised of aged inorganic carbon. The Δ^{14}C-DIC spanned a wide range of values (-161 to -437 ‰), corresponding to ^{14}C ages of ~1342 to 4456 yBP (Table 4.1A). Δ^{14}C-DIC was linearly correlated with δ^{13}C-DIC ($R^2 = 0.91$; $p < 0.05$), showing the most ^{14}C ancient DIC also had the most negative δ^{13}C-DIC (Figure 4.5). However, since neither δ^{13}C-DIC nor Δ^{14}C-DIC was correlated to [DIC], the amount of DIC did not control its isotopic character (Figure 4.6A-D). Differing levels of equilibration with the atmosphere were therefore not expected to have impacted δ^{13}C-DIC and Δ^{14}C-DIC in glacial headwaters. A sample taken from Henrietta-Nesmith (July 2016) with the most negative Δ^{14}C-DIC (-437 ‰), also had particularly negative δ^{13}C-DIC (-4.0 ‰) and a high PC concentration (10.1 mg L^{-1}; Table 4.1A). A principal component analysis (PCA; Pearson, $\alpha = 0.05$) was conducted on normalized data for glacial headwater samples for a range of geochemical variables with an explained variance of ~52% for 9 variables. The correlation matrix only showed a few significant relationships between measures of general chemistry, but not with respect to δ^{13}C-DIC (Table 4.3A). Similarly, the subset of glacial headwater samples for which the ^{14}C of DIC was analyzed did not show significant relationships between general chemistry parameters and Δ^{14}C-DIC. These findings suggest that variability in the

isotopic character of DIC ($\delta^{13}C$, $\Delta^{14}C$) in glacial headwaters was not shaped by the DIC concentration gradient, but perhaps rather by changes in the prevalence of geochemical process that affect DIC.

4.3.2 Downriver evolution of meltwater geochemistry and $\delta^{13}C$-DIC

Geochemistry of glacial headwaters evolved rapidly along glacial river downstream transects, and was shaped by meltwater flow conditions and physical characteristics of glacial rivers. Specific electrical conductance (SEC) and total dissolved solids (TDS) increased in all rivers spanning headwaters (39 ± 26 μS cm^{-1}; 26 ± 15 mg L^{-1}), to mid-river (89 ± 45 μS cm^{-1}; 43 ± 28 mg L^{-1}), and downriver sites (114 ± 46 μS cm^{-1}; 61 ± 27 mg L^{-1}; Figure 4.1A-B). On the other hand, total suspended solids (TSS) and particulate carbon (PC) had extreme inter-river and interannual variability in these measures (Figure 4.1C-D). For instance, the Abbé River had smaller downriver increases in TSS and PC during lower flow conditions of 2017 (12 mg L^{-1}; 0.1 mg L^{-1}) and 2018 (5 mg L^{-1}; 0.2 mg L^{-1}), relative to higher flow conditions during 2019 (354 mg L^{-1}; 0.8 mg L^{-1}) (Figure 4.7A-G). Turnabout River also had downriver increases in TSS and PC relative to glacial headwaters that were of considerably different magnitudes in 2018 (34 mg L^{-1}; 0.6 mg L^{-1}) compared to 2019 (1083 mg L^{-1}; 22.7 mg L^{-1}). Downriver increases in TSS and PC were also apparent in all transects of the Gilman River, and were highest in 2016 (1017 ± 213; 25.2 ± 9.7 mg L^{-1}). By contrast, transects of smaller glacial rivers (Blister and Snowgoose) did not show reproducible downriver trends in TSS and PC spanning all sampling years (Figure 4.7A-G). Inter-river and interannual variability in TSS and PC were much lower for glacial headwaters compared to downriver sites, but the distance of sampling sites from glacier termini did not exclusively control TSS and PC along river transects (Figure 4.8A-D). Meltwater flow conditions and the availability of fine-grain freshly eroded particulate material were likely more impactful to the concentrations of TSS and PC measured in glacial rivers. Based on the amount of suspended sediment in meltwaters, in-field observations of glacial rivers ranged from appearing nearly clear and colourless to faintly cloudy, to opaque and even dark-brown.

Meltwater geochemistry also changed along glacial river transects with respect to DIC, pH, and dissolved CO_2. Overall, downriver increases in [DIC] from glacial headwaters (227 ± 116 μM), to mid-river (390 ± 160 μM), to downriver sites (646 ± 204 μM) indicate an addition of DIC along the river length, which typically coincided with small shifts towards more alkaline conditions (Figure 4.7A-G). The lowest average downriver DIC concentrations belonged to the extensively glacier covered Gilman River (~71 %; 472 ± 99 μM) and Abbe River (~52 %; 381 ± 84 μM), which were

comparable to that of the Henrietta-Nesmith glacial discharge (~82 %; 322 ± 103 µM). The remaining glacial rivers had higher [DIC] and stemmed from more sparingly glacier covered terrain (< 40% glaciated), but had a wide range of river lengths. Even so, variable river lengths and meltwater transit times did not solely dictate differences in [DIC] at downriver sites of Blister (10.5 km; 778 ± 228 µM), Snowgoose (16.6 km; 581 ± 123 µM), Turnabout (41.9 km; 699 ± 38 µM), and Very (39.0 km; 823 ± 65 µM) rivers (Figure 4.8A-D). Whereas transects typically shifted towards more alkaline conditions downriver, this trend was not significant across the entire dataset, based largely on an anomalous (pH ~ 9.2) glacial headwater sample of the Abbe River (2017), and four slightly acidic samples (pH ~ 6.4 to 6.9) taken from Blister River and Snowgoose River deltas (July 2016). Apart from these samples, the pH of glacial headwaters (~ 6.9 to 8.4; n = 22), mid-river (~ 7.3 to 8.6; n = 15), and downriver sites (~7.5 to 8.7; n = 43) spanned relatively narrow ranges in pH values (Figure 4.7A-G; Figure 4.8A-D). For instance, Gilman and Turnabout glacial headwaters were less alkaline (7.6 ± 0.1; 7.2 ± 0.1) when compared to their respective downriver sites (8.4 ± 0.3; 8.0 ± 0.2). Dissolved CO_2 was almost ubiquitously undersaturated in glacial rivers, but did not show strong or reproducible downriver shifts along glacial river transects. The most undersaturated CO_2 belonged to glacial rivers with more negative $\delta^{18}O\text{-}H_2O$ values that stemmed from extensively glacier covered terrain, although this did not explain the wide ranges in CO_2 % sat. spanning different sampling years. Instead, CO_2 % sat. was significantly ($p < 0.05$) higher for glacial river transects sampled during lower flow years (2017, 2018; 87 ± 12 %), when compared to higher flow years (2016, 2019; 66 ± 23 %), suggesting that the volume or intensity of glacial meltwater fluxes was linked to CO_2 % sat. This undersaturation in CO_2 was not shared by dissolved O_2 (% sat. O_2 ~ 101 ± 4 %), which confirmed that geochemical processes specifically affect gas exchange of CO_2 and the carbonate system in glacial meltwaters.

Glacial river transects had variable $\delta^{13}C$-DIC values, both between years and rivers, that were linked to other geochemical indices, flow conditions, and riverine features (Figure 4.3A-F). For instance, the Gilman River catchment is the most extensively glaciated system (~71%) for which a complete river transect (21.5 km) was sampled over several years. During high flow years (2016, 2019) the Gilman River had downriver increases in TSS and PC that were accompanied by CO_2 becoming extremely undersaturated downriver (~18 ± 6 % sat.), whereas $\delta^{13}C$-DIC remained unchanged along these transects (-3.9 ± 0.6 ‰; Figure 4.7C). Gilman River also had downriver increases in TSS and PC during lower flow years (2017, 2018); however, CO_2 was only slightly undersaturated at downriver sites (79 ± 10 % sat.) and $\delta^{13}C$-DIC was less negative -1.5 ± 0.3 ‰. By

comparison, the Turnabout River catchment was less glaciated (~38%), much longer (~42 km), and flowed through a small lake. There were intense downriver increases in TSS and PC during higher flow 2019 that were not shared during the lower flow 2018. Furthermore, while dissolved CO_2 remained undersaturated along the Turnabout River transect during 2019 (<73 % sat.), it was slightly oversaturated during low flow 2018 (107 ± 3 % sat.). Turnabout River glacial headwater samples had a narrow range in δ^{13}C-DIC (-6.2 to -6.5 ‰), that shifted downriver towards less negative values during 2018 (-1.4 ‰) and 2019 (-4.4 ‰) (Figure 4.7F). Thus, despite differences in glacier cover and river length, interannual variability and flow conditions appeared to render similar dynamics in suspended sediment concentrations, CO_2 % sat., and δ^{13}C-DIC along glacial rivers. The Very River was comparable to the Turnabout River based on its length (~39 km), percent glaciated (~26%), geochemical properties at downriver sites, and also shared this interannual variability (Figure 4.7D). The Very River spanned δ^{13}C-DIC of -1.7 to -3.5 ‰, with the most negative values belonging to samples collected during high flow 2019 and 2016 (~Aug), which also had the most undersaturated CO_2 (~55 % sat.). The importance of temporal variability in meltwater flow conditions to glacial river geochemistry were further exemplified by regular sampling of the Blister and Snowgoose River deltas during 2016. These samples yielded theoretical equilibrium δ^{13}C-DIC values within a narrow range (0 to -1 ‰) compared to measured δ^{13}C-DIC values (-0.5 to -5.5‰; Figure 4.9A). The most negative δ^{13}C-DIC values were for samples taken mid-July, which coincided with particularly high meltwater flow conditions, elevated concentrations of TSS and PC, as well as undersaturated CO_2 (Figure 4.9B-D). This regular sampling illustrated that in short time spans, intense geochemical shifts can become apparent at glacial river deltas, compounding variability already observed along transects, amongst different glacial rivers, and spanning sampling years.

Despite intense inter-river and interannual variability, there were overarching relationships between δ^{13}C-DIC and other measures of glacial river geochemistry. The PCA for glacial headwater samples (Table 4.3A) was replicated for other data subsets, namely mid-river, and downriver sites (Table 4.3B-C), as well as the complete glacial rivers dataset (Table 4.3D). Whereas [DIC] was not found to be significantly correlated with measured δ^{13}C-DIC, there was a negative correlation ($p < 0.05$) between δ^{13}C-DIC and pH within the downriver samples bin (Figure 4.3B-C; Table 4.3B-C). This was contrary to the relationship between calculated theoretical equilibrium δ^{13}C-DIC and pH spanning pH values of 6.5 to 8.5 (*Appendix B*). Negative correlations ($p < 0.05$) were present between TSS and PC with δ^{13}C-DIC at mid-river and downriver sites (Table 4.3B-D). There was also significant separation between low flow (2017, 2018) and high flow (2016, 2019) years, the latter of

which showed a shift towards higher TSS and PC, and more isotopically depleted δ^{13}C-DIC (Figure 4.3D-E). At mid-river and downriver sites, the percent saturation of CO_2 was correlated with δ^{13}C-DIC, and anti-correlated with TSS and PC (Table 4.3B-C). A biplot for the PCA for the complete glacial river dataset showed relationships between geochemical variables and binning of samples based on their positions along transects, as well as sampling year (Figure 4.10A-C). Comparatively, different glacial river transects had less leverage on the distribution of data points (Figure 4.10D). The position along the glacial river created separation along the F1 axis based on downriver increases in temperature, SEC, TDS, and DIC. On the other hand, TSS, PC and pH were anti-correlated with δ^{13}C-DIC and CO_2 (sat. %), and separated moreso along the F2 axis. These results showed that higher concentrations of suspended sediment (TSS, PC) in higher flow years (2016, 2019) were associated with lower CO_2 % sat. and more negative δ^{13}C-DIC for mid-river and downriver sites along glacial river transects when compared to lower flow years (2017, 2018).

Although glacial river transects did not show reproducible downriver shifts in measured δ^{13}C-DIC, the δ^{13}C of DIC added to solution along glacial river transects was calculated using a mass weighted approach to help constrain the isotopic nature of this inorganic carbon. In these calculations, where glacial headwaters were the 'starting point' and downriver sites were the 'end', the δ^{13}C of DIC added spanned a narrow range of values from -0.3 to -4.5 ‰ (~ -2.3 ± 1.4 ‰). PIC was a likely source of δ^{13}C to the DIC pool, based on correlations between suspended sediment concentrations (TSS, PC) and δ^{13}C-DIC along glacial river transects. Undersaturation of CO_2 along glacial river transects, coupled with O_2 being fully saturated, also implied that carbonation mineral weathering reactions of this PIC may have been an important source of material to the DIC pool. Overall, δ^{13}C-PIC values for samples collected during 2019 spanned a wide range (-0.4 to -8.1 ‰), but were similar for individual transects of the Abbe (~ -4.6 ± 0.5 ‰), Gilman (~ -2.2 ± 0.4 ‰), Snowgoose (~ -3.7 ± 0.6 ‰), and Turnabout (~ -6.8 ± 1.4 ‰) rivers. These findings indicate differences in carbonate mineral composition among glacial river transects, likely based on variable contributions of primary marine carbonates (~ 0 ‰) and secondary freshwater carbonates (~ -15 to 2 ‰)[111]. The mass weighted δ^{13}C of DIC added to solution along glacial river continua was within -2.4 to 2.6 ‰ (0.4 ± 2.1 ‰) of the average δ^{13}C-PIC for the corresponding river transect. However, the δ^{13}C-PIC was not strongly related to either the mass balance calculated δ^{13}C of DIC added to solution along river transects, or to the complete array of δ^{13}C-DIC values spanning glacial headwaters, mid-river, and downriver sites (Figure 4.4). This implied that, in absence of other biogeochemical processes acting on the δ^{13}C of DIC, bulk PIC was not solely responsible for the stable carbon isotopic character of DIC.

4.3.3 Relationship of Δ^{14}C-DIC with δ^{13}C-DIC and geochemical parameters in meltwaters spanning glacial rivers transects, and in Lake Hazen

Radiocarbon of DIC (Δ^{14}C-DIC) was linearly related to δ^{13}C-DIC in glacial river transects (Figure 4.5; $R^2 = 0.61$; $p < 0.05$), suggesting a linkage between these isotopic measures. However, since [DIC] was not strongly related to either Δ^{14}C-DIC or δ^{13}C-DIC (Figure 4.6A-D), their isotopic character was not shaped by additions of DIC along glacial river transects. Downriver samples had ^{14}C ages that spanned ~ 1513 to 4982 yBP (Δ^{14}C-DIC of ~ -178 to -466 ‰), which were similar to the range of Δ^{14}C-DIC for glacial headwaters (Table 4.1B). Among the four transects, the Abbe (2017) remained relatively unchanged in Δ^{14}C-DIC downriver (-18 ‰), the Gilman (2017) and Snowgoose (2016) shifted towards slightly more negative values (-48 and -74 ‰, respectively), and Blister (2016) showed a more moderate downriver shift (-246 ‰; Figure 4.5). Mass weighted calculations indicate that the DIC added to solution along these transects had Δ^{14}C ~ -186 to -353 ‰ (~ 1588 to 3427 yBP), and δ^{13}C ~ -0.9 to -2.8 ‰. The Gilman and Abbe River deltas were the only sites that were analyzed for Δ^{14}C-DIC during both 2016 and 2017, for which the higher flow year (2016) yielded more negative Δ^{14}C-DIC values. For instance, the Gilman River delta ranged in Δ^{14}C-DIC from -466 ‰ (4982 yBP; July 2016) and -433 ‰ (4491 yBP; ~Aug 2016), compared to less negative -324 ‰ during 2017 (3083 yBP; Table 4.1B). Similarly, the Abbe River delta was more negative in 2016 (-300 ‰, or 2797 yBP) relative to 2017 (-178 ‰, or 1513 yBP).

PCAs were conducted for subsets of samples for which Δ^{14}C-DIC (Table 4.3E; Figure 4.11), and both Δ^{14}C-DIC and CO_2 % sat. (Table 4.3F) were measured. Among these PCAs, Δ^{14}C-DIC showed correlations with δ^{13}C-DIC and CO_2 % sat., whereas Δ^{14}C-DIC was anti-correlated with concentrations of suspended material (TSS, PC; Table 4.3E-F). Measures of pH and [DIC] also tended to be higher for samples with the most negative Δ^{14}C-DIC, although not at the same level of significance ($p < 0.05$). Isotopic and geochemical variables created separation of glacial headwater and downriver samples along F1 and F2 axes (Figure 4.11). The glacial headwater sample (HN, July 2016) with the most depleted Δ^{14}C-DIC, that plotted more similarly to downriver samples, had much higher PC ~ 11 mg L^{-1} than the remaining glacial headwater samples assessed in these PCAs (<1.6 mg L^{-1}). On the other hand, downriver sites had PC spanning 4 to 34 mg L^{-1}, apart from two samples (SG 2016, Abbe, 2017) with extremely low PC (<1 mg L^{-1}). These two samples also had the least negative Δ^{14}C-DIC among the downriver sites, suggesting that the proximity to glacier termini, or position along a glacial river transect, did not exclusively dictate isotopic or geochemical

characteristics. Instead, given that the presence of suspended sediment and CO_2 % sat. were more strongly predictive of δ^{13}C-DIC and Δ^{14}C-DIC, proglacial meltwater routing / flow intensity, riverbank / riverbed characteristics, and local geology may be important considerations.

Lake Hazen was almost exclusively glacially fed and was hydrologically dominated by a confluence of meltwaters from glacial rivers sampled herein. Sampling comprising the vertical profile (0, 15, and 250 m) collected near the centre of Lake Hazen during the 2016 field season (Aug 8th) showed that the lake was unstratified and waters were uniformly cold (3.0 ± 0.3 ºC) and slightly alkaline (pH ~ 7.9), with high DIC concentrations (853 ± 42 µM), and fully saturated in dissolved O_2 (100 ± 1 % sat.; Table 4.1C). Dissolved CO_2 was only slightly undersaturated at the surface (0 m) and 15 m (~82 % sat.) as well as at 250 m (~94 % sat.). Indeed, apart from increased suspended material (TSS, PC) in the deep-waters (250 m), other geochemical variables remained relatively stable throughout the profile (Table 4.1C). This was also the case isotopically, with δ^{13}C-DIC in the surface (0.33 ‰) and deep water (-0.1 ‰) being highly similar and within the range of theoretical δ^{13}C-DIC expected under equilibrium conditions (*Appendix B*). A sample collected for Δ^{14}C-DIC from the surface of Lake Hazen was less negative (-140 ‰, or 1142 yBP) compared to the entire array of glacial river discharges measured in this study (-178 to -466 ‰; Table 4.1B-C). Isotopic flow and mass weighted calculations were made for the seven major glacial inflows to Lake Hazen during 2016, using averaged DIC data from mid-July and early August surveys, and modelled glacial river runoff from a recent study[95]. The flow and mass weighted mean glacial input value during 2016 was determined to have lower DIC concentrations (~ 663 µM), as well as more negative δ^{13}C-DIC (-2.4 ‰) and Δ^{14}C-DIC (-326 ‰, or 3102 yBP), when compared to Lake Hazen. These findings implied in-lake mixing with a comparatively ^{14}C-modern source of carbon to the DIC pool, such as atmospheric CO_2. However, in-lake CO_2 remained slightly undersaturated, suggesting that mineral weathering reactions continued to compete with atmospheric exchange and equilibration of CO_2 over time.

4.4 Discussion

4.4.1 Biogeochemical processing in the supraglacial environment, ice-marginal flow, and proglacial meltwater routing shaped glacial river geochemistries and isotopic (δ^{13}C, Δ^{14}C) composition of DIC

Biogeochemistries of glacial meltwaters are the product of a variety of factors, such as the thermal regimes of the glaciers they drain. Warm-based, polythermal, and cold-based glaciers can yield

meltwaters with different chemistries, primarily based on meltwater routing and its propensity to drain through the subglacial environment[257,370]. Distinct biogeochemistries have even been found in basal ice sampled from glaciers with different thermal regimes[219]. Subglacial meltwater drainage is heavily limited in cold-based glacier systems, such as those in the Lake Hazen watershed, where the supraglacial environment dominates bulk meltwater flux. Given that supraglacial meltwaters are in contact primarily with ice, snow, and cryoconite, they typically have extremely low concentrations of dissolved species[186,234,371]. This is contrasted strongly by the chemical environment of meltwaters that flow over the edges of glaciers and come into contact with the local geology, which could explain some of the variability in concentrations of dissolved species (SEC, TDS, DIC) and suspended solids (TSS, PC) in glacial headwaters of the Lake Hazen watershed. For instance, the proportion of supraglacial meltwaters flowing over the glacier tongue at the terminus compared to that flowing over the sides of the glaciers and along ice-marginal flowpaths could impact the chemistry of meltwaters based on differences in the extent of contact with the local geology and suspension of freshly eroded sediments in solution[372]. Indeed, ice marginal channels have been previously attributed to the chemistry of glacial meltwaters in a cold-based high Arctic system, and contrasted to extremely dilute supra/englacial meltwaters[291]. In the Lake Hazen watershed, the most expansive glaciers (Henrietta-Nesmith and Gilman) had at least several hundred meters of ice-marginal flow along the side(s) of the glaciers prior to mixing with supraglacial overflow at glacier termini, for which their respective headwaters had among the highest SEC, TDS, and DIC concentrations. Rapid geochemical evolution may have even taken place in the short distance (<100 m) between glacier termini and our 'starting point' at glacial headwater sampling sites. These considerations are important when placing glacial headwaters in the context of their hydrologic connectivity to the supraglacial environment, but also the interactions of meltwaters with the local geology along ice-marginal channels and in the immediate proglacial environment.

There are many potential sources of inorganic carbon to the DIC pool in glacial headwaters, such as drawdown of atmospheric CO_2, mineral weathering, and OC mineralization via abiotic (photolysis) and biotic (microbial) pathways, that can affect both the concentration and the isotopic values of DIC. Glacial headwaters of the Lake Hazen watershed had wide ranges of DIC concentrations ([DIC] ~ 30 to 420 μM), for which higher [DIC] are likely more strongly decoupled from bulk unadulterated supraglacial meltwaters. Glacial headwaters were rarely at chemical equilibrium with respect to CO_2 (i.e., undersaturated), and had δ^{13}C-DIC ranging from 2.3 to -6.9 ‰. The Δ^{14}C-DIC (-77 to -437 ‰) are suggestive of ^{14}C-ancient material (~ 582 to 4556 yBP) of geologic origin, although the exact

mechanism of its incorporation to the DIC pool, and its balance with atmospheric exchange and equilibration with ^{14}C-modern CO_2, is less clear. It should be noted that whereas organic carbon mineralization can be an important source of DIC in aquatic ecosystems, it was expected to have a negligible effect on DIC in glacial rivers of the Lake Hazen watershed. Supraglacial productivity could have resulted in an isotopic effect to (δ^{13}C, Δ^{14}C), although it is highly unlikely that organic carbon mineralization could have been impactful to DIC in cold, light limited (i.e., turbid), fast flowing meltwaters, evidenced in part by slow rates photo- and microbial degradation rates reported for Lake Hazen and surrounding sub-catchments[373]. Given that a considerable amount of DIC was added downriver, and that the isotopically negative δ^{13}C-DIC and Δ^{14}C-DIC remained relatively stable, other processes and/or sources of inorganic carbon controlled DIC dynamics in glacial rivers.

One hypothesis is that bulk supraglacial meltwaters already had negative δ^{13}C-DIC and/or Δ^{14}C-DIC values prior to overflowing glacier edges. Indeed, biogeochemical processing in the supraglacial environment, including the dynamic balance between carbon fixation and respiration, mineral weathering, and atmospheric exchange[186,282,374–376], could have subsequently affected the isotopic composition of inorganic carbon in supraglacial meltwaters. In one study, Antarctic glacier ice was reported to have ^{14}C ancient DIC (7430 ± 60 yBP), compared to DIC sampled from an adjacent supraglacial meltwater pool (570 ± 60 yBP) that had presumably mixed with comparatively ^{14}C modern CO_2[377]. In another study, supraglacial streams flowing through ice on the surface of a polythermal glacier of the Greenland Ice Sheet (Russell Glacier) were sparingly concentrated in DIC (44 to 70 µM), negative in δ^{13}C-DIC (-9.7 to -14.3 ‰), and Δ^{14}C-DIC spanning – 16 to -330 ‰[378]. In the Lake Hazen watershed, mineral deposits on glacier surfaces (cryoconite) likely originated principally from aeolian deposition, which would be reflective of ^{14}C and δ^{13}C of inorganic carbon (PIC) from the local geology. Alternatively, given that supraglacial environments have recently been highlighted as being unprecedentedly productive, there is the possibility that supraglacial mineralization of POC could have liberated ^{14}C-ancient inorganic carbon to the DIC pool prior to being mobilized to ice-marginal channels and glacial headwaters of rivers in the Lake Hazen watershed. However, because large quantities of DIC are added to solution in the proglacial environment, and there was no relationship between [DIC] and either Δ^{14}C-DIC or δ^{13}C-DIC, supraglacial microbial activity was not expected to be the primary driver of glacial headwater geochemistry in our study.

The origin of PIC in suspended sediment of glacial meltwaters was key to resolving $\delta^{13}C$ and $\Delta^{14}C$ of DIC in glacial rivers. The geology of the Lake Hazen watershed is comprised of rocks that range in ages spanning the Early Paleozoic to the Cenozoic, for which there are metamorphic (slate, quartzite, schist, soapstone) and sedimentary (limestone, sandstone, siltstone, mudstone, shale, coal, siliciclastic) components[297–299]. Although PIC was expected to be principally composed of ^{14}C-dead primary carbonate minerals in local sedimentary rock, the $\delta^{13}C$-PIC (~ -0.9 to -6.8 ‰) suggested that there must also be inclusion of comparative $\delta^{13}C$ negative inorganic carbon. This complicates our interpretation of PIC, given that there are several pathways by which $\delta^{13}C$-PIC could become slightly more negative than primary carbonates (~ 0 ‰)[111]. One possibility involves isotopic exchange of negative $\delta^{13}C$-DIC in glacial meltwaters to PIC surfaces. This process could occur rapidly during turbulent mixing of meltwaters in suspended sediment, or over time in the river bed, followed by resuspension. In either of these media, carbonation reactions of carbonates could impart negative $\delta^{13}C$ of reacting CO_2 (i.e., $\delta^{13}C$-DIC) to PIC, giving rise to more negative $\delta^{13}C$-PIC in suspended sediment than otherwise expected. Alternatively, historic microbially mediated organic carbon oxidation in the subglacial environment in the absence of atmospheric contact could have resulted in the formation of negative $\delta^{13}C$-PIC. For instance, in warm or polythermal glacier systems microbially mediated OC degradation can proceed over time in the subglacial environment, serving as an important under-ice source of CO_2[191,370,379], that could then be isotopically reflected in the precipitation of carbonate minerals (PIC)[380]. Whereas subglacial inputs of meltwaters were expected to be minor for cold-based glaciers of the Lake Hazen watershed, negative $\delta^{13}C$-PIC may have become exposed in the proglacial environment following thousands of years of glacier retreat. A final possible explanation of $\delta^{13}C$-PIC could involve precipitation of secondary carbonates in the river bed and hyporheic zones of the proglacial environment. The Lake Hazen watershed is a polar dessert environment, such that moisture is quickly 'wicked away', similarly to a desiccator. As annual melt seasons draw to an end, intense evaporation of moisture from riverbeds and riverine hyporheic zones may have resulted in precipitation of secondary carbonate minerals (PIC) with negative $\delta^{13}C$, and ^{14}C ages < 5.3 ka, based on the glacial history of the Lake Hazen watershed[85,328]. However, regardless of the precise origin(s) of $\delta^{13}C$-PIC, carbonate minerals comprising bulk PIC would be ~ ^{14}C-dead, principally comprised of primary carbonates with smaller amounts of secondary carbonates, the latter of which were likely derived by a combination of the aforementioned mechanisms.

Mineral weathering reactions are expected to control the liberation of ^{14}C-ancient inorganic carbon from PIC to the DIC pool in both supraglacial and proglacial meltwaters. Microbial decomposition of

^{14}C-ancient terrigenous organic carbon may also be a minor source of inorganic carbon to the DIC pool, but does not explain the magnitude of DIC additions in the proglacial environment. Carbonate minerals derived from the local geology can enter the supraglacial environment via atmospheric transport to glacier surfaces (aeolian deposition), or enter proglacial meltwaters by interactions with heavily eroded riverbanks, and resuspension of sediment from the riverbank. Indeed, proglacial meltwaters are in constant contact with riverbeds and hyporheic zones, the spatial extent of which increases during high flow conditions and widening meltwater channels, which can affect the supply of weathered solutes to meltwaters[381,382]. Whereas it is not surprising that mineral weathering reactions of PIC in meltwaters supplied ^{14}C-ancient inorganic carbon to the DIC pool, isotopic (δ^{13}C, Δ^{14}C) and geochemical data may help resolve the specific mineral weathering reactions, and their balance with atmospheric exchange of CO_2, that were important in shaping the evolution of DIC along glacial river continua.

4.4.2 The role of mineral weathering reactions of carbonates in suspended sediment (PIC) in shaping meltwater geochemistry and DIC isotopes (δ^{13}C, Δ^{14}C) along glacial river transects

The carbonate system in glacial headwaters was rarely at either chemical equilibrium (CO_2 % sat.), or isotopic equilibrium, based on measured δ^{13}C-DIC that were almost exclusively more negative than theoretical equilibrium δ^{13}C-DIC. For instance, meltwaters at chemical and isotopic equilibrium, at physical and chemical conditions common to glacial headwaters (pH ~ 7 to 8; temperature ~ 0 to 5 ºC), would have δ^{13}C-DIC ~ 0 to -2 ‰, which is more positive than the majority of corresponding measured δ^{13}C-DIC values. Atmospheric δ^{13}C-$CO_{2\,(g\text{-}air)}$ is estimated as –8.3 ‰ based on the study site location and time of year[368], and isotopic fractionation of CO_2 across the gas-water interface[367] is ~ 1.1 ‰, such that δ^{13}C-$CO_{2\,(g\text{-}water)}$ is approximately -9.4 ‰. Ice formation involves the rejection of the majority of gases and solutes from the ice crystalline lattice structure, and melting of glacier ice allows for gases to be drawn down and mixed in these meltwaters. Given the 1:1 stoichiometry associated with carbonate rock (δ^{13}C-PIC) and $CO_{2\,(g\text{-}water)}$ end-members, carbonation reactions of carbonate minerals alone would presumably yield δ^{13}C-DIC at a minimum of approximately -4.7 ‰ in the case of primary marine carbonates (δ^{13}C ~ 0 ‰) in a closed system, beyond which any degree of atmospheric equilibration would yield more positive δ^{13}C-DIC due to the increase in alkalinity and pH associated with carbonate weathering[383]. In glacial headwaters of the Lake Hazen watershed, secondary carbonates influenced the δ^{13}C of bulk PIC (δ^{13}C-PIC ~ -0.9 to -6.8 ‰), which suggests

that reaction with $CO_{2\ (g\text{-}water)}$ (~ -9.4 ‰) in a closed system could yield δ^{13}C-DIC as negative as ~ -8.1 ‰. This constrains the δ^{13}C-DIC in glacial headwaters sampled herein (2.5 to -6.5 ‰). It should be noted that kinetic isotopic fractionation effects for the favorable dissolution of lighter $Ca^{12}CO_3$ have also been reported, with experimentally determined enrichment factors of δ^{13}C-DIC relative to chemical grade $CaCO_3$ (-7.8 ‰) and glacial sediment (-17.4 ‰) under closed system conditions at 5ºC[360]. In fast-flowing meltwaters that traverse glacial rivers on the order of hours, the rate of gas transfer of $CO_{2\ (g\text{-}water)}$ to $CO_{2\ (aq)}$ may limit the extent to which other carbonate species (HCO_3^-, CO_3^{2-}) reach chemical equilibrium[384], and consequently retain negative δ^{13}C-DIC values. This intense isotopic fractionation did not appear to be prevalent in glacial headwaters of our study, where δ^{13}C-PIC of suspended sediment and δ^{13}C-DIC of meltwaters were not significantly different. It is possible that kinetic isotopic effects for carbonation reactions of carbonates were obscured by other coinciding mineral weathering processes. The thermodynamic favorability of weathering of $Ca^{12}CO_3$ would result in preferential retention of $Ca^{13}CO_3$ on the surfaces of weathered mineral particles, which seems contrary to the negative δ^{13}C-PIC measured for suspended sediment. However, if the reacting CO_2 is isotopically negative in non-equilibrium conditions, which are pervasive amongst glacial meltwaters sampled herein, then isotopic exchange associated with carbonation reactions of carbonates could explain isotopically negative δ^{13}C-PIC.

Sulphide oxidation weathering reactions are also taking place in glacial rivers of the Lake Hazen watershed. Sulphate isotopes measured at several (n = 8) glacial river sites during 2016, had ranges in δ^{34}S-SO_4 (-4.3 to 8.6 ‰) and δ^{18}O-SO_4 (-8.9 to -21.7 ‰; unpublished data) that were strongly suggestive of sulphide (i.e., pyrite; FeS_2) oxidation in H_2O saturated, anoxic conditions[111,383,385]. For instance, the particularly negative δ^{18}O-SO_4 indicated that pyrite was oxidized preferentially by δ^{18}O-H_2O (-26.3 to -30.3 ‰) for these eight samples, compared to δ^{18}O-O_2 (~ +24 ‰). When coupled to carbonate dissolution, pyrite oxidation releases 2 moles of HCO_3^- for every 1 mole of SO_4^{2-}, if accompanied by $Fe(OH)_3$ (s) formation[110]. Dissolved Fe concentrations were typically below the detection limit in glacial rivers (< 0.5 µM), as expected in higher pH, oxic systems, although microbially mediated sulphide oxidation by ferric iron reduction may have taken place in anoxic porewaters of the riverbed (hyporheic zone) where Fe would be higher. Sulphate concentrations were low in glacial rivers, but increased from glacial headwaters (~39 ± 20 µM) to downriver sites (~146 ± 78 µM; 2017 data). For these samples, the sulphate mass fraction (SMF = SO_4^{2-}/ SO_4^{2-} + HCO_3^-) decreased from glacial headwaters (~ 0.38) to downriver sites (~ 0.24), suggesting that sulphide oxidation coupled to carbonate dissolution (SOC-CD) became less important relative to carbonation

weathering reactions with progression downstream. These glacial river samples all had ratios of alkalinity to DIC concentration that were greater than 1 (Alk: DIC > 1), that also highlighted a greater prevalence of carbonation reactions relative to SOC-CD[205]. In absence of kinetic effects, SOC-CD may have added DIC to solution with δ^{13}C-DIC that was little changed from its parent carbonate mineral δ^{13}C-PIC. However, while SOC-CD likely helped shape the δ^{13}C-DIC and Δ^{14}C-DIC in glacial rivers, carbonation of carbonates is expected to be the primary driver of their δ^{13}C character. A major line of evidence involves the almost ubiquitous undersaturation of glacial rivers in dissolved CO_2 (fully saturated in dissolved O_2), whereas SOC-CD is source of CO_2. Furthermore, downriver increases in pH suggest that any acidity generated by SOC-CD was readily buffered by carbonate alkalinity associated with carbonation reactions, and carbonate hydrolysis. The linear relationship between δ^{13}C-DIC and Δ^{14}C-DIC supported the hypothesis that the mineral source of ^{14}C-ancient DIC in poorly equilibrated meltwaters was also associated with negative δ^{13}C-DIC. As such, the δ^{13}C-DIC measured in glacial rivers was representative of a dynamic balance of ^{14}C-ancient DIC released from mineral weathering reactions, for which the carbonate system isotopes of DIC (δ^{13}C, Δ^{14}C) had limited opportunity to equilibrate with atmospheric CO_2.

Carbonate mineral weathering has been highlighted as an important geochemical process in subglacial environments, in particular based on its favorable dissolution kinetics relative to silicates[109,110,360,386]. Recently, this research scope has been expanded to include the role of mineral weathering reactions in proglacial environments, and under what conditions meltwater-impacted aquatic systems may act as sources or sinks of CO_2[203,205,206,363,387]. Principally, this has to do with the prevalence of different weathering reactions, such as CO_2 drawdown to fuel carbonation reactions (CO_2 sink) versus sulphide oxidation coupled (SOC) weathering reactions (CO_2 source). Isotopically, these weathering reactions would also have unique effects on the resultant δ^{13}C-DIC and Δ^{14}C-DIC in solution. With respect to the Δ^{14}C-DIC evolved in solution via weathering reactions, the Δ^{14}C of carbonate minerals and Δ^{14}C-CO_2 are important considerations. A carbonate mineral end-member would be ^{14}C-dead, where the Δ^{14}C associated with a theoretical minimum F^{14}C detection limit would be ~ -1000 ‰. DIC added to solution by SOC-CD would be more representative of this carbonate mineral ^{14}C end-member than carbonation weathering reactions, the latter of which also relying on Δ^{14}C-CO_2. On one hand, recent (2010) atmospheric CO_2 sampled near Alert, NU was reported to have Δ^{14}C-CO_2 ~ 50 ‰[388], and a global trajectory towards fossils fuels induced depletion in ^{14}C-CO_2[389] may have placed the local atmospheric Δ^{14}C-CO_2 closer to 0 ‰ for the sampling years in this study (2016-19). However, glacial meltwaters were not at atmospheric saturation, so Δ^{14}C-CO_2 would be

indicative of Δ^{14}C-DIC in supraglacial meltwaters and glacial headwaters. While ^{14}C of CO_2 bubbles trapped in glacier ice cores have been used primarily for dating the Earth's atmosphere[390,391], fast flowing seasonal pulses of meltwaters would likely preserve isotopically negative Δ^{14}C-CO_2 into the immediate proglacial environment because of lack atmospheric equilibration, which is rate limited. It should also be noted, that in the case of carbonation reactions of silicates, the ^{14}C of CO_2 would be the sole source of inorganic carbon to Δ^{14}C-DIC. However, the favourable reaction kinetics of carbonate minerals and the endless supply of fresh fine-grain reactive surfaces in suspended sediment (PIC) make carbonation of carbonate minerals the dominant source of undersaturated CO_2 and negative Δ^{14}C-DIC in glacial rivers. To complicate matters further, the 'drawing down' of disparate sources of Δ^{14}C-CO_2 during carbonation weathering reactions, is in constant competition with gas exchange and equilibration of atmospheric CO_2. As such, the net isotopic (δ^{13}C, Δ^{14}C) effects to DIC along glacial river continua will be a product of a confluence of mineral weathering reactions, and atmospheric exchange.

4.4.3 The extent of the mineral weathering, isotopes of DIC (δ^{13}C, Δ^{14}C), and geochemical evolution of meltwaters is controlled primarily by meltwater flow conditions

Glacial meltwater hydrochemistry can evolve rapidly over the course of the ablation season[392,393], and also as meltwaters traverse the proglacial environment[291,394]. In glacial rivers transects of the Lake Hazen watershed, downriver sites were almost exclusively more concentrated in dissolved species (SEC, TDS) than their respective glacial headwaters. This was often also the case for suspended material (TSS, PC), although there was a great deal of temporal and inter-river variability in suspended sediment concentrations amongst glacial rivers. For instance, TSS and PC were higher during the high flow years (2016, 2019), and spiked mid-July 2016 during peak flow. Glacial river samples represent 'snapshots in time' that were strongly linked to the magnitude of glacial meltwater flux, and likely also physical characteristics of glacial rivers (river length, local geology, meltwater routing). Meltwaters overflowing glacier termini, or routed along the margins of glaciers, generally coalesced into a main stem at glacial headwater sampling sites, which remained intact at mid-river sites, and then became extensively braided towards river deltas. However, these features were not only variable amongst glacial rivers, but were also re-shaped rapidly (hours, days) by changing flow conditions, river bank erosion, and the diverse ways in which meltwaters were channelized in the proglacial environment. As such, more extensively glacier covered watersheds (Henrietta-Nesmith,

Gilman), with higher overall meltwater flux *volumes* compared to smaller glacier watersheds (Blister, Snowgoose), cannot exclusively be attributed to higher meltwater flux *intensities* at specific sampling sites if the sites are composed of unconsolidated, braided tributaries. This rationale necessitated the assessment of glacial river geochemistry and isotopic character not only based on overarching sampling site bins (headwaters, mid-river, downriver), inter-river, and interannual variability, but also along individual glacial river transects.

The DIC at downriver sites had much older ^{14}C ages (1513 to 4982 yBP) than those common for temperate river systems where ^{14}C ancient inorganic carbon is typically a less important component of the DIC pool[395,396]. Even in the case of a recent study of the Arctic-Subarctic (Nunavik, Québec), the oldest ^{14}C-DIC ages for the permafrost thaw water impacted Sasapimakwananisikw River were only ~1000 to 1100 yBP[397]. Indeed, the comparatively lower ^{14}C activity of DIC in glacial rivers of the Lake Hazen watershed were based not only on an abundance of ^{14}C-ancient inorganic material from carbonate minerals, but also lower contributions of modern inorganic carbon sources from both organic matter mineralization and atmospheric exchange. In our study, downriver sites in individual glacial river transects had $\Delta^{14}C$-DIC that were slightly (-18 to -246 ‰) more negative than their respective glacial headwaters. Indeed, while the DIC concentration was almost exclusively found to increase along glacial river transects, the position along a transect (or proximity to glacier termini) was not the key driver of either the $\delta^{13}C$ or $\Delta^{14}C$ of DIC. In other words, the balance of source(s) of negative $\delta^{13}C$-DIC and $\Delta^{14}C$-DIC in glacial headwaters, mid-river, and downriver sites were similar along the length of the river and between rivers.

Dissolved gases in all sampled rivers were not simply undersaturated following the melting of gas poor glacier ice in the supraglacial environment. Rather, geochemical processes that specifically impacted dissolved CO_2 concentrations as opposed to overall gas solubility were of consequence to meltwaters along glacial river transects. Although SOC-CD and carbonate hydrolysis could explain the $\delta^{13}C$-DIC and $\Delta^{14}C$-DIC of glacial rivers the undersaturation of dissolved CO_2 contrasted by full saturation of dissolved O_2 were key points identifying the role of carbonation mineral weathering reactions. Not only is SOC-CD a source of CO_2 and acidity, but low sulphate concentrations in glacial rivers of the Lake Hazen watershed[95], low sulphate mass fractions (SMF < 0.5), and Alk: DIC > 1, imply that pyrite oxidation played a comparatively minor role in meltwater geochemistry relative to carbonation of carbonates minerals.

Availability of mineral surfaces in suspended sediment (TSS, PC), and the isotopic character of the inorganic fraction (δ^{13}C-PIC), were key to assessing effects of carbonate mineral weathering reactions to DIC isotopes (δ^{13}C-DIC, Δ^{14}C-DIC). Significant relationships emerged between PC, TSS, CO_2 % sat. and δ^{13}C-DIC along glacial river transects (mid-river, downriver), that were not apparent in glacial headwater sites alone. For instance, higher TSS and PC were associated with increasingly undersaturated CO_2, as well as more negative δ^{13}C-DIC and Δ^{14}C-DIC. Carbonate minerals in suspended sediment of mid-river and downriver sites had highly similar δ^{13}C-PIC to their respective glacial headwaters, but also varied considerably between rivers, exemplified by average δ^{13}C-PIC for transects of Abbe (-4.6 ± 0.5 ‰), Gilman (-2.2 ± 0.4 ‰), Snowgoose (-3.7 ± 0.6 ‰), and Turnabout (-6.8 ± 1.4 ‰) during 2019. This variability in δ^{13}C-PIC was not strongly related to the δ^{13}C-DIC, the latter of which were also isotopically negative and remained relatively unchanged along glacial river transects. Riverbed and hyporheic zone processes likely also supplied weathered material to meltwaters along glacial river transects, supported in part by slight downriver increases in ^{3}H and δ^{18}O-H_2O. In fact, higher flow and suspended sediment concentrations (TSS, PC) would also coincide with the lateral expansion of the hyporheic zone, so mineral weathering in proglacial meltwaters was likely associated with both fine-grain suspended particles, and riverbed processes. The limited downriver changes in δ^{13}C-DIC and Δ^{14}C-DIC suggest that mineral weathering products in bulk supraglacial meltwaters (i.e., glacial headwaters) may have been isotopically similar to those further into proglacial environment, despite downriver increases in DIC and solutes. This was unusual, given the distinct physical and chemical conditions of supraglacial and proglacial meltwaters, and must be explained by a complex balance of processes controlling the carbonate system in glacial rivers.

Mass weighted calculations of the δ^{13}C of the DIC added to solution along glacial river transects were negative during 2019, and relatively similar for Abbé (-3.5 ‰), Blister (-2.3 ‰), Gilman (-4.5 ‰), Snowgoose -3.5 ‰), and Turnabout (-4.3 ‰). Furthermore, mass weighted calculations yielded Δ^{14}C of DIC added downriver for Abbé (2017; -186 ‰), Blister (2016; -353 ‰), Gilman (2017; -332 ‰), and Snowgoose (2016; -256 ‰) river transects, which corresponds to ^{14}C ages of DIC added to solution that ranged from ~1588 to 3427 yBP. Assuming all DIC added was generated by weathering of carbonate minerals (-1000 ‰) with atmospheric CO_2 (0 ‰), the Δ^{14}C-DIC could not be less negative than -500 ‰. Without factoring in potential kinetic effects, reaction of $CO_{2\,(g\text{-}water)}$ (~ -9.4 ‰) with δ^{13}C-PIC (-0.4 to 8.1 ‰) would yield negative δ^{13}C-DIC (-2.6 to -8.8 ‰). A degree of equilibration of meltwaters with atmospheric CO_2 would push both δ^{13}C-DIC and Δ^{14}C-DIC towards more positive values that more closely align with mass weighted calculation results. Together, this

data presents a compelling case for increased concentrations of suspended sediment (TSS, PC) resulting in elevated prevalence of mineral weathering reactions of carbonates (PIC) fueling CO_2 drawdown, and the addition of DIC to solution that had negative δ^{13}C-DIC and Δ^{14}C-DIC.

Flow conditions and physical characteristics of glacial rivers were impactful to the prevalence of mineral weathering reactions and atmospheric exchange. For instance, lower CO_2 % sat. coupled with higher suspended sediment concentrations (TSS, PC) during higher flow years (2016, 2019), compared to lower flow years (2017, 2018), likely supplied an abundance of fine-grain mineral surfaces to engage in weathering reactions. Furthermore, fast flowing meltwaters that traverse glacial headwaters to river deltas on the order of hours would have a limited opportunity to equilibrate with the atmosphere, which would be suppressed even more heavily in higher flow conditions. As a general case, this was reflected in δ^{13}C-DIC remaining relatively stable along the length of most glacial river transects. Perhaps only in the case of the Turnabout River that flowed through a small lake with an unknown residence time could appreciable atmospheric equilibration take place to be reflected in the CO_2 % sat. and δ^{13}C-DIC. High flow conditions explain dissolved CO_2 that was particularly undersaturated (lower CO_2 % sat.), and δ^{13}C-DIC that was highly negative during 2019. The δ^{13}C-DIC was less negative in flow years (2017, 2018), and was variable during 2016 (repeat sampling). Indeed, temporal variability in flow conditions during 2016 were reflected in regular sampling of the Blister and Snowgoose River deltas, for which peak discharge in mid-July resulted in spikes in concentrations of suspended sediment, increasingly undersaturated CO_2, and negative δ^{13}C-DIC. Temporal variability in flow conditions during 2016 may have also affected proglacial meltwater routing such that repeat samplings of the Henrietta-Nesmith River were impacted. For instance, the first sampling of the Henrietta-Nesmith (July 2016) captured a turbulently flowing meltwater channel with high suspended particulate carbon, and negative δ^{13}C-DIC (-4.0 ‰) and Δ^{14}C-DIC (-437 ‰; 4556 yBP). Later that summer (~Aug 2016), when the Henrietta-Nesmith was more extensively braided, much lower PC, and less negative δ^{13}C-DIC (-0.9 ‰) and Δ^{14}C-DIC (-279 ‰; 2565 yBP), were detected. In contrast, the Gilman River had very similar geochemical and isotopic character during both 2016 surveys, which likely had to do with the river main stem remaining converged and flowing strongly in both instances. Gilman River δ^{13}C-DIC (-3.4 ‰) and Δ^{14}C-DIC (-466 to -433 ‰) were in line with those of Henrietta-Nesmith during the first sampling event (July 2016), suggesting the importance of proglacial meltwater routing under variable flow conditions to glacial river geochemistry. Therefore, in addition to overarching flow conditions during a given

season, the timing of glacial river sampling relative to the ramping up (or down) of meltwater flux intensity over the course of the summer, or perhaps even daily, affects the δ^{13}C-DIC and Δ^{14}C-DIC.

4.4.4 Implications to Lake Hazen

Lake Hazen has responded to climate warming in a number of ways, including an increased receipt of sediment-laden meltwaters from glacial rivers, an increased likelihood of ice-free conditions during the summer, and a decreased lake residence time (~25 years)[89]. Enhanced glacial melt and carbonation mineral weathering reactions within the lake have been proposed to increase the way in which Lake Hazen acts as an annual sink for CO_2[95], which could be of significance to global carbon cycling as glaciers continue to retreat. The δ^{13}C-DIC of Lake Hazen surface water (0.33 ‰) and deep water (-0.11 ‰) were within the range of values expected at equilibrium conditions, and were less negative than the flow and concentration weighted results for the seven major glacial rivers (-2.3 ‰). This was not surprising given that Lake Hazen was well-mixed, with a long residence time, and an abundance of surface area for atmospheric exchange of CO_2. At the same time, this ultra-oligotrophic lake would have had minimal influence on the isotopic values from non-glacial inputs (hydrologically dwarfed by glacial meltwaters), *in situ* biological processes (C fixation vs. respiration), or abiotic mineralization of organic carbon (photolysis). In fact, a recent study found that only ~13% of DIC exported from Lake Hazen could be assigned to respiration processes, whereas the remainder came from CO_2 drawdown and carbonate dissolution[95]. As such, comparatively negative δ^{13}C-DIC either delivered to Lake Hazen via by glacial rivers, or produced *in-situ*, would have become more equilibrated with atmospheric CO_2 over time, shifting towards less negative δ^{13}C-DIC values. Given that atmospheric CO_2 is ^{14}C modern, this rationale also applies to Δ^{14}C-DIC measured in Lake Hazen surface waters (-140 ‰, or 1142 yBP), which was less negative than the flow and concentration weighted Δ^{14}C-DIC for the seven major glacial rivers (-326 ‰, or 3102 yBP). The short transit time of fast-flowing glacial rivers (hours) versus the seasonally well-mixed nature of Lake Hazen was expected to be instrumental in their isotopic delineation. Even so, carbonation reactions have been attributed to be a continued source of DIC within Lake Hazen[95], which were reflected in the slight undersaturation of CO_2 and ^{14}C ancient DIC retained in the Lake Hazen water column.

Studies of the isotopic character of DIC in lakes are sparse, and are particularly rare for glacially fed systems. Temperate lakes often have ^{14}C-modern DIC, or slightly isotopically depleted ^{14}C-DIC signatures even when there are appreciable additions of aged inorganic material to the DIC pool[398–400]. Unlike most other lakes, ultra-oligotrophic Lake Hazen was largely devoid of modern inorganic

carbon sources, other than atmospheric exchange of ^{14}C-modern CO_2, and had $\Delta^{14}C$-DIC that was more negative than these temperate lakes. On the other hand, much more ^{14}C ancient DIC measurements have been reported for samples of perennially frozen lakes of the McMurdo Dry Valleys. In particular, DIC in West Lake Bonney had ^{14}C ages ranging from ~3531 yBP near surface (6 m) to > 27,000 yBP at 25 m[401] attributed to intense stratification, evidence of direct subglacial brine inputs, and perennial ice cover that limits atmospheric contact[402]. Lake Hazen is well-mixed and often has a short ice-free period, but does have a turbidity maximum at depth associated with 'diving' sediment-laden glacial meltwaters upon their inflows to the lake from glacial river deltas. As such, adding a $\Delta^{14}C$-DIC measurement for Lake Hazen bottom waters (~250 m) would be an interesting opportunity to compare and contrast the vertical profile in ^{14}C ages of DIC reported for West Lake Bonney.

4.5 Summary and Conclusions

The CO_2 undersaturation and isotopic character of DIC ($\delta^{13}C$, $\Delta^{14}C$) in glacial rivers stemming from cold-based glaciers of the Lake Hazen watershed are a result of mineral weathering reactions. Stable carbon isotopes of the PIC in suspended sediment ($\delta^{13}C$-PIC) were much more negative than expected for primary marine carbonates, indicating the presence of the secondary freshwater carbonate minerals, and/or isotopic exchange of isotopically negative CO_2 with PIC surfaces during carbonation weathering reactions of carbonate minerals. The $\delta^{13}C$-PIC were different amongst glacial rivers, suggesting either variability in the mineral composition of suspended sediments, or the extent of isotopic exchange between DIC and PIC during carbonation mineral weathering reactions. However, the $\delta^{13}C$-PIC remained stable along river transects, implying that neither the historic retreat of glaciers, erosion of isotopically distinct soil horizons along riverbanks, nor long-term weathering reactions, had resulted in downriver changes in $\delta^{13}C$-PIC. Downriver increases in weathered materials (solutes, DIC) were associated with weathering of PIC, that took place in the suspended sediment, along the riverbanks, and in the riverbed and hyporheic zone. Higher flow conditions would increase contact area of meltwaters with PIC in each of these media, and was linked to increased mineral weathering during higher flow years.

Carbonation reactions of carbonate minerals was the primary mineral weathering process that controlled glacial river geochemistry. Suspended sediment loads (TSS, PC), undersaturated CO_2, and isotopically negative $\delta^{13}C$-DIC and $\Delta^{14}C$-DIC were correlated across the dataset. The availability of fresh fine-grain mineral surfaces for carbonation reactions fueling CO_2 drawdown resulted in

increasingly negative δ^{13}C-DIC and Δ^{14}C-DIC. Carbonation of silicates were expected to have minimal effects on DIC isotopes, based not only on unfavorable reaction kinetics, but also because Δ^{14}C-DIC was much more negative than expected for meltwaters that were equilibrated with the atmosphere. On the other hand, sulphate isotopes (δ^{34}S-SO_4, δ^{18}O-SO_4) confirmed pyrite weathering as a source of SO_4^{2-} to glacial rivers, for which SOC-CD would release ^{14}C-dead DIC from carbonates minerals. Whereas SOC-CD could not be discounted as a source of DIC along glacial river transects, the almost ubiquitous undersaturation of dissolved CO_2, fully saturated dissolved O_2, downriver increases in pH and alkalinity, and only small downriver increases in SO_4^{2-} concentrations, were key pieces of evidence proving that carbonation reactions of carbonates were the dominant mineral weathering process.

Meltwater flow conditions affected the isotopic character of DIC in glacial rivers. The DIC added along glacial river transects had negative δ^{13}C (-0.3 to -4.5 ‰; n = 18), for which the most negative values, most undersaturated CO_2, and higher concentrations of suspended sediment typically belong to the higher flow years (2016, 2019). Furthermore, complete transects of Δ^{14}C-DIC (n = 4) identified that the DIC added was ^{14}C-ancient (-186 to -353 ‰, or 1588 to 3427 yBP). Overall, neither the δ^{13}C-DIC nor Δ^{14}C-DIC showed significant downriver changes, although DIC increased indicating that reactions affecting the isotopic character of glacial headwaters were similar to those downriver. More negative δ^{13}C-DIC and Δ^{14}C-DIC during higher flow conditions may have not only indicated an increased prevalence of carbonate mineral weathering reactions, but also less chance for atmospheric exchange and equilibration to push DIC isotopes towards less negative values. Glacial rivers exhibit a dynamic balance of carbonate mineral weathering reactions and atmospheric exchange that take place rapidly in fast-flowing meltwaters traversing the proglacial environment. Indeed, regular monitoring and repeat sampling of transects during 2016 highlighted the importance of temporality in flow conditions and geochemical evolution of meltwaters, which can happen during narrow windows of time (hours, days), and affect the δ^{13}C and Δ^{14}C of DIC in glacial meltwaters.

The isotopic character of DIC in Lake Hazen was different than that in glacial rivers. Using modelled runoff data for the seven major glacial rivers, flow and mass weighted inflows to Lake Hazen had more negative δ^{13}C-DIC (-2.3 ‰) and Δ^{14}C-DIC (-326 ‰, or 3102 yBP), when compared to those of lake surface waters (0.33 ‰, and -140 ‰, or 1142 yBP, respectively). Lake Hazen is well-mixed, with a current residence time of ~25 years[89], so it is not surprising that atmospheric exchange and equilibration of lake waters with ^{14}C-modern CO_2 resulted in less negative δ^{13}C and Δ^{14}C of DIC.

However, the legacy of ^{14}C-ancient DIC, and undersaturated CO_2, indicates the persistence of in-lake carbonate mineral weathering over time. The deep lake water (~250 m) sample has yet to be analyzed for Δ^{14}C-DIC, but it is possible that sinking, sediment-laden meltwaters may accentuate carbonate mineral weathering at depth, and consequently result in more negative Δ^{14}C-DIC compared to surface waters.

In the short term, increased glacial meltwater fluxes are therefore expected to result in increased suspended sediment loads, and increased CO_2 drawdown fueled by carbonate mineral weathering reactions. These processes will be reflected by more isotopically negative δ^{13}C-DIC and Δ^{14}C-DIC in receiving aquatic systems, and could be incorporated into the dissolved organic pool via microbial processing of particulate carbon or autochthonous production. Glacier ice meltwater flux will likely continue to increase for several decades, exacerbating the extent to which these geochemical processes take place in meltwaters, and the legacy of ^{14}C-ancient inorganic carbon in glacier ice meltwater impacted aquatic systems. In the long term, (i.e., hundreds of years), effects of unmitigated climate change could involve decreases in meltwater fluxes once sufficient glacier ice mass has been lost. In this long-term scenario, carbonate mineral weathering will become less important to DIC cycling, the legacy of ^{14}C-ancient DIC will subside as terrestrial ecosystem succession proceeds, and ^{14}C-modern sources of carbon become more important to the DIC pool. Therefore, these findings apply to ultra-oligotrophic, glacier meltwater impacted aquatic systems in high Arctic environments, and should be considered when modelling future trajectories of carbon sources and sinks based on variable climate change scenarios.

Table 4.1: Geochemical data for **A)** glacial headwaters, **B)** downriver sites, and **(C)** Lake Hazen for which Δ^{14}C-DIC was analyzed.

A) Glacial Headwaters

River	Date	Temp (ºC)	pH	O_2 (% sat.)	CO_2 (% sat.)	SEC (µS cm^{-1})	TDS (mg L^{-1})	PC (mg L^{-1})	TSS (mg L^{-1})	[DIC] µM	δ^{13}C-DIC (‰)	Δ^{14}C-DIC (‰)	yBP
Abbe	20-07-2017	0.9	9.2	99	63	44.3	14	0.1	4.7	133	2.3	-161	1342
Blister	15-07-2016	1.2	8.2	---	---	---	---	---	---	82	---	-77	582
Blister	19-07-2016	1.5	7.7	---	86	---	6	1.7	529.2	100	---	---	---
Gilman	20-07-2017	0.6	7.8	102	60	16.7	<MDL	0.2	9.9	54	-0.6	-276	2531
Henrietta-N.	11-07-2016	4.2	8.4	110	---	55.9	27	**10.7**	75.0	**420**	**-4.0**	**-437**	**4556**
Henrietta-N.	02-08-2016	2.5	7.8	103	56	52.9	22	1.0	54.7	406	-0.9	-279	2565
Snowgoose	11-07-2016	0.9	7.0	102	---	11.6	14	0.8	26.5	89	0.5	-187	1596
Snowgoose	01-08-2016	1.1	7.4	96	81	33.2	33	1.6	137.2	109	0.6	-169	1425

B) Glacial River Deltas

River	Date	Temp (ºC)	pH	O_2 (% sat.)	CO_2 (% sat.)	SEC (µS cm^{-1})	TDS (mg L^{-1})	PC (mg L^{-1})	TSS (mg L^{-1})	[DIC] µM	δ^{13}C-DIC (‰)	Δ^{14}C-DIC (‰)	yBP
Abbe	13-07-2016	8.1	7.6	111	61	65.3	33	9.4	246.6	554	-1.2	-300	2797
Abbe	20-07-2017	4.5	7.9	102	90	93.9	13	**0.2**	**16.8**	**308**	**-1.3**	**-178**	**1513**
Blister	14-07-2016	10.9	7.6	99	82	79.9	40	8.8	1786.0	737	-4.7	---	---
Blister	15-07-2016	10.1	8.2	---	---	---	---	---	---	---	-5.7	-323	3064
Blister	16-07-2016	9.4	8.0	98	73	98.0	17	20.8	2448.6	904	---	---	---
Gilman	11-07-2016	3.6	8.7	108	15	69.2	29	34.0	910.0	477	-3.4	-466	4982
Gilman	01-08-2016	3.2	8.5	101	25	69.8	44	18.5	1218.5	522	-3.4	-433	4491
Gilman	20-07-2017	4.1	8.1	101	73	93.0	26	16.9	536.4	321	-1.7	-324	3083
Snowgoose	30-07-2016	8.3	7.6	102	91	120.5	60	**0.4**	**34.4**	**605**	**-0.7**	**-243**	**2169**
Turnabout	11-07-2016	12.2	7.7	108	89	108	54	5.6	180.0	687	-1.0	-290	2686
Very	11-07-2016	9.4	8.2	109	---	131.8	75	4.1	238	840	-1.9	-274	2506

C) Lake Hazen (centre buoy)

River	Date	Temp (ºC)	pH	O_2 (% sat.)	CO_2 (% sat.)	SEC (µS cm^{-1})	TDS (mg L^{-1})	PC (mg L^{-1})	TSS (mg L^{-1})	[DIC] µM	δ^{13}C-DIC (‰)	Δ^{14}C-DIC (‰)	yBP
Surface	08-08-2016	2.9	8.0	101	82	---	65	<0.1	1.9	814	0.3	-140	1142
15 m	08-08-2016	2.8	7.9	101	82	---	67	<0.1	2.2	847	---	---	---
250 m	08-08-2016	3.4	7.9	98	94	---	66	0.3	14.7	897	-0.1	---	---

Table 4.2: δ^{13}C-PIC and δ^{13}C-DIC for glacial river transects sampled during 2019:

River	Type	Temp (ºC)	pH	O_2 (% sat.)	CO_2 (% sat.)	SEC (µS cm^{-1})	TDS (mg L^{-1})	PC (mg L^{-1})	TSS (mg L^{-1})	[DIC] µM	δ^{13}C-DIC (‰)	δ^{13}C-PIC (‰)
Abbe	Headwater	1.3	7.5	98	56	39	28	1.3	282	155	-2.8	-4.7
Abbe	Mid-River	2.9	7.7	100	59	52	35	2.5	232	271	-3.5	-4.6
Abbe	Downriver	3.8	7.8	101	51	64	39	2.0	636	346	-3.3	-4.1
Blister	Headwater	1.4	7.1	94	88	18	36	1.3	160	57	-4.6	---
Blister	Mid-River	5.2	7.3	97	80	87	12	0.5	52	274	-2.7	---
Blister	Downriver	6.4	7.6	99	85	130	86	0.3	33	415	-2.6	---
Gilman	Headwater	0.7	7.6	100	41	36	29	1.6	114	165	-4.7	-2.4
Gilman	Mid-River	2.1	8.5	100	20	69	40	10.0	487	405	-4.7	-1.7
Gilman	Downriver	3.0	8.6	100	15	82	50	8.8	600	453	-4.6	-2.4
Henrietta-N.	Headwater	2.6	7.7	107	63	47	28	1.1	136	285	-3.5	-0.9
Snowgoose	Headwater	0.7	7.8	95	100	26	17	0.3	34	59	-5.0	-2.0
Snowgoose	Mid-River	4.1	7.8	98	73	53	35	1.2	145	260	-3.4	-3.1
Snowgoose	Downriver	5.0	8.0	99	56	68	48	0.6	279	335	-3.7	-3.7
Turnabout	Headwater	0.8	7.2	98	73	16	10	1.4	243	71	-6.5	-6.8
Turnabout	Mid-River	6.1	8.2	99	29	67	37	18.6	1960	406	-5.0	-5.3
Turnabout	Downriver	9.5	8.0	100	66	106	60	24.2	1325	713	-4.4	-8.1
Very	Downriver	10.6	8.2	101	54	128	78	5.2	257	773	-3.5	-0.4

Table 4.3: Correlation matrices for principal component analyses (PCA; Pearson; $\alpha = 0.05$) for **A)** glacial headwaters, **B)** mid-river, **C)** downriver sites, **D)** the complete glacial rivers dataset, and **E)** the subset of samples with Δ^{14}C-DIC (**significant relationships in bold text**)

A) Glacial Headwaters

F1 axis 27.5 %, F2 axis 24.7 %, total = 52.2 %, n = 15

	Temp (ºC)	**pH**	**SEC (µS cm^{-1})**	**TDS (mg L^{-1})**	**TSS (mg L^{-1})**	**PC** (mg L^{-1})	**[DIC]** µM	**CO_2** (% sat.)	**δ^{13}C-DIC** (‰)
Temp (ºC)	**1**	-0.08	0.18	0.13	0.26	0.05	-0.08	0.01	-0.26
pH		**1**	0.07	-0.19	-0.31	0.10	0.37	-0.29	0.32
SEC (µS cm^{-1})			**1**	**0.84**	0.22	0.39	**0.45**	-0.018	0.16
TDS (mg L^{-1})				**1**	0.36	0.34	0.12	0.15	0.17
TSS (mg L^{-1})					**1**	0.39	-0.25	0.26	-0.14
PC (mg L^{-1})						**1**	0.35	0.17	-0.16
[DIC] µM							**1**	**-0.56**	0.02
CO_2 (% sat.)								**1**	-0.21
δ^{13}C-DIC (‰)									**1**

B) Mid-river sites

F1 axis 47.4 %, F2 axis 26.7 %, total = 74.1 %, n = 11

	Temp (ºC)	**pH**	**SEC (µS cm^{-1})**	**TDS (mg L^{-1})**	**TSS (mg L^{-1})**	**PC** (mg L^{-1})	**[DIC]** µM	**CO_2** (% sat.)	**δ^{13}C-DIC** (‰)
Temp (ºC)	**1**	0.0	**0.64**	**0.59**	0.16	-0.06	**0.68**	**0.63**	0.41
pH		**1**	-0.01	-0.12	0.19	0.21	0.20	-0.36	-0.22
SEC (µS cm^{-1})			**1**	**0.86**	-0.26	-0.30	**0.69**	**0.60**	0.45
TDS (mg L^{-1})				**1**	-0.20	-0.13	**0.70**	**0.51**	0.29
TSS (mg L^{-1})					**1**	**0.80**	0.14	**-0.50**	**-0.79**
PC (mg L^{-1})						**1**	-0.01	**-0.64**	**-0.79**
[DIC] µM							**1**	0.22	0.19
CO_2 (% sat.)								**1**	**0.91**
δ^{13}C-DIC (‰)									**1**

C) Downriver

F1 axis 37.8 %, F2 axis 22.2 %, total = 60.0 %, n = 39

	Temp (ºC)	pH	SEC (µS cm^{-1})	TDS (mg L^{-1})	TSS (mg L^{-1})	PC (mg L^{-1})	[DIC] µM	CO_2 (% sat.)	δ^{13}C-DIC (‰)
Temp (ºC)	**1**	-0.26	0.23	0.14	-0.13	-0.08	**0.54**	**0.56**	0.19
pH		**1**	0.05	0.05	**0.31**	0.28	0.04	**-0.48**	**-0.46**
SEC (µS cm^{-1})			**1**	**0.79**	**-0.31**	**-0.34**	**0.43**	**0.32**	0.22
TDS (mg L^{-1})				**1**	**-0.30**	**-0.30**	**0.55**	0.26	0.04
TSS (mg L^{-1})					**1**	**0.45**	0.08	**-0.43**	**-0.72**
PC (mg L^{-1})						**1**	-0.06	**-0.37**	**-0.47**
[DIC] µM							**1**	0.24	-0.06
CO_2 (% sat.)								**1**	**0.52**
δ^{13}C-DIC (‰)									**1**

D) Complete glacial rivers dataset

F1 axis 35.5 %, F2 axis 26.5 %, total = 62.0 %, n = 65

	Temp (ºC)	pH	SEC (µS cm^{-1})	TDS (mg L^{-1})	TSS (mg L^{-1})	PC (mg L^{-1})	[DIC] µM	CO_2 (% sat.)	δ^{13}C-DIC (‰)
Temp (ºC)	**1**	-0.03	**0.55**	**0.49**	0.11	0.17	**0.80**	**0.39**	0.10
pH		**1**	0.17	0.06	**0.25**	**0.25**	0.20	**-0.45**	-0.13
SEC (µS cm^{-1})			**1**	**0.85**	-0.05	-0.06	**0.66**	**0.32**	**0.24**
TDS (mg L^{-1})				**1**	-0.07	-0.04	**0.67**	**0.27**	0.11
TSS (mg L^{-1})					**1**	**0.50**	**0.23**	**-0.35**	**-0.46**
PC (mg L^{-1})						**1**	0.19	**-0.29**	**-0.31**
[DIC] µM							**1**	0.11	0.03
CO_2 (% sat.)								**1**	**0.34**
δ^{13}C-DIC (‰)									**1**

E) Subset of glacial rivers dataset with Δ^{14}C-DIC

F1 axis 44.4 %, F2 axis 30.2 %, total = 74.6 %, n = 15

	Temp (ºC)	pH	SEC (µS cm^{-1})	TDS (mg L^{-1})	TSS (mg L^{-1})	PC (mg L^{-1})	[DIC] µM	δ^{18}O-H_2O (‰)	δ^{13}C-DIC (‰)	Δ^{14}C-DIC (‰)
Temp (ºC)	**1**	-0.06	**0.73**	**0.71**	0.31	0.11	**0.89**	**0.61**	-0.42	-0.17
pH		**1**	0.37	-0.01	0.32	0.47	0.19	-0.40	-0.28	-0.43
SEC (µS cm^{-1})			**1**	**0.69**	0.15	0.07	**0.73**	0.38	-0.19	-0.05
TDS (mg L^{-1})				**1**	0.10	0.09	**0.77**	**0.76**	-0.20	-0.18
TSS (mg L^{-1})					**1**	**0.66**	0.51	-0.08	**-0.76**	-0.50
PC (mg L^{-1})						**1**	0.33	-0.18	**-0.67**	**-0.83**
[DIC] µM							**1**	0.49	**-0.64**	-0.42
δ^{18}O-H_2O (‰)								**1**	0.21	0.27
δ^{13}C-DIC (‰)									**1**	**0.79**
Δ^{14}C-DIC (‰)										**1**

Note: CO_2 (% sat.) was omitted from this PCA as these values were not available in several instances for corresponding Δ^{14}C-DIC measurements. δ^{18}O-H_2O values were added to this analysis to test for significant relationships with other geochemical variables. However, the further subset of the dataset with *both* Δ^{14}C-DIC and CO_2 % sat. (Table 3.2F) yielded similar results, and was important to highlight the correlation between CO_2 % sat. and Δ^{14}C-DIC (below):

F) Subset of glacial rivers dataset with both Δ^{14}C-DIC and CO_2 % sat.

F1 axis 44.0 %, F2 axis 30.7 %, total = 74.7 %, n = 12

	Temp (ºC)	pH	SEC (µS cm^{-1})	TDS (mg L^{-1})	TSS (mg L^{-1})	PC (mg L^{-1})	[DIC] µM	CO_2 (% sat.)	δ^{13}C-DIC (‰)	Δ^{14}C-DIC (‰)
Temp (ºC)	**1**	-0.30	**0.67**	**0.68**	0.31	0.11	**0.87**	0.41	-0.42	-0.16
pH		**1**	0.16	-0.27	0.33	0.45	-0.04	-0.56	-0.10	-0.30
SEC (µS cm^{-1})			**1**	0.54	0.10	0.04	**0.61**	0.41	-0.13	0.02
TDS (mg L^{-1})				**1**	0.14	0.16	**0.67**	0.15	-0.17	-0.24
TSS (mg L^{-1})					**1**	**0.66**	**0.61**	-0.32	**-0.89**	**-0.61**
PC (mg L^{-1})						**1**	0.38	**-0.70**	**-0.69**	**-0.88**
[DIC] µM							**1**	0.05	**-0.70**	-0.48
CO_2 (% sat.)								**1**	0.31	**0.75**
δ^{13}C-DIC (‰)									**1**	**0.73**
Δ^{14}C-DIC (‰)										**1**

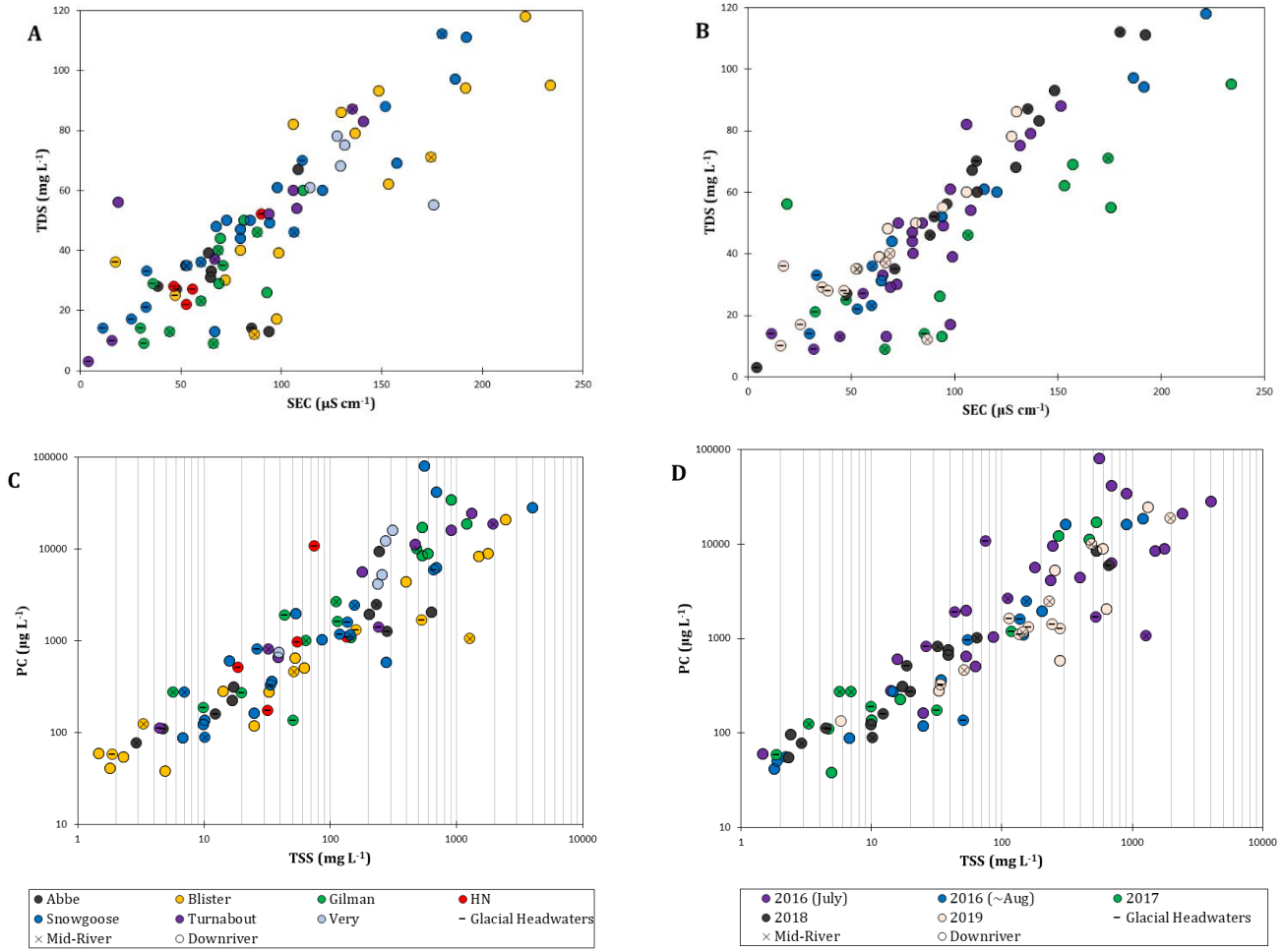

Figure 4.1: Specific electrical conductivity (SEC; µS cm^{-1}), total dissolved solids (TDS; mg L^{-1}), particulate carbon (PC; µg C L^{-1}), and total suspended solids (TSS; mg L^{-1}) for glacial headwaters, mid-river, and downriver sites sampled along glacial rivers (Abbe, Blister, Gilman, Henrietta-Nesmith (HN), Snowgoose, Turnabout, Very) of the Lake Hazen watershed spanning 2016, 2017, 2018, and 2019.

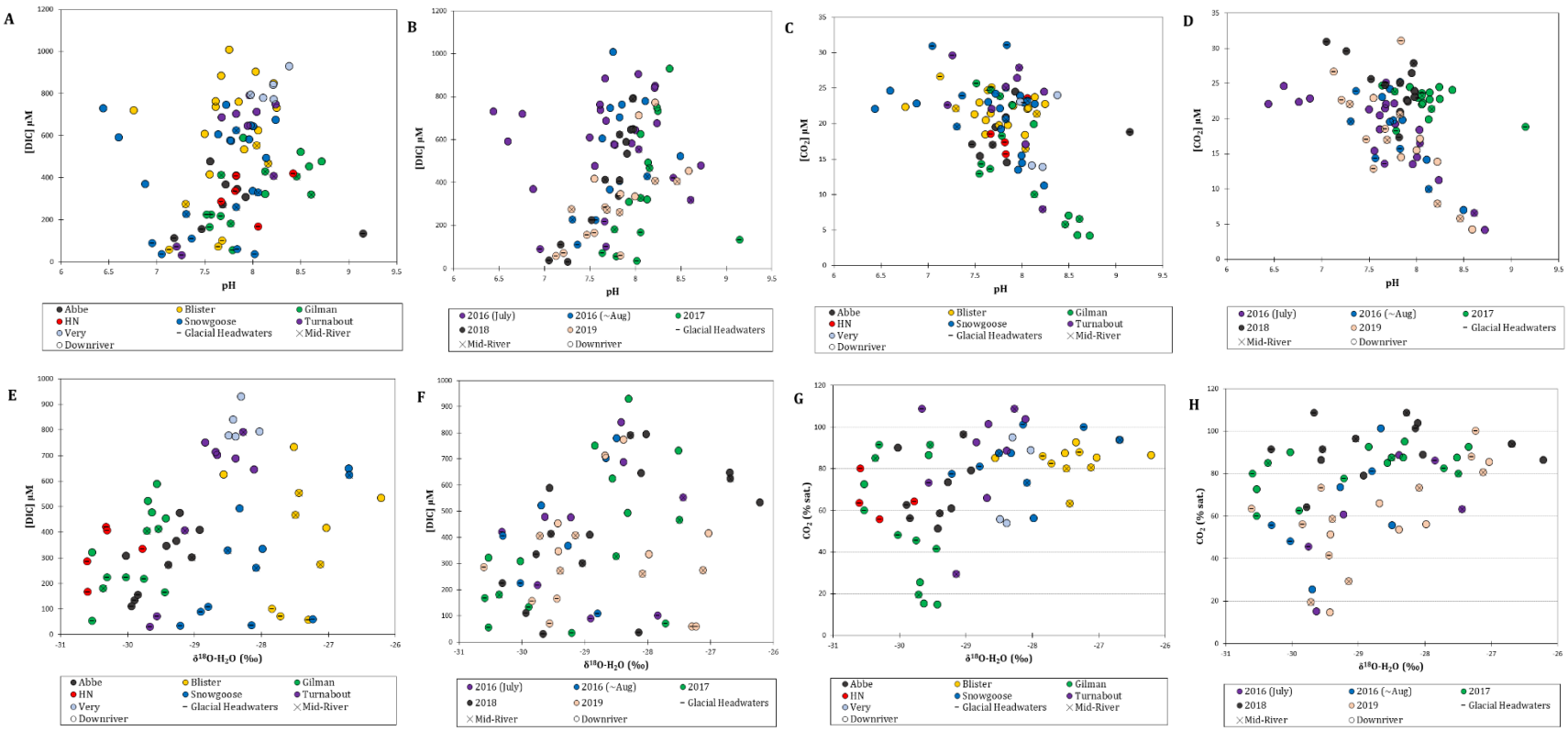

Figure 4.2A-H: Evolution of Measures of the carbonate system ([DIC], [CO_2], CO_2 sat. %), pH, and water isotopes ($\delta^{18}O$-H_2O) along glacial river transects (headwaters → mid-river → downriver) for 7 glacial rivers for sampling years spanning 2016 to 2019.

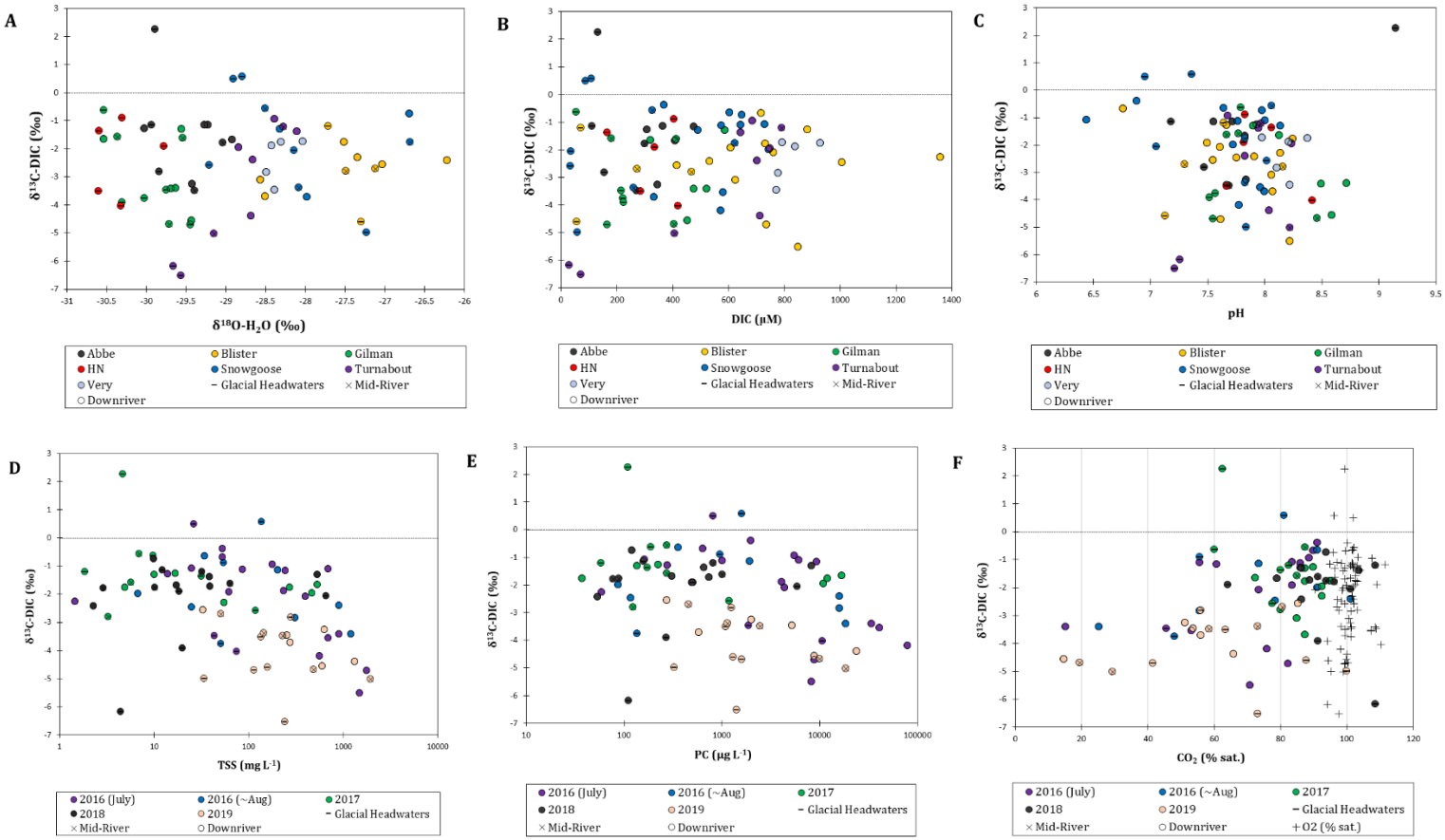

Figure 4.3A-F: Measured δ^{13}C-DIC plotted versus various geochemical parameters.

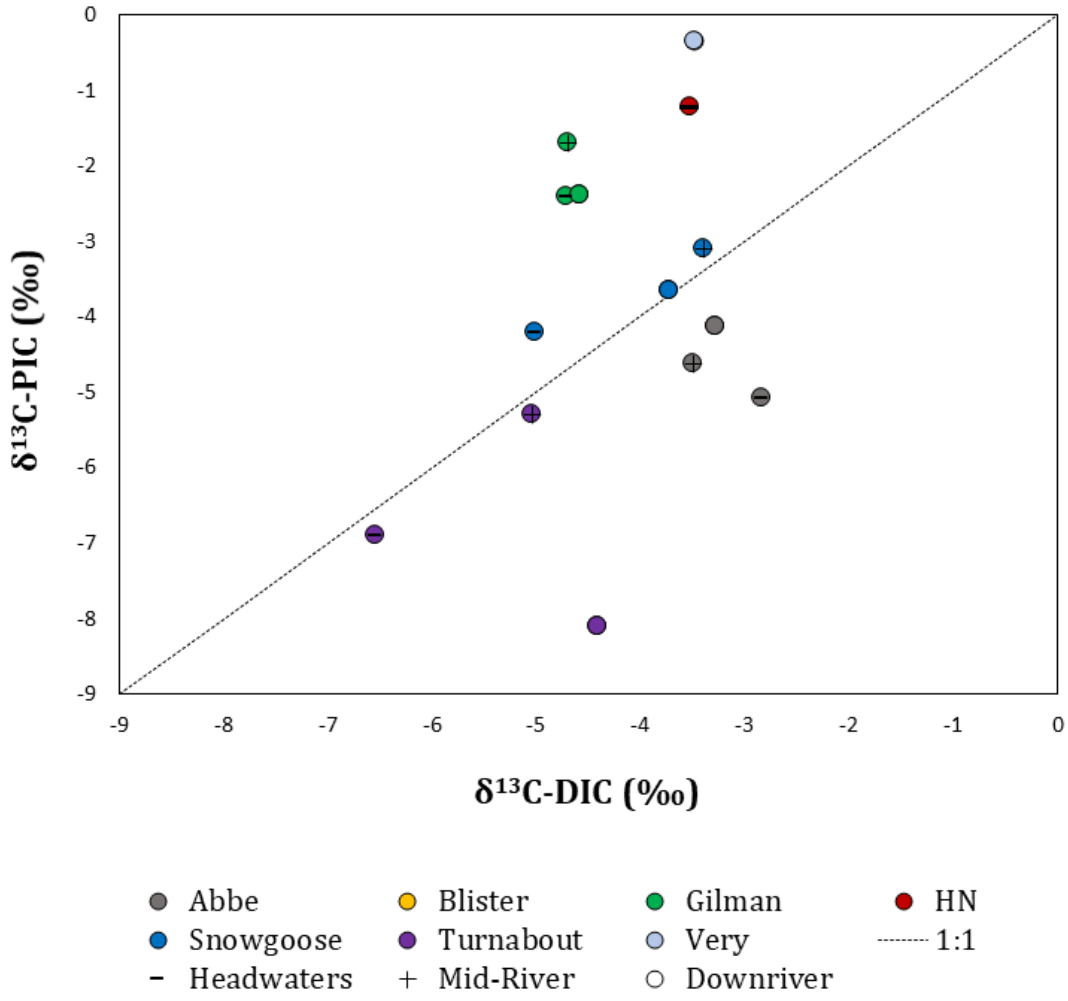

Figure 4.4: δ^{13}C-PIC of suspended sediment and δ^{13}C-DIC of corresponding glacial river samples spanning headwaters, mid-river, and downriver sites, collected during 2019.

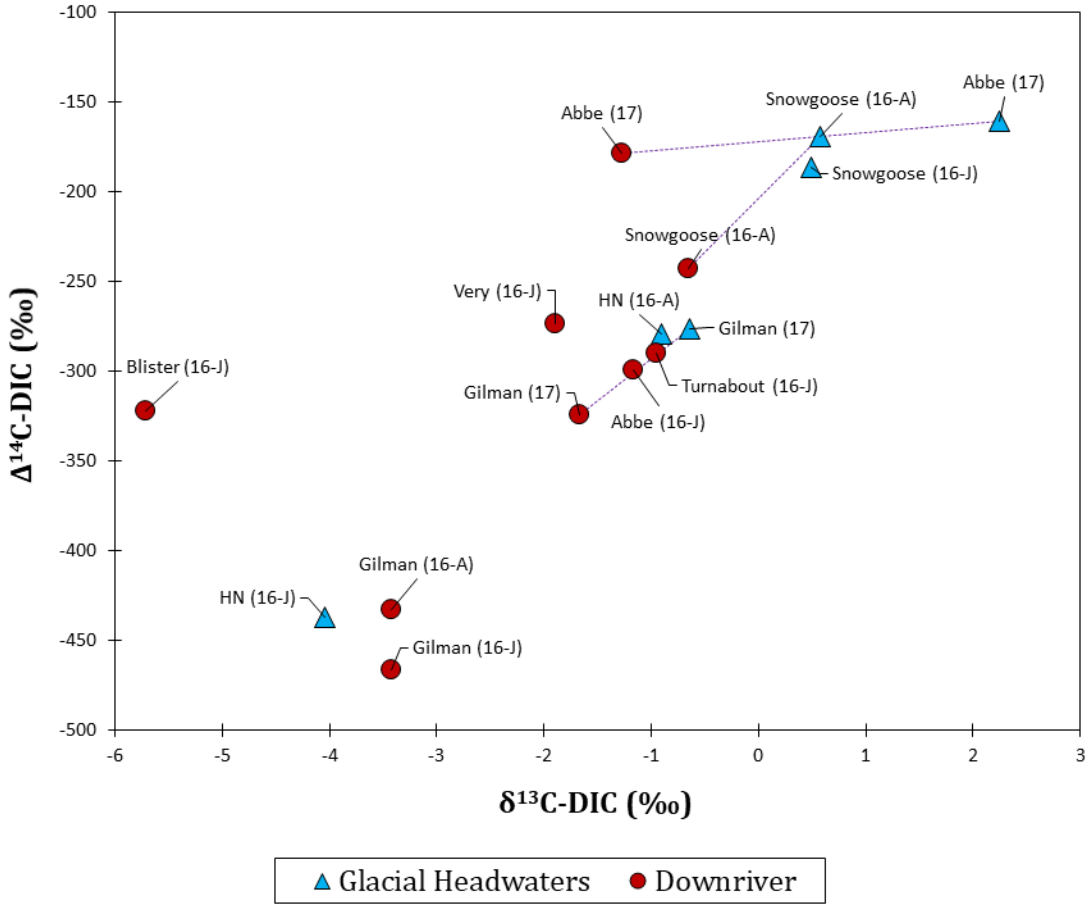

Figure 4.5: Δ^{14}C-DIC and δ^{13}C-DIC in glacial headwaters and downriver sites for samples collected during July 2016 (16-J), August 2016 (16-J; includes July 30th onward), and 2017 (17). Transects are connected with dashed lines. **Important: Blister River glacial headwaters (July 2016) had Δ^{14}C-DIC = -77 ‰, but no corresponding δ^{13}C-DIC for this plot.** Also note that the Snowgoose (16-A) transect samples were collected within 48 hours rather than same day sampling. **There was a significant ($p < 0.05$; $R^2 = 0.61$) linear relationship between δ^{13}C-DIC and Δ^{14}C-DIC overall, that was particularly strong among glacial headwater samples (0.91).**

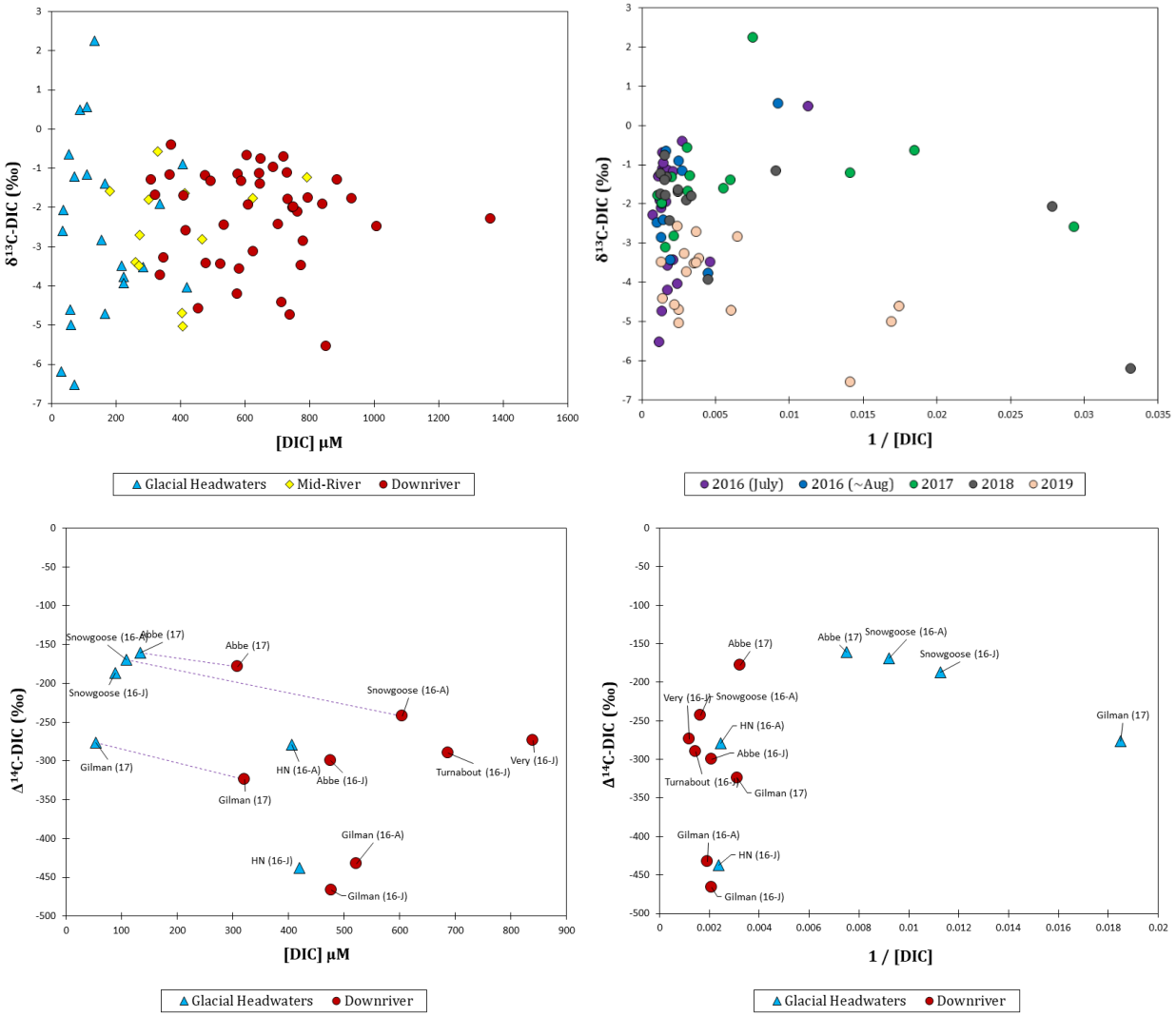

Figure 4.6A-D: Relationships of DIC and 1/DIC with δ^{13}C-DIC and Δ^{14}C along glacial river transects spanning sampling years.

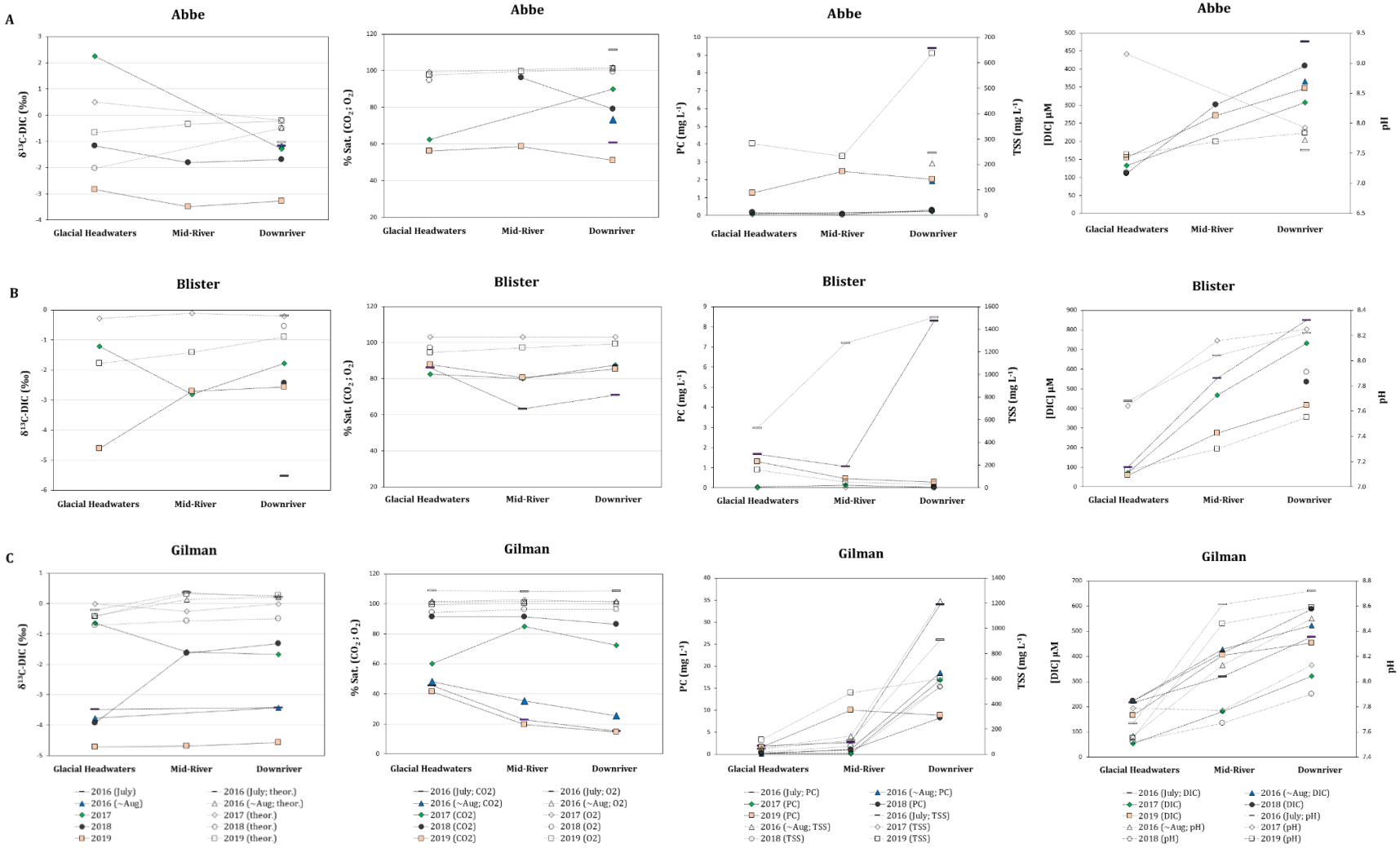
A
Abbe
δ13C-DIC (‰)
% Sat. (CO2 ; O2)
PC (mg L-1)
TSS (mg L-1)
[DIC] µM
pH
Glacial Headwaters
Mid-River
Downriver
B
Blister
C
Gilman
2016 (July)
2016 (~Aug)
2017
2018
2019
2016 (July; theor.)
2016 (~Aug; theor.)
2017 (theor.)
2018 (theor.)
2019 (theor.)
2016 (July; CO2)
2016 (~Aug; CO2)
2017 (CO2)
2018 (CO2)
2019 (CO2)
2016 (July; O2)
2016 (~Aug; O2)
2017 (O2)
2018 (O2)
2019 (O2)
2016 (July; PC)
2016 (~Aug; PC)
2017 (PC)
2018 (PC)
2019 (PC)
2016 (July; TSS)
2016 (~Aug; TSS)
2017 (TSS)
2018 (TSS)
2019 (TSS)
2016 (July; DIC)
2016 (~Aug; DIC)
2017 (DIC)
2018 (DIC)
2019 (DIC)
2016 (July; pH)
2016 (~Aug; pH)
2017 (pH)
2018 (pH)
2019 (pH)

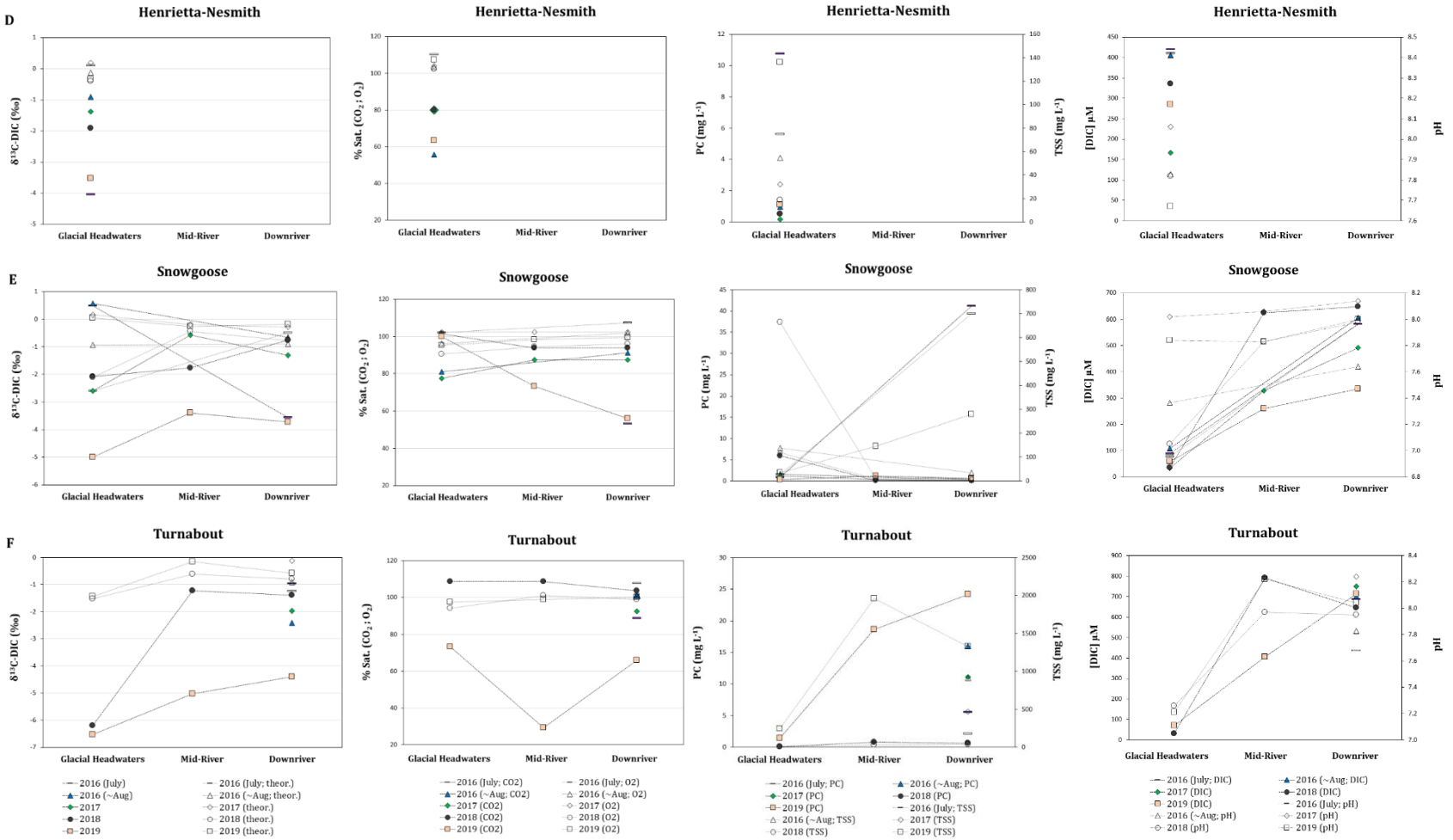
D
Henrietta-Nesmith
δ13C-DIC (‰)
% Sat. (CO2 ; O2)
PC (mg L-1)
TSS (mg L-1)
[DIC] µM
pH
Glacial Headwaters
Mid-River
Downriver
E
Snowgoose
F
Turnabout
2016 (July)
2016 (July; theor.)
2016 (~Aug)
2016 (~Aug; theor.)
2017
2017 (theor.)
2018
2018 (theor.)
2019
2019 (theor.)
2016 (July; CO2)
2016 (July; O2)
2016 (~Aug; CO2)
2016 (~Aug; O2)
2017 (CO2)
2017 (O2)
2018 (CO2)
2018 (O2)
2019 (CO2)
2019 (O2)
2016 (July; PC)
2016 (~Aug; PC)
2017 (PC)
2018 (PC)
2019 (PC)
2016 (July; TSS)
2016 (~Aug; TSS)
2017 (TSS)
2018 (TSS)
2019 (TSS)
2016 (July; DIC)
2016 (~Aug; DIC)
2017 (DIC)
2018 (DIC)
2019 (DIC)
2016 (July; pH)
2016 (~Aug; pH)
2017 (pH)
2018 (pH)
2019 (pH)

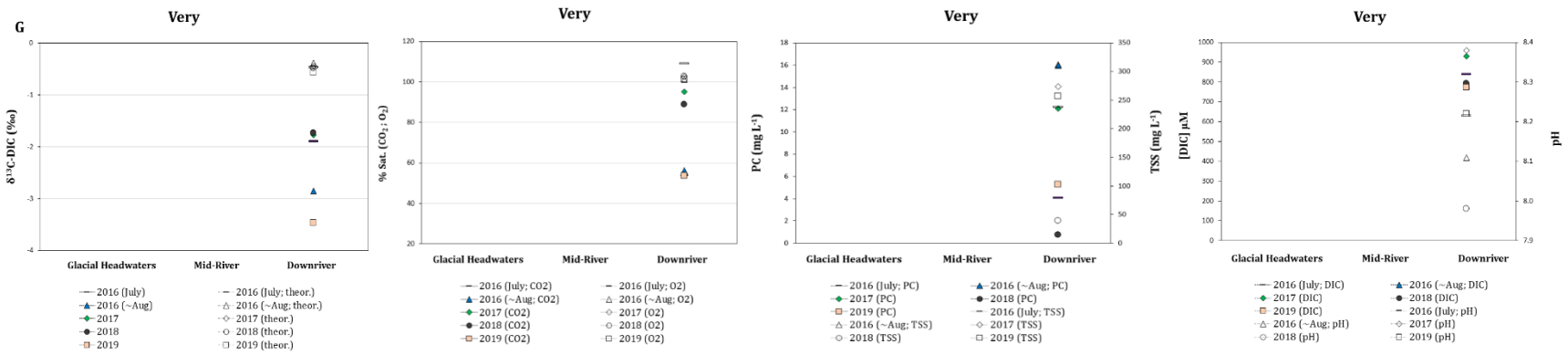

Figure 4.7A-G: Evolution of total suspended solids (TSS), suspended particulate carbon (PC), [DIC], pH, dissolved gases (CO_2; O_2 % sat.), and δ^{13}C-DIC (measured vs theoretical equilibrium along glacial river transects (Abbe **(A)**, Blister **(B)**, Gilman **(C)**, Henrietta-Nesmith **(D)**, Snowgoose **(E)**, Turnabout **(F)**, and Very **(G)**). Samples were collected as part of helicopter surveys during lower flow (2017, 2018) and higher flow conditions (July 2016, ~Aug 2016, 2019). Note: Snowgoose transects sampled during 2016 were collected within 48 hours, instead of same-day collection, which was the case for the remainder of the samples.

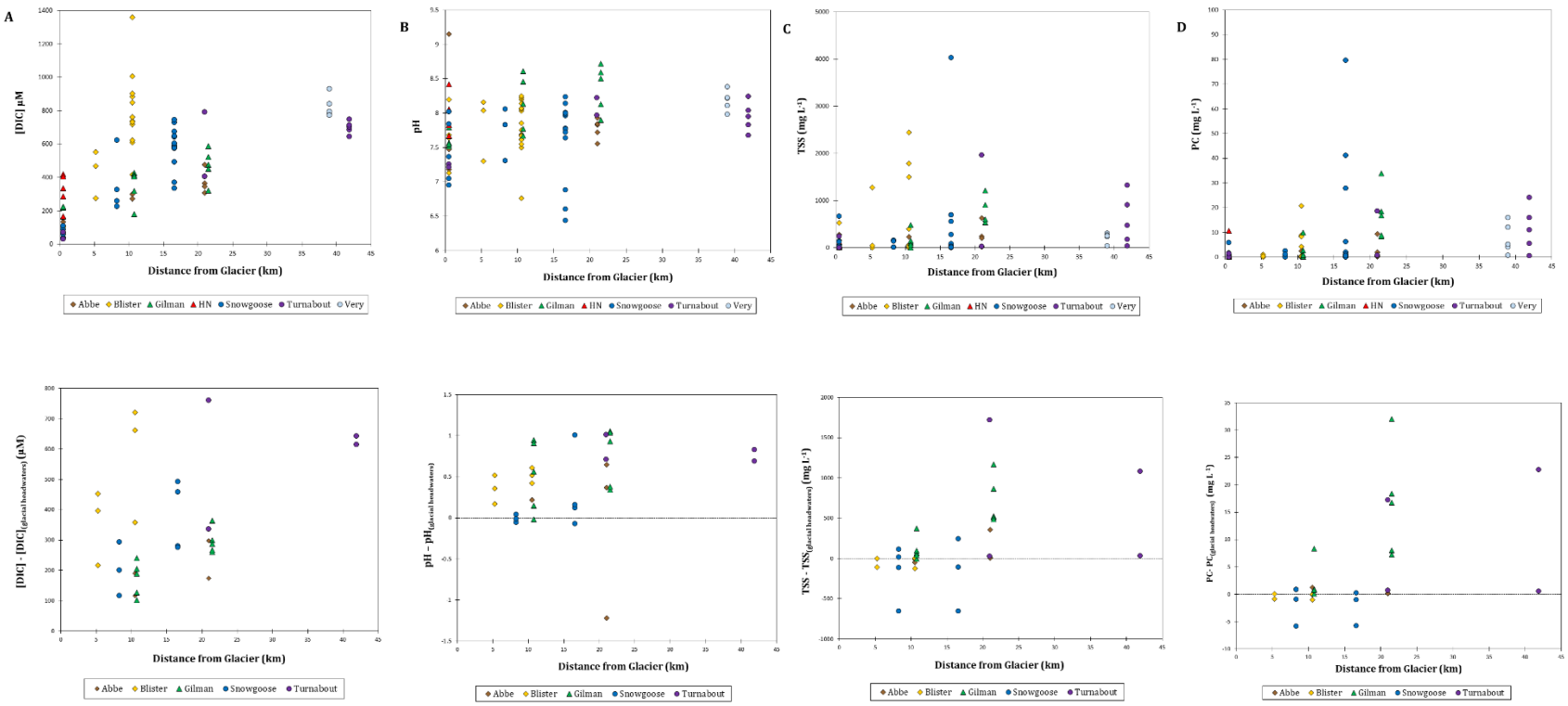

Figure 4.8A-D: Relationships of [DIC], pH, TSS, and PC with distance from glacier termini for all glacial rivers. Changes in these measured parameters relative to glacial headwaters are also presented for transects of Abbe, Blister, Gilman, Snowgoose, and Turnabout River. **Note:** glacial headwater sites were all plotted at ~0.5 km, which is only an approximation.

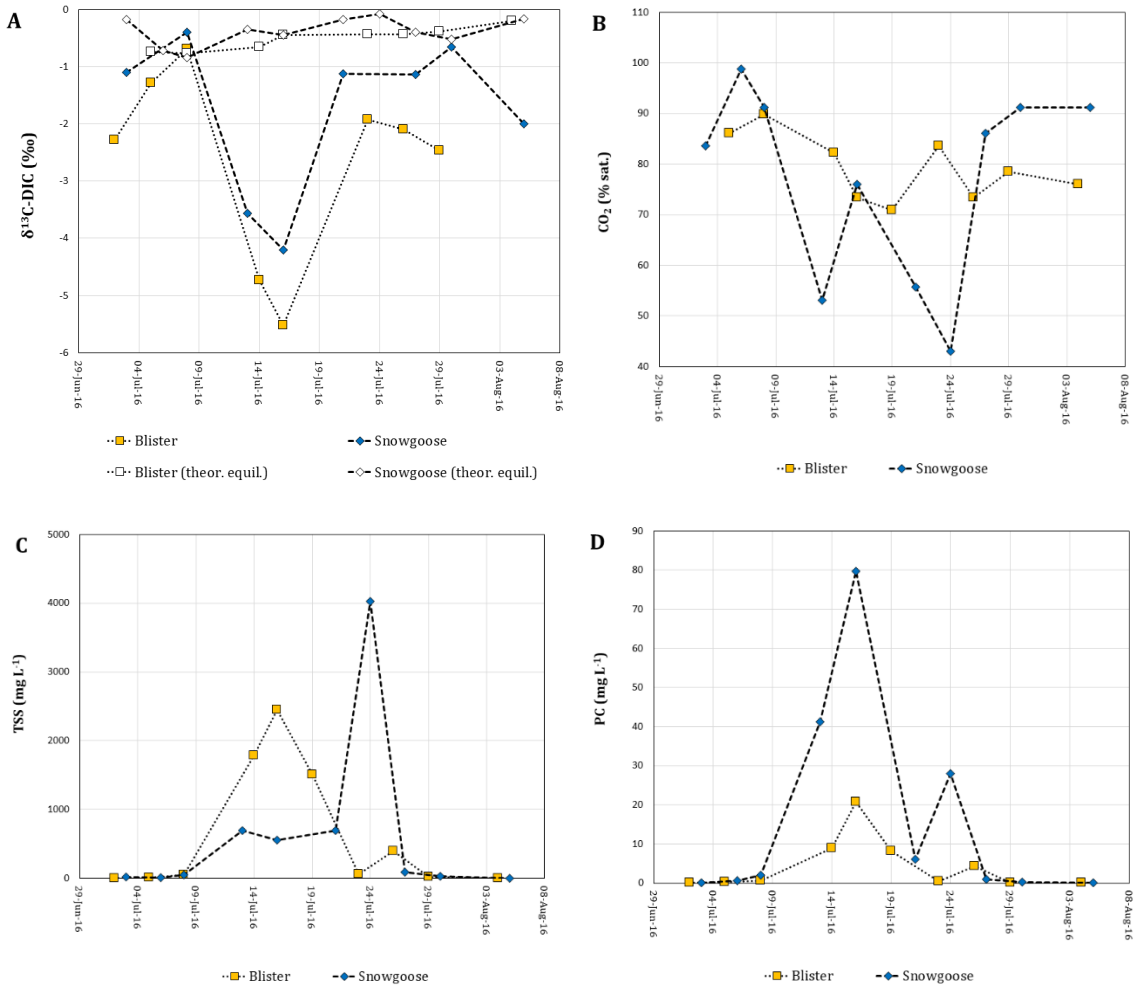

Figure 4.9A-D: Temporal variability in geochemistries of Blister and Snowgoose River deltas during summer 2016. **Note:** peak glacial meltwater flux was in mid-July.

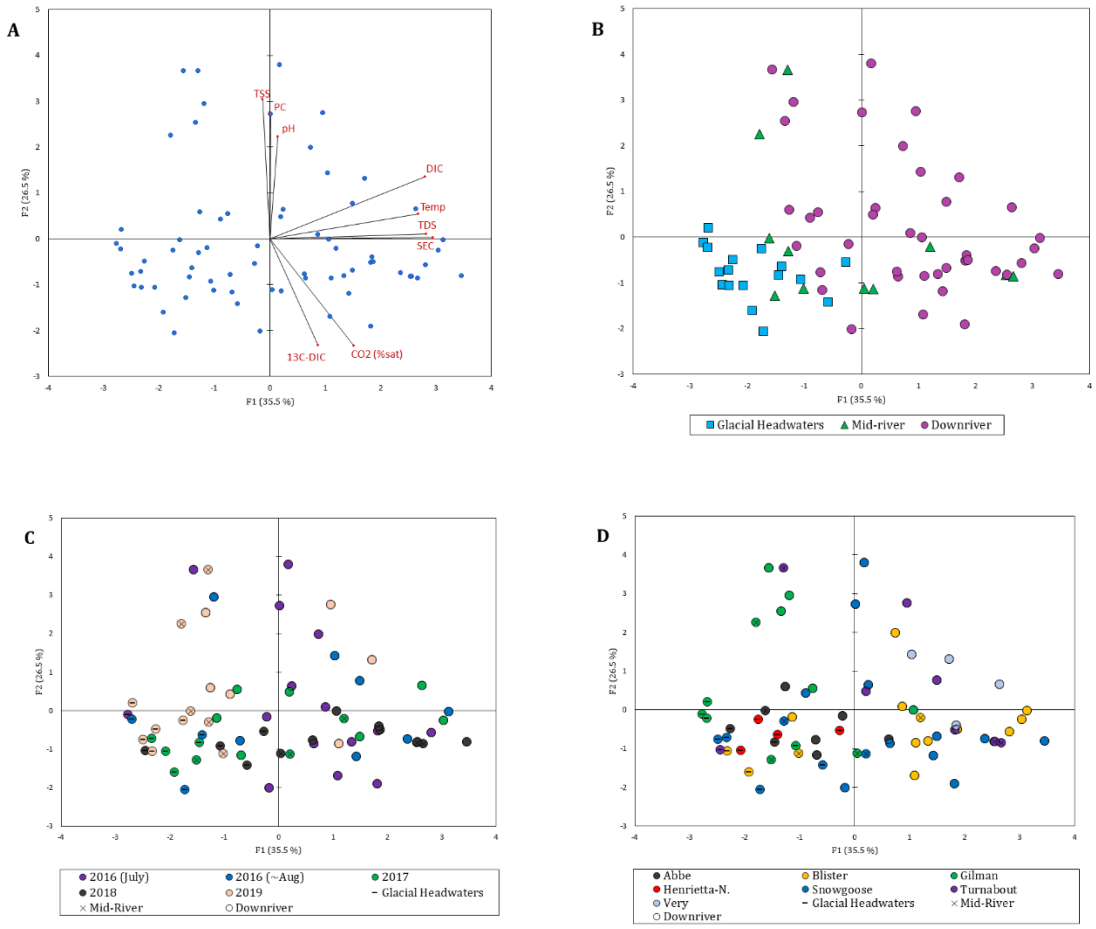

Figure 4.10A-D: Biplots for Pearson's PCA ($\alpha = 0.05$) for complete glacial rivers dataset. Data has been binned based on position along glacial river continua, sampling year, and different glacial river catchments. Corresponding correlation matrix presented in Table 4.3D.

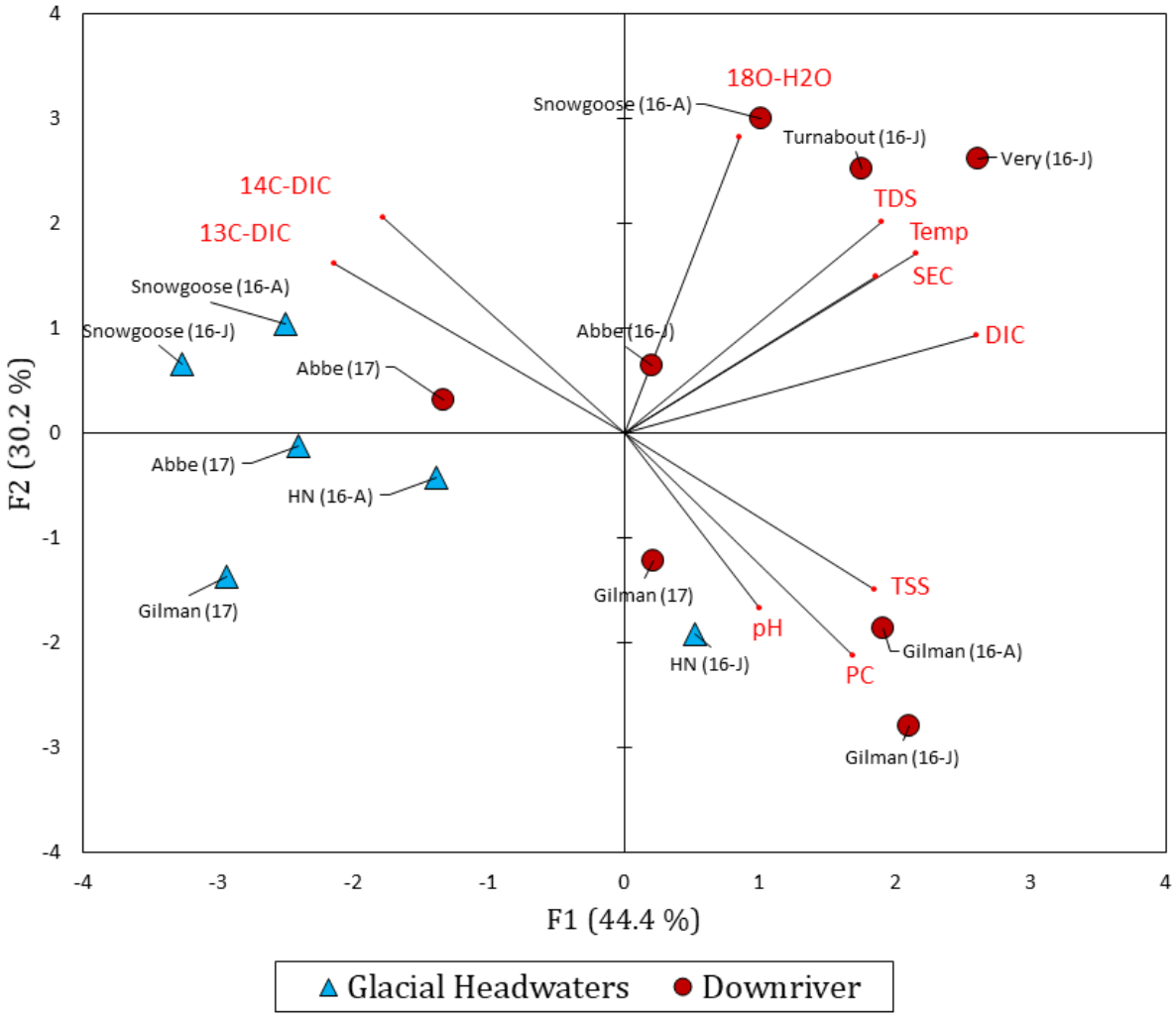

Figure 4.11: Principal component analysis (Pearson's PCA; $\alpha = 0.05$) for subset of glacial rivers dataset with measures of Δ^{14}C-DIC. Glacial headwaters and downriver samples were collected during July 2016 (16-J), August 2016 (16-A; includes July 30th onward), and 2017 (17). The associated correlation matrix is presented in Table 4.3E. One observation of Δ^{14}C-DIC (Blister 16-J) was not included in this analysis as it was missing the complete suite of geochemical variables assessed. By similar rationale CO_2 % sat. (unavailable for several samples) was omitted here, but can be assessed based on its relationships with Δ^{14}C-DIC, δ^{13}C-DIC and other geochemical variables in a companion correlation matrix (Table 4.3F).

Chapter 5
Effect of Fe and pH on Dissolved Organic Matter Fluorescence Indices

5.1 Introduction

Dissolved organic matter (DOM) is a complex and multifarious mixture of chemical constituents, including humic/fulvic acids, lignin, proteins, lipids, and other weak acids[117] with extreme chemical diversity[403]. DOM plays important biogeochemical roles in natural waters, serving as a key source of nutrients for biota[404] and a vehicle for the transport of DOM-complexed heavy metals[405,406]. DOM contains light absorbing chemical functionalities that contribute to the attenuation of light in the water column and consequently, the depth of the photic zone[407,408]. These roles depend on the mixture of organic compounds comprising DOM that can be evaluated using a number of analytical techniques. Excitation-emission matrix spectra (EEMS) generated from fluorescence spectroscopy[409] has received widespread application as a fast, inexpensive, and non-destructive measure of DOM composition. Characterization of DOM with EEMs can involve peak-picking techniques[139], indices calculated at strategic wavelengths pairs[141,143,224], or parallel factor analysis (PARAFAC). PARAFAC uses a trilinear regression to deconvolute arrays of EEMS datasets to their underlying principal components or chemically distinct fluorophore compositions[144] and has been used increasingly over the past decade[146] to trace distinct fluorescent fractions of DOM in natural waters[410–412]. EEMS/PARAFAC analysis has aided advances describing spatial and temporal variability in DOM composition based on sources and sinks[413–415], photolytic[416,417] and biological labilities[126,418], and metal binding tendencies[419,420].

Complications can arise when comparing samples from freshwaters of highly differing chemistries. For instance, while fluorescence quenching of DOM by heavy metals can yield insight into the propensity of DOM for metal complexation[421,422] and precipitation of metal-DOM complexes[423–425], it can also present challenges when assessing DOM fluorescence intensity and composition for samples taken from water bodies with a range of concentrations in dissolved heavy metals[426,427]. In particular, dissolved iron (Fe) as ferrous Fe (Fe (II)) and ferric Fe (Fe (III)), is an important micronutrient that is ubiquitous with natural waters, exhibiting variable concentrations based on local hydrology, redox chemistry, water residence time, and biological productivity[428,429]. Although Fe affects overall DOM fluorescence[430], more recently, researchers have started to investigate the Fe quenching of specific molecular weight fractions[426] and fluorescent moieties of DOM[427]. Furthermore, natural waters can

cover a range of pH values that have also been shown to impact DOM fluorescence[430] including fluorescence peaks identified in EEMS[431,432] and modelled using PARAFAC[433]. The sensitivity of DOM fluorescence to pH has shown potential to be informative of the relative densities, or propensity for ionization, of carboxylic and phenolic functionalities in DOM[433]. However, there is also the risk for misinterpretation of DOM fluorescence properties or comparison of samples that vary in pH[431,432]. There is still disparity amongst findings regarding the effects of Fe (II) versus Fe (III) and pH on DOM fluorescence given that the few systematic studies typically rely on chemical grade DOM standard solutions. Such DOM standards may not be representative of the breadth of variability in DOM composition in natural waters and consequently the range of fluorescence responses to chemical conditions such as dissolved heavy metal concentrations and pH, thus warranting further investigation using natural DOM samples.

The objective of this study was to quantify the impact of Fe (II), Fe (III), and pH on DOM EEMS fluorescence for diverse freshwater systems. DOM was sampled from aquatic environments spanning physiographic regions of the Mixed Wood Plains and Boreal Shield of Southern Ontario to the Taiga Shield and Southern Arctic Tundra of Yellowknife, Northwest Territories (NT) Canada and ranging from regions highly impacted by agriculture and urban activities to remote, pristine sites. Stream, river, pond, and subsurface samples were targeted to capture a range in DOM composition. In separate trials, DOM samples were spiked with Fe (II) or Fe (III) or treated to span a range of pH values and subsampled for EEMS analyses. EEMS were used to identify fluorescent peaks (A, C, M, and T) and calculate biological, fluorescence, and humification indices (BIX, FI, and HIX, respectively). PARAFAC modelling was then used to delineate the fluorescent components that best described the EEMS dataset. The effects of Fe (II) and Fe (III) concentrations and pH were assessed based on i) the extent and nature of their impact on DOM fluorescence, ii) the reproducibility of this response based on the environmental variability in DOM composition captured, and iii) the feasibility of establishing empirical formulae for correcting for the effects of Fe and pH in DOM samples across diverse aquatic freshwater systems.

5.2 Methods

5.2.1 Sampling

A total of 12 freshwater samples were collected from the Grand River watershed (n=2) and Dorset Region of southern Ontario (n=5), the International Institute for Sustainable Development -

Experimental Lakes Area (IISD-ELA) in northwestern Ontario near Kenora (n=3), and Yellowknife, N.W.T. (n=2) (Figure 5.1). A Suwannee River fulvic acid standard (SRFA) from the International Humic Substance Society (IHSS) was also prepared using NANOpure (≥18.2 mΩ-cm) water to a pH of 4.5. DOM samples were collected using HDPE syringes and filtered in-line using 0.45 µm filter cartridges (Whatman) into acid-washed glass vials. DOM samples were stored in the dark at 4ºC until lab analyses were conducted. Natural freshwater samples were taken as part of research conducted by Mead (2017) and were described in detail therein. For continuity, an abbreviated version of the site descriptions found in the aforementioned reference is provided here for samples taken from the Grand River watershed, Dorset Region, IISD-ELA, and Yellowknife.

The Grand River is a seventh order river with a length of ~290 km, underlain by heavily carbonate mineralogy, and located in the Mixed Woods Plains of Southwestern Ontario [434]. The Grand River was sampled at the outflow from Belwood Lake, a major reservoir on the Grand River main stem, and further downstream at a weir within the Brant Conservation Area (BCA), prior to its eventual discharge to Lake Eerie. Streams inflowing to Dickie (DE), Harp (H), and Plastic (P) lakes were sampled within the Dorset Region, which is located within the Boreal Shield of south-central Ontario. DE10, H421, and P1-08 are headwater streams, whereas H4 1.0 and H4 2.0 are both indicative of the same second order stream that was sampled during both 2014 and 2015, respectively. IISD-ELA is located in northwestern Ontario near Kenora, within the Boreal Shield. Headwater streams were sampled in the IISD-ELA that included northeast (NEIF) and northwest (NWIF) inflows to Lake 239, as well as an upland headwater stream (U8) inflowing to Lake 302. Finally, Airport Pond (Pond) and Airport P2 (P2) were situated within the subarctic Taiga Shield in an area underlain by sporadic discontinuous permafrost located ~5 km west of Yellowknife, NWT. The Pond sample was taken from the surface layer of a small pond from a peatland laden with hummocks. Adjacent to the pond a piezometer was installed to allow sampling of the subsurface conditions at ~1.4 m (P2). A summary of the sampling sites is provided in Table 5.1. An in-depth review of sample site locations, including their local geologic features and vegetation, can be found elsewhere[96].

5.2.2 Fe (II), Fe (III), and pH Titrations

Solutions of $FeCl_2$ and $FeCl_3$ (250 mg L^{-1}) were made with NANOpure water and anhydrous ferrous chloride (Alfa Aesar) or anhydrous ferric chloride (Anachemia), respectively. For $FeCl_2$ titration experiments, anoxic conditions were maintained via bubbling both the samples and reagents with N_2 followed by acidification to pH ~3.5 with 0.1 M HCl made using NANOpure water. $FeCl_2$ and $FeCl_3$

solutions were filtered to 0.45μm and titrated into DOM samples targeting Fe (II) concentrations of 1.0, 2.0, 3.0, and 4.0 mg L^{-1} and Fe (III) concentrations of 0.5, 1.0, 1.5, and 2.0 mg L^{-1}. The Fe amended DOM samples were allowed to stand for at least 24 hours to allow complexation with Fe followed by basification with NaOH to their original pH and re-filtration to 0.45 μm. For pH titration experiments, pH values of ~3.0, 4.5, 6.0, 7.5, and 9.0 were selected to span the pH range in natural waters. The initial sample was left unaltered and ascribed to the closest representative pH increment. The remaining four target pH values were then obtained by titration of DOM sample replicates with 0.1 or 1 M HCl and NaOH. DOM samples were allowed to stabilize overnight before taking final pH measurements, readjusting if necessary.

5.2.3 Chemical Analyses

During analyte preparation and titration experiments, pH measurements were made using a calibrated Hach HQ40d meter equipped with an IntelliCAL PH301 probe. Fe (II) and Fe (III) samples were filtered into 15 mL Celltreat® Scientific Centrifuge Tubes and acidified with 0.3 mL of Omni*Trace* Ultra® Nitric Acid (67-70%). Fe (II) and Fe (III) concentrations were analyzed using a Perkin Elmer Optima 8000 ICP-EOS. DOC concentration was measured using a Shimadzu Total Organic Carbon (TOC-L) analyzer with a detection limit of 0.2 mg C/L. Samples were analyzed in triplicates, with a standard deviation less than 5% of the average concentration.

5.2.4 Fluorescence EEMS

Fluorescence measurements and the calculation of peaks (A, C, M, T), specific peaks normalized to DOC concentration (spA, spC, spM, spT), their ratios (C:A, M:C) and fluorescence indices (BIX, FI, and HIX) are outlined in Table 2.5. Parallel factor analysis (PARAFAC) was used to decompose EEMs for the 156 DOC samples into independent fluorescent components. No outliers were flagged and omitted prior to PARAFAC analysis as leverages for all samples were generally uniform and <0.08. The analysis was carried out in Matlab R2015a (MathWorks) using drEEM[146] and DOMFluor[145] toolboxes. The model was constrained to non-negative values and run for three to ten components. The appropriate number of components was determined by split-half and Tucker congruence coefficient analyses[145,146]. A 3-component model was split-half validated for 6 dataset halves using PARAFAC[145,146], with residual fluorescence intensities typically low and featureless (<10%) for all samples. EEMS fluorescence fingerprints are presented for the PARAFAC components (C1, C2, and C3; Figure 5.2), and their fluorescence features are discussed in detail in

Appendix C. PARAFAC component fluorescence intensities (C1-3 r.u.), component ratios (C2:C1, C3:C2), proportions (i.e. C1% = C1 / (C1+C2+C3) * 100), and specific component fluorescence normalized to DOC concentration (i.e. spC1 = C1 / [DOC]) are reported. The proportions of fluorescence peaks (i.e. A% = A / (A+C+M+T)) are discussed in some instances as well, although care should be used in their interpretation given that they are not proportions of total fluorescence, but only used semi-quantitatively relative to each other. In this study, the propagation of inner filtering effects during Fe titration experiments likely contributed to preferential fluorescence quenching at shorter excitation wavelengths, and consequently the quantification of protein-like fluorescence.

5.3 Results

5.3.1 Initial DOM Fluorescence Composition

Natural waters in this study encompassed a large range in DOC concentrations from 2.5 to 75 mg C L^{-1} (Table 5.2A). Total fluorescence intensity (C1+C2+C3) spanned a wide range (~0.6 to 15.5 r.u.) and was linearly related to DOC concentration (R^2 = 0.97). DOM characteristics for initial freshwater samples were dominated by humic-like A, C, and M fluorescence peaks. The protein-like 'T peak' was only faintly discernible from spectral noise with very low contributions to DOM for all samples (~1.1 to 3.4%; Table 5.2A), and will not be discussed further. C:A and M:C captured variability in DOM fluorescence composition amongst these natural water samples. For instance, the boreal stream samples had relatively high C:A (1.00 to 1.12) accompanied by low M:C (0.68 to 0.78), whereas 7th order river samples had comparatively low C:A (0.71 to 0.80) and high M:C (1.02 to 1.12; Figure 5.3; Table 5.2B). Compositional differences in PARAFAC components were also found amongst DOM samples. In particular, C1% was higher ($p < 0.05$) for high DOC subarctic samples and low DOC 7th order river samples (52 ± 3%) relative to samples taken from boreal and subboreal streams (38 ± 4%) of more intermediate DOC concentrations (Figure 5.4). High C2% (34 ± 2), C3% (30 ± 2), and C peak% (40 ± 1) for boreal streams were also accompanied by higher HIX values (29 ± 3) compared to all other samples (22 ± 4; $p < 0.05$). Conversely, lower C2% (24 ± 2), C3% (25 ± 3), and C peak% (34 ± 2; $p < 0.05$) were found for subarctic and 7th order river samples. A Pearson's correlation principal component analysis with 78.7% explained variance (PCA; Figure 5.5) showed strongly correlated C1% and M:C (r = 0.93), C2% and HIX (r = 0.61), and C3% and C:A (r = 0.60). Separation of DOM fluorescence characteristics was captured along the primary F1 axis based on distinct physiographic regions and hydrologic environments for sample clusters. For instance, Grand River and Yellowknife

samples adhered to negative F1 axis values (C1% and M:C), whereas IISD-ELA and Dorset samples generally shifted towards positive values along the F1 axis (HIX, C2%, and C:A).Thus, fluorescence indices captured variability in DOM composition spanning sample sites and provided distinct 'starting points' for subsequent titration experiments.

5.3.2 Concentrations of DOC, Fe (II), and Fe (III) during titration experiments

Responses of DOC, Fe (II), and Fe (III) concentrations varied amongst titration experiments. Importantly, only the 7th order river samples with naturally alkaline conditions (pH ~ 8.2) were unable to hold any additional Fe in solution, evidenced by unresponsive Fe (II) and Fe (III) concentrations (Figure 5.6). The remainder of samples exhibited modest increases in Fe (II) and Fe (III) concentrations over the course of titrations. Normalization of DOM fluorescence peaks and PARAFAC components to DOC concentration helped account for changes to DOC during Fe (II) and Fe (III) titrations. Apart from a few outliers, DOC concentrations typically remained within ± 0.5 mg C L^{-1} for Fe (II) treatments. However, Fe (III) additions elicited considerable (>15%) losses in DOC concentration for several boreal and subboreal stream samples (DE10, H4 2.0, NEIF, NWIF, P1-08, U8), and the IHSS standard. Thus, co-precipitation of Fe-DOM and Fe-(oxy)-hydroxide complexes was an important consideration for Fe (III) titration experiments. As such, the 7th order river samples that could not hold additional Fe in solution were not assessed based on inferred changes to DOM fluorescence, as were samples with >15% DOC concentration loss during Fe (III) titrations.

5.3.3 Effects of Fe (II) and Fe (III) on DOM fluorescence

Over the course of Fe (II) titration experiments, specific humic-like fluorescent peaks (spA, spC, and spM) and PARAFAC components (spC1, spC2, and spC3) decreased significantly ($p<0.05$) for boreal and subboreal streams, and subarctic samples (Figure 5.7). Greatest decreases were observed for the dominant PARAFAC component (spC1) and 'spA peak', which was reflected in higher slopes for regression analyses (Table 5.3). Where the increase in Fe (II) concentration (Δ Fe (II)) was greater than 2.2 mg L^{-1}, decreases in specific peaks and PARAFAC components corresponded to ~40 to 60% reductions relative to initial untreated samples. For samples where Δ Fe (II) was 1.0 to 1.6 mg L^{-1} the reduction in specific peaks and PARAFAC components were less (20 to 40%), but still significant ($p<0.05$; except for spC3) when compared to samples of Δ Fe (II) <0.8 mg L^{-1}. Different magnitudes of DOM fluorescence responses to Fe (II) were thus reflected in measures of C:A and C3:C2 shifting towards higher values as Fe (II) increased ($p <0.05$) (*Appendix C – S5.1*). Initial DOM fluorescence

characteristics were also linked to responses during Fe (II) additions. For instance, samples with the highest naturally occurring C2% (~36%, DE10 and NEIF) showed the most extreme decreases in C2:C1 for Fe (II) > 2.2 mg L^{-1}. Conversely, subarctic samples with lower initial C2% (~25%) had slightly positive shifts in C2:C1 for Fe (II) > 2.2 mg L^{-1}. This suggested that higher initial peak fluorescence intensities translated to more pronounced responses to Fe (II). Variability in initial DOM fluorescence composition thereby translated to different inferred shifts in fluorescence characteristics with Fe (II) addition.

The impact of Fe (III) induced static fluorescence quenching to DOM fluorescence character could not be directly assessed for all samples due to significant changes in DOC concentration. Samples least influenced by DOM loss were two of the subboreal samples (H4 1.0, H421), and subarctic samples (P2 and Pond). Increases in Fe (III) concentrations for P2 and Pond (~0.7 to 0.8 mg L-1) as well as H4 1.0 and H421 (~ 1.6 to 2.2 mg L-1) were achieved over the course of the titrations. Linear regressions of specific peaks and PARAFAC components yielded slopes and R^2 values that were comparable to those of Fe (II) titrations (Table 5.3). This implied that when dissolved in solution, both Fe (II) and Fe (III) had similar relationships with DOM fluorescence quenching. Maximum Fe (III) additions for H4 1.0 and H421 showed decreases in specific peaks and PARAFAC components (Figure 5.8), eliciting a shift towards higher ($p<0.05$) C3:C2 values for Fe (III) > 1.6 mg L^{-1} (*Appendix C – S5.2*). On the other hand, subarctic samples did not show significant changes in specific peaks, PARAFAC components, or their ratios as Fe (III) increased. BIX, FI, and HIX fluorescence parameters were moreso affected by spectral noise when compared to peak ratios of C:A and M:C, and were less suited to assessing impacts to DOM fluorescence composition over the course of Fe (II) and Fe (III) titration experiments in this case (*Appendix C – S5.3*).

5.3.4 Effects of pH on DOM fluorescence

The natural pH of the sampled waters ranged from acidic for the boreal streams (4.52 to 5.03), to weakly acidic for subboreal streams and subarctic samples (5.23 to 6.72), and weakly basic for 7th order river samples (8.22 and 8.23; Table 5.2A). Measures of DOM fluorescence were found to remain relatively stable for more neutral pH targets (i.e. pH ~5 to 9). Changes only emerged when considering more extreme pH values in acidic conditions (pH ~ 3 to 4.5) for which fluorescence quenching was more prevalent. For pH extremes, changes in DOC normalized peaks (spA, spC, spM) and most PARAFAC components (spC1, spC2) amounted to values that were only ~12 to 27% lower at pH ~3 compared to pH ~9 ($p <0.05$; *Appendix C – S5.4*). The minor PARAFAC component spC3

did not respond to changes in pH, resulting in a shift towards significantly higher C3:C2 as samples became more acidic and C2 was preferentially quenched (Figure 5.9). In increasingly acidic conditions C:A and BIX were higher, whereas C2:C1, M:C, and normalized HIX decreased ($p < 0.05$; *Appendix C – S5.5*). The overall decrease in M:C was intensified by particularly strong responses of subarctic samples that had higher initial proportional contribution of the M peak compared to most other samples. Apart from an anomalous response from one headwater stream sample (P1-08), the FI was also higher in strongly acidic conditions. The natural variability in indices of DOM fluorescence characteristics amongst freshwater samples overshadowed pH induced changes identified herein, except for C3:C2 that showed a pronounced difference (~0.28 ± 0.07) between pH extremes.

5.4 Discussion

5.4.1 Initial variability of DOM fluorescence character in natural waters

DOC concentration and total fluorescence intensity did not dictate DOM fluorescence composition for natural water samples of this study, and fluorescence characteristics were likely based on different sources of organic material. For instance, elevated HIX, C:A, C2, and C3% for IISD-ELA samples favoured fluorescence at longer emission wavelengths indicating a shift towards more heavily humified and extensively conjugated organic material[139,144,435]. In general, separation in fluorescence characteristics was apparent when comparing stream samples from the Dorset Region and IISD-ELA versus those from the Grand River and Yellowknife. DOM sampled from the 7th order Grand River was likely further along the degradation continuum as effects of slow acting processes such as photolysis and microbial processing may have accumulated during transit and resulted in comparatively blue-shifted fluorescence[436,437].

Yellowknife pond and subsurface samples had similarly blue-shifted fluorescence characteristics (i.e., M peak, C1), but the rationale behind this observation is likely different. At high latitudes the depth of the active layer gets suppressed relative to more southerly field locations, which is an important consideration when comparing samples taken from the taiga shield versus those from the boreal shield and mixedwood plains. The Yellowknife subsurface sample (P2) was taken from a depth of ~1.4 m, which may have rendered an ancient soil and or permafrost DOM fluorescence signature in not only P2, but also the nearby and downgradient surface water (Pond). Ancient soil organic carbon has been subject to long-term degradation given that soil microbes progressively consume OC and nutrients as active layer material becomes buried and soil horizons advance vertically over time.

Not only would the soil active layer be deeper and more OC-rich for samples taken from the Dorset Region and IISD-ELA, but these headwaters and second order streams likely also capture DOM leaching from surface layer detritus along stream banks and/or overflowing surface water inflowing to the streams during transit. In this sense, red-shifted fluorescence characteristics favouring indices such as C:A, C2, C3, and HIX resemble heavily conjugated humic-like material from more recently degraded vascular plants in IISD-ELA samples. This was generally the case for samples from the Dorset Region as well, apart from the high elevation low vegetation upland stream sample P1-08, that also had the lowest DOC concentration (~2.5 mg C L^{-1}) of all samples taken as part of this study.

Autochthonous production was expected to have a minimal contribution to the overall DOM fluorescence pool for samples in this study as extremely low protein-like T peak (spT ~ 0.003 to 0.017 r.u. L mg C^{-1}, or T / A+C+M+T ~1.3 to 3.7 %) and BIX values (0.37 to 0.67) were found. This was consistent with the inability of the PARAFAC model to identify a protein-like fluorescent component. Given its spectral features, C1 likely captured any residual protein-like fluorescence intensities in the blue portion of its emission decay band. Relationships of PARAFAC components and fluorescence peaks/indices illustrated in the PCA were in line with findings of other studies showing the complimentary nature of fluorescent peak ratios, indices, and PARAFAC components in assessing DOM fluorescence composition in freshwater samples[438–440].

5.4.2 How do Fe (II) and Fe (III) concentrations impact DOM fluorescence?

The ability of paramagnetic heavy metals to quench DOC fluorescence has been recognized for many years[430,441], including a particularly high fluorescence quenching efficiency of Fe when compared to chromate, lead, copper, and nickel[442]. In addition to potential inner-filtering effects by suspended particles[443] static fluorescence quenching mechanisms exist[444]. These include the formation of Fe-DOM complexation products for which certain moieties do not fluoresce, which have been attributed to Fe-induced DOM fluorescence quenching[421,426,427]. Changes in Fe concentrations of ~ 1.4 mg L^{-1} have been found to result in DOM fluorescence loss of ~30% for DOM leached from soil of a deciduous forest stand[421]. In this study, a similar degree of fluorescence loss was found for DOC normalized PARAFAC components and peaks when considering similar increases in Fe (II) and Fe (III) concentrations during titration experiments. Linear relationships between Fe (II) and DOM fluorescence were found to be much stronger than those of Fe (III), which could be based on a confluence of factors. For instance, higher solubility of Fe (II) compared to Fe (III) could have resulted in elevated co-precipitation Fe (oxy) hydroxides and Fe-DOM complexes during Fe (III)

titration experiments, the latter of which having ramifications on the nature of findings in this study. In fact, several samples were identified as having considerable losses in DOC concentration over the course of Fe (III) titration experiments, which was particularly noteworthy given that a narrower range in Fe (III) concentrations was used relative to those in Fe (II) titrations. This complicated interpretations of findings and ascribing responses in DOM fluorescence character with Fe (III) additions to either co-precipitation, or differences in static fluorescence quenching by Fe-DOC complexes in solution. Normalization of PARAFAC components and fluorescence peaks to DOC concentration helped to constrain the impact of dissolved Fe quenching to DOM fluorescence loss by accounting for changes in DOC concentration. The role of DOM-Fe precipitation in OC fractionation has been reported previously, including potential implications of carbon sedimentation and burial in aquatic systems to global carbon storage[423,424]. Recent findings have highlighted that co-precipitation of DOM-Fe complexes with Fe (oxy) hydroxides selected more strongly for high molecular weight terrestrial humic-like material of elevated aromaticity as inferred by measures of absorbance, fluorescence, and size exclusion[425]. Fe titration experiments, while primarily capturing impacts of dissolved Fe-DOM on measures of DOM fluorescence, likely also was influenced by co-precipitation mechanisms, especially in the case of Fe (III).

In natural waters, redox conditions and propensity for DOM-Fe complexation all factor into brownification and in turn analytical discrepancies based on Fe induced DOC fluorescence quenching. A primary objective of this study was to assess susceptibilities of PARAFAC components, fluorescence peaks, and fluorescence indices to changes in Fe (II) and Fe (III) concentrations. Shifts in DOM fluorescence composition with Fe additions could have resulted from the nature of organic fluorophores comprising the PARAFAC components or peaks in question. For instance, the density of ionizable functional groups available for complexation with Fe and consequent fluorescence loss could have impacted DOM fluorescence composition. However, in this study there was evidence of a concentration bias on inferred effects of Fe on DOM fluorescence composition. For instance, during Fe (II) treatments the highest naturally occurring C2% samples (DE10, NEIF) showed the most intense decreases in C2:C1, whereas there were actually slight increases in C2:C1 for the lowest C2% samples (P2, Pond) over the course of Fe (II) titration experiments. Similar rationale applies to overall shifts towards higher C:A and C3:C2 with increased Fe (II) concentrations. In the case of these ratios, the A peak and C2 tended to have higher naturally occurring fluorescence intensities than their counterparts (C peak, C3) and were also subject to more extensive fluorescence quenching. PARAFAC components with spectral features similar to C2 that

had particularly intense and long emission A and C peaks have been proposed to include fluorophore groups of greater susceptibility to Fe fluorescence quenching[421,427]. In fact, a recent study showed extreme loss of the A peak with elevated Fe (II) concentrations in groundwater samples of an anoxic aquifer[445].

The heightened sensitivity of shorter excitation wavelengths to fluorescence quenching has to do with the inner filter effect (IFE), which can be corrected for via sample dilution, or by using DOC absorption spectra and an algorithm either executed by the fluorometer, or post-hoc[145,444,446]. In this study, IFEs associated with Fe additions were allowed to impart an effect on DOM fluorescence. For instance, while DOM samples were diluted to *reduce* the IFE, absorption increases of samples with successive Fe additions[96,137] would have caused the IFE to increase. Given that the IFE has a heightened impact on shorter excitation and emission wavelength fluorescence[145,446,447] the A peak, and PARAFAC components that contain it (C1, C2) would be expected to have heightened sensitivities to increases in Fe concentrations. Furthermore, this likely contributed to the inability of the PARAFAC model to identify a protein-like component, given that tyrosine and tryptophan-like fluorescence peaks exist at particularly blue-shifted excitation and emission wavelengths. Findings herein underscore the importance of not only diluting highly absorptive DOM samples to minimize IFEs, but also that supplementary IFE correction should also be conducted if comparing samples of highly variable Fe concentrations.

5.4.3 DOM fluorescence across a pH gradient

The pH of a solution has also been known to influence the molecular conformation of DOC, which adopts a more coiled structure in acidic conditions and a more elongated structure in basic conditions. The unfolding of DOM molecules with increasing pH exposes otherwise hidden chromophores[448] resulting in changes in the electron accepting/donating capacities of DOM[449]. These changes in the electronic environment of DOM are ubiquitous with its capacity to fluoresce[436], and changes in DOM fluorescence across pH gradients have been reported previously for DOM standards[433,450]. A few studies have also studied the effect of pH on DOM fluorescence for natural waters, including rivers of the Amazon basin[431] and freshwaters draining peatlands and agricultural areas across the UK[432]. Carboxylic (pKa ~ 2 to 5) and phenolic (pKa ~ 8 to 10) fluorophore groups dominate at different pH values, rendering fluorescence quenching/enhancement mechanisms dependent on the density of these functionalities as they contribute to DOM fluorescence. As pH increases and DOM molecules

become elongated, functional groups may become exposed for binding with dissolved chemical species in solution.

In this study, DOM fluorescence measurements were not found to be affected for samples belonging to pH targets of ~6, 7.5, and 9. Changes in DOM fluorescence emerged when considering more extreme pH values (pH < 5) not normally encountered in lakes, but apparent for IISD-ELA streams (pH ~4.5 to 5) and the subsurface sample (P2; pH ~4.8). DOM fluorescence loss became intense in more strongly acidic conditions (pH ~3) that were likely based on carboxylic-like functional groups becoming protonated and limiting available electrons for excitation[433]. For these acidic conditions (pH ~3) there was a shift towards significantly higher C3:C2, C:A, and BIX, accompanied by lower C2:C1, M:C, and normalized HIX. Together these results highlight the heightened sensitivity and preferential fluorescence quenching of the A peak and dominant PARAFAC component C1 with increasingly acidic conditions. C1 and C2 both contain intense A peaks at short excitation wavelengths that likely accounted for their strong responses to changes in pH compared to C3, the latter of which having a fluorescence fingerprint centered around the C peak. Heightened sensitivity of the A peak to changes in pH relative to the C peak has been reported previously[431]. The M:C shifting towards lower values in acidic (pH ~3) conditions suggested that the C peak was slightly more sensitive to fluorescence quenching when compared to the M peak. The lack of response of C3 to changes in pH was unexpected given the aforementioned sensitivity of the C peak. A possible explanation was that the fluorescence signature of C3 may have been overshadowed by C2, which had a strong emission band that coincided with the spectral region used to quantify the C peak (Ex. 350 Em. 420-480). When considering the impacts of pH to DOM fluorescence characteristics, both the chemical nature of the underlying fluorophores and the magnitudes of their initial fluorescence intensities relative to one another were expected to be important[432].

5.5 Conclusions

A range of samples from freshwater environments spanning ecoregions and hydrologic environments were analyzed based on Fe (II) and Fe (III) concentrations, as well as pH gradients, to assess impacts to common measures of DOM fluorescence composition. Redox conditions complicated the interpretation of results for Fe (III) titrations given evidence of considerable DOC concentration loss from solution via co-precipitation of Fe (oxy) hydroxyl and Fe-DOM complexes for several samples. Normalization of DOM fluorescence peaks and PARAFAC components to DOC concentration was thus found to be important in the context of reducing the leverage of changes in DOC concentration to

measures of fluorescence. Fe (II) titration experiments elicited decreases in specific peaks and PARAFAC components, as well as changes in fluorescence composition, namely increases in C:A and C3:C2. It was expected that Fe (II) and Fe (III) additions increased DOM absorption and consequently amplified the inner filtering effect (IFE), contributing to preferential fluorescence quenching at short excitation wavelengths. A concentration bias inherent to measures of DOM fluorescence composition was also apparent in that peaks or PARAFAC components with higher initial fluorescence intensities had stronger responses to changes in Fe (II) and Fe (III) concentrations. These coalescing mechanisms, and the underlying chemical properties of the organic fluorophores themselves, contributed to changes in DOM fluorescence characteristics and complicate interpretations of findings herein. For pH titration experiments, samples began to show loss in DOM fluorescence at pH ~4.5, which became more intense in strongly acidic conditions (pH ~ 3) where higher C3:C2, C:A, and BIX, and lower C2:C1, M:C, and normalized HIX were found. This could have to do with DOM adopting a more coiled structure in strongly acidic conditions serving to hide fluorophores, or the protonation of carboxylic (pKa ~ 2 to 5) fluorophore groups. Similar to Fe titration experiments, the A peak and PARAFAC components or fluorescence indices that contained strong A peak signals (C1, C2, HIX) were found to be most sensitive to changes in pH. Future work would couple DOM absorption spectra with fluorescence measurements, particularly to correct for IFEs that can be exacerbated by Fe-DOM induced increases in absorption. This practice, and selecting samples from more productive freshwaters or algal exudates, could reveal responses of autochthonous character (i.e., protein-like) DOM fluorescence during Fe and pH titrations. A follow-up study that corrected for IFEs, used a greater number of increments for Fe additions, monitored pH for each Fe treatment, and increased EEMS acquisition integration time to improve spectral resolution of fluorescence measurements, would therefore be a valuable addition to the literature in the future.

Table 5.1: Summary of sampling sites from the Grand River watershed, Dorset Region, International Institute for Sustainable Development – Experimental Lakes Area (IISD-ELA), Yellowknife, N.W.T., and the reference standard

Region	ID	Type	Description
Grand River watershed	**BCA**	7th order river	Grand River sampled at Brant Conservation Area (BCA) and at the outflow of Belwood Reservoir on Grand River, ON.
	Belwood		
Dorset Region	**DE10**	Headwater stream	Wetland stream inflow to Dickie Lake, Baysville, ON.
	H4 1.0	Headwater stream	Wetland stream inflow to Harp Lake, Huntsville, ON collected during 2014 (1.0) and 2015 (2.0).
	H4 2.0		
	H421	Headwater stream	Upland stream inflow to Harp Lake, Huntsville, ON.
	P1-08	Headwater stream	Upland stream inflow to Plastic Lake, Dorset, ON.
IISD-ELA	**NEIF**	Headwater stream	Northeast (NEIF) and northwest (NWIF) inflows through a swamp/wetland valley and into Lake 239, Kenora, ON.
	NWIF	Headwater stream	
	U8	Headwater stream	High elevation, low vegetation upland stream inflowing to Lake 302, Kenora, ON.
Yellowknife, N.T.	**P2**	Subsurface (1.4m) sample	Airport Pond (Pond) sample ~ 5km NW of Yellowknife, N.T. P2 collected from a piezometer nearby Pond.
	Pond	Surface water	
Standard	**IHSS**	Suwannee River Fulvic Acid	International Humic Substance Society

Table 5.2: (A) DOC concentrations (mg C L^{-1}), pH, Fe (II) and Fe (III) (mg L^{-1}), and DOC fluorescence characteristics of initial untreated natural water samples using peak picking, **(B)** fluorescence indices, and PARAFAC modeling. Fluorescence measures normalized to DOC concentration given in r.u. L mg C^{-1}

A)

ID	[DOC] Pre-dilution	[DOC] Post-dilution	Fe (II)	Fe (III)	pH	spA	spC	spM	spT	C:A	M:C
BCA	6.70	6.70	0.04	0	8.23	0.179	0.143	0.147	0.017	0.80	1.02
Belwood	6.35	6.35	0.03	0	8.22	0.183	0.129	0.144	0.013	0.71	1.12
DE10	19.10	6.47	0.20	0.2	5.33	0.081	0.088	0.061	0.004	1.08	0.69
H41.0	6.47	6.47	0.17	0.2	6.70	0.114	0.109	0.091	0.008	0.96	0.83
H42.0	6.75	6.75	0.17	0.2	6.73	0.088	0.088	0.071	0.004	1.01	0.81
H421	3.23	3.23	0.06	0.1	6.70	0.141	0.122	0.104	0.004	0.87	0.85
IHSS	21.23	6.39	0.18	0.1	5.23	0.107	0.099	0.081	0.006	0.92	0.82
NEIF	39.89	6.64	0.10	0.1	4.52	0.080	0.089	0.068	0.003	1.12	0.76
NWIF	20.74	6.50	0.10	0.1	5.03	0.098	0.102	0.075	0.005	1.04	0.74
P2	75.35	6.23	0.23	0.2	4.77	0.124	0.113	0.107	0.006	0.91	0.95
P108	2.52	2.52	0.06	0.1	6.60	0.143	0.132	0.109	0.006	0.92	0.83
Pond	32.55	6.09	0.06	0.1	6.72	0.117	0.091	0.102	0.007	0.78	1.12
U8	15.86	6.27	0.10	0.1	4.50	0.118	0.117	0.079	0.004	1.00	0.68

B)

ID	spC1	spC2	spC3	C1%	C2%	C3%	C2:C1	C3:C2	BIX	FI	HIX	HIX (norm)
BCA	0.149	0.065	0.081	50.6	21.9	27.5	0.43	0.79	0.67	1.19	19.4	0.95
Belwood	0.151	0.061	0.066	54.2	22.1	23.7	0.41	0.93	0.58	1.15	25.5	0.96
DE10	0.050	0.052	0.042	34.6	36.1	29.2	1.04	1.23	0.47	0.94	22.3	0.96
H41.0	0.078	0.062	0.057	39.5	31.4	29.1	0.79	1.08	0.40	1.15	23.7	0.96
H42.0	0.058	0.052	0.045	37.5	33.7	28.8	0.90	1.17	0.43	0.95	30.4	0.97
H421	0.093	0.065	0.061	42.5	29.6	27.9	0.70	1.06	0.49	1.01	22.1	0.96
IHSS	0.088	0.054	0.046	47.0	28.9	24.2	0.61	1.20	0.46	0.99	19.7	0.95
NEIF	0.053	0.054	0.043	35.4	36.1	28.6	1.02	1.26	0.37	1.07	29.5	0.97
NWIF	0.064	0.059	0.052	36.5	33.7	29.9	0.92	1.13	0.46	1.10	25.5	0.96
P2	0.100	0.052	0.054	48.6	25.1	26.3	0.52	0.95	0.48	1.19	19.3	0.95
P108	0.104	0.045	0.077	46.0	20.1	33.9	0.44	0.59	0.57	1.09	18.5	0.95
Pond	0.102	0.047	0.038	54.6	25.0	20.4	0.46	1.22	0.54	1.10	24.1	0.96
U8	0.070	0.067	0.066	34.5	33.0	32.5	0.96	1.02	0.54	1.12	32.2	0.97

Table 5.3: Linear regression analyses of DOC normalized fluorescence peaks and PARAFAC components versus changes in Fe (II) and Fe (III) concentrations relative to initial untreated samples

Equations of linear regression analyses	R^2
Δ spA = -0.00780 – 0.0187 Δ Fe (II)	0.60
Δ spC = -0.00677 – 0.0161 Δ Fe (II)	0.55
Δ spM = -0.00123 – 0.0146 Δ Fe (II)	0.64
Δ spC1 = -0.00266 – 0.0142 Δ Fe (II)	0.64
Δ spC2 = -0.00624 – 0.00996 Δ Fe (II)	0.63
Δ spC3 = -0.00202 – 0.00692 Δ Fe (II)	0.43
Δ spA = 0.00164 – 0.0146 Δ Fe (III)	0.10
Δ spC = -0.00122 – 0.0119Δ Fe (III)	0.09
Δ spM = -0.00826 + 0.0149 Δ Fe (III)	0.19
Δ spC1 = 0.00475 – 0.0123 Δ Fe (III)	0.16
Δ spC2 = -0.00197 – 0.00985 Δ Fe (III)	0.22
Δ spC3 = 0.000546 – 0.00415 Δ Fe (III)	0.03

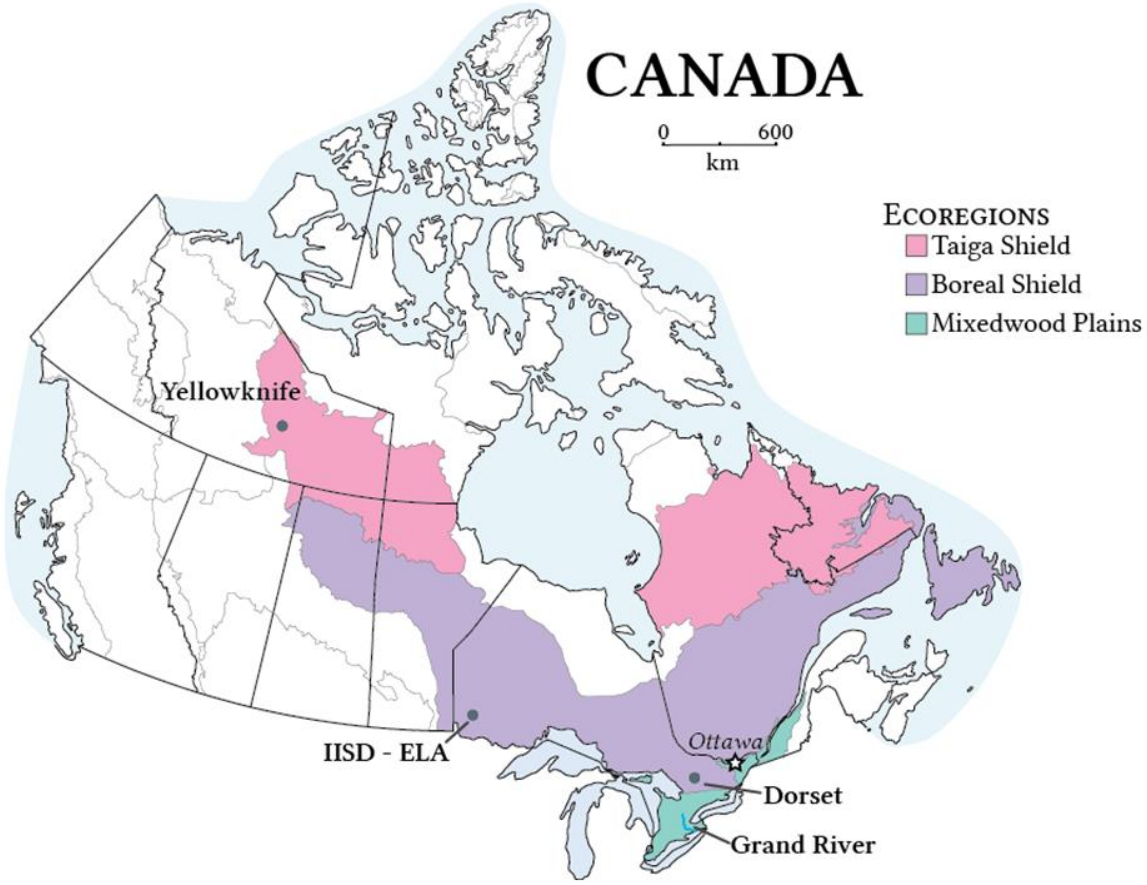

Figure 5.1: Map of sampling sites spanning ecoregions of Canada.

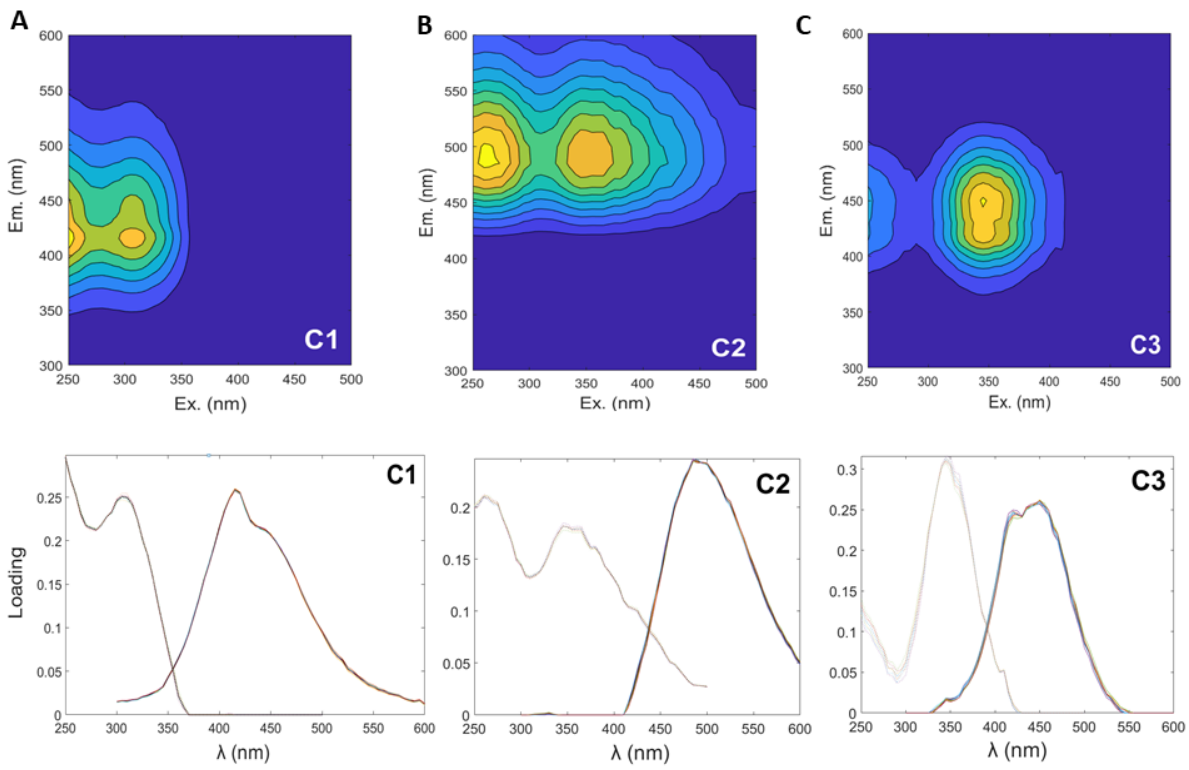

Figure 5.2: PARAFAC component **(A)** C1, **(B)** C2, and **(C)** C3 spectral features and loadings plots.

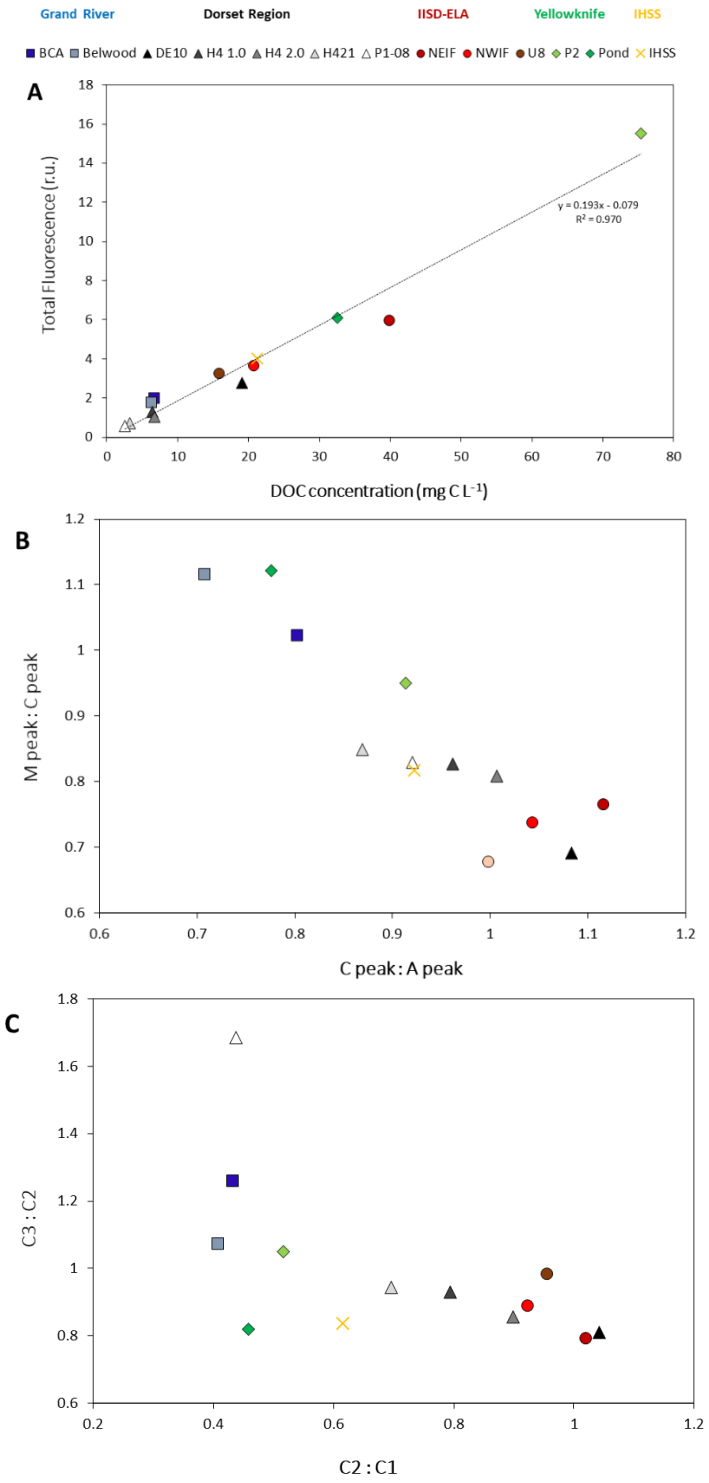

Figure 5.3: For initial untreated freshwater samples **(A)** Dilution corrected DOC concentrations (mg C L^{-1}) vs. total fluorescence (C1 + C2 + C3; Raman units, r.u.), **(B)** ratios of fluorescence peaks (C:A and M:C), and **(C)** ratios of PARAFAC components (C2:C1 and C3:C2).

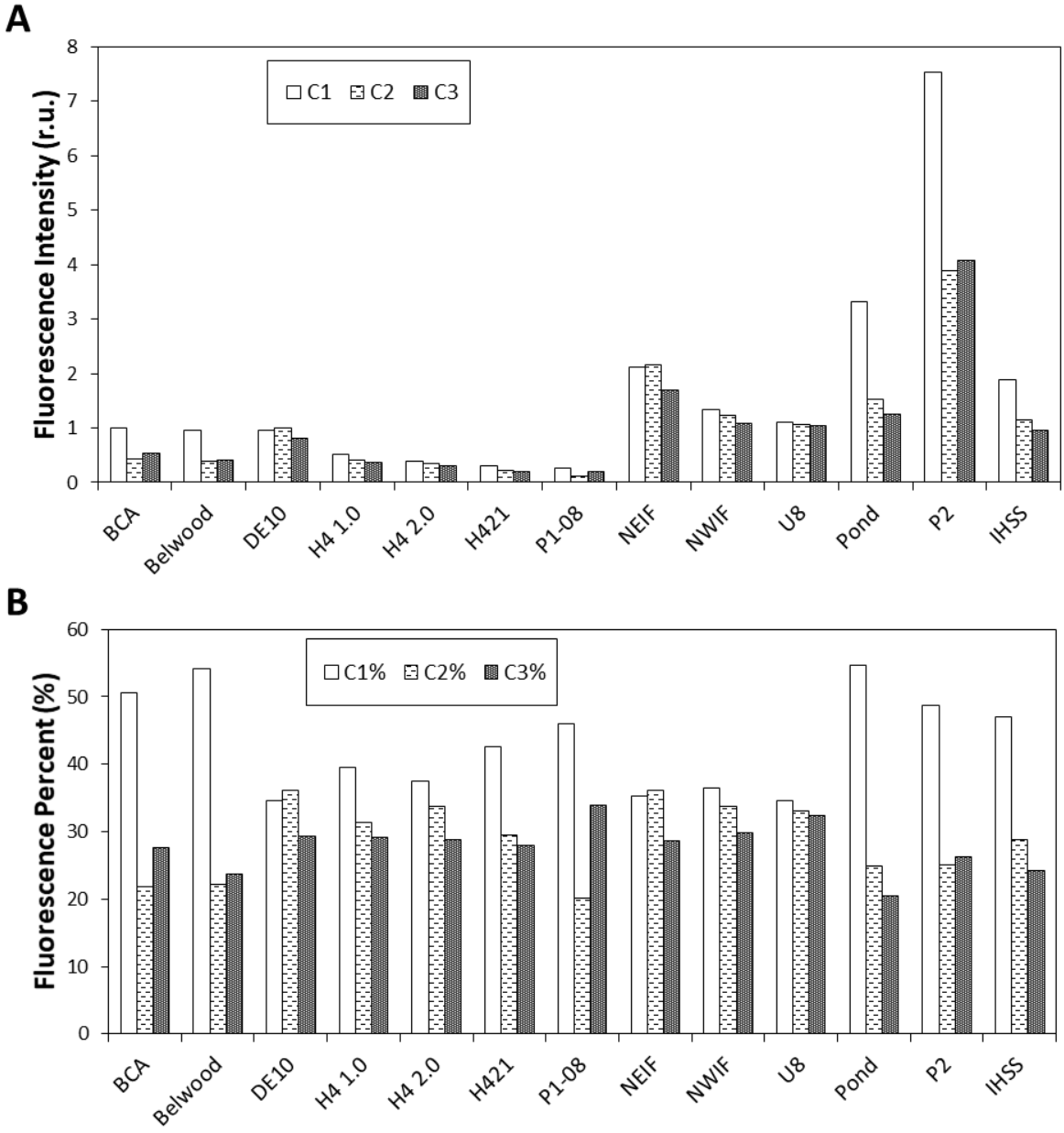

Figure 5.4: (A) Fluorescence intensities of PARAFAC components (C1, C2, and C3; corrected for dilution), and **(B)** their percent contribution to total fluorescence for initial untreated DOC samples from Grand River (BCA, Belwood), Dorset Region (DE10, H41.0, H4 2.0, H421, P1-08), IISD-ELA (NEIF, NWIF, U8), Yellowknife (Pond, P2), and a Suwannee River fulvic acid standard from the International Humic Substance Society (IHSS).

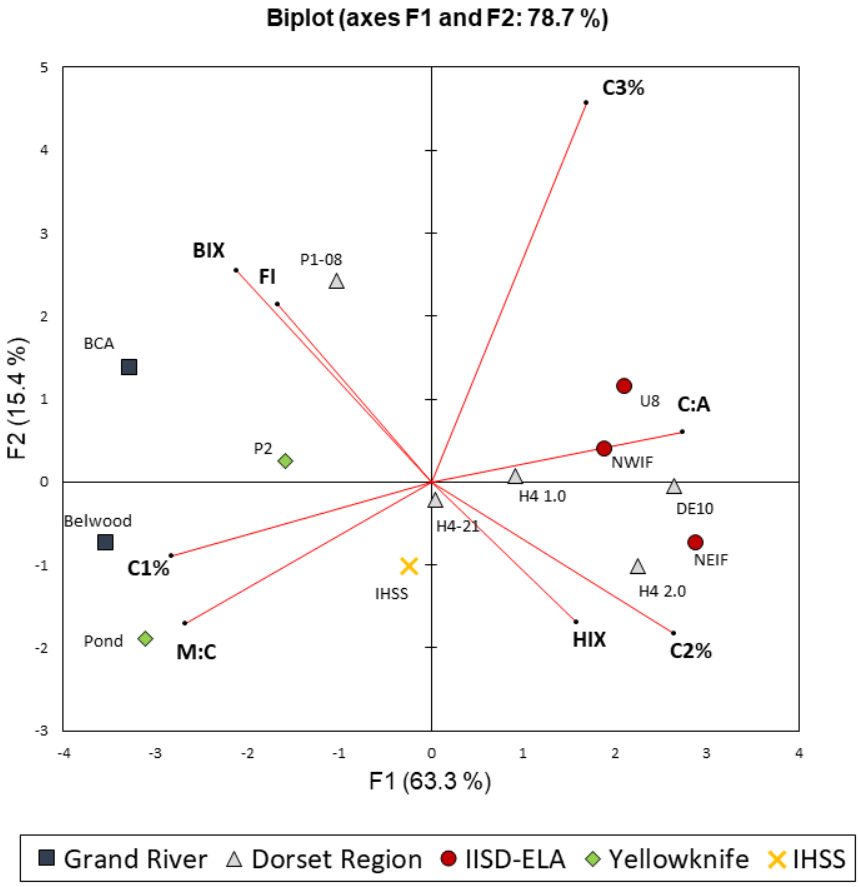

Figure 5.5: Principal component analysis (PCA) for initial untreated DOC samples (n = 13) for common measures of DOC fluorescence composition.

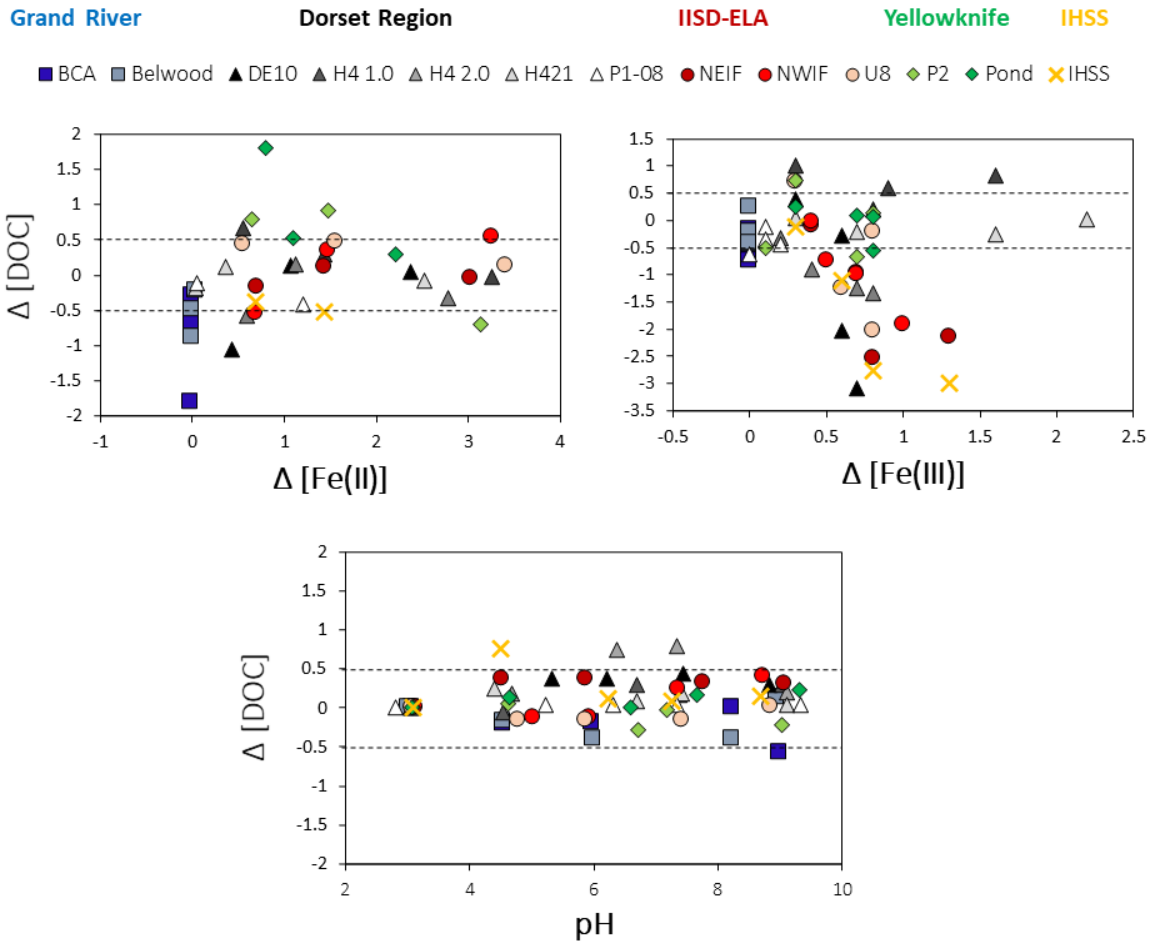

Figure 5.6: Changes in DOC concentrations based on increases in Fe (II) and Fe (III) concentrations relative to initial untreated natural water samples, and across the pH gradient.

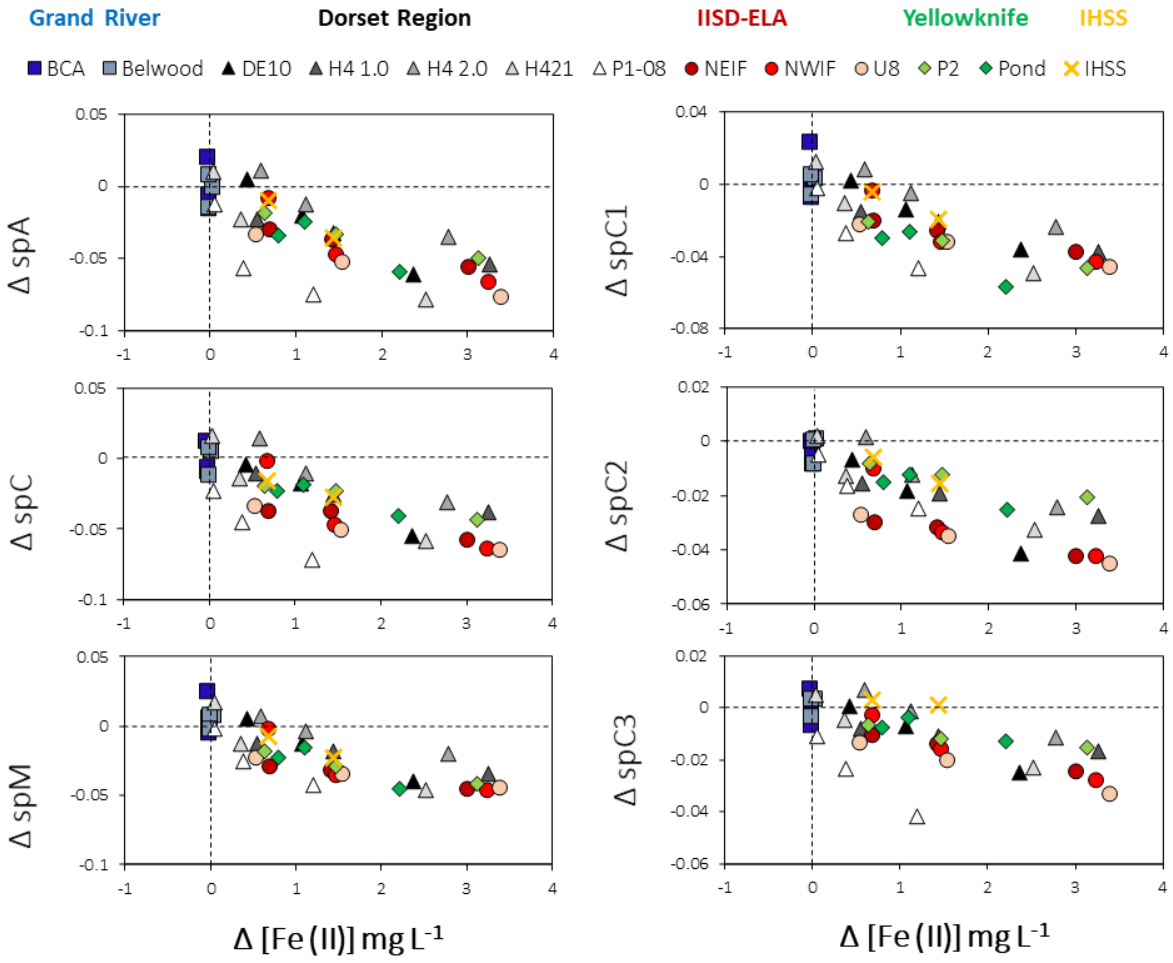

Figure 5.7: Change in DOC normalized fluorescence peaks (spA, spC, spM) and PARAFAC components (spC1, spC2, spC3) versus change in Fe (II) concentrations relative to each initial untreated water sample.

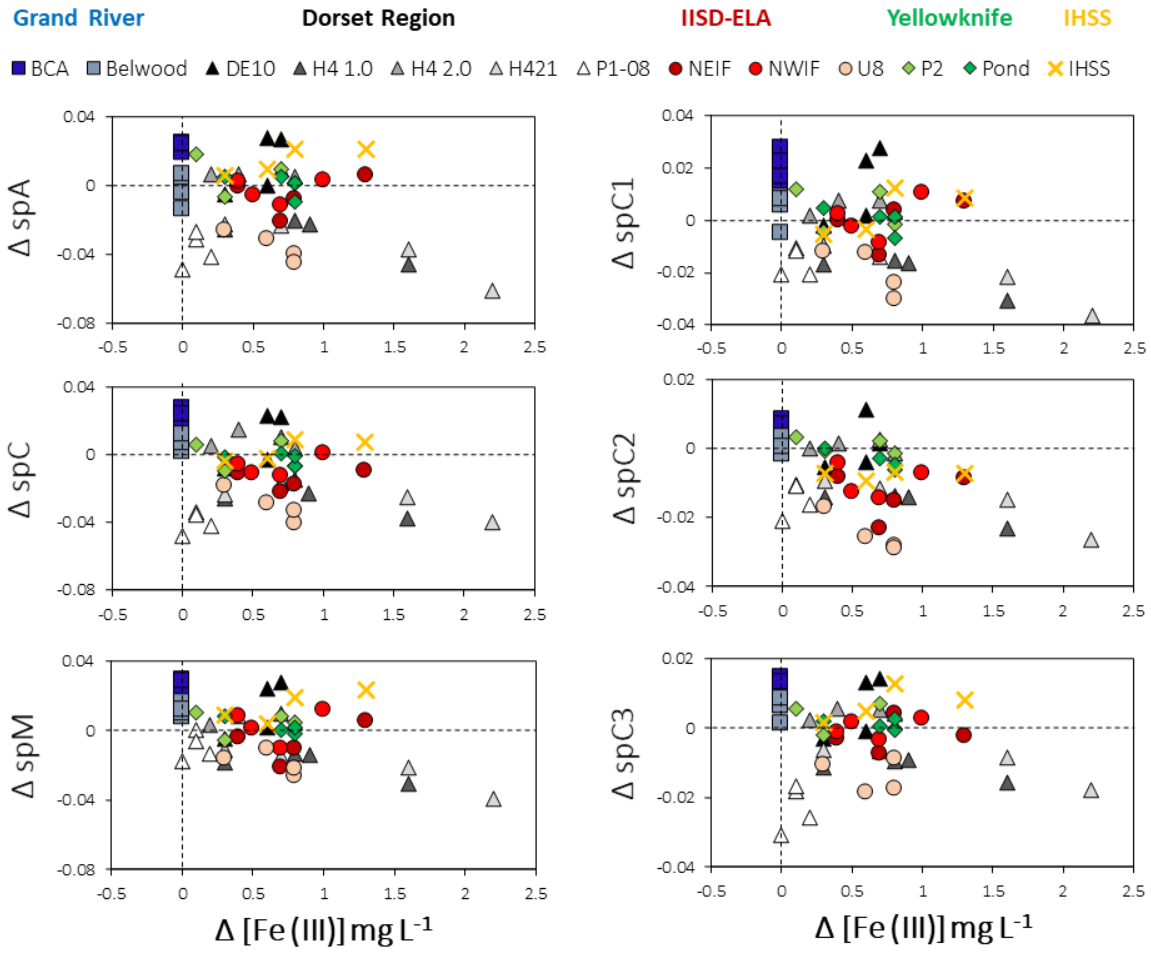

Figure 5.8: Change in DOC normalized fluorescence peaks (spA, spC, spM) and PARAFAC components (spC1, spC2, spC3) versus change in Fe (III) concentrations relative to each initial untreated water sample.

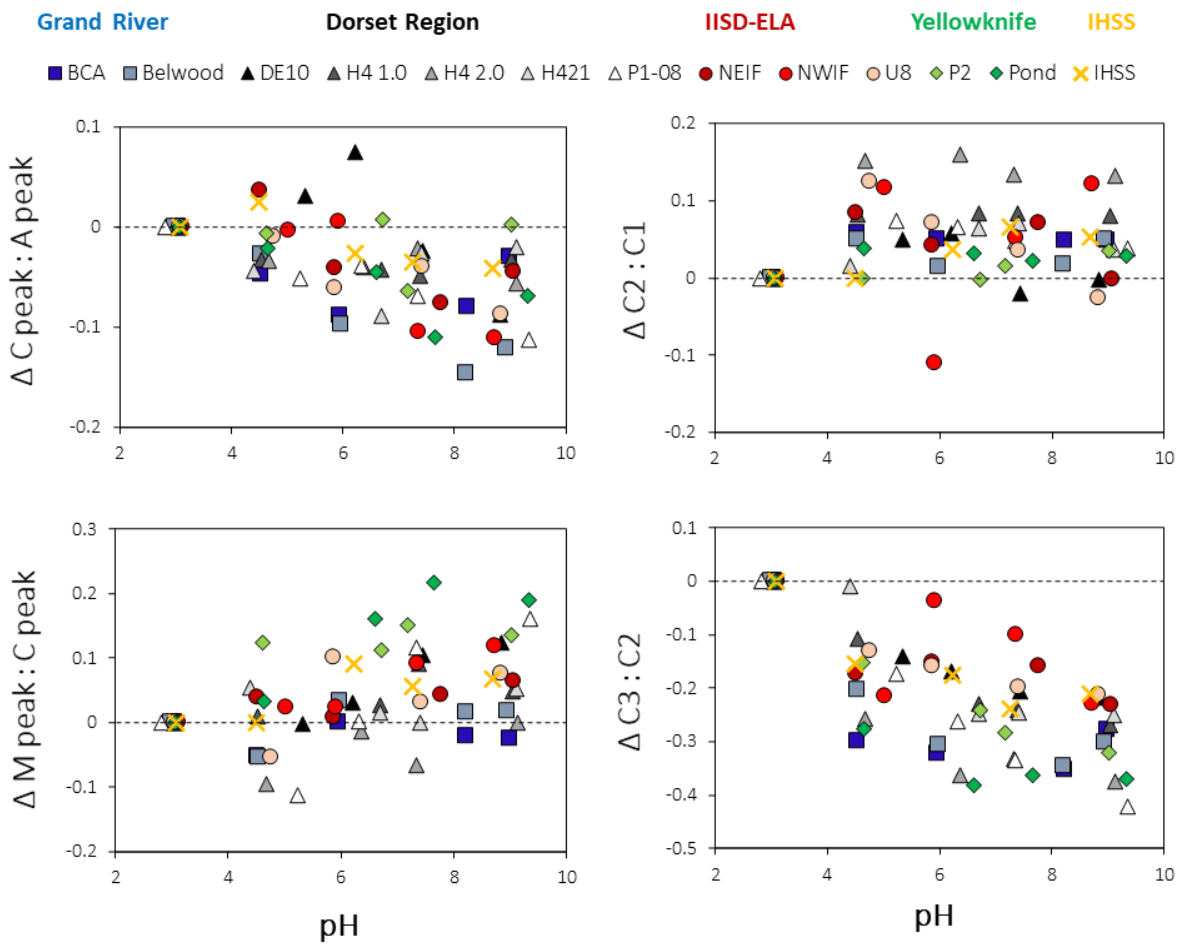

Figure 5.9: Changes in the ratios of fluorescence peaks and PARAFAC components across a pH gradient (Note: changes expressed relative to pH ~ 3 for each sample).

Chapter 6
Conclusions

6.1 Summary of Contributions

Research comprising this thesis was well-positioned to investigate sources and processes controlling carbon cycling in the glacier ice meltwater impacted Lake Hazen watershed of the Canadian high Arctic. In order to best approach the objectives in research chapters, a review of carbon cycling in a warming climate, carbon chemistry, stable carbon ($\delta^{12}C$, $\delta^{13}C$) and radiocarbon ($\Delta^{14}C$) isotopes, and techniques used to characterize DOC chemical composition, was required (Chapter 2). An overview of how carbon chemistry is shaped by physical and chemical conditions, sources of carbon, and biogeochemical processes, was put in the context of isotopic fractionation processes in natural systems. This background was key to interpreting $\delta^{13}C$ values in various phases of carbon considered as part of this research (i.e., DIC, DOC, PIC, POC, CO_2). A similar approach was applied when reviewing the use of $\Delta^{14}C$ values and ^{14}C ages in environmental studies, and their bearing when assessing mixing, or reactions, between differently aged sources of (i.e., ^{14}C-modern ^{14}C-ancient). Technical details regarding the correct derivation and notation of $\delta^{13}C$ and $\Delta^{14}C$ values were detailed to facilitate ease of interpretation, and comparison with other studies. A review of various DOC characterization techniques was then conducted, including absorption, fluorescence, size exclusion, and molecular characterization. It was critical to deconvolute the various indices of DOC chemical composition derived from these characterization techniques, and assess how these data may be used in tandem to provide the best interpretation of DOC. Together, these theoretical and analytical tools are poised to support research of carbon cycling in various natural systems, and also in our study of the Lake Hazen watershed.

Building on this foundation, it was key to determine what was known, and knowledge gaps, pertaining to carbon cycling in glacier-covered environments. Accordingly, supraglacial, subglacial, ice-marginal, and proglacial environments were reviewed in the context of sources of carbon, and biogeochemical processes controlling carbon cycling. This review was imperative to subsequent research chapters, where carbon chemistry in 1) the supraglacial environment, 2) glacial runoff, 3) along proglacial continua, and 4) in Lake Hazen, were areas of focus. Spanning globally diverse glacier covered systems, there are many commonalities amongst findings, as well as some differences. Carbon cycling in glacier meltwater impacted freshwater systems may be affected by a

confluence of factors, including variability in a) sources and extent of atmospheric deposition to the supraglacial environment, b) regimes of supraglacial productivity and heterotrophy, c) physical features and thermal regimes of glaciers, d) magnitude and routing of glacier ice meltwaters, e) proglacial water sources, f) local geology and terrestrial ecosystem succession, and f) proglacial meltwater transit times (i.e., residence time). This list is not exhaustive, but highlights many ways in which carbon cycling may vary amongst global glacier systems, and their respective watersheds. Accordingly, while a review of these factors may support inferences of carbon cycling in glacial meltwater impacted systems, research programs where field data are collected are needed to confirm our understanding of these factors, sources of carbon, and biogeochemical processes controlling carbon sources and sinks. This is particularly true for the Canadian high Arctic, which has been understudied despite being extensively covered by glaciers, and highly sensitive to climate change. There is a need to refine our understanding of carbon chemistry, and DOC characterization in glacial meltwater impacted systems of the Canadian high Arctic, for which the heavily glaciated Lake Hazen watershed is an ideal candidate. In addressing these research objectives, we approach the question: how might sources and sinks of carbon be affected by future climate induced changes to glacier ice meltwater fluxes?

In order to address these research questions, water sources to glacial rivers of the Lake Hazen watershed were assessed using stable (δ^2H, $\delta^{18}O$) and radioactive (^3H) water isotopes (Chapter 3). Supraglacial water isotopes were highly similar to those in glacial headwaters, as expected for cold-based glaciers where supraglacial meltwaters are the dominant proglacial water source. Low ^3H concentrations in glacial headwaters suggested that bulk supraglacial meltwaters were primarily comprised of older water released from melting glacier ice, but also from younger water in recent precipitation. This was the first time, to our knowledge, that ^3H was used to interpret water sources in glacial runoff of cold-based glaciers in the Canadian high Arctic. There was interannual separation of stable water isotope data distributions for higher flow (2015) and lower flow (2017) years, for which local water lines plotted below and above the global meteoric water line, respectively. However, spanning the length of glacial rivers, stable water isotopes typically adhered strongly to annual local water lines, suggesting that ground ice thaw water inputs were minimal. This was not surprising given the minimal hydrologic contributions of overland seepage runoff and small streams inflowing to glacial rivers. Downriver increases in ^3H concentrations were a novel and surprising finding, that could not be explained by proglacial inputs of ^3H derived from recent precipitation. There must have been small contributions of more highly concentrated ^3H, such as the 1960s bomb peak ^3H in ground

ice. In fact, higher ^{3}H concentrations in glacial river discharges were found during higher flow (2015) versus lower flow (2017) conditions. High flow likely resulted in the lateral expansion of the hyporheic zone, whereby meltwaters could contact higher surface areas of higher ^{3}H in ground ice corresponding to earlier warm periods in the 1960s, and release this ground ice thaw water to glacial rivers. Therefore, although the hydrologic significance of proglacial water sources to glacial rivers were minimal overall, they were of greater importance during higher flow conditions. The legacy of bomb-peak ^{3}H derived from thawing ground ice was also detected along the length of glacial river transects, and was similarly linked to meltwater flow conditions.

Glacial headwater DOC was ^{14}C-ancient, had a heterogeneous chemical composition, and was derived from a confluence of supraglacial meltwater sources (glacier ice, snow, firn) that coalesced in supraglacial meltwater channels (i.e., streams) (Chapter 3). Polycondensed aromatic 'black carbon' compounds were only sparingly detected in glacial headwaters, but were abundantly present in a snow sample from Gilman Glacier. This is a major finding that highlights not only that atmospheric deposition of anthropogenic aerosols to glacier surfaces was an important source of supraglacial polycondensed aromatic DOC, but also that processes in the supraglacial environment preferentially removed this material. We postulate that dissolved black carbon was either rapidly consumed by supraglacial micro-organisms, or adsorbed to sinking particles (cryoconite), prior to ablation and the flushing of meltwaters to the proglacial environment. Glacial headwaters had low DOC concentrations, and had significant contributions of both larger, humic-like organic molecules, as well as smaller, aliphatic, protein-like material. In several cases, the ^{14}C-ages of DOC in glacial headwaters unexpectedly exceeded maximum ages of soils formed since the last deglaciation (~5 ka BP), indicating that older sources of organic carbon must have been incorporated into the DOC pool. Older (^{14}C-dead) organic may have been derived from glacial till formed prior to the Wisconsin glaciation (< 75 ka BP), or geogenic sedimentary rock from the early Paleozoic to the Cenozoic era. In fact, $\delta^{13}C$-DOC values for glacial headwaters were less negative than expected for soil-derived organic carbon, suggesting that geogenic organic carbon was an unprecedently important component of DOC in glacial till, and/or that $\delta^{13}C$ was altered via long-term microbial processing of aeolian deposition, or autochthonously produced, in the supraglacial environment. These are important considerations when interpreting the chemical composition of DOC in glacial headwaters that are sparingly concentrated in DOC, are primarily comprised of ^{14}C-ancient humic substances, but also have $\delta^{13}C$-DOC that is indicative of limited terrigenous plant-derived organic carbon (> -25 ‰). We find that DOC in glacial runoff of the Lake Hazen watershed was compositionally and isotopically

comparable to that in glacial systems worldwide (among the most ^{14}C-ancient DOC), and that the sources of DOC to glacial runoff proposed above may be widely applicable.

Downriver additions of DOC to glacial rivers were primarily humic-like, unsaturated aromatic organic molecules, that became increasing negative in δ^{13}C-DOC and Δ^{14}C-DOC (Chapter 3). This is an important finding that contradicts a well-established paradigm that pertains to the evolution of DOC along proglacial aquatic continua: namely, that proglacial additions of DOC are comparatively ^{14}C-modern relative to glacier runoff. Although overland seepage sites and small streams were observed to be flowing into Blister River, and were likely apparent in other glacial river watersheds, they could not explain downriver shifts towards even more ^{14}C-ancient DOC. This implied that additions of ^{14}C-ancient DOC became more impactful along glacial river continua than DOC derived from younger soils (< 5.3 ka BP) and ^{14}C-modern vegetation. Furthermore, since δ^{13}C-DOC also became more negative downriver, ancient soil organic carbon (i.e., glacial till < 75 ka BP) must have been the primary source of ^{14}C-dead OC. The mechanism by which this ^{14}C-ancient soil organic carbon entered the DOC pool likely involved the exfiltration of meltwaters through loose riverbed sediment and the laterally expanded hyporheic zone. This process would have been more prevalent during higher meltwater flow conditions, resulting in more negative Δ^{14}C-DOC and higher ^{3}H concentrations. High flow conditions often coincide with higher concentrations of suspended sediment (TSS, PC) in glacial rivers, for which ultra-fine (< 0.45 μm) particles may have also affected DOC quantification and characterization. Ultra-fine particles are an important consideration for researchers studying waters of extremely low DOC concentrations and high suspended sediment loads, with potential ramifications for correctly interpreting sources and sinks of DOC in these unique systems.

Flow-weighted calculations for DOC delivered to Lake Hazen by the seven major glacial rivers predicted in-lake DOC concentrations (~ 0.5 mg C L^{-1}), δ^{13}C-DOC (-25.8 ‰), and Δ^{14}C-DOC (~ -502 ‰, or 5535 yBP) during 2016. This identifies the quantity and isotopic character of DOC mobilized in bulk glacial meltwaters to this high Arctic great lake (Lake Hazen) and captures the character of this previously unsampled input to the nearshore marine environment. DOC concentration was highly similar in Lake Hazen surface waters (centre buoy; ~ 0.4 mg C L^{-1}), but Δ^{14}C-DOC was less negative (~ -415 ‰, or 4247 yBP). This discrepancy is most likely due to mixing of lake waters from previous years (i.e., lake residence time of ~25 years), that had different Δ^{14}C-DOC compared to the flow-weighted year (2016). Alternatively, small non-glacial surface water inputs of comparatively ^{14}C-

modern DOC to Lake Hazen, in-lake autochthonous production, removal of ^{14}C-ancient DOC via mineralization processes (microbial, photochemical), and/or adsorption to sinking particles to the sediment could also have minor effects on DOC within shorter time scales (i.e., during a single melt season). Overall, ^{14}C-ancient DOC in glacial rivers is largely passed downstream to other systems, which may be anticipated for other high Arctic, ultra-oligotrophic freshwater lakes impacted by meltwaters stemming from cold-based glaciers.

The evolution of the carbonate system and DIC along glacial river transects is principally controlled by carbonate mineral weathering reactions, but also the extent of equilibration with atmospheric CO_2 (Chapter 4). Downriver increases in pH, DIC, and solutes are consistent with the release of weathered materials from carbonate minerals. In fact, carbonation reactions of carbonate minerals consume dissolved CO_2, facilitating the drawdown of atmospheric CO_2 to meltwaters, and are supported by the almost ubiquitous undersaturation of CO_2 (and fully saturated O_2) in glacial rivers. Whereas sulphate oxidation coupled to carbonate dissolution (SOC-CD) is a CO_2 source, it could not be entirely discounted as being impactful to DIC. This is based principally on sulphate isotopes (δ^{34}S-SO_4, δ^{18}O-SO_4), that pointed towards pyrite oxidation being the source of SO_4^{2-} to glacial rivers. However, SO_4^{2-} concentrations were low, the sulphate mass fraction (SMF = SO_4^{2-}/ SO_4^{2-} + HCO_3^-) decreased downriver, and the alkalinity to DIC ratio was greater than 1 (Alk: DIC > 1). These indices, in conjunction with undersaturated CO_2 and downriver increases in pH, together suggested that DIC liberated from SOC-CD were minor relative to carbonation reactions of carbonate minerals.

Stable (δ^{13}C) and radiocarbon (Δ^{14}C) isotopes strongly supported the importance of carbonation reactions of carbonate minerals supplying DIC to these glacial rivers (Chapter 4). Increased suspended sediment (TSS, PC), undersaturated CO_2, and isotopically negative δ^{13}C-DIC and Δ^{14}C-DIC were correlated across the dataset. This shows that higher concentrations of fine-grain particle surfaces in suspended sediment were associated with an increased prevalence of carbonate mineral weathering and CO_2 drawdown, and liberation of isotopically negative DIC to meltwaters, the latter of which is a principal and novel finding of this research. These weathering reactions must have taken place in meltwater-particle contact areas, including the riverbed and hyporheic zone, the riverbanks, and suspended sediment in solution, all of which would be enhanced under higher flow conditions. The δ^{13}C-PIC of suspended sediment was unexpectedly found to be more isotopically negative than conventional marine carbonates, suggesting that secondary carbonates were present, and/or that

isotopic exchange during carbonate mineral weathering reactions had affected the δ^{13}C-PIC. This is an original finding for PIC in proglacial meltwaters that provides valuable insight to the role of carbonate weathering reactions in shaping δ^{13}C-PIC and δ^{13}C-DIC. In fact, the δ^{13}C of DIC added along glacial rivers were comparable to the δ^{13}C-PIC of suspended sediment, identifying a linkage between the isotopic character of dissolved and particulate phases. Although kinetic isotopic effects can also be associated with carbonate mineral weathering reactions, similarities between the δ^{13}C-PIC and δ^{13}C-DIC added downriver implied that they were not a major factor in shaping the isotopic character of δ^{13}C-DIC herein. Weathering reactions of ^{14}C-dead PIC with comparatively ^{14}C-modern CO_2 explains the ^{14}C-ancient DIC additions along glacial river transects. The Δ^{14}C-DIC added along 4 glacial river transects ranged from -186 to -353 ‰ (~ 1588 to 3427 yBP), for which differences in the balance between weathering reactions and extent of equilibration with atmospheric CO_2 must have been principal factors controlling this range. Indeed, measured δ^{13}C-DIC were typically more negative than theoretical values calculated assuming equilibrium conditions, which was not surprising based on weathering induced CO_2 drawdown, and the limited chance for the carbonate system to equilibrate with the atmosphere in fast-flowing meltwaters (i.e., transit times of hours). This was most prevalent during high flow conditions (mid-July 2016, 2019), where δ^{13}C-DIC were significantly more negative. However, neither δ^{13}C-DIC nor Δ^{14}C-DIC showed significant downriver changes, indicating that the isotopic character of DIC was typically 'set' in glacial headwaters. This finding is intriguing, and was found almost exclusively amongst glacial river transects during high flow conditions, implying that the overall balance of mineral weathering reactions and atmospheric exchange of CO_2 in supraglacial, ice-marginal, and glacial headwaters, may have been similar to that further into the proglacial environment, despite downriver additions of DIC. This is new and applicable to the balance of biogeochemical processes controlling the isotopic character of DIC in fast flowing meltwaters traversing the proglacial environment.

The balance of carbonation weathering reactions and atmospheric exchange was different in Lake Hazen than in glacial rivers. Flow-weighted calculations for the 2016 dataset revealed that the 7 major glacial river discharges had modest DIC concentrations (~ 663 µM), negative δ^{13}C-DIC (-2.3 ‰) and ^{14}C-ancient DIC (-326 ‰, or 3102 yBP). Fast-flowing turbulent meltwaters of glacial rivers can have high suspended sediment concentrations (TSS, PC), and much of this particulate material sinks towards bottom waters (~250 m) upon being discharged to Lake Hazen. In this fashion, carbonate mineral weathering reactions persist at depth, and become well-mixed with the remainder of the lake during ice-off conditions. Lake Hazen had comparatively higher DIC concentrations (~814

to 897 μM), less negative δ^{13}C-DIC (-0.1 to 0.3 ‰), and Δ^{14}C-DIC (-140 ‰, or 1142 yBP), all of which support an ingress of ^{14}C modern CO_2. However, Lake Hazen remained undersaturated in CO_2 and had ^{14}C-ancient DIC, confirming that in-lake carbonate mineral weathering reactions persisted over long periods of time (i.e., lake residence time). This finding is particularly impactful, given that atmospheric exchange and equilibration of CO_2 could not keep up with long-term carbonate mineral weathering reactions, resulting in a legacy of ^{14}C-ancient DIC in Lake Hazen, and potentially other glacial meltwater impacted aquatic systems of the Canadian high Arctic.

Overall, we find that glacial rivers were not simple pipelines for DOC or DIC in glacial meltwaters, and that different carbon sources and processes controlled their downriver evolution. Downriver additions of DOC primarily originated from ^{14}C-ancient soils (i.e., glacial till), whereas DIC was derived from carbonation weathering reactions of carbonate minerals, but also atmospheric CO_2. Despite this apparent decoupling of DOC and DIC cycling along glacial rivers, the extent of meltwater contact with particulate phases (i.e., POC and PIC) was important in both cases. In fact, higher flow conditions coincided with the observed lateral expansion of the hyporheic zone and higher concentrations of suspended sediment in meltwaters, both of which were avenues for increased release of ^{14}C-ancient material to DOC and DIC pools. This phenomenon was apparent based on more isotopically negative Δ^{14}C-DOC and Δ^{14}C-DIC during higher flow (2016) vs lower flow (2017) years. The legacy of ^{14}C-ancient DOC and DIC in glacial meltwaters were also different upon their discharge to Lake Hazen. DOC was highly similar in Lake Hazen to bulk glacial river discharge, whereas an ingress of ^{14}C-modern atmospheric CO_2 partially compensated for in-lake carbonation mineral weathering reactions and CO_2 drawdown.

The effects of iron concentrations and pH were assessed on measures of DOM fluorescence using excitation emission matrix spectra (EEMS) (Chapter 5). Fluorescence EEMS are commonly used by researchers to quantify and characterize DOM fluorescence in natural waters, so it is important to understand how different chemical conditions can affect these measurements. Fe (II) and Fe (III) titration experiments were found to result in DOM fluorescence loss due to a combination of mechanisms. In the case of Fe (III) titrations, co-precipitation of Fe (oxy) hydroxyl and Fe-DOM complexes rendered significant DOC concentration loss from solution for several samples. The goal of these titrations was to identify the effects of dissolved iron on DOM fluorescence, so only samples with small changes in DOC concentrations (< 15 %) over the course of Fe titrations were considered further. Normalization of DOM fluorescence peaks and PARAFAC components to DOC

concentration was found to be helpful in this context, as it reduced the leverage of small changes in DOC concentration on DOM fluorescence. These incidental findings call attention to how redox conditions of natural waters can implicate the fate of DOM, and its propensity to precipitate out of solution.

For the remaining samples that had relative stable DOC concentrations during Fe titrations, both dissolved Fe (II) and Fe (III) additions were found to result in quenching of fluorescence peaks and PARAFAC components. Preferential fluorescence loss at shorter excitation wavelengths resulted in shifts in DOM fluorescence composition to favour higher C:A and C3:C2 at higher Fe concentrations. A concentration bias also existed, whereby fluorescence peaks and PARAFAC components associated with the highest fluorescence intensities were typically most susceptible to DOM fluorescence loss. Dissolved Fe-DOM complexes likely increased DOM absorption and the inner filtering effect (IFE), causing DOM fluorescence at shorter excitation wavelengths to be 'self-shadowed'. Accordingly, the concentration of dissolved Fe and the initial DOM composition are both important considerations when assessing how DOM fluorescence composition will change across Fe (II) and Fe (III) concentration gradients. However, effects of Fe (II) and Fe (III) were minimal at Fe <0.5 mg L^{-1}, and could likely be suppressed further by applying an IFE correction algorithm.

DOM fluorescence was stable across a broad pH range (~ 5 to 9), and was only impacted in more strongly acidic conditions. For instance, natural water DOM samples started to show fluorescence loss for the pH ~ 4.5 treatment, that became more significant in strongly acidic conditions (pH ~ 3). This may be based on structural changes of DOM in acidic conditions that involve 'coiling' of DOM molecules and 'hiding' fluorescent moieties. Alternatively, protonation of carboxylic fluorophore groups (pKa ~ 2 to 5) would change the electronic environment of DOM, and may have suppressed DOM fluorescence. Changes in DOM fluorescence composition at pH ~ 3 included a shift towards higher C3:C2, C:A, and BIX, as well as lower C2:C1, M:C, and normalized HIX. These findings suggested that the fluorescent peaks and PARAFAC components with the highest fluorescence intensities had the greatest leverage on DOM fluorescence loss in acidic conditions, and affected the fluorescence characteristics of DOM.

6.2 Future implications to carbon cycling in high Arctic environments

Carbon cycling in cold-based glacier ice meltwater impacted freshwater systems may be impacted differently in the short-term and long-term based on the magnitude of meltwater fluxes. In the short-

term, increased glacier ice ablation and intense meltwater pulses will result in the mobilization of high concentrations of suspended sediment along proglacial continua. High flow conditions result in the lateral expansion of the hyporheic zone, enhancing the addition of ^{14}C-ancient carbon to meltwaters from the local geology and soils. High concentrations of fine-grain mineral surfaces will increase the prevalence of carbonation weathering reactions of carbonate minerals, and consequently the drawdown of atmospheric CO_2. Particulate carbon will be transported along proglacial continua by turbulent meltwaters, and into receiving aquatic ecosystems. In the case of the Lake Hazen watershed, high flow conditions will enhance the ability of the lake to behave as a sink for ^{14}C-ancient carbon delivered by glacial rivers.

A much different reality may unveil itself in the long-term, if glacier ice mass loss proceeds to a point where annual meltwater fluxes have significantly declined. In this scenario, fluxes of ^{14}C-ancient carbon along proglacial continua will be greatly reduced, including those in suspended sediment loads. Non-glacial water sources may become more hydrologically important to Lake Hazen, such that comparatively ^{14}C-modern carbon sources will be present in lake waters. In particular, in-lake organic carbon pool will be more reflective of that leached from younger soils formed since the last glaciation (< 5.3 ka BP). Warmer temperatures and terrestrial ecosystem succession may also result in higher rates of in-lake organic carbon mineralization (microbial, photochemical), as well as autochthonous production. Furthermore, decreased hydrologic input of meltwaters will suppress carbonate mineral weathering reactions, such that Lake Hazen may no longer act as a significant sink for atmospheric CO_2. Inevitably, changes in meltwater flow conditions will impact the processes governing carbon cycling in glacial rivers, and receiving freshwater systems.

The implications of these projected changes are far-reaching. Most prominently, changes in glacier ice meltwater flux regimes will affect carbon cycling, and sources and sinks of carbon in high Arctic freshwater systems. Year-over-year increases in anthropogenic GHG emissions makes it imperative to understand how natural systems are responding to climate change, and their feedback to the global carbon cycle. Impacts to high Arctic freshwaters systems could include changes in thermal regimes of the water column, the balance between primary productivity and heterotrophy, biodiversity, nutrient availability, and fate of contaminants. Biogeochemistries of high Arctic freshwaters will be reflected in their discharges to coastal margins, and circulation in the Arctic Ocean.

6.3 Future Research Directions

Major findings of this thesis have identified new research questions, and set the stage for future studies pertaining to carbon cycling in high Arctic glacier covered systems. For instance, the few opportunistic supraglacial samples sparked several new questions, including **1)** are polycondensed aromatic 'black carbon' molecules processed by microbes in supraglacial snow, or do they adsorb to sinking particles in meltwaters and fall out of solution (i.e., to cryoconite), **2)** what are the mechanisms of release of the aeolian deposition of particulate carbon to dissolved organic and inorganic carbon pools in the supraglacial environment, **3)** can we further distinguish between proportions of autochthonous and extensively degraded terrigenous organic carbon at such low DOC concentrations, **4)** is the quantity and composition of Gilman Glacier supraglacial organic carbon similar to that of other (i.e., smaller) glaciers of the Lake Hazen watershed, **5)** what is the extent of CO_2 drawdown by carbonation weathering reactions of carbonate minerals in supraglacial meltwaters, **6)** are $\delta^{13}C$ and $\Delta^{14}C$ of supraglacial meltwaters the same as their respective glacial headwaters, and **7)** at what depth are the bomb-peak ^{3}H in glacier ice of the Lake Hazen watershed? Given the logistical challenges of collecting large volumes of supraglacial ice, snow, and meltwater, it will be challenging to achieve spatial and temporal resolution among these samples for glacier surfaces in the Canadian high Arctic. However, there are a couple questions above that are of particular pertinence to expanding on findings of this thesis, and are also realistic from a scientific perspective. Firstly, sampling glacier snow, an adjacent supraglacial meltwater channel, and cryoconite for polycondensed aromatic molecules could help resolve the fate of anthropogenic black carbon in the supraglacial environment. Secondly, conducting incubation experiments wherein cryoconite was added to a filtered supraglacial meltwater sample could provide insight to mechanisms controlling the release of particulate carbon to the dissolved phase. Thirdly, and perhaps most relevant to this thesis, would be collecting $\delta^{13}C$ and $\Delta^{14}C$ of dissolved organic and inorganic carbon in supraglacial meltwaters to compare with glacial headwaters. This would be key to determining whether sources and processes that shaped the isotopic character of carbon along proglacial continua were common to the supraglacial environment as well.

The proglacial environment was explored in our study, and several directions remain for future research projects. These ideas include **1)** obtaining modelled runoff data for remaining sampling years (2017 to 2019) and comparing mass balanced results for high and low flow conditions, **2)** studying the temporality in glacial runoff (i.e., month of semi-regular sampling) of $\delta^{13}C$, $\Delta^{14}C$, and flow

measurements, for a major glacier (i.e., Henrietta-Nesmith Glacier, or Gilman Glacier), **3)** measure additional glacial river transects for $\delta^{13}C$ and $\Delta^{14}C$ to improve resolution of downriver isotopic changes, **4)** measure $\delta^{13}C$, and $\Delta^{14}C$ for sediment-meltwater incubation experiments, **5)** measure ^{3}H, $\delta^{13}C$, and $\Delta^{14}C$ in a vertical soil profile of thaw waters (or leachate) spanning from the active layer to the permafrost, **6)** add sampling resolution to Lake Hazen centre buoy vertical profile for ^{3}H, $\delta^{13}C$, and $\Delta^{14}C$, **7)** refine mass balance results by measuring $\delta^{13}C$ and $\Delta^{14}C$ for the non-glacial Salor Creek inflow to Lake Hazen, **8)** expand scope of study to include C exported to coastal margins (i.e., Ruggles River). Many of these points are accessible by analyzing additional water samples for ^{3}H, $\delta^{13}C$, and $\Delta^{14}C$ that were collected during previous field seasons, and coupling with modelled flow measurements. Indeed, meltwater flow conditions are a principal vector impacting carbon sources along proglacial continua in a changing climate, so a critical next step of future research will be to add modelled flow data to our interpretation of carbon chemistry along glacial river transects, and in Lake Hazen. Meltwater flow intensity can ramp-up rapidly during the melt season, and it would be valuable to better understand the temporality of $\delta^{13}C$ and $\Delta^{14}C$ in glacial headwaters. Furthermore, is the temporality in $\delta^{13}C$ and $\Delta^{14}C$ glacial headwaters more significant than downriver changes, or lack thereof, along glacial river transects? With respect to carbon sources in the proglacial environment, future research could take a closer look at leachate from a local soil profile. However, since soils rarely retain well-defined layers in heavily eroded glacial till along river banks, the river sediment would likely be more important in this context. For instance, incubation experiments of sediment-meltwater samples could be conducted to identify changes in $\delta^{13}C$ and $\Delta^{14}C$ from microbial processing of particulate organic carbon, or from the persistence of weathering reactions over time in a closed system. The fate of $\delta^{13}C$ and $\Delta^{14}C$ in Lake Hazen was a key component of this thesis, and could be expanded upon in future work. For instance, adding $\delta^{13}C$ and $\Delta^{14}C$ of small non-glacial inputs, precipitation, or perhaps even in-lake carbon production and processing to mass balance calculations could help account for differences in carbon isotopes between bulk glacial river discharges and lake water. Finally, adding $\delta^{13}C$ and $\Delta^{14}C$ characterization to the Ruggles River, the solitary discharge from Lake Hazen, could be valuable to determine the legacy of ^{14}C-ancient organic and inorganic carbon exported to coastal margins.

References

1. Allègre, C. J., Manhès, G. & Göpel, C. The age of the Earth. *Geochim. Cosmochim. Acta* **59**, 1445–1456 (1995).
2. Crowley, T. J. Causes of climate change over the past 1000 years. *Science* **289**, 270–277 (2000).
3. Bauer, E., Claussen, M., Brovkin, V. & Huenerbein, A. Assessing climate forcings of the Earth system for the past millennium. *Geophys. Res. Lett.* **30**, 1–4 (2003).
4. Jungclaus, J. H. *et al.* Climate and carbon-cycle variability over the last millennium. *Clim. Past* **6**, 723–737 (2010).
5. Joos, F. & Spahni, R. Rates of change in natural and anthropogenic radiative forcing over the past 20,000 years. *Proc. Natl. Acad. Sci. U. S. A.* **105**, 1425–1430 (2008).
6. Tanaka, K., O'Neill, B. C., Rokityanskiy, D., Obersteiner, M. & Tol, R. S. J. Evaluating global warming potentials with historical temperature. *Climatic Change* **96**, 443–466 (2009).
7. Meinshausen, M. *et al.* Historical greenhouse gas concentrations for climate modelling (CMIP6). *Geosci. Model Dev.* **10**, 2057–2116 (2017).
8. New, M., Liverman, D., Schroder, H. & Anderson, K. Four degrees and beyond: The potential for a global temperature increase of four degrees and its implications. *Philos. Trans. R. Soc. A Math. Phys. Eng. Sci.* **369**, 9–19 (2011).
9. Peters, G. P. *et al.* The challenge to keep global warming below 2C. *Nat. Clim. Chang.* **3**, 4–6 (2013).
10. Schleussner, C. F. *et al.* Differential climate impacts for policy-relevant limits to global warming: The case of 1.5°C and 2°C. *Earth Syst. Dyn.* **7**, 327–351 (2016).
11. Stocker, T. F. *et al. IPCC, 2013: Climate Change 2013: The Physical Science Basis, contribution of Working Group I to the Fifth Assessment Report of the Intergovernmental Panel on Climate Change*. *Contribution of Working Group I to the Fifth Assessment Report of the Intergovernmental Panel on Climate Change* (2013) doi:10.1017/CBO9781107415324.
12. Karim, M. F. & Mimura, N. Impacts of climate change and sea-level rise on cyclonic storm surge floods in Bangladesh. *Glob. Environ. Chang.* **18**, 490–500 (2008).
13. Hallegatte, S. *et al.* Assessing climate change impacts, sea level rise and storm surge risk in port cities: A case study on Copenhagen. *Climatic Change* **104**, 113–137 (2011).
14. Bosello, F., Nicholls, R. J., Richards, J., Roson, R. & Tol, R. S. J. Economic impacts of climate change in Europe: Sea-level rise. *Climatic Change* **112**, 63–81 (2012).
15. Scott, D., Simpson, M. C. & Sim, R. The vulnerability of Caribbean coastal tourism to scenarios of climate change related sea level rise. *J. Sustain. Tour.* **20**, 883–898 (2012).
16. Galbraith, H. *et al.* Global climate change and sea level rise: Potential losses of intertidal habitat for shorebirds. *Waterbirds* **25**, 173–183 (2002).
17. Courchamp, F., Hoffmann, B. D., Russell, J. C., Leclerc, C. & Bellard, C. Climate change, sea-level rise, and conservation: Keeping island biodiversity afloat. *Trends Ecol. Evol.* **29**, 127–130 (2014).
18. Ellison, J. C. Vulnerability assessment of mangroves to climate change and sea-level rise impacts. *Wetl. Ecol. Manag.* **23**, 115–137 (2015).
19. Osland, M. J. *et al.* Beyond just sea-level rise: Considering macroclimatic drivers within coastal wetland vulnerability assessments to climate change. *Glob. Chang. Biol.* **22**, 1–11 (2016).
20. Rosenzweig, C., Iglesias, A., Yang, X. B., Epstein, P. R. & Chivian, E. Implications for food production, plant diseases, and pests. *Glob. Chang. Hum. Heal.* **2**, 90–104 (2001).

21. Stott, P. How climate change affects extreme weather events. *Science* **352**, 1517–1518 (2016).

22. Breshears, D. D. *et al.* Regional vegetation die-off in response to global-change-type drought. *Proc. Natl. Acad. Sci. U. S. A.* **102**, 15144–15148 (2005).

23. Veijalainen, N., Lotsari, E., Alho, P., Vehviläinen, B. & Käyhkö, J. National scale assessment of climate change impacts on flooding in Finland. *J. Hydrol.* **391**, 333–350 (2010).

24. Armah, F. A. *et al.* Food security and climate change in drought-sensitive savanna zones of Ghana. *Mitig. Adapt. Strateg. Glob. Chang.* **16**, 291–306 (2011).

25. Dettinger, M. Climate change, atmospheric rivers, and floods in California - a multimodel analysis of storm frequency and magnitude changes. *J. Am. Water Resour. Assoc.* **47**, 514–523 (2011).

26. Huong, H. T. L. & Pathirana, A. Urbanization and climate change impacts on future urban flooding in Can Tho city, Vietnam. *Hydrol. Earth Syst. Sci.* **17**, 379–394 (2013).

27. Easterling, D. R. Recent changes in frost days and the frost-free season in the United States. *Bull. Am. Meteorol. Soc.* **83**, 1327–1332 (2002).

28. Cutforth, H., O'Brien, E. G., Tuchelt, J. & Rickwood, R. Long-term changes in the frost-free season on the Canadian prairies. *Can. J. Plant Sci.* **84**, 1085–1091 (2004).

29. Christiansen, D. E., Markstrom, S. L. & Hay, L. E. Impacts of climate change on the growing season in the United States. *Earth Interact.* **15**, 1–17 (2011).

30. Reyes-Fox, M. *et al.* Elevated CO2 further lengthens growing season under warming conditions. *Nature* **510**, 259–262 (2014).

31. Smit, B. & Skinner, M. W. Adaptation options in agriculture to climate change: A typology. *Mitig. Adapt. Strateg. Glob. Chang.* **7**, 85–114 (2002).

32. Smith, P. & Olesen, J. E. Synergies between the mitigation of, and adaptation to, climate change in agriculture. *J. Agric. Sci.* **148**, 543–552 (2010).

33. Walthall, C. L. *et al.* Climate Change and Agriculture in the United States: Effects and Adaptation. *USDA Tech. Bull. 1935* i–186 (2013) doi:10.1017/CBO9781107415324.004.

34. Lovejoy, T. Lovejoy 2008 Climate change and biodiversity. **27**, 1–8 (2008).

35. Nunez, S., Arets, E., Alkemade, R., Verwer, C. & Leemans, R. Assessing the impacts of climate change on biodiversity: is below 2 °C enough? *Climatic Change* **154**, 351–365 (2019).

36. Hellmann, J. J., Byers, J. E., Bierwagen, B. G. & Dukes, J. S. Five potential consequences of climate change for invasive species. *Conserv. Biol.* **22**, 534–543 (2008).

37. Mainka, S. A. & Howard, G. W. Climate change and invasive species: Double jeopardy. *Integr. Zool.* **5**, 102–111 (2010).

38. Crutzen, P. J. *Earth System Science in the Anthropocene*. *The Anthropocene* (2006). doi:https://doi.org/10.1007/3-540-26590-2_3.

39. Steffen, W., Grinevald, J., Crutzen, P. & Mcneill, J. The anthropocene: Conceptual and historical perspectives. *Philos. Trans. R. Soc. A Math. Phys. Eng. Sci.* **369**, 842–867 (2011).

40. Ruddiman, W. F. The anthropocene. *Annu. Rev. Earth Planet. Sci.* **41**, 45–68 (2013).

41. Lewis, S. L. & Maslin, M. A. Defining the Anthropocene. *Nature* **519**, 171–180 (2015).

42. Polyakov, I. V. *et al.* Observationally based assessment of polar amplification of global warming. *Geophys. Res. Lett.* **29**, 3–6 (2002).

43. Holland, M. M. & Bitz, C. M. Polar amplification of climate change in coupled models. *Clim. Dyn.* **21**,

221–232 (2003).

44. Serreze, M. C. & Francis, J. A. The arctic amplification debate. *Climatic Change* **76**, 241–264 (2006).

45. Serreze, M. C. & Barry, R. G. Processes and impacts of Arctic amplification: A research synthesis. *Glob. Planet. Change* **77**, 85–96 (2011).

46. Vavrus, S. The influence of Arctic amplification on mid-latitude weather and climate. *Curr. Clim. Chang. Reports* **9**, 238–249 (2018).

47. Cohen, J. *et al.* Divergent consensuses on Arctic amplification influence on midlatitude severe winter weather. *Nat. Clim. Chang.* **10**, 20–29 (2020).

48. Kwok, R. Near zero replenishment of the Arctic multiyear sea ice cover at the end of 2005 summer. *Geophys. Res. Lett.* **34**, 1–6 (2007).

49. Maslanik, J. A. *et al.* A younger, thinner Arctic ice cover: Increased potential for rapid, extensive sea-ice loss. *Geophys. Res. Lett.* **34**, 2004–2008 (2007).

50. Kurtz, N. T. & Farrell, S. L. Large-scale surveys of snow depth on Arctic sea ice from Operation IceBridge. *Geophys. Res. Lett.* **38**, 1–5 (2011).

51. Webster, M. A. *et al.* Interdecadal changes in snow depth on Arctic sea ice. 5395–5406 (2014) doi:10.1002/2014JC009985.

52. Stroeve, J., Holland, M. M., Meier, W., Scambos, T. & Serreze, M. Arctic sea ice decline: Faster than forecast. *Geophys. Res. Lett.* **34**, 1–5 (2007).

53. Polyakov, I. V., Walsh, J. E. & Kwok, R. Recent changes of Arctic multiyear sea ice coverage and the likely causes. *Bull. Am. Meteorol. Soc.* **93**, 145–151 (2012).

54. Stroeve, J. C. *et al.* The Arctic's rapidly shrinking sea ice cover: A research synthesis. *Climatic Change* **110**, 1005–1027 (2012).

55. Shu, Q. *et al.* Assessment of Sea Ice Extent in CMIP6 With Comparison to Observations and CMIP5. *Geophys. Res. Lett.* **47**, 1–9 (2020).

56. Overland, J. E. & Wang, M. Large-scale atmospheric circulation changes are associated with the recent loss of Arctic sea ice. *Tellus, Ser. A Dyn. Meteorol. Oceanogr.* **62**, 1–9 (2010).

57. Vihma, T. *Effects of Arctic Sea Ice Decline on Weather and Climate: A Review*. *Surveys in Geophysics* vol. 35 (2014).

58. Arrigo, K. R., van Dijken, G. & Pabi, S. Impact of a shrinking Arctic ice cover on marine primary production. *Geophys. Res. Lett.* **35**, 1–6 (2008).

59. Heginbottom, J. A. Permafrost mapping: A review. *Prog. Phys. Geogr.* **26**, 623–642 (2002).

60. Jorgenson, T. *et al.* Permafrost Characteristics of Alaska. *Holocene* 500–500 (2008).

61. Throop, J., Lewkowicz, A. G. & Smith, S. L. Climate and ground temperature relations at sites across the continuous and discontinuous permafrost zones, northern Canada. *Can. J. Earth Sci.* **49**, 865–876 (2012).

62. Kokelj, S. V. & Jorgenson, M. T. Advances in thermokarst research. *Permafr. Periglac. Process.* **24**, 108–119 (2013).

63. Liljedahl, A. K. *et al.* Pan-Arctic ice-wedge degradation in warming permafrost and its influence on tundra hydrology. *Nat. Geosci.* **9**, 312–318 (2016).

64. O'Donnell, J. A., Aiken, G. R., Walvoord, M. A. & Butler, K. D. Dissolved organic matter composition of winter flow in the Yukon River basin: Implications of permafrost thaw and increased groundwater discharge. *Global Biogeochem. Cy.* **26**, 1–18 (2012).

65. Walvoord, M. A. & Kurylyk, B. L. Hydrologic Impacts of Thawing Permafrost-A Review. *Vadose Zone J.* **15**, vzj2016.01.0010 (2016).

66. Natali, S. M. *et al.* Permafrost thaw and soil moisture driving CO2 and CH4 release from upland tundra. *J. Geophys. Res. Biogeosciences* **120**, 525–537 (2015).

67. Mu, C. C. *et al.* Permafrost collapse shifts alpine tundra to a carbon source but reduces N2O and CH4 release on the northern Qinghai-Tibetan Plateau. *Geophys. Res. Lett.* **44**, 8945–8952 (2017).

68. Voigt, C. *et al.* Ecosystem carbon response of an Arctic peatland to simulated permafrost thaw. *Glob. Chang. Biol.* **25**, 1746–1764 (2019).

69. Frey, K. E. & McClelland, J. W. Impacts of permafrost degradation on arctic river biogeochemistry. *Hydrol. Process.* **23**, 169–182 (2009).

70. Loiko, S. V. *et al.* Abrupt permafrost collapse enhances organic carbon, CO2, nutrient and metal release into surface waters. *Chem. Geol.* **471**, 153–165 (2017).

71. IPCC. *Special Report on the Ocean and Cryosophere in a Changing Climate*. (2019).

72. Marzeion, B., Cogley, J. G., Richter, K. & Parkes, D. Glaciers. Attribution of global glacier mass loss to anthropogenic and natural causes. *Science* **345**, 919–921 (2014).

73. Zemp, M. *et al.* Historically unprecedented global glacier decline in the early 21st century. *J. Glaciol.* **61**, 745–762 (2015).

74. Gardner, A. S. *et al.* Sharply increased mass loss from glaciers and ice caps in the Canadian Arctic Archipelago. *Nature* **473**, 357–360 (2011).

75. Sasgen, I. *et al.* Timing and origin of recent regional ice-mass loss in Greenland. *Earth Planet. Sci. Lett.* **333**–**334**, 293–303 (2012).

76. Harig, C. & Simons, F. J. Ice mass loss in Greenland, the Gulf of Alaska, and the Canadian Archipelago: Seasonal cycles and decadal trends. *Geophys. Res. Lett.* **43**, 3150–3159 (2016).

77. Radić, V. *et al.* Regional and global projections of twenty-first century glacier mass changes in response to climate scenarios from global climate models. *Clim. Dyn.* **42**, 37–58 (2014).

78. Shannon, S. *et al.* Global glacier volume projections under high-end climate change scenarios. *Cryosphere* **13**, 325–350 (2019).

79. Marzeion, B., Kaser, G., Maussion, F. & Champollion, N. Limited influence of climate change mitigation on short-term glacier mass loss. *Nat. Clim. Chang.* **8**, 1–4 (2018).

80. Meier, M. F. *et al.* Glaciers dominate eustatic sea-level rise in the 21st century. *Science* **317**, 1064–1067 (2007).

81. Jacob, T., Wahr, J., Pfeffer, W. T. & Swenson, S. Recent contributions of glaciers and ice caps to sea level rise. *Nature* **482**, 514–518 (2012).

82. Radić, V. & Hock, R. Glaciers in the Earth's Hydrological Cycle: Assessments of Glacier Mass and Runoff Changes on Global and Regional Scales. *Surv. Geophys.* **35**, 813–837 (2014).

83. Jansson, P., Hock, R. & Schneider, T. The concept of glacier storage: A review. *J. Hydrol.* **282**, 116–129 (2003).

84. Huss, M. & Hock, R. Global-scale hydrological response to future glacier mass loss. *Nat. Clim. Chang.* **8**, 135–140 (2018).

85. Smith, I. R. Late Quaternary glacial history of Lake Hazen Basin and eastern Hazen Plateau, northern Ellesmere Island, Nunavut, Canada. *Can. J. Earth Sci.* **36**, 1547–1565 (1999).

86. Thompson, B. Climate. in *Parks Canada. Resource Description and Analysis - Ellesmere Island*

National Park Reserve. Natural Resource Conservation Section, Prairie and Northern Region, Parks Canada, Department of Canadian Heritage. 5.1-5.78 (1994).

87. Babaluk, J. A., Heuring, L. G., Reist, J. D. & Billeck, B. N. *Selected chemical analyses of water from lakes in Ellesmere Island National Park Reserve, Nunavut*. *Canadian Data Report of Fisheries and Aquatic Sciences 1050: iv* (1999).

88. France, R. L. The Lake Hazen Trough: A late winter oasis in a polar desert. *Biol. Conserv.* **63**, 149–151 (1993).

89. Lehnherr, I. *et al.* The world's largest High Arctic lake responds rapidly to climate warming. *Nat. Commun.* **9**, 1–9 (2018).

90. Köck, G. *et al.* Bathymetry and sediment geochemistry of Lake Hazen (Quttinirpaaq National Park, Ellesmere Island, Nunavut). *Arct. Inst. North Am.* **65**, 56–66 (2012).

91. St. Pierre, K. A. *et al.* Contemporary limnology of the rapidly changing glacierized watershed of the world's largest High Arctic lake. *Sci. Rep.* **9**, 1–15 (2019).

92. Keatley, B. E., Douglas, M. S. V & Smol, J. P. Limnological Characteristics of a High Arctic Oasis and Comparisons across Northern Ellesmere Island. **60**, 294–308 (2007).

93. Babaluk, J. A. *et al. Chemical Analyses of Water from Lakes and Streams in Quttinirpaaq National Park, Nunavut, 2001-2008*. (2009).

94. Cavaco, M. A. *et al.* Freshwater microbial community diversity in a rapidly changing High Arctic watershed. *FEMS Microbiol. Ecol.* **95**, 1–13 (2019).

95. St Pierre, K. A. *et al.* Proglacial freshwaters are significant and previously unrecognized sinks of atmospheric CO<inf>2</inf>. *Proc. Natl. Acad. Sci. U. S. A.* **116**, (2019).

96. Mead, J. The Control of Fe and pH on the Photodegradation and Characterization of Dissolved Organic Matter in Small, Oligotrophic Canadian Shield Freshwaters. (University of Waterloo, 2017).

97. Olivier, J. G. J. & Peters, J. A. H. W. *Trends in Global CO2 and Total Greenhouse Gas Emissions: Report 2019*. *PBL Netherlands Environmental Assessment Agency 5* (2017).

98. Tokarska, K. B., Gillett, N. P., Weaver, A. J., Arora, V. K. & Eby, M. The climate response to five trillion tonnes of carbon. *Nat. Clim. Chang.* **6**, 851–855 (2016).

99. Le Quéré, C. *et al.* Global Carbon Budget 2016. *Earth Syst. Sci. Data* **8**, 605–649 (2016).

100. National Oceanic and Atmospheric Administration.

101. Le Quéré, C., Takahashi, T., Buitenhuis, E. T., Rödenbeck, C. & Sutherland, S. C. Impact of climate change and variability on the global oceanic sink of CO2. *Global Biogeochem. Cy.* **24**, 1–10 (2010).

102. Kurihara, H. Effects of CO2-driven ocean acidification on the early developmental stages of invertebrates. *Mar. Ecol. Prog. Ser.* **373**, 275–284 (2008).

103. Doney, S. C., Fabry, V. J., Feely, R. A. & Kleypas, J. A. Ocean acidification: The other CO2 problem. *Ann. Rev. Mar. Sci.* **1**, 169–192 (2009).

104. Ries, J. B., Cohen, A. L. & McCorkle, D. C. Marine calcifiers exhibit mixed responses to CO2-induced ocean acidification. *Geology* **37**, 1131–1134 (2009).

105. Gullison, R. E. *et al.* Tropical forests and climate policy. *Science* **316**, 985–986 (2007).

106. Houghton, R. A. & Nassikas, A. A. Global and regional fluxes of carbon from land use and land cover change 1850–2015. *Global Biogeochem. Cy.* **31**, 456–472 (2017).

107. Stumm, W. & Morgan, J. J. *Aquatic chemistry: chemical equilibria and rates in natural waters*. (Wiley, 1996).

108. Drever, J. I. *The geochemistry of natural waters: surface and groundwater environments*. (Prentice Hall, 1997).

109. Tranter, M., Brown, G., Raiswell, R., Sharp, M. & Gurnell, A. A conceptual model of solute acquisition by Alpine glacial meltwaters. *J. Glaciol.* **39**, 573–581 (1993).

110. Tranter, M. *et al.* Geochemical weathering at the bed of Haut glacier d'Arolla, Switzerland - A new model. *Hydrol. Process.* **16**, 959–993 (2002).

111. Clark, I. D. & Fritz, P. *Environmental isotopes in hydrogeology.* (CRC press, 1997).

112. O'Leary, M. H., Madhavan, S. & Paneth, P. Physical and chemical basis of carbon isotope fractionation in plants. *Plant. Cell Environ.* **15**, 1099–1104 (1992).

113. Stuiver, M. & Polach, H. A. Reporting of 14C data. *Radiocarbon* **19**, 355–363 (1977).

114. Stuiver, M. International Agreements and the use of the new Oxalic Acid Standard. *Radiocarbon* **25**, 793–795 (1983).

115. Reimer, P. J. *et al.* Discussion: Reporting and calibration of post-bomb 14C data. *Radiocarbon* **46**, 1299–1304 (2004).

116. Stenström, K. E., Skog, G., Georgiadou, E., Genberg, J. & Johansson, A. *A guide to radiocarbon units and calculations*. *Lund University, Department of Physics internal report* (2011).

117. Nebbioso, A. & Piccolo, A. Molecular characterization of dissolved organic matter (DOM): A critical review. *Anal. Bioanal. Chem.* **405**, 109–124 (2013).

118. Repeta, D. J. *Chemical characterization and cycling of dissolved organic matter. In Biogeochemistry of marine dissolved organic matter. Academic Press* (2015). doi:10.1016/B978-0-12-405940-5.00002-9.

119. Jobbagy, E. G. & Jackson, R. B. The Vertical Distribution of Soil Organic Carbon and Its Relation to Climate and Vegetation. *Ecol. Appl.* **10**, 423 (2000).

120. Aitkenhead, J. A., Hope, D. & Billett, M. F. The relationship between dissolved organic carbon in stream water and soil organic carbon pools at different spatial scales. *Hydrol. Process.* **13**, 1289–1302 (1999).

121. Neff, J. C. & Asner, G. P. Dissolved organic carbon in terrestrial ecosystems: Synthesis and a model. *Ecosystems* **4**, 29–48 (2001).

122. Biddanda, B. A. & Cotner, J. B. Love handles in aquatic ecosystems: The role of dissolved organic carbon drawdown, resuspended sediments, and terrigenous inputs in the carbon balance of Lake Michigan. *Ecosystems* **5**, 431–445 (2002).

123. Von Wachenfeldt, E. & Tranvik, L. J. Sedimentation in boreal lakes - The role of flocculation of allochthonous dissolved organic matter in the water column. *Ecosystems* **11**, 803–814 (2008).

124. Spencer, R. G. M. *et al.* Photochemical degradation of dissolved organic matter and dissolved lignin phenols from the Congo River. *J. Geophys. Res. Biogeosciences* **114**, 1–12 (2009).

125. Benner, R. & Kaiser, K. Biological and photochemical transformations of amino acids and lignin phenols in riverine dissolved organic matter. *Biogeochemistry* **102**, 209–222 (2011).

126. Hansen, A. M. *et al.* Optical properties of dissolved organic matter (DOM): Effects of biological and photolytic degradation. *Limnol. Oceanogr.* **61**, 1015–1032 (2016).

127. Cory, R. M. & Kling, G. W. Interactions between sunlight and microorganisms influence dissolved organic matter degradation along the aquatic continuum. *Limnol. Oceanogr. Lett.* **3**, 102–116 (2018).

128. Kellerman, A. M., Dittmar, T., Kothawala, D. N. & Tranvik, L. J. Chemodiversity of dissolved organic matter in lakes driven by climate and hydrology. *Nat. Commun.* **5**, 1–8 (2014).

129. Kellerman, A. M. *et al.* Unifying Concepts Linking Dissolved Organic Matter Composition to Persistence in Aquatic Ecosystems. *Environ. Sci. Technol.* **52**, 2538–2548 (2018).

130. Massicotte, P., Asmala, E., Stedmon, C. & Markager, S. Global distribution of dissolved organic matter along the aquatic continuum: Across rivers, lakes and oceans. *Sci. Total Environ.* **609**, 180–191 (2017).

131. Coble, A. A., Koenig, L. E., Potter, J. D., Parham, L. M. & McDowell, W. H. Homogenization of dissolved organic matter within a river network occurs in the smallest headwaters. *Biogeochemistry* **143**, 85–104 (2019).

132. Roebuck, J. A., Seidel, M., Dittmar, T. & Jaffé, R. Controls of Land Use and the River Continuum Concept on Dissolved Organic Matter Composition in an Anthropogenically Disturbed Subtropical Watershed. *Environ. Sci. Technol.* (2020) doi:10.1021/acs.est.9b04605.

133. Kothawala, D. N. *et al.* The relative influence of land cover, hydrology, and in-stream processing on the composition of dissolved organic matter in boreal streams. *J. Geophys. Res. G Biogeosciences* **120**, 1491–1505 (2015).

134. Casas-Ruiz, J. *et al. Delineating the continuum of dissolved organic matter in temperate river networks*. *Global Biogeochemical Cycles* (2020). doi:10.1029/2019GB006495.

135. Dahlen, J., Bertilsson, S. & Pettersson, C. Effects of UV-A irradiation on dissolved organic matter in humic surface waters. *Environ. Int.* **22**, 501–506 (1996).

136. Helms, J. R. *et al.* Absorption spectral slopes and slope ratios as indicators of molecular weight, source, and photobleaching of chromophoric dissolved organic matter. *Limnol. Oceanogr.* **53**, 955–969 (2008).

137. Weishaar, J. L. *et al.* Evaluation of specific ultraviolet absorbance as an indicator of the chemical composition and reactivity of dissolved organic carbon. *Environ. Sci. Technol.* **37**, 4702–4708 (2003).

138. Li, P. & Hur, J. Utilization of UV-Vis spectroscopy and related data analyses for dissolved organic matter (DOM) studies: A review. *Crit. Rev. Environ. Sci. Technol.* **47**, 131–154 (2017).

139. Coble, P. Coble - 1996.pdf. *Marine Chemistry* vol. 51 325–346 (1996).

140. Baker, A., Bolton, L., Newson, M. & Spencer, R. G. M. Spectrophotometric properties of surface water dissolved organic matter in an afforested upland peat catchment. *Hydrol. Process.* **22**, 2325–2336 (2008).

141. Zsolnay, A., Baigar, E., Jimenez, M., Steinweg, B. & Saccomandi, F. Differentiating with fluorescence spectroscopy the sources of dissolved organic matter in soils subjected to drying. *Chemosphere* **38**, 45–50 (1999).

142. Ohno, T. Fluorescence inner-filtering correction for determining the humification index of dissolved organic matter. *Environ. Sci. Technol.* **36**, 742–746 (2002).

143. Huguet, A. *et al.* Properties of fluorescent dissolved organic matter in the Gironde Estuary. *Org. Geochem.* **40**, 706–719 (2009).

144. Stedmon, C. A., Markager, S. & Bro, R. Tracing dissolved organic matter in aquatic environments using a new approach to fluorescence spectroscopy. *Mar. Chem.* **82**, 239–254 (2003).

145. Stedmon, C. A. & Bro, R. Characterizing dissolved organic matter fluorescence with parallel factor analysis: A tutorial. *Limnol. Oceanogr. Methods* **6**, 572–579 (2008).

146. Murphy, K. R., Stedmon, C. A., Graeber, D. & Bro, R. Fluorescence spectroscopy and multi-way techniques. PARAFAC. *Anal. Methods* **5**, 6557–6566 (2013).

147. Kennedy, M. D., Chun, H. K., Quintanilla Yangali, V. A., Heijman, B. G. J. & Schippers, J. C. Natural organic matter (NOM) fouling of ultrafiltration membranes: Fractionation of NOM in surface water and characterisation by LC-OCD. *Desalination* **178**, 73–83 (2005).

148. Lankes, U., Müller, M. B., Weber, M. & Frimmel, F. H. Reconsidering the quantitative analysis of organic carbon concentrations in size exclusion chromatography. *Water Res.* **43**, 915–924 (2009).

149. Huber, S. A., Balz, A., Abert, M. & Pronk, W. Characterisation of aquatic humic and non-humic matter with size-exclusion chromatography - organic carbon detection - organic nitrogen detection (LC-OCD-OND). *Water Res.* **45**, 879–885 (2011).

150. Aukes, P. Use of Liquid Chromatography – Organic Carbon Detection to Characterize Dissolved Organic Matter from a Variety of Environments by. (2012).

151. Marshall, A. G., Hendrickson, C. L. & Jackson, G. S. Fourier transform ion cyclotron resonance mass spectrometry: A primer. *Mass Spectrom. Rev.* **17**, 1–35 (1998).

152. Kim, S., Kramer, R. W. & Hatcher, P. G. Graphical Method for Analysis of Ultrahigh-Resolution Broadband Mass Spectra of Natural Organic Matter, the Van Krevelen Diagram. *Anal. Chem.* **75**, 5336–5344 (2003).

153. Gonsior, M. *et al.* Photochemically induced changes in dissolved organic matter identified by ultrahigh resolution fourier transform ion cyclotron resonance mass spectrometry. *Environ. Sci. Technol.* **43**, 698–703 (2009).

154. Sleighter, R. L., Cory, R. M., Kaplan, L. A., Abdulla, H. A. N. & Hatcher, P. G. A coupled geochemical and biogeochemical approach to characterize the bioreactivity of dissolved organic matter from a headwater stream. *J. Geophys. Res. G Biogeosciences* **119**, 1520–1537 (2014).

155. Hutchins, R. H. S. *et al.* The Optical, Chemical, and Molecular Dissolved Organic Matter Succession Along a Boreal Soil-Stream-River Continuum. *J. Geophys. Res. Biogeosciences* **122**, 2892–2908 (2017).

156. Niu, X. Z., Harir, M., Schmitt-Kopplin, P. & Croué, J. P. Characterisation of dissolved organic matter using Fourier-transform ion cyclotron resonance mass spectrometry: Type-specific unique signatures and implications for reactivity. *Sci. Total Environ.* **644**, 68–76 (2018).

157. Simpson, A. J. *et al.* Molecular structures and associations of humic substances in the terrestrial environment. *Naturwissenschaften* **89**, 84–88 (2002).

158. Hertkorn, N., Harir, M., Koch, B. P., Michalke, B. & Schmitt-Kopplin, P. High-field NMR spectroscopy and FTICR mass spectrometry: Powerful discovery tools for the molecular level characterization of marine dissolved organic matter. *Biogeosciences* **10**, 1583–1624 (2013).

159. Akhter, M. *et al.* Identification of aquatically available carbon from algae through solution-state NMR of whole 13C-labelled cells. *Anal. Bioanal. Chem.* **408**, 4357–4370 (2016).

160. Dutta Majumdar, R. *et al.* Analysis of DOM phototransformation using a looped NMR system integrated with a sunlight simulator. *Water Res.* **120**, 64–76 (2017).

161. Minor, E. C., Swenson, M. M., Mattson, B. M. & Oyler, A. R. Structural characterization of dissolved organic matter: A review of current techniques for isolation and analysis. *Environ. Sci. Process. Impacts* **16**, 2064–2079 (2014).

162. Bullard, J. E. *et al.* High latitude dust in the Earth system Reviews of Geophysics. *Rev. Geophys.* **54**, 447–485 (2016).

163. Li, C. *et al.* Carbonaceous matter deposition in the high glacial regions of the Tibetan Plateau. *Atmos. Environ.* **141**, 203–208 (2016).

164. Wei, T., Dong, Z., Kang, S., Qin, X. & Guo, Z. Geochemical evidence for sources of surface dust deposited on the Laohugou glacier, Qilian Mountains. *Appl. Geochem.* **79**, 1–8 (2017).

165. Koch, D. & Hansen, J. Distant origins of Arctic black carbon: A Goddard Institute for Space Studies ModelE experiment. *J. Geophys. Res. D Atmos.* **110**, 1–14 (2005).

166. Aamaas, B. *et al.* Elemental carbon deposition to Svalbard snow from Norwegian settlements and long-range transport. *Tellus, Ser. B Chem. Phys. Meteorol.* **63**, 340–351 (2011).

167. Ziolkowski, L. A., Chamberlin, A. R., Greaves, J. & Druffel, E. R. M. Quantification of black carbon in marine systems using the benzene polycarboxylic acid method: A mechanistic and yield study. *Limnol. Oceanogr. Methods* **9**, 140–140 (2011).

168. Wagner, S., Jaffé, R. & Stubbins, A. Dissolved black carbon in aquatic ecosystems. *Limnol. Oceanogr. Lett.* **3**, 168–185 (2018).

169. Masiello, C. A. New directions in black carbon organic geochemistry. *Mar. Chem.* **92**, 201–213 (2004).

170. Nguyen, T. H., Brown, R. A. & Ball, W. P. An evaluation of thermal resistance as a measure of black carbon content in diesel soot, wood char, and sediment. *Org. Geochem.* **35**, 217–234 (2004).

171. Han, Y. *et al.* Evaluation of the thermal/optical reflectance method for discrimination between char- and soot-EC. *Chemosphere* **69**, 569–574 (2007).

172. O'Connor, J. A., Lu, K., Guo, L., Rosenheim, B. E. & Liu, Z. Composition and lability of riverine dissolved organic matter: Insights from thermal slicing ramped pyrolysis GC–MS, amino acid, and stable isotope analyses. *Org. Geochem.* **149**, 104100 (2020).

173. Kaspari, S., Skiles, S. M., Delaney, I., Dixon, D. & Painter, T. H. Accelerated glacier melt on Snow Dome, Mount Olympus, Washington, USA, due to deposition of black carbon and mineral dust from wildfire. *J. Geophys. Res. Atmos.* **120**, 2793–2807 (2015).

174. Li, Y. *et al.* Impacts of black carbon and mineral dust on radiative forcing and glacier melting during summer in the Qilian Mountains, northeastern Tibetan Plateau. *Cryosph. Discuss.* 1–14 (2016) doi:10.5194/tc-2016-32.

175. Anesio, A. M., Hodson, A. J., Fritz, A., Psenner, R. & Sattler, B. High microbial activity on glaciers: Importance to the global carbon cycle. *Glob. Chang. Biol.* **15**, 955–960 (2009).

176. Antony, R. *et al.* Molecular Insights on Dissolved Organic Matter Transformation by Supraglacial Microbial Communities. *Environ. Sci. Technol.* **51**, 4328–4337 (2017).

177. Musilova, M. *et al.* Microbially driven export of labile organic carbon from the Greenland ice sheet. *Nat. Geosci.* **10**, 360–365 (2017).

178. Smith, H. J. *et al.* Microbial formation of labile organic carbon in Antarctic glacial environments. *Nat. Geosci.* **10**, 356–359 (2017).

179. Stubbins, A. *et al.* Anthropogenic aerosols as a source of ancient dissolved organic matter in glaciers. *Nat. Geosci.* **5**, 198–201 (2012).

180. Hamilton, T. L. & Havig, J. R. Inorganic carbon addition stimulates snow algae primary productivity. *ISME J.* **14**, 857–860 (2020).

181. Langford, H., Hodson, A. J., Banwart, S. & Boggild, C. the Microstructure, Biogeochemistry and Aggregation of Arctic Cryoconite Granules. *Ann. Glaciol.* **51**, 87–94 (2010).

182. Zarsky, J. D. *et al.* Large cryoconite aggregates on a Svalbard glacier support a diverse microbial community including ammonia-oxidizing archaea. *Environ. Res. Lett.* **8**, (2013).

183. Fyffe, C. L. *et al.* The impact of supraglacial debris on proglacial runoff and water chemistry. *J. Hydrol.* **576**, 41–57 (2019).

184. Pautler, B. G., Dubnick, A., Sharp, M. J., Simpson, A. J. & Simpson, M. J. Comparison of cryoconite organic matter composition from Arctic and Antarctic glaciers at the molecular-level. *Geochim. Cosmochim. Acta* **104**, 1–18 (2013).

185. Sanyal, A., Antony, R., Samui, G. & Thamban, M. Microbial communities and their potential for

degradation of dissolved organic carbon in cryoconite hole environments of Himalaya and Antarctica. *Microbiol. Res.* **208**, 32–42 (2018).

186. Fortner, S. K., Tranter, M., Fountain, A., Lyons, W. B. & Welch, K. A. The geochemistry of supraglacial streams of Canada Glacier, Taylor Valley (Antarctica), and their evolution into proglacial waters. *Aquat. Geochem.* **11**, 391–412 (2005).

187. Wharton, R. A., McKay, C. P., Simmons, G. M. & Parker, B. C. Cryoconite holes on glaciers. *Bioscience* **35**, 499–503 (1985).

188. MacDonell, S. & Fitzsimons, S. The formation and hydrological significance of cryoconite holes. *Prog. Phys. Geogr.* **32**, 595–610 (2008).

189. Takeuchi, N., Kohshima, S. & Seko, K. Structure, Formation, and Darkening Process of Albedo-reducing Material (Cryoconite) on a Himalayan Glacier: A Granular Algal Mat Growing on the Glacier. *Arctic, Antarct. Alp. Res.* **33**, 115–122 (2001).

190. Cook, J. M., Hodson, A. J. & Irvine-Fynn, T. D. L. Supraglacial weathering crust dynamics inferred from cryoconite hole hydrology. *Hydrol. Process.* **30**, 433–446 (2016).

191. Sharp, M. *et al.* Widespread bacterial populations at glacier beds and their relationship to rock weathering and carbon cycling. *Geology* **27**, 107–110 (1999).

192. Skidmore, M., Anderson, S. P., Sharp, M., Foght, J. & Lanoil, B. D. Comparison of microbial community compositions of two subglacial environments reveals a possible role for microbes in chemical weathering processes. *Appl. Environ. Microbiol.* **71**, 6986–6997 (2005).

193. Graly, J. A., Drever, J. I. & Humphrey, N. F. Calculating the balance between atmospheric CO2 drawdown and organic carbon oxidation in subglacial hydrochemical systems. *Global Biogeochem. Cy.* **31**, 709–727 (2017).

194. Deuerling, K. M., Martin, J. B., Martin, E. E. & Scribner, C. A. Hydrologic exchange and chemical weathering in a proglacial watershed near Kangerlussuaq, west Greenland. *J. Hydrol.* **556**, 220–232 (2018).

195. Urra, A. *et al.* Weathering Dynamics Under Contrasting Greenland Ice Sheet Catchments. *Front. Earth Sci.* **7**, (2019).

196. Ahmad, S. & Ansari, Z. Characteristics of rock–water interaction in Gangotri proglacier meltwater streams at higher altitude catchment Garhwal Himalaya, Uttarakhand, India. *J. Earth Syst. Sci.* **129**, (2020).

197. Bhatia, M. P., Das, S. B., Longnecker, K., Charette, M. A. & Kujawinski, E. B. Molecular characterization of dissolved organic matter associated with the Greenland ice sheet. *Geochim. Cosmochim. Acta* **74**, 3768–3784 (2010).

198. Bhatia, M. P. *et al.* Organic carbon export from the Greenland ice sheet. *Geochim. Cosmochim. Acta* **109**, 329–344 (2013).

199. Skidmore, M. L. & Sharp, M. J. Drainage system behaviour of a High-Arctic polythermal glacier. *Ann. Glaciol.* **28**, 209–215 (1999).

200. Wadham, J. L., Hodgkins, R., Cooper, R. J. & Tranter, M. Evidence for seasonal subglacial outburst events at a polythermal glacier, Finsterwalderbreen, Svalbard. *Hydrol. Process.* **15**, 2259–2280 (2001).

201. Irvine-Fynn, T. D. L., Hodson, A. J., Moorman, B. J., Vatne, G. & Hubbard, A. L. Polythermal glacier hydrology: A review. *Rev. Geophys.* **49**, 1–37 (2011).

202. Dubnick, A. Hydrological Controls on the Biogeochemistry of Polar Glacier Ice and its Meltwater. (2018).

203. St Pierre, K. A. *et al.* Proglacial freshwaters are significant and previously unrecognized sinks of atmospheric CO2. *Proc. Natl. Acad. Sci. U. S. A.* **116**, 17690–17695 (2019).

204. Sharp, M. & Tranter, M. Rates of chemical weathering in glaciated terrain (MT). *Geochemical Perspect.* **6**, 261–265 (2017).

205. Torres, M. A., Moosdorf, N., Hartmann, J., Adkins, J. F. & West, A. J. Glacial weathering, sulfide oxidation, and global carbon cycle feedbacks. *Proc. Natl. Acad. Sci. U. S. A.* **114**, 8716–8721 (2017).

206. Deuerling, K. M. *et al.* Chemical weathering across the western foreland of the Greenland Ice Sheet. *Geochim. Cosmochim. Acta* **245**, 426–440 (2019).

207. Fellman, J. B. *et al.* The impact of glacier runoff on the biodegradability and biochemical composition of terrigenous dissolved organic matter in near-shore marine ecosystems. *Mar. Chem.* **121**, 112–122 (2010).

208. Hood, E. *et al.* Glaciers as a source of ancient and labile organic matter to the marine environment. *Nature* **462**, 1044–1047 (2009).

209. Spencer, R. G. M. *et al.* Source and biolability of ancient dissolved organic matter in glacier and lake ecosystems on the tibetan plateau. *Geochim. Cosmochim. Acta* **142**, 64–74 (2014).

210. Hemingway, J. D. *et al.* Glacier meltwater and monsoon precipitation drive Upper Ganges Basin dissolved organic matter composition. *Geochim. Cosmochim. Acta* **244**, 216–228 (2019).

211. Lawson, E. C. *et al.* Greenland ice sheet exports labile organic carbon to the arctic oceans. *Biogeosciences* **11**, 4015–4028 (2014).

212. Singer, G. A. *et al.* Biogeochemically diverse organic matter in Alpine glaciers and its downstream fate. *Nat. Geosci.* **5**, 710–714 (2012).

213. Spencer, R. G. M. *et al.* Seasonal variability of organic matter composition in an Alaskan glacier outflow: Insights into glacier carbon sources. *Environ. Res. Lett.* **9**, (2014).

214. Behnke, M. I. *et al.* Dissolved organic matter sources in glacierized watersheds delineated through compositional and carbon isotopic modeling. *Limnol. Oceanogr.* **9999**, 1–14 (2020).

215. Aiken, G. R., Spencer, R. G. M., Striegl, R. G., Schuster, P. F. & Raymond, P. A. Global Biogeochemical Cycles in the Yukon River basin. *Global Biogeochem. Cy.* 525–537 (2014) doi:10.1002/2013GB004764.Received.

216. Chifflard, P., Fasching, C., Reiss, M., Ditzel, L. & Boodoo, K. S. Dissolved and particulate organic carbon in icelandic proglacial streams: A first estimate. *Water* **11**, (2019).

217. Hood, E., Battin, T. J., Fellman, J., O'neel, S. & Spencer, R. G. M. Storage and release of organic carbon from glaciers and ice sheets. *Nat. Geosci.* **8**, 91–96 (2015).

218. Kohler, T. J. *et al.* Carbon dating reveals a seasonal progression in the source of particulate organic carbon exported from the Greenland Ice Sheet. *Geophys. Res. Lett.* **44**, 6209–6217 (2017).

219. Dubnick, A., Sharp, M., Danielson, B., Saidi-Mehrabad, A. & Barker, J. Basal thermal regime affects the biogeochemistry of subglacial systems. *Biogeosciences* **17**, 963–977 (2020).

220. Bhatia, M., Sharp, M. & Foght, J. Distinct bacterial communities exist beneath a high arctic polythermal Glacier. *Appl. Environ. Microbiol.* **72**, 5838–5845 (2006).

221. Dubnick, A. *et al.* Characterization of dissolved organic matter (DOM) from glacial environments using total fluorescence spectroscopy and parallel factor analysis. *Ann. Glaciol.* **51**, 111–122 (2010).

222. Pautler, B. G. *et al.* Molecular characterization of dissolved organic matter in glacial ice: Coupling natural abundance 1H NMR and fluorescence spectroscopy. *Environ. Sci. Technol.* **46**, 3753–3761 (2012).

223. Donahue, D. J., Linick, T. W. & Jull, A. J. T. Isotope-ratio and background corrections for accelerator mass spectrometry radiocarbon measurements. *Radiocarbon* **32**, 135–142 (1990).

224. McKnight, D. M. *et al.* Spectrofluorometric characterization of dissolved organic matter for indication of precursor organic material and aromaticity. *Limnol. Oceanogr.* **46**, 38–48 (2001).

225. Parlanti, E., Wörz, K., Geoffroy, L. & Lamotte, M. Dissolved organic matter fluorescence spectroscopy as a tool to estimate biological activity in a coastal zone submitted to anthropogenic inputs. *Org. Geochem.* **31**, 1765–1781 (2000).

226. Wilson, H. F. & Xenopoulos, M. A. Effects of agricultural land use on the composition of fluvial dissolved organic matter. *Nat. Geosci.* **2**, 37–41 (2009).

227. Antony, R. *et al.* Origin and sources of dissolved organic matter in snow on the east antarctic ice sheet. *Environ. Sci. Technol.* **48**, 6151–6159 (2014).

228. Antony, R. *et al.* Photo-biochemical transformation of dissolved organic matter on the surface of the coastal East Antarctic ice sheet. *Biogeochemistry* **141**, 229–247 (2018).

229. Bagshaw, E. A. *et al.* Biogeochemical evolution of cryoconite holes on Canada Glacier, Taylor Valley, Antarctica. *J. Geophys. Res. Biogeosciences* **112**, 1–8 (2007).

230. Bagshaw, E. A. *et al.* Do cryoconite holes have the potential to be significant sources of C, N, and P to downstream depauperate ecosystems of Taylor Valley, Antarctica? *Arctic, Antarct. Alp. Res.* **45**, 440–454 (2013).

231. Barker, J., Dubnick, A., Lyons, W. & Chin, Y. P. Changes in dissolved organic matter (DOM) fluorescence in proglacial Antarctic streams. *Arctic, Antarct. Alp. Res.* **45**, 305–317 (2013).

232. Boix Canadell, M., Escoffier, N., Ulseth, A. J., Lane, S. N. & Battin, T. J. Alpine Glacier Shrinkage Drives Shift in Dissolved Organic Carbon Export From Quasi-Chemostasis to Transport Limitation. *Geophys. Res. Lett.* **46**, 8872–8881 (2019).

233. Colombo, N. *et al.* High export of nitrogen and dissolved organic carbon from an Alpine glacier (Indren Glacier, NW Italian Alps). *Aquat. Sci.* **81**, 1–13 (2019).

234. Dubnick, A. *et al.* Trickle or treat: The dynamics of nutrient export from polar glaciers. *Hydrol. Process.* **31**, 1776–1789 (2017).

235. Fellman, J. B., Hood, E., Spencer, R. G. M., Stubbins, A. & Raymond, A. Watershed glacier coverage influences dissolved organic matter biogeochemistry in watersheds of Southeast Alaska. *Ecosystems* **17**, 1014–1025 (2014).

236. Fellman, J. B., Hood, E., Raymond, P. A., Stubbins, A. & Spencer, R. G. M. Spatial Variation in the Origin of Dissolved Organic Carbon in Snow on the Juneau Icefield, Southeast Alaska. *Environ. Sci. Technol.* **49**, 11492–11499 (2015).

237. Feng, L. *et al.* Chemical composition of microbe-derived dissolved organic matter in cryoconite in tibetan plateau glaciers: Insights from fourier transform ion cyclotron resonance mass spectrometry analysis. *Environ. Sci. Technol.* **50**, 13215–13223 (2016).

238. Feng, L., An, Y., Xu, J. & Kang, S. Characteristics and sources of dissolved organic matter in a glacier in the northern Tibetan Plateau: Differences between different snow categories. *Ann. Glaciol.* **59**, 31–40 (2018).

239. Feng, L. *et al.* Molecular Insights into Glacial Cryoconite Dissolved Organic Matter Evolution under Dark Conditions during the Ablation Season on the Tibetan Plateau. *ACS Earth Sp. Chem.* **5**, 870–879 (2021).

240. Foreman, C. M. *et al.* Microbial growth under humic-free conditions in a supraglacial stream system on the Cotton Glacier, Antarctica. *Environ. Res. Lett.* **8**, (2013).

241. Hagler, G. S. W. *et al.* Particulate and water-soluble carbon measured in recent snow at Summit, Greenland. *Geophys. Res. Lett.* **34**, 1–5 (2007).

242. Holt, A. D. *et al.* The evolution of stream dissolved organic matter composition following glacier retreat in coastal watersheds of southeast Alaska. *Biogeochemistry* **6**, (2021).

243. Hood, E., Fellman, J. B. & Spencer, R. G. M. Glacier Loss Impacts Riverine Organic Carbon Transport to the Ocean. *Geophys. Res. Lett.* **47**, 1–9 (2020).

244. Hu, Z. *et al.* Dissolved organic carbon fractionation accelerates glacier-melting: A case study in the northern Tibetan Plateau. *Sci. Total Environ.* **627**, 579–585 (2018).

245. Kellerman, A. M. *et al.* Glacier Outflow Dissolved Organic Matter as a Window Into Seasonally Changing Carbon Sources: Leverett Glacier, Greenland. *J. Geophys. Res. Biogeosciences* **125**, 1–16 (2020).

246. Koziol, K. A., Moggridge, H. L., Cook, J. M. & Hodson, A. J. Organic carbon fluxes of a glacier surface: A case study of Foxfonna, a small Arctic glacier. *Earth Surf. Process. Landforms* **44**, 405–416 (2019).

247. Legrand, M. *et al.* Water-soluble organic carbon in snow and ice deposited at Alpine, Greenland, and Antarctic sites: a critical review of available data and their atmospheric relevance. *Clim. Past Discuss.* **9**, 2357–2399 (2013).

248. Li, X. *et al.* Importance of Mountain Glaciers as a Source of Dissolved Organic Carbon. *J. Geophys. Res. Earth Surf.* **123**, 2123–2134 (2018).

249. Preunkert, S. *et al.* Quantification of dissolved organic carbon at very low levels in natural ice samples by a uv-induced oxidation method. *Environ. Sci. Technol.* **45**, 673–678 (2011).

250. Smith, H. J. *et al.* Dynamic processing of DOM: Insight from exometabolomics, fluorescence spectroscopy, and mass spectrometry. *Limnol. Oceanogr. Lett.* **3**, 225–235 (2018).

251. Smith, H. J., Dieser, M., McKnight, D. M., SanClements, M. D. & Foreman, C. M. Relationship between dissolved organic matter quality and microbial community composition across polar glacial environments. *FEMS Microbiol. Ecol.* **94**, 1–10 (2018).

252. Yan, F. *et al.* Concentration, sources and light absorption characteristics of dissolved organic carbon on a medium-sized valley glacier, northern Tibetan Plateau. *Cryosphere* **10**, 2611–2621 (2016).

253. Zhang, Y. *et al.* Dissolved organic carbon in glaciers of the southeastern Tibetan Plateau: Insights into concentrations and possible sources. *PLoS One* **13**, (2018).

254. Smith, L. C., Sheng, Y. & MacDonald, G. M. A first pan-arctic assessment of the influence of glaciation, permafrost, topography and peatlands on northern hemisphere lake distribution. *Permafr. Periglac. Process.* **18**, 201–208 (2007).

255. Slemmons, K. E. H., Saros, J. E. & Simon, K. The influence of glacial meltwater on alpine aquatic ecosystems: A review. *Environ. Sci. Process. Impacts* **15**, 1794–1806 (2013).

256. Collins, D. N. Hydrochemistry of meltwaters draining from an Alpine glacier (Gornergletsher Switzerland). *Arct. Alp. Res.* **11**, 307–324 (1979).

257. Wadham, J. L., Hodson, A. J., Tranter, M. & Dowdeswell, J. A. The hydrochemistry of meltwaters draining a polythermal-based, high Arctic glacier, south Svalbard: I. The ablation season. *Hydrol. Process.* **12**, 1825–1849 (1998).

258. Hindshaw, R. S. *et al.* Hydrological control of stream water chemistry in a glacial catchment (Damma Glacier, Switzerland). *Chem. Geol.* **285**, 215–230 (2011).

259. Bliss, A., Hock, R. & Radić, V. Global response of glacier runoff to twenty-first century climate

change. *J. Geophys. Res. Earth Surf.* **119**, 717–730 (2014).

260. Haeberli, W., Frauenfelder, R., Hoelzle, M. & Maisch, M. On Rates and Acceleration Trends of Global Glacier Mass Changes. **81**, 585–591 (1999).

261. Kaser, G., Cogley, J. G., Dyurgerov, M. B., Meier, M. F. & Ohmura, A. Mass balance of glaciers and ice caps: Consensus estimates for 1961-2004. *Geophys. Res. Lett.* **33**, 1–5 (2006).

262. Sharp, M. *et al.* Extreme melt on Canada's Arctic ice caps in the 21st century. *Geophys. Res. Lett.* **38**, 3–7 (2011).

263. Lenaerts, J. T. M. *et al.* Irreversible mass loss of Canadian Arctic Archipelago glaciers. *Geophys. Res. Lett.* **40**, 870–874 (2013).

264. Solomon, S., Plattner, G. K., Knutti, R. & Friedlingstein, P. Irreversible climate change due to carbon dioxide emissions. *Proc. Natl. Acad. Sci. U. S. A.* **106**, 1704–1709 (2009).

265. Duarte, C. M., Lenton, T. M., Wadhams, P. & Wassmann, P. Abrupt climate change in the Arctic. *Nat. Clim. Chang.* **2**, 60–62 (2012).

266. Vavrus, S. J., Holland, M. M., Jahn, A., Bailey, D. A. & Blazey, B. A. Twenty-first-century arctic climate change in CCSM4. *J. Clim.* **25**, 2696–2710 (2012).

267. Jacobsen, D., Milner, A. M., Brown, L. E. & Dangles, O. Universities of Leeds , Sheffield and York Biodiversity under threat in glacier-fed river systems. *Nat. Clim. Chang.* **2**, 361–364 (2012).

268. Milner, A. M. *et al.* Glacier shrinkage driving global changes in downstream systems. *Proc. Natl. Acad. Sci. U. S. A.* **114**, 9770–9778 (2017).

269. Fell, S. C., Carrivick, J. L., Kelly, M. G., Füreder, L. & Brown, L. E. Declining glacier cover threatens the biodiversity of alpine river diatom assemblages. *Glob. Chang. Biol.* **24**, 5828–5840 (2018).

270. IPCC. *Climate change 2007: the physcal science basis*. *Summary for Policymakers* (2007).

271. Meire, L. *et al.* Glacial meltwater and primary production are drivers of strong CO2 uptake in fjord and coastal waters adjacent to the Greenland Ice Sheet. *Biogeosciences* **12**, 2347–2363 (2015).

272. Ding, Y., Yamashita, Y., Jones, J. & Jaffé, R. Dissolved black carbon in boreal forest and glacial rivers of central Alaska: assessment of biomass burning versus anthropogenic sources. *Biogeochemistry* **123**, 15–25 (2015).

273. Müller-Tautges, C. *et al.* Historic records of organic compounds from a high Alpine glacier: Influences of biomass burning, anthropogenic emissions, and dust transport. *Atmos. Chem. Phys.* **16**, 1029–1043 (2016).

274. Schmidt, M. W. I. & Noack, A. G. Black carbon in soils and sediments: analysis, distribution, implications, and current challenges. *Global Biogeochem. Cy.* **14**, 777–793 (2000).

275. Shrestha, G., Traina, S. J. & Swanston, C. W. Black carbon's properties and role in the environment: A comprehensive review. *Sustainability* **2**, 294–320 (2010).

276. Liu, J., Fan, S., Horowitz, L. W. & Levy, H. Evaluation of factors controlling long-range transport of black carbon to the Arctic. *J. Geophys. Res. Atmos.* **116**, (2011).

277. Kim, H., Zhang, Q. & Heo, J. Influence of intense secondary aerosol formation and long-range transport on aerosol chemistry and properties in the Seoul Metropolitan Area during spring time: Results from KORUS-AQ. *Atmos. Chem. Phys.* **18**, 7149–7168 (2018).

278. Nagorski, S. A., Kaspari, S. D., Hood, E., Fellman, J. B. & Skiles, S. M. K. Radiative Forcing by Dust and Black Carbon on the Juneau Icefield, Alaska. *J. Geophys. Res. Atmos.* **124**, 3943–3959 (2019).

279. Hu, Z., Kang, S., Li, X., Li, C. & Sillanpää, M. Relative contribution of mineral dust versus black

carbon to Third Pole glacier melting. *Atmos. Environ.* **223**, (2020).

280. Hedges, J. I. *et al.* The molecularly-uncharacterized component of nonliving organic matter in natural environments. *Org. Geochem.* **31**, 945–958 (2000).

281. Anesio, A. M. *et al.* Carbon fluxes through bacterial communities on glacier surfaces. *Ann. Glaciol.* **51**, 32–40 (2010).

282. Bagshaw, E. A. *et al.* Processes controlling carbon cycling in Antarctic glacier surface ecosystems. *Geochemical Perspect. Lett.* **2**, 44–54 (2016).

283. Franzetti, A. *et al.* Light-dependent microbial metabolisms drive carbon fluxes on glacier surfaces. *ISME J.* **10**, 2984–2988 (2016).

284. Edwards, A. *et al.* A metagenomic snapshot of taxonomic and functional diversity in an alpine glacier cryoconite ecosystem. *Environ. Res. Lett.* **8**, (2013).

285. Takeuchi, N., Kohshima, S., Shiraiwa, T. & Kubota, K. Characteristics of cryoconite (surface dust on glaciers) and surface albedo of a Patagonian glacier, Tyndall Glacier, Southern Patagonia Icefield. *Bull. Glaciol. Res.* **18**, 65–69 (2001).

286. Cook, J., Edwards, A., Takeuchi, N. & Irvine-Fynn, T. Cryoconite: The dark biological secret of the cryosphere. *Prog. Phys. Geogr.* **40**, 66–111 (2016).

287. O'Donnell, E. C. *et al.* Identification and analysis of low-molecular-weight dissolved organic carbon in subglacial basal ice ecosystems by ion chromatography. *Biogeosciences* **13**, 3833–3846 (2016).

288. Waller, R. I. The influence of basal processes on the dynamic behaviour of cold-based glaciers. *Quat. Int.* **86**, 117–128 (2001).

289. Lloyd Davies, M. T., Atkins, C. B., van der Meer, J. J. M., Barrett, P. J. & Hicock, S. R. Evidence for cold-based glacial activity in the Allan Hills, Antarctica. *Quat. Sci. Rev.* **28**, 3124–3137 (2009).

290. Atkins, C. B. Geomorphological evidence of cold-based glacier activity in South Victoria Land, Antarctica. *Geol. Soc. Spec. Publ.* **381**, 299–318 (2013).

291. Hodgkins, R., Tranter, M. & Dowdeswell, J. A. The hydrochemistry of runoff from a 'cold-based' glacier in the High Artic (Scott Turnerbreen, Svalbard). *Hydrol. Process.* **12**, 87–103 (1998).

292. Pain, A. J., Martin, J. B., Martin, E. E., Rahman, S. & Ackermann, P. Differences in the Quantity and Quality of Organic Matter Exported From Greenlandic Glacial and Deglaciated Watersheds. *Global Biogeochem. Cy.* **34**, 1–20 (2020).

293. O'Donnell, J. A., Aiken, G. R., Kane, E. S. & Jones, J. B. Source water controls on the character and origin of dissolved organic matter in streams of the Yukon River basin, Alaska. *J. Geophys. Res. Biogeosciences* **115**, 1–12 (2010).

294. Zhou, Y. *et al.* Variability in Dissolved Organic Matter Composition and Biolability across Gradients of Glacial Coverage and Distance from Glacial Terminus on the Tibetan Plateau. *Environ. Sci. Technol.* **53**, 12207–12217 (2019).

295. Kida, M. *et al.* Origin, distributions, and environmental significance of ubiquitous humic-like fluorophores in Antarctic lakes and streams. *Water Res.* **163**, 114901 (2019).

296. Emmerton, C. A. *et al.* The importance of freshwater systems to the net atmospheric exchange of carbon dioxide and methane with a rapidly changing high Arctic watershed. *Biogeosciences* **13**, 5849–5863 (2016).

297. Christie, R. L. *Bedrock geology. In: Hattersley-Smith, G., ed. Operation Hazen: Narrative and preliminary reports for the 1957 season. Ottawa: Defence Research Board Canada, Dept. of National Defence*. (1958).

298. Dewing, K., Turner, E. & Harrison, J. C. Geological History , Mineral Occurrences and Mineral Potential of the Sedimentary Rocks of the Canadian Arctic Achipelago. *Evolution (N. Y).* 733–753 (2007).

299. Canada, G. S. of. *Mineral and hydrocarbon resource potential of the proposed Northern Ellesmere Island National Park, District of Franklin, N.W.T. (Phase 1). Ottawa: Department of Energy, Mines, and Resources*. (1981).

300. Stedmon, C. A., Markager, S. & Kaas, H. Optical properties and signatures of chromophoric dissolved organic matter (CDOM) in Danish coastal waters. *Estuar. Coast. Shelf Sci.* **51**, 267–278 (2000).

301. Guéguen, C. & Kowalczuk, P. Colored dissolved organic matter in frontal zones. *Chem. Oceanogr. Front. Zo.* (2013) doi:10.1007/698_2013_244.

302. Lawaetz, A. J. & Stedmon, C. A. Fluorescence intensity calibration using the Raman scatter peak of water. *Appl. Spectrosc.* **63**, 936–940 (2009).

303. Huber, S. A. & Frimmel, F. H. Flow Injection Analysis of Organic and Inorganic Carbon in the Low-ppb Range. *Anal. Chem.* **63**, 2122–2130 (1991).

304. Her, N. *et al.* Optimization of method for detecting and characterizing NOM by HPLC-size exclusion chromatography with UV and on-line DOC detection. *Environ. Sci. Technol.* **36**, 1069–1076 (2002).

305. Kawasaki, N. *et al.* Fast and precise method for HPLC-size exclusion chromatography with UV and TOC (NDIR) detection: Importance of multiple detectors to evaluate the characteristics of dissolved organic matter. *Water Res.* **45**, 6240–6248 (2011).

306. St-Jean, G., Kieser, W. E., Crann, C. A. & Murseli, S. Semi-Automated Equipment for CO2 Purification and Graphitization at the A.E. Lalonde AMS Laboratory (Ottawa, Canada). *Radiocarbon* **59**, 941–956 (2017).

307. Crann, C. A. *et al.* First Status Report on Radiocarbon Sample Preparation Techniques at the A.E. Lalonde AMS Laboratory (Ottawa, Canada). *Radiocarbon* **59**, 695–704 (2017).

308. International Atomic Energy Agency. *WISER water isotope system for data analysis, visualization and electronic retrieval* http://www.nucleus.iaea.org.

309. Fourré, E. *et al.* Past and recent tritium levels in Arctic and Antarctic polar caps. *Earth Planet. Sci. Lett.* **245**, 56–64 (2006).

310. Cauquoin, A., Jean-Baptiste, P., Risi, C., Fourré, É., Stenni, B., & Landais, A. The global distribution of natural tritium in precipitation simulated with an Atmospheric General Circulation Model and comparison with observations. *Earth Planet. Sci. Lett.* **427**, 160–170 (2015).

311. Stichler, W. *et al.* Influence of sublimation on stable isotope records recovered from high-altitude glaciers in the tropical Andes. *J. Geophys. Res.* **106**, 613–620 (2001).

312. Ham, J. Y. *et al.* Isotopic variations of meltwater from ice by isotopic exchange between liquid water and ice. *J. Glaciol.* **65**, 1035–1043 (2019).

313. Miller, L. G. & Aiken, G. R. Effects of glacial meltwater inflows and moat freezing on mixing in an ice-covered antarctic lake as interpreted from stable isotope and tritium distributions. *Limnol. Oceanogr.* **41**, 966–976 (1996).

314. Yao, T. *et al.* Climatological significance of δ18O in north Tibetan ice cores. *J. Geophys. Res. Atmos.* **101**, 29531–29537 (1996).

315. Thompson, L. G. *et al.* Tropical glacier and ice core evidence of climate change on annual to millennial time scales. *Climatic Change* **59**, 137–155 (2003).

316. Kotzer, T. G., Kudo, A., Zheng, J. & Workman, W. Natural and anthropogenic levels of tritium in a

Canadian Arctic ice core, Agassiz Ice Cap, Ellesmere Island, and comparison with other radionuclides. *J. Glaciol.* **46**, 35–40 (2000).

317. Kang, S. *et al.* Dramatic loss of glacier accumulation area on the Tibetan Plateau revealed by ice core tritium and mercury records. *Cryosphere* **9**, 1213–1222 (2015).

318. Van Der Wel, L. G. *et al.* Using high-resolution tritium profiles to quantify the effects of melt on two Spitsbergen ice cores. *J. Glaciol.* **57**, 1087–1097 (2011).

319. Schuster, P. F., White, D. E., Naftz, D. L. & Cecil, L. D. Chronological refinement of an ice core record at Upper Fremont Glacier in south central North America. *J. Geophys. Res.* **105**, 4657–4666 (2000).

320. Fourré, E. *et al.* Past and recent tritium levels in Arctic and Antarctic polar caps. *Earth Planet. Sci. Lett.* **245**, 56–64 (2006).

321. Michel, R. L. & Naftz, D. L. Use of sulfur-35 and tritium to study runoff from an alpine glacier, Wind River Range, Wyoming. in *Biogeochemistry of Seasonally Snow-Covered Catchments* vol. 1 441–444 (1995).

322. Cauquoin, A. *et al.* The global distribution of natural tritium in precipitation simulated with an Atmospheric General Circulation Model and comparison with observations. *Earth Planet. Sci. Lett.* **427**, 160–170 (2015).

323. Rai, S. P. *et al.* Identifying contribution of snowmelt and glacier melt to the Bhagirathi River (Upper Ganga) near snout of the Gangotri Glacier using environmental isotopes. *Catena* **173**, 339–351 (2019).

324. Yi, Y. *et al.* Isotopic signals (18O, 2H, 3H) of six major rivers draining the pan-Arctic watershed. *Global Biogeochem. Cy.* **26**, (2012).

325. Bond, M. J. & Carr, J. Permafrost thaw and implications for the fate and transport of tritium in the Canadian north. *J. Environ. Radioact.* **192**, 295–311 (2018).

326. Wan, C. *et al.* Using tritium and 222Rn to estimate groundwater discharge and thawing permafrost contributing to surface water in permafrost regions on Qinghai-Tibet Plateau. *J. Radioanal. Nucl. Chem.* **322**, 561–578 (2019).

327. Burn, C. R. & Michel, F. A. Evidence for recent temperature-induced water migration into permafrost from the tritium content of ground ice near Mayo, Yukon Territory, Canada. *Can. J. Earth Sci.* **25**, 909–915 (1988).

328. Blake, W. J. *Geological Survey of Canada Radiocarbon Dates XXV. Geological Survey of Canada*. (1986).

329. Guo, L., Ping, C. L. & Macdonald, R. W. Mobilization pathways of organic carbon from permafrost to arctic rivers in a changing climate. *Geophys. Res. Lett.* **34**, 1–5 (2007).

330. Vonk, J. E. *et al.* High biolability of ancient permafrost carbon upon thaw. *Geophys. Res. Lett.* **40**, 2689–2693 (2013).

331. Hilton, R. G., Galy, A., Hovius, N., Horng, M. J. & Chen, H. The isotopic composition of particulate organic carbon in mountain rivers of Taiwan. *Geochim. Cosmochim. Acta* **74**, 3164–3181 (2010).

332. Raymond, P. A. *et al.* Controls on the variability of organic matter and dissolved inorganic carbon ages in northeast US rivers. *Mar. Chem.* **92**, 353–366 (2004).

333. McClelland, J. W. *et al.* Particulate organic carbon and nitrogen export from major Arctic rivers. *Global Biogeochem. Cy.* **30**, 629–643 (2016).

334. Kalks, F. *et al.* Geogenic organic carbon in terrestrial sediments and its contribution to total soil carbon. *Soil* **7**, 347–362 (2021).

335. Clark, K. E. *et al.* New views on 'old' carbon in the Amazon River: Insight from the source of organic

carbon eroded from the Peruvian Andes. *Geochem. Geophy. Geosy.* **14**, 1644–1659 (2013).

336. Hilton, R. G. *et al.* Erosion of organic carbon in the Arctic as a geological carbon dioxide sink. *Nature* **524**, 84–87 (2015).

337. Lafrenière, M. J. & Sharp, M. J. The concentration and fluorescence of dissolved organic carbon (DOC) in glacial and nonglacial catchments: Interpreting hydrological flow routing and DOC sources. *Arctic, Antarct. Alp. Res.* **36**, 156–165 (2004).

338. Abbott, B. W., Larouche, J. R., Jones, J. J. B., Bowden, W. B. & Balser, A. W. Elevated dissolved organic carbon biodegradability from thawing and collapsing permafrost. *J. Geophys. Res. Biogeosciences* **119**, 2049–2063 (2014).

339. Vonk, J. E. *et al.* Biodegradability of dissolved organic carbon in permafrost soils and aquatic systems: a meta-analysis. *Biogeosciences* **12**, 6915–6930 (2015).

340. Lamoureux, S. F. & Lafrenière, M. J. Seasonal fluxes and age of particulate organic carbon exported from Arctic catchments impacted by localized permafrost slope disturbances. *Environ. Res. Lett.* **9**, (2014).

341. Wild, B. *et al.* Rivers across the Siberian Arctic unearth the patterns of carbon release from thawing permafrost. *Proc. Natl. Acad. Sci. U. S. A.* **116**, 10280–10285 (2019).

342. Campeau, A., Soerensen, A., Martma, T., Åkerblom, S. & Zdanowicz, C. Controls on the 14 C-content of dissolved and particulate organic carbon mobilized across the Mackenzie River basin, Canada . *Global Biogeochem. Cy.* (2020) doi:10.1029/2020gb006671.

343. Shakil, S., Tank, S. E., Kokelj, S. V., Vonk, J. E. & Zolkos, S. Particulate dominance of organic carbon mobilization from thaw slumps on the Peel Plateau, NT: Quantification and implications for stream systems and permafrost carbon release. *Environ. Res. Lett.* **15**, (2020).

344. Sharp, M. Burgess, D.O. Cawkwell, F. Copland, L. Davis, J.A. Dowdeswell, E.K. Dowdeswell, J.A. Gardner, A.S. Mair, D. Wang, L. & Williamson, S.N. Wolken, G.J. Wyatt, F. Remote sensing of recent glacier changes in the Canadian Arctic. in *Global land ice measurements from space* (Springer, 2014).

345. Noël, B. *et al.* Six decades of glacial mass loss in the Canadian arctic archipelago. *J. Geophys. Res. Earth Surf.* **123**, 1430–1449 (2018).

346. Yang, K. *et al.* A new surface meltwater routing model for use on the Greenland Ice Sheet surface. *Cryosphere* **12**, 3791–3811 (2018).

347. Shugar, D. H. *et al.* River piracy and drainage basin reorganization led by climate-driven glacier retreat. *Nat. Geosci.* **10**, 370–375 (2017).

348. Preston, D. L. *et al.* Climate regulates alpine lake ice cover phenology and aquatic ecosystem structure. *Geophys. Res. Lett.* **43**, 5353–5360 (2016).

349. Dubnick, A. *et al.* Hydrological controls on glacially exported microbial assemblages. *J. Geophys. Res. Biogeosciences* **122**, 1049–1061 (2017).

350. Kohler, T. J. *et al.* Patterns in Microbial Assemblages Exported From the Meltwater of Arctic and Sub-Arctic Glaciers. *Front. Microbiol.* **11**, (2020).

351. Yde, J. C., Knudsen, N. T., Hasholt, B. & Mikkelsen, A. B. Meltwater chemistry and solute export from a Greenland Ice Sheet catchment, Watson River, West Greenland. *J. Hydrol.* **519**, 2165–2179 (2014).

352. Hawkings, J. R. *et al.* The effect of warming climate on nutrient and solute export from the Greenland Ice Sheet. *Geochemical Perspect. Lett.* **1**, 94–104 (2015).

353. Burpee, B. T., Anderson, D. & Saros, J. E. Assessing ecological effects of glacial meltwater on lakes fed by the Greenland Ice Sheet: The role of nutrient subsidies and turbidity. *Arctic, Antarct. Alp. Res.*

50, 1–15 (2018).

354. Bhatia, M.P. Waterman, S. Burgess, D.O. Williams, P.L. Bundy, R.M. Mellet, T. Roberts, M. Bertrand, E. M. Glaciers and nutrients in the Canadian Arctic Archipelago marine system. *Global Biogeochem. Cy.* (2021).

355. Wadham, J. L. *et al.* Ice sheets matter for the global carbon cycle. *Nat. Commun.* **10**, (2019).

356. Smith, H.J. Schmit, A. Foster, R. Littman, S. Kuypers, M.M. Foreman, C. . Biofilms on glacial surfaces: hotspots for biological activity. *npj Biofilms Microbiomes* **2**, (2016).

357. Marsh, N. B. *et al.* Sources of solutes and carbon cycling in perennially ice-covered Lake Untersee, Antarctica. *Sci. Rep.* **10**, 1–12 (2020).

358. Yallop, M. L. *et al.* Photophysiology and albedo-changing potential of the ice algal community on the surface of the Greenland ice sheet. *ISME J.* **6**, 2302–2313 (2012).

359. Cook, J. M. *et al.* Glacier algae accelerate melt rates on the south-western Greenland Ice Sheet. *Cryosphere* **14**, 309–330 (2020).

360. Skidmore, M., Sharp, M. & Tranter, M. Kinetic isotopic fractionation during carbonate dissolution in laboratory experiments: implications for detection of microbial CO2 signatures using 13C-DIC. *Goechimica Cosmoscimica Acta* **68**, 4309–4317 (2004).

361. Montross, S. N., Skidmore, M., Tranter, M., Kivimäki, A. L. & Parkes, R. J. A microbial driver of chemical weathering in glaciated systems. *Geology* **41**, 215–218 (2013).

362. Pain, A. J., Martin, J. B., Martin, E. E., Rennermalm, Å. K. & Rahman, S. Heterogeneous CO2and CH4content of glacial meltwater from the Greenland Ice Sheet and implications for subglacial carbon processes. *Cryosphere* **15**, 1627–1644 (2021).

363. Shukla, T., Sundriyal, S., Stachnik, L. & Mehta, M. Carbonate and silicate weathering in glacial environments and its relation to atmospheric CO2 cycling in the Himalaya. *Ann. Glaciol.* **59**, 159–170 (2018).

364. Dlugokencky, E. J., Mund, J. W., Crotwell, A. M., Crotwell, M. J. & Thoning, K. W. *Atmospheric carbon dioxide dry air mole fractions from the NOAA GML carbon cycle cooperative global air sampling network, 1968-2020, Version 2021-07-30*. (2021) doi:10.15138/wkgj-f215.

365. Zeebe, R.E. Wolf-Gladrow, D. *CO2 in seawater: equilibrium, kinetics, isotopes*. (Gulf Professional Publishing, 2001).

366. Vogel, J. C., Grootes, P. M. & Mook, W. G. Isotopic fractionation between gaseous and dissolved carbon dioxide. *Z. Phys. A Hadron. Nucl.* **230**, 225–238 (1970).

367. Mook, W. G., Bommerson, J. C. & Staverman, W. H. Carbon isotope fractionation between dissolved bicarbonate and gaseous carbon dioxide. *Earth Planet. Sci. Lett.* **22**, 169–176 (1974).

368. White, J. W. C., Vaughn, B. H. & Michel, S. E. Isotopic Composition of Atmospheric Carbon Dioxide (13C and 18O) from the NOAA ESRL Carbon Cycle Cooperative Global Air Sampling Network. *University of Colorado* (2015).

369. Deines, P., Langmuir, D. & Harmon, R. S. Stable carbon isotope ratios and the existence of a gas phase in the evolution of carbonate ground waters. *Geochim. Cosmochim. Acta* **38**, 1147–1164 (1974).

370. Tranter, M. Sharp, M.J. Brown, G.H. Willis, I.C. Hubbard, B.P. Nielsen, M.K. Smart, C.C. Gordon, S. Tulley, M. Lamb, H. R. Variability in the chemical composition of in situ subglacial meltwaters. *Hydrol. Process.* **11**, 59–77 (1997).

371. Carling, G. T., Rupper, S. B., Fernandez, D. P., Tingey, D. G. & Harrison, C. B. Effect of Atmospheric Deposition and Weathering on Trace Element Concentrations in Glacial Meltwater at Grand Teton

National Park, Wyoming, U.S.A. *Arctic, Antarct. Alp. Res.* **49**, 427–440 (2017).

372. Brown, G. H., Tranter, M. & Sharp, M. J. Experimental investigations of the weathering of suspended sediment by alpine glacial meltwater. *Hydrol. Process.* **10**, 579–597 (1996).

373. Aukes, P. J. K. Dissolved organic matter in the Canadian Arctic and Sub-Arctic: Importance of DOM Quality and Quantity in a Warming Climate. (2019).

374. Mindl, B. *et al.* Factors influencing bacterial dynamics along a transect from supraglacial runoff to proglacial lakes of a high Arctic glacieri. *FEMS Microbiol. Ecol.* **59**, 307–317 (2007).

375. Bhatt, M. P., Takeuchi, N. & Acevedo, M. F. Chemistry of Supraglacial Ponds in the Debris-Covered Area of Lirung Glacier in Central Nepal Himalayas. *Aquat. Geochem.* **22**, 35–64 (2016).

376. Cook, J. M. *et al.* An improved estimate of microbially mediated carbon fluxes from the Greenland ice sheet. *J. Glaciol.* **58**, 1098–1108 (2012).

377. Doran, P. T. *et al.* Dating Quaternary lacustrine sediments in the McMurdo Dry Valleys, Antarctica. *Palaeogeogr. Palaeoclimatol. Palaeoecol.* **147**, 223–239 (1999).

378. Andrews, M. G., Jacobson, A. D., Osburn, M. R. & Flynn, T. M. Dissolved Carbon Dynamics in Meltwaters From the Russell Glacier, Greenland Ice Sheet. *J. Geophys. Res. Biogeosciences* **123**, 2922–2940 (2018).

379. Skidmore, M. L., Foght, J. M. & Sharp, M. J. Microbial life beneath a high Arctic glacier. *Appl. Environ. Microbiol.* **66**, 3214–3220 (2000).

380. Fairchild, I. J. & Spiro, B. Carbonate minerals in glacial sediments: Geochemical clues to palaeoenvironment. *Geol. Soc. London, Spec. Publ.* **53**, 201–216 (1990).

381. Gooseff, M. N., McKnight, D. M., Lyons, W. B. & Blum, A. E. Weathering reactions and hyporheic exchange controls on stream water chemistry in a glacial meltwater stream in the McMurdo Dry Valleys. *Water Resour. Res.* **38**, 15-1-15–17 (2002).

382. Harmon, R. S., Leslie, D. L., Lyons, W. B., Welch, K. A. & Mcknight, D. M. Geochemistry of contrasting stream types, Taylor Valley, Antarctica. *Bulletin* **133**, 425–448 (2021).

383. Wadham, J. L., Bottrell, S., Tranter, M. & Raiswell, R. Stable isotope evidence for microbial sulphate reduction at the bed of a polythermal high Arctic glacier. *Earth Planet. Sci. Lett.* **219**, 341–355 (2004).

384. Dreybrodt, W., Lauckner, J., Zaihua, L., Svensson, U. & Buhmann, D. The kinetics of the reaction CO2 + H2O → H+ + HCO-3 as one of the rate limiting steps for the dissolution of calcite in the system H2O-CO2-CaCO3. *Geochim. Cosmochim. Acta* **60**, 3375–3381 (1996).

385. Heidel, C. & Tichomirowa, M. The isotopic composition of sulfate from anaerobic and low oxygen pyrite oxidation experiments with ferric iron - New insights into oxidation mechanisms. *Chem. Geol.* **281**, 305–316 (2011).

386. Sharp, M., Tranter, M., Brown, G. H. & Skidmore, M. Rates of chemical denudation and CO2 drawdown in a glacier-covered alpine catchment. *Geology* **23**, 61–64 (1995).

387. Li, X. *et al.* Intense chemical weathering at glacial meltwater-dominated Hailuogou basin in the southeastern Tibetan Plateau. *Water* **11**, 1–22 (2019).

388. Levin, I. *et al.* Observations and modelling of the global distribution and long-term trend of atmospheric 14CO2. *Tellus, Ser. B Chem. Phys. Meteorol.* **62**, 26–46 (2010).

389. Graven, H. D. Impact of fossil fuel emissions on atmospheric radiocarbon and various applications of radiocarbon over this century. *Proc. Natl. Acad. Sci. U. S. A.* **112**, 9542–9545 (2015).

390. Wilson, A. T. Application of AMS 14C dating to ice core research. *Radiocarbon* **37**, 637–641 (1995).

391. Petrenko, V. V. *et al.* Measurements of 14C in ancient ice from Taylor Glacier, Antarctica constrain in situ cosmogenic 14CH4 and 14CO production rates. *Geochim. Cosmochim. Acta* **177**, 62–77 (2016).

392. Han, T. *et al.* Electrical conductivity during the ablation process of the Glacier No. 1 at the headwaters of the Urumqi River in the Tianshan Mountains. *Arctic, Antarct. Alp. Res.* **47**, 327–334 (2015).

393. Yde, J. C., Riger-Kusk, M., Christiansen, H. H., Knudsen, N. T. & Humlum, O. Hydrochemical characteristics of bulk meltwater from an entire ablation season, Longyearbreen, Svalbard. *J. Glaciol.* **54**, 259–272 (2008).

394. Hodson, A., Tranter, M., Gurnell, A., Clark, M. & Hagen, J. O. The hydrochemistry of Bayelva, a high Arctic proglacial stream in Svalbard. *J. Hydrol.* **257**, 91–114 (2002).

395. McCallister, S. L. & Del Giorgio, P. A. Direct measurement of the δ13C signature of carbon respired by bacteria in lakes: Linkages to potential carbon sources, ecosystem baseline metabolism, and CO2 fluxes. *Limnol. Oceanogr.* **53**, 1204–1216 (2008).

396. Caraco, N., Bauer, J. E., Cole, J. J., Petsch, S. & Raymond, P. Millennial-aged organic carbon subsidies to a modern river food web. *Ecology* **91**, 2385–2393 (2010).

397. Gonzalez Moguel, R. *et al.* Radiocarbon Data Reveal Contrasting Sources for Carbon Fractions in Thermokarst Lakes and Rivers of Eastern Canada (Nunavik, Quebec). *J. Geophys. Res. Biogeosciences* **126**, 1–16 (2021).

398. Keaveney, E. M., Reimer, P. J. & Foy, R. H. Young, old, and weathered carbon - Part 1: using radiocarbon and stable isotopes to idetify carbon sources in an alkaline, humic lake. *Radiocarbon* **57**, 407–423 (2015).

399. Aravena, R., Schiff, S. L., Trumbore, S. E., Dillon, P. J. & Elgood, R. Evaluating dissolved inorganic carbon cycling in a forested lake watershed using carbon isotopes. *Radiocarbon* **34**, 636–645 (1992).

400. Zigah, P. K., Minor, E. C., Werne, J. P. & Leigh McCallister, S. An isotopic (δ14C, δ13C, and δ15N) investigation of the composition of particulate organic matter and zooplankton food sources in Lake Superior and across a size-gradient of aquatic systems. *Biogeosciences* **9**, 3663–3678 (2012).

401. Doran, P. T., Kenig, F., Knoepfle, J. L., Mikucki, J. A. & Berry Lyons, W. Radiocarbon distribution and the effect of legacy in lakes of the McMurdo Dry Valleys, Antarctica. *Limnol. Oceanogr.* **59**, 811–826 (2014).

402. Lawrence, J. P., Doran, P. T., Winslow, L. A. & Priscu, J. C. Subglacial brine flow and wind-induced internal waves in Lake Bonney, Antarctica. *Antarct. Sci.* **32**, 223–237 (2020).

403. Hawkes, J. A. *et al.* Regional diversity of complex dissolved organic matter across forested hemiboreal headwater streams. *Sci. Rep.* **8**, 1–11 (2018).

404. Fellman, J. B., D'Amore, D. V., Hood, E. & Boone, R. D. Fluorescence characteristics and biodegradability of dissolved organic matter in forest and wetland soils from coastal temperate watersheds in southeast Alaska. *Biogeochemistry* **88**, 169–184 (2008).

405. Kalbitz, K. & Wennrich, R. Mobilization of heavy metals and arnseic in polluted wetland soils and its dependence on dissolved organic matter. *Sci. Total Environ.* **209**, 27–39 (1998).

406. Baken, S., Degryse, F., Verheyen, L., Merckx, R. & Smolders, E. Metal complexation properties of freshwater dissolved organic matter are explained by its aromaticity and by anthropogenic ligands. *Environ. Sci. Technol.* **45**, 2584–2590 (2011).

407. Jaffé, R. *et al.* Spatial and temporal variations in DOM composition in ecosystems: The importance of long-term monitoring of optical properties. *J. Geophys. Res. Biogeosciences* **113**, 1–15 (2008).

408. Strock, K. E., Theodore, N., Gawley, W. G., Ellsworth, A. C. & Saros, J. E. Increasing dissolved organic carbon concentrations in northern boreal lakes: Implications for lake water transparency and

thermal structure. *J. Geophys. Res. Biogeosciences* **122**, 1022–1035 (2017).

409. Mopper, K. & Schultz, C. A. Fluorescence as a possible tool for studying the nature and water column distribution of DOC components. *Mar. Chem.* **41**, 229–238 (1993).

410. Kothawala, D. N., von Wachenfeldt, E., Koehler, B. & Tranvik, L. J. Selective loss and preservation of lake water dissolved organic matter fluorescence during long-term dark incubations. *Sci. Total Environ.* **433**, 238–246 (2012).

411. Graeber, D. *et al.* Global effects of agriculture on fluvial dissolved organic matter. *Sci. Rep.* **5**, 1–8 (2015).

412. Yamashita, Y., Fichot, C. G., Shen, Y., Jaffé, R. & Benner, R. Linkages among fluorescent dissolved organic matter, dissolved amino acids and lignin-derived phenols in a river-influenced ocean margin. *Front. Mar. Sci.* **2**, (2015).

413. Fellman, J. B., Petrone, K. C. & Grierson, P. F. Source, biogeochemical cycling, and fluorescence characteristics of dissolved organic matter in an agro-urban estuary. *Limnol. Oceanogr.* **56**, 243–256 (2011).

414. Li, P., Chen, L., Zhang, W. & Huang, Q. Spatiotemporal distribution, sources, and photobleaching imprint of dissolved organic matter in the Yangtze Estuary and its adjacent sea using fluorescence and parallel factor analysis. *PLoS One* **10**, 1–18 (2015).

415. Dainard, P. G., Guéguen, C., Yamamoto-Kawai, M., Williams, W. J. & Hutchings, J. K. Interannual Variability in the Absorption and Fluorescence Characteristics of Dissolved Organic Matter in the Canada Basin Polar Mixed Waters. *J. Geophys. Res. Ocean.* **124**, 5258–5269 (2019).

416. Helms, J. R. *et al.* Photochemical bleaching of oceanic dissolved organic matter and its effect on absorption spectral slope and fluorescence. *Mar. Chem.* **155**, 81–91 (2013).

417. Dainard, P. G., Guéguen, C., McDonald, N. & Williams, W. J. Photobleaching of fluorescent dissolved organic matter in Beaufort Sea and North Atlantic Subtropical Gyre. *Mar. Chem.* **177**, 630–637 (2015).

418. Lapierre, J. F. & Del Giorgio, P. A. Partial coupling and differential regulation of biologically and photochemically labile dissolved organic carbon across boreal aquatic networks. *Biogeosciences* **11**, 5969–5985 (2014).

419. Yamashita, Y. & Jaffé, R. Characterizing the interactions between trace metals and dissolved organic matter using excitation-emission matrix and parallel factor analysis. *Environ. Sci. Technol.* **42**, 7374–7379 (2008).

420. Chen, W. B., Smith, D. S. & Guéguen, C. Influence of water chemistry and dissolved organic matter (DOM) molecular size on copper and mercury binding determined by multiresponse fluorescence quenching. *Chemosphere* **92**, 351–359 (2013).

421. Ohno, T., Amirbahman, A. & Bro, R. Parallel factor analysis of excitation-emission matrix fluorescence spectra of water soluble soil organic matter as basis for the determination of conditional metal binding parameters. *Environ. Sci. Technol.* **42**, 186–192 (2008).

422. Wu, J., Zhang, H., He, P. J. & Shao, L. M. Insight into the heavy metal binding potential of dissolved organic matter in MSW leachate using EEM quenching combined with PARAFAC analysis. *Water Res.* **45**, 1711–1719 (2011).

423. Eusterhues, K. *et al.* Fractionation of organic matter due to reaction with ferrihydrite: Coprecipitation versus adsorption. *Environ. Sci. Technol.* **45**, 527–533 (2011).

424. Chen, C., Dynes, J. J., Wang, J. & Sparks, D. L. Properties of Fe-organic matter associations via coprecipitation versus adsorption. *Environ. Sci. Technol.* **48**, 13751–13759 (2014).

425. Du, Y., Ramirez, C. E. & Jaffé, R. Fractionation of Dissolved Organic Matter by Co-Precipitation with

Iron: Effects of Composition. *Environ. Process.* **5**, 5–21 (2018).

426. Pullin, M. J., Anthony, C. & Maurice, P. A. Effects of iron on the molecular weight distribution, light absorption, and fluorescence properties of natural organic matter. *Environ. Eng. Sci.* **24**, 987–997 (2007).

427. Poulin, B. A., Ryan, J. N. & Aiken, G. R. Supporting Information The effects of iron on optical properties of dissolved organic matter. *Environ. Sci. Technol.* **48**, 1–20 (2014).

428. Neubauer, E., Köhler, S. J., Von Der Kammer, F., Laudon, H. & Hofmann, T. Effect of pH and stream order on iron and arsenic speciation in boreal catchments. *Environ. Sci. Technol.* **47**, 7120–7128 (2013).

429. Xiao, Y. H. *et al.* The effect of iron on the biodegradation of natural dissolved organic matter. *J. Geophys. Res. Biogeosciences* **121**, 2544–2561 (2016).

430. Senesi, N. Molecular and quantitative aspects of the chemistry of fulvic acid and its interactions with metal ions and organic chemicals. Part II. The fluorescence spectroscopy approach. *Anal. Chim. Acta* **232**, 77–106 (1990).

431. Patel-Sorrentino, N., Mounier, S. & Benaim, J. Y. Excitation-emission fluorescence matrix to study pH influence on organic matter fluorescence in the Amazon basin rivers. *Water Res.* **36**, 2571–2581 (2002).

432. Spencer, R. G. M., Bolton, L. & Baker, A. Freeze/thaw and pH effects on freshwater dissolved organic matter fluorescence and absorbance properties from a number of UK locations. *Water Res.* **41**, 2941–2950 (2007).

433. Yan, M., Fu, Q., Li, D., Gao, G. & Wang, D. Study of the pH influence on the optical properties of dissolved organic matter using fluorescence excitation-emission matrix and parallel factor analysis. *J. Lumin.* **142**, 103–109 (2013).

434. Rosamond, M. S. Nitrous oxide and nitrate in the Grand River , Ontario : Sources , production pathways and predictability by. (University of Waterloo, 2013).

435. Kalbitz, K., Schmerwitz, J., Schwesig, D. & Matzner, E. Biodegradation of soil-derived dissolved organic matter as related to its properties. *Geoderma* **113**, 273–291 (2003).

436. Cory, R. M. & McKnight, D. M. Fluorescence spectroscopy reveals ubiquitous presence of oxidized and reduced quinones in dissolved organic matter. *Environ. Sci. Technol.* **39**, 8142–8149 (2005).

437. Kothawala, D. N. *et al.* Controls of dissolved organic matter quality: Evidence from a large-scale boreal lake survey. *Glob. Chang. Biol.* **20**, 1101–1114 (2014).

438. Graeber, D., Gelbrecht, J., Pusch, M. T., Anlanger, C. & von Schiller, D. Agriculture has changed the amount and composition of dissolved organic matter in Central European headwater streams. *Sci. Total Environ.* **438**, 435–446 (2012).

439. Kellerman, A. M., Kothawala, D. N., Dittmar, T. & Tranvik, L. J. Persistence of dissolved organic matter in lakes related to its molecular characteristics. *Nat. Geosci.* **8**, 454–457 (2015).

440. Lupon, A., Catalán, N., Martí, E. & Bernal, S. Influence of dissolved organic matter sources on in-stream net dissolved organic carbon uptake in a mediterranean stream. *Water* **12**, (2020).

441. Esteves Da Silva, J. C. G., MacHado, A. A. S. C., Oliveira, C. J. S. & Pinto, M. S. S. D. S. Fluorescence quenching of anthropogenic fulvic acids by Cu(II), Fe(III) and UO2/2+. *Talanta* **45**, 1155–1165 (1998).

442. Piana, M. J. & Zahir, K. O. Investigation of metal ions binding of humic substances using fluorescence emission and synchronous-scan spectroscopy. *J. Environ. Sci. Heal. - Part B Pestic. Food Contam. Agric. Wastes* **35**, 87–102 (2000).

443. Downing, B. D., Pellerin, B. A., Bergamaschi, B. A., Saraceno, J. F. & Kraus, T. E. C. Seeing the light: The effects of particles, dissolved materials, and temperature on in situ measurements of DOM

fluorescence in rivers and streams. *Limnol. Oceanogr. Methods* **10**, 767–775 (2012).

444. Lakowicz, J. R. *Principles of fluorescence spectroscopy*. *Principles of Fluorescence Spectroscopy* (2006). doi:10.1007/978-0-387-46312-4.

445. Jia, K., Manning, C., Jollymore, A. & Beckie, R. Technical note: Effects of iron(II) on fluorescence properties of dissolved organic matter at circumneutral pH. *Hydrol. Earth Syst. Sci. Discuss.* 1–18 (2020) doi:10.5194/hess-2020-150.

446. Kothawala, D. N., Murphy, K. R., Stedmon, C. A., Weyhenmeyer, G. A. & Tranvik, L. J. Inner filter correction of dissolved organic matter fluorescence. *Limnol. Oceanogr. Methods* **11**, 616–630 (2013).

447. Sgroi, M., Gagliano, E., Vagliasindi, F. G. A. & Roccaro, P. Inner filter effect, suspended solids and nitrite/nitrate interferences in fluorescence measurements of wastewater organic matter. *Sci. Total Environ.* **711**, (2020).

448. Pace, M. L. *et al.* pH change induces shifts in the size and light absorption of dissolved organic matter. *Biogeochemistry* **108**, 109–118 (2012).

449. Lu, Q., Yuan, Y., Tao, Y. & Tang, J. Environmental pH and ionic strength influence the electron-transfer capacity of dissolved organic matter. *J. Soils Sediments* **15**, 2257–2264 (2015).

450. Westerhoff, P., Chen, W. & Esparza, M. Fluorescence Analysis of a Standard Fulvic Acid and Tertiary Treated Wastewater. *J. Environ. Qual.* **30**, 2037–2046 (2001).

451. Rubinson, M. Clayton, R. N. Carbon-13 fractionation between aragonite and calcite. *Geochim. Cosmochim. Acta* **33**, 997–1002 (1969).

452. Romanek, C.S. Grossman, E. Morse, J. W. Carbon isotopic fractionation in synthetic aragonite and calcite: effects of temperature and precipitation rate. *Geochim. Cosmochim. Acta* **56**, 419–430 (1992).

453. Bottinga, Y. Calculation of fractionation factors for carbon and oxygen isotopic exchange in the system calcite-carbon dioxide-water. *J. Phys. Chem.* **72**, 800–808 (1968).

454. McIntyre, A. M. & Guéguen, C. Binding interactions of algal-derived dissolved organic matter with metal ions. *Chemosphere* **90**, 620–626 (2013).

455. Garcia, R. D., Reissig, M., Queimaliños, C. P., Garcia, P. E. & Dieguez, M. C. Climate-driven terrestrial inputs in ultraoligotrophic mountain streams of Andean Patagonia revealed through chromophoric and fluorescent dissolved organic matter. *Sci. Total Environ.* **521**–**522**, 280–292 (2015).

456. Guéguen, C. & Cuss, C. W. Characterization of aquatic dissolved organic matter by asymmetrical flow field-flow fractionation coupled to UV-Visible diode array and excitation emission matrix fluorescence. *J. Chromatogr. A* **1218**, 4188–4198 (2011).

Appendix A

Chapter 3 – Supplementary Information

Sampling Year	Meltwater Flow Conditions	Research Chapters
2015	High	3
2016	Medium-High	3+4
2017	Low	3+4
2018	Very Low	3+4
2019	High	4

Figure S3.1A-F: Rough estimate of flow conditions spanning sampling years (2015 to 2019), based on modelled runoff for 2015-16 from another study[95] (used for flow-weighted calculations), in field observations, and dialogue with Water Survey Canada (i.e., Ruggles River stage data). Also noted, are the research chapters relevant for each sampling year.

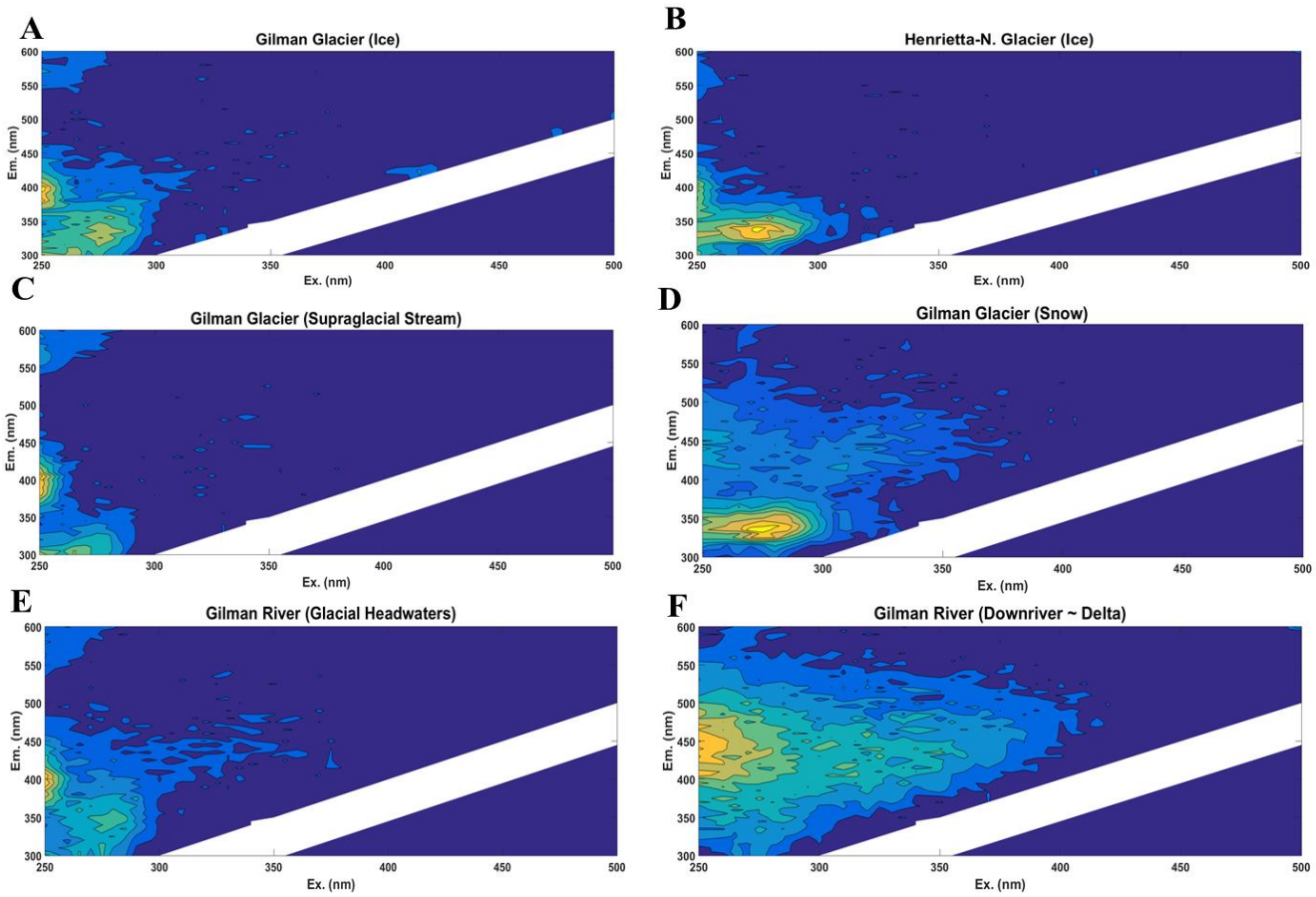

Figure S3.2A-F: Excitation emission matrix spectra (EEMS) for a **(A)** glacial ice, **(C)** supraglacial stream, **(D)** snow, **(E)** glacial headwater, and **(F)** downriver site for the Gilman River sampled during July 2017. A glacial ice sample **(B)** from the Henrietta-Nesmith glacier (July 2017) is also depicted.

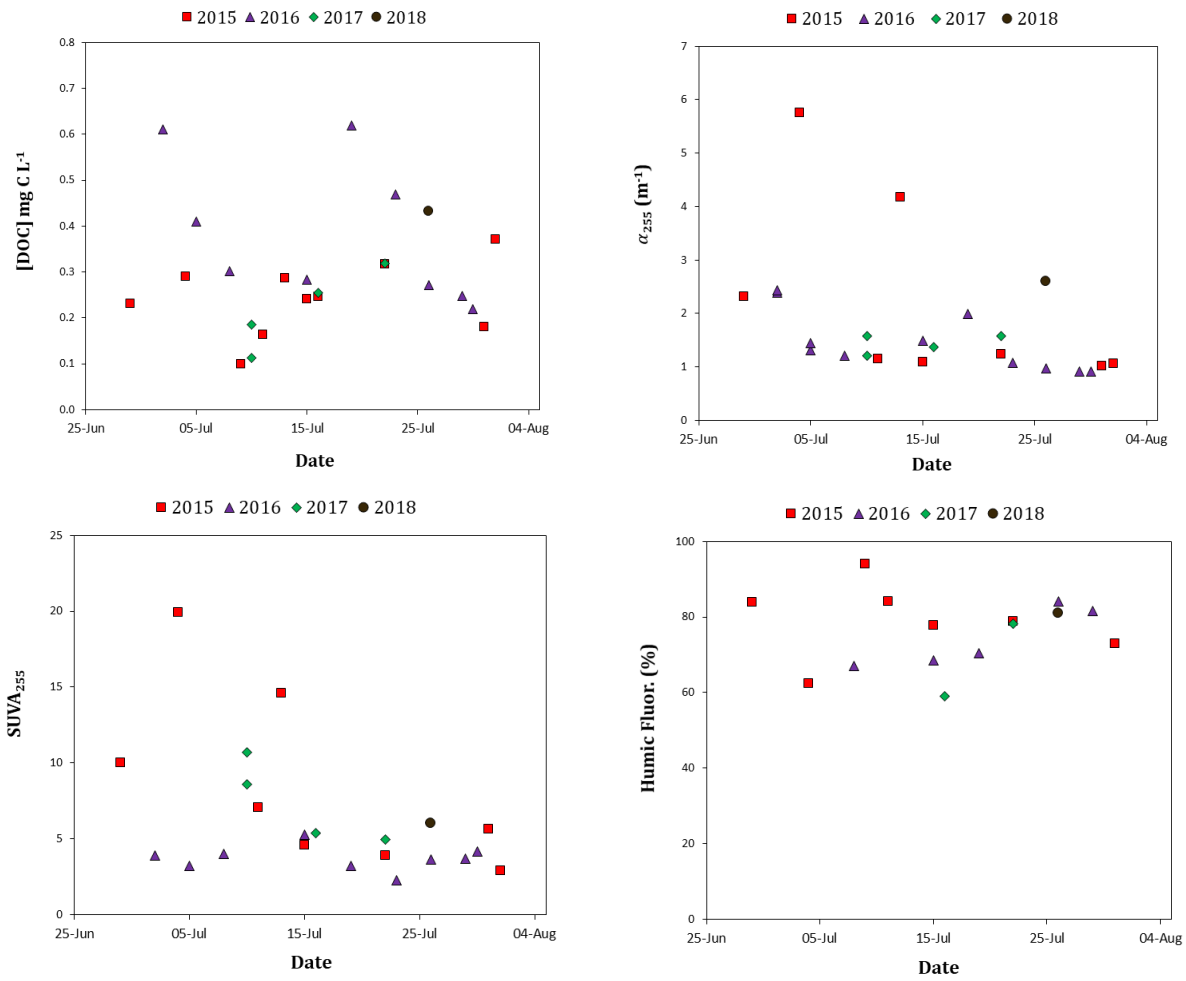

Figure S3.3A-B: Temporal variability in DOC concentration, α_{255}, $SUVA_{255}$, and humic fluorescence (%) for downriver sites (i.e. river deltas) of **(A)** Blister River and **(B)** Snowgoose River during 2015 to 2018.

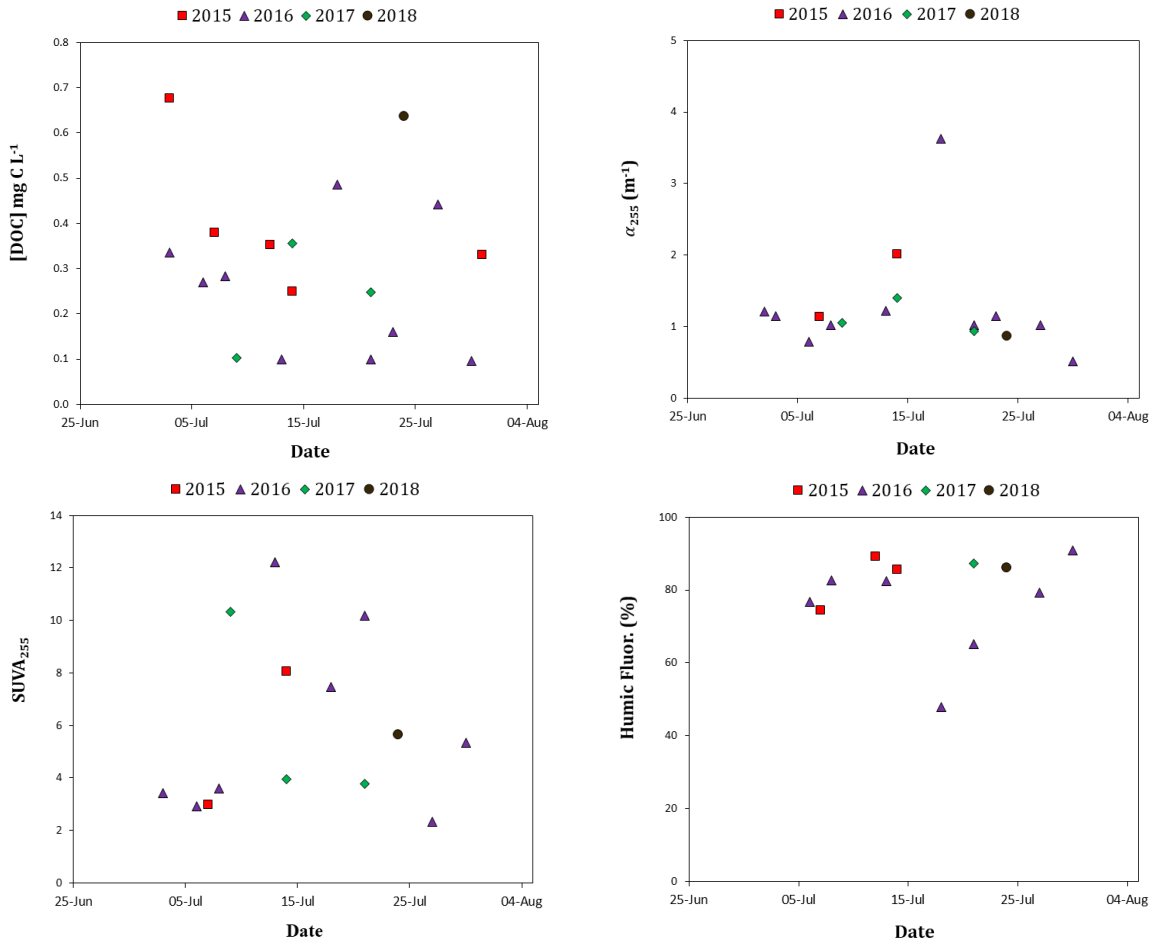

Figure S3.3A-B (*continued*): Temporal variability in DOC concentration, α_{255}, $SUVA_{255}$, and humic fluorescence (%) for downriver sites (i.e. river deltas) of **(A)** Blister River and **(B)** Snowgoose River during 2015 to 2018.

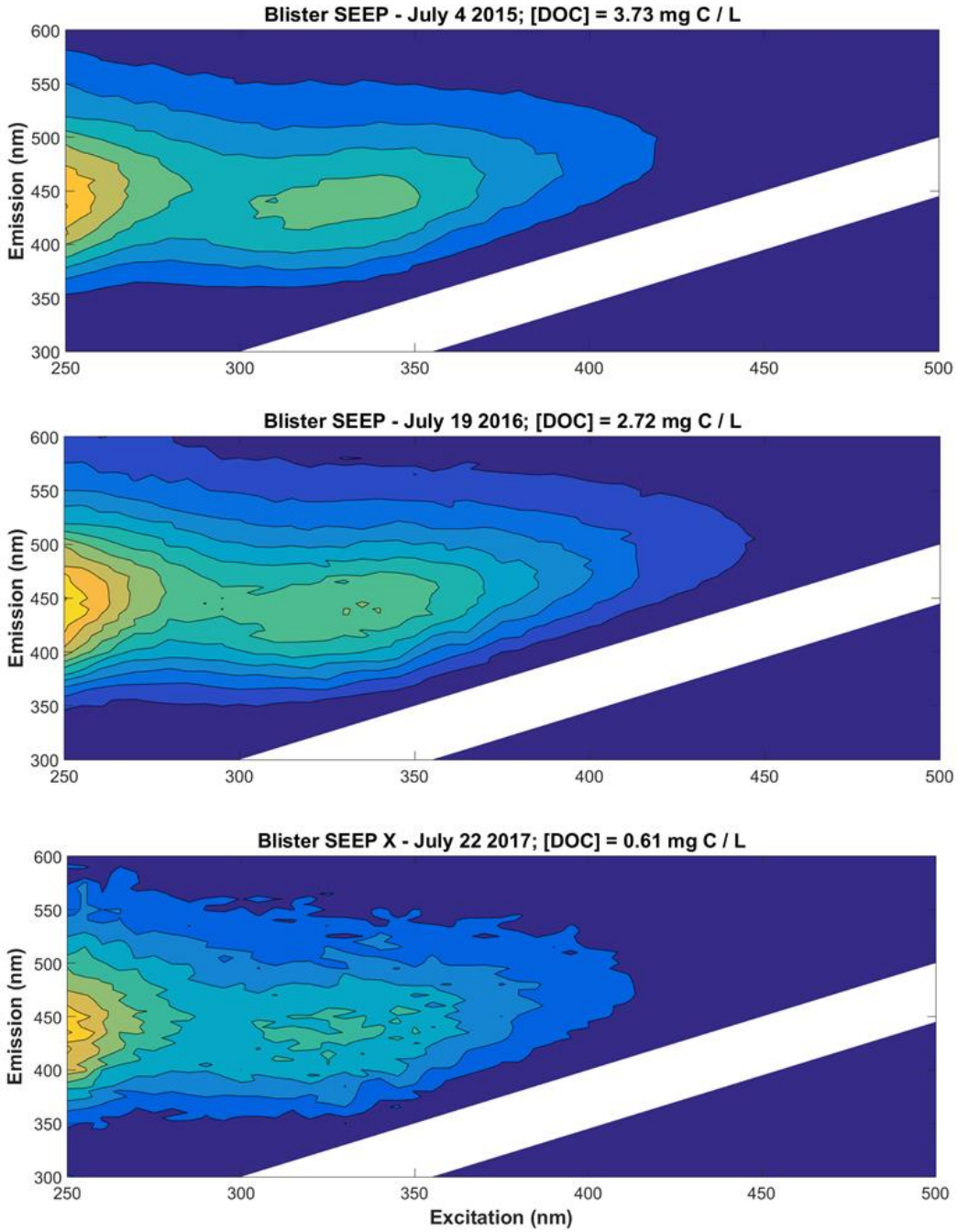

Figure S3.4: Excitation emission matrix spectra (EEMS) for an overland seepage site sampled along the Blister River (Blister SEEP) during July of 2015 and 2016. During the low flow year (2017) this site was not observed to be flowing and was sampled instead on the other side of the river (Blister SEEP X).

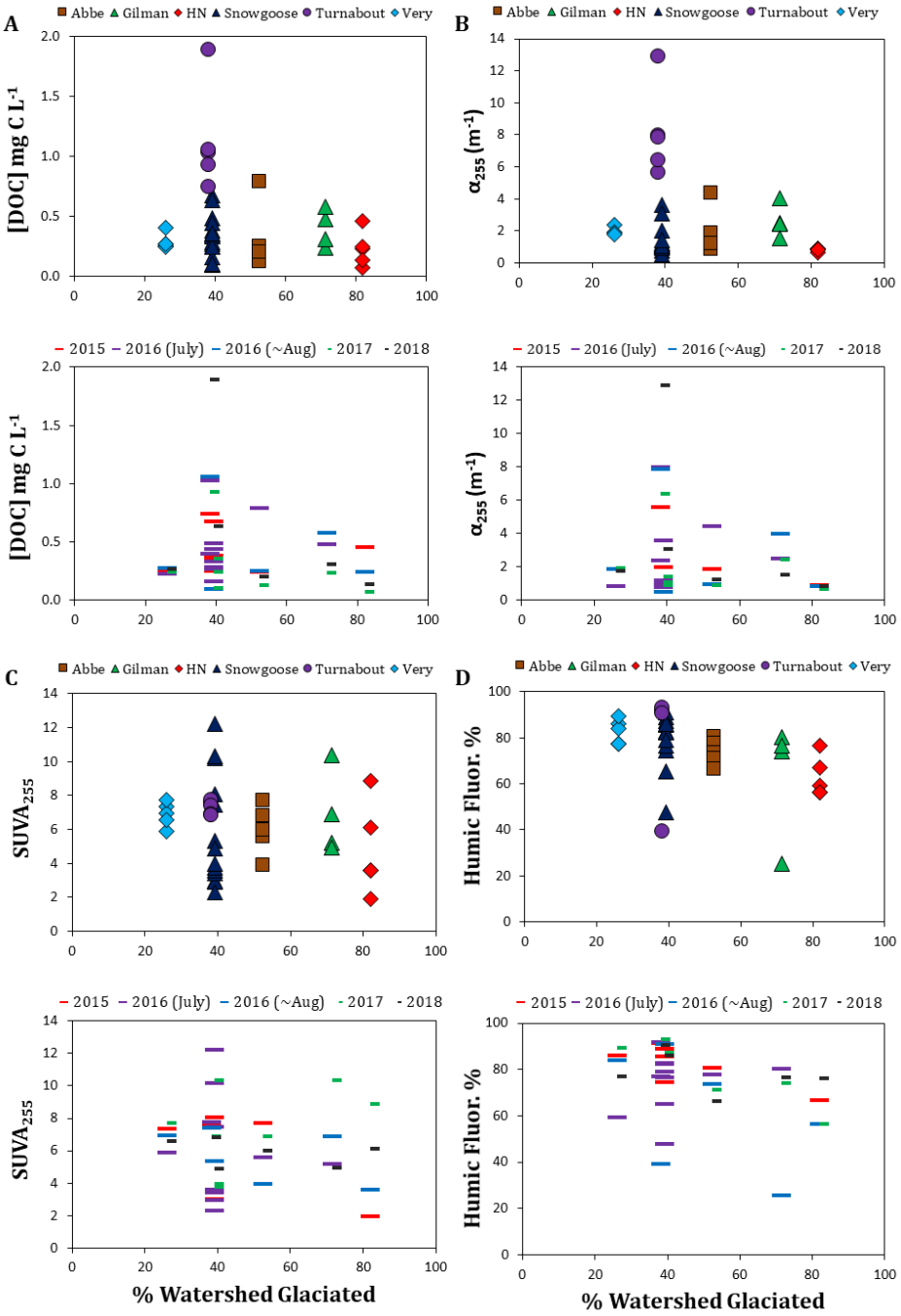

Figure S3.5: Percent of the watershed surface area that was glaciated versus **(A)** DOC concentrations, **(B)** absorption coefficient at 255 nm (α_{255}), **(C)** specific ultraviolet absorption ($SUVA_{255}$) %, **(D)** humic fluorescence %, proportions of **(E)** humic substances **(F)** low molecular weight neutrals (LMW-N) and **(G)** biopolymers from SEC data, and **(H)** Δ^{14}C-DOC for sampling years spanning 2015 to 2018. **see following page**

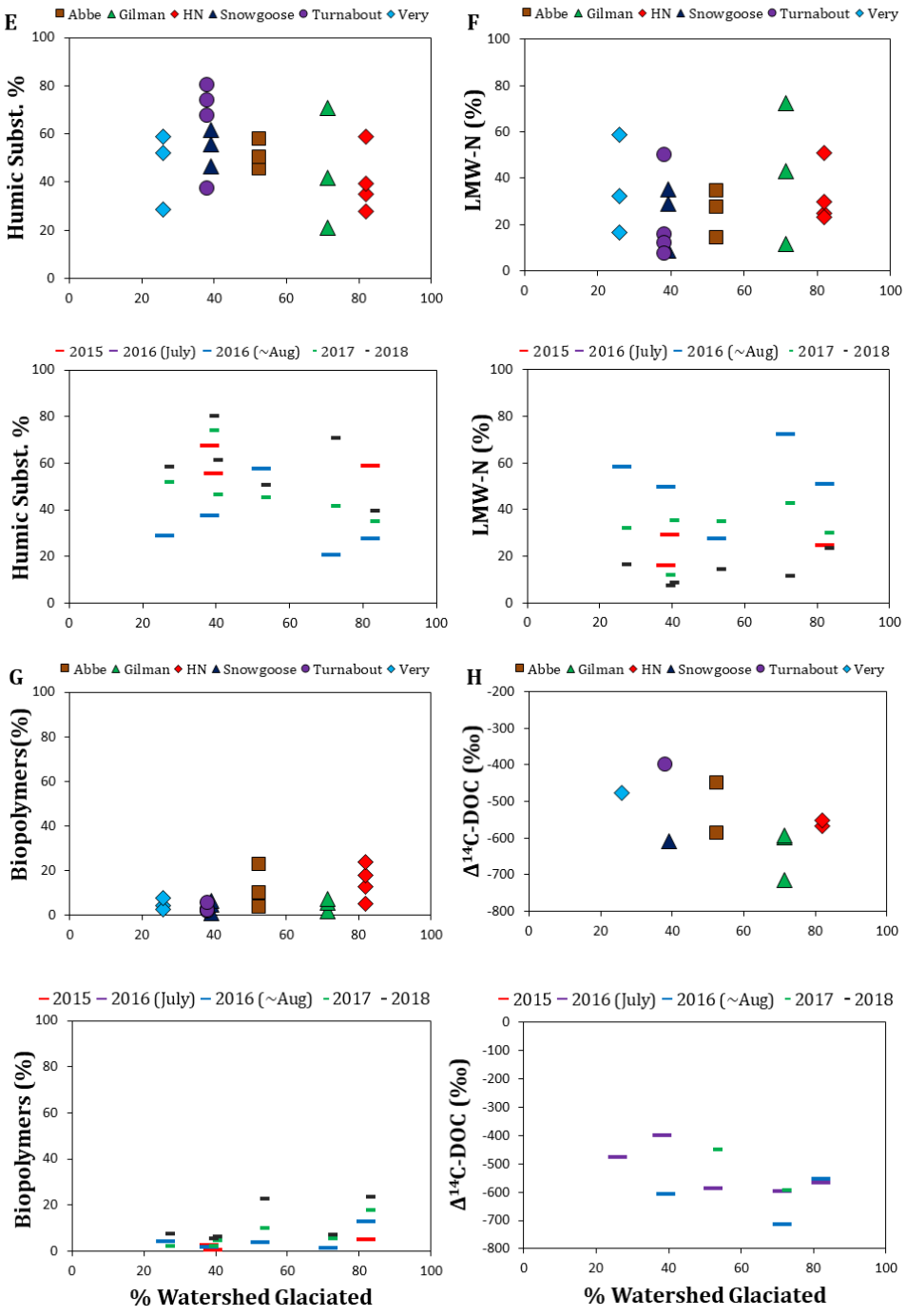

Figure S3.5 (*continued*): Note that samples were all taken at downriver sites proximal to the delta, apart from Henrietta-Nesmith River that was sampled <1 km from the glacier terminus. ~Aug 2016 includes a sample of Snowgoose delta taken July 30th 2016 (i.e., before the 2nd helicopter survey).

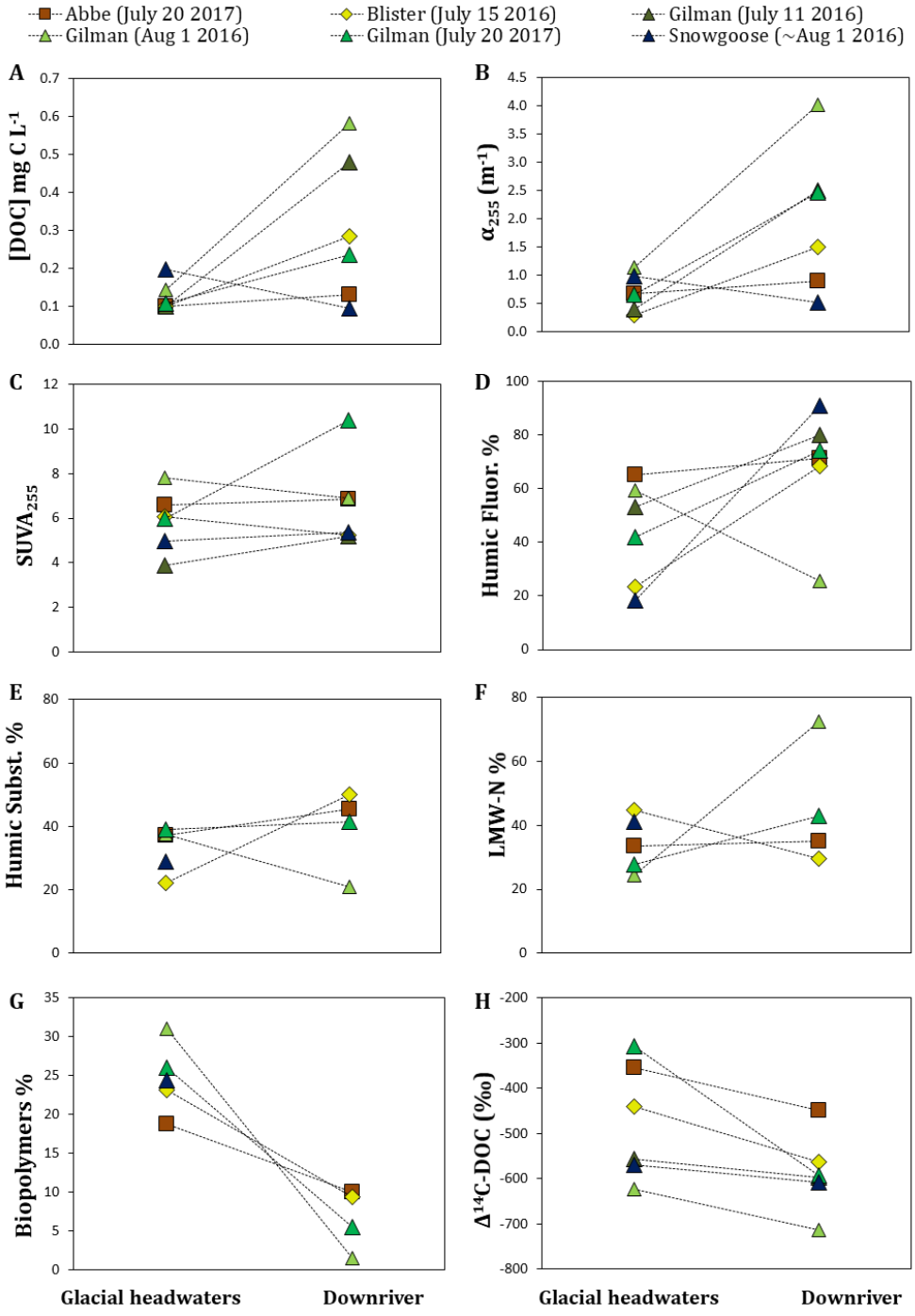

Figure S3.6-H: (A) DOC concentrations, **(B)** absorption coefficient at 255 nm (α_{255}), **(C)** specific ultraviolet absorption coefficient $SUVA_{255}$, **(D)** humic fluorescence %, proportions of **(E)** humic substances, **(F)** low molecular weight neutrals (LMW-N) and **(G)** biopolymers from SEC data**,** and **(H)** radiocarbon (Δ^{14}C-DOC) along the 6 glacial river transects for which Δ^{14}C-DOC was quantified. Note: Snowgoose delta sample was collected on July 30 2016.

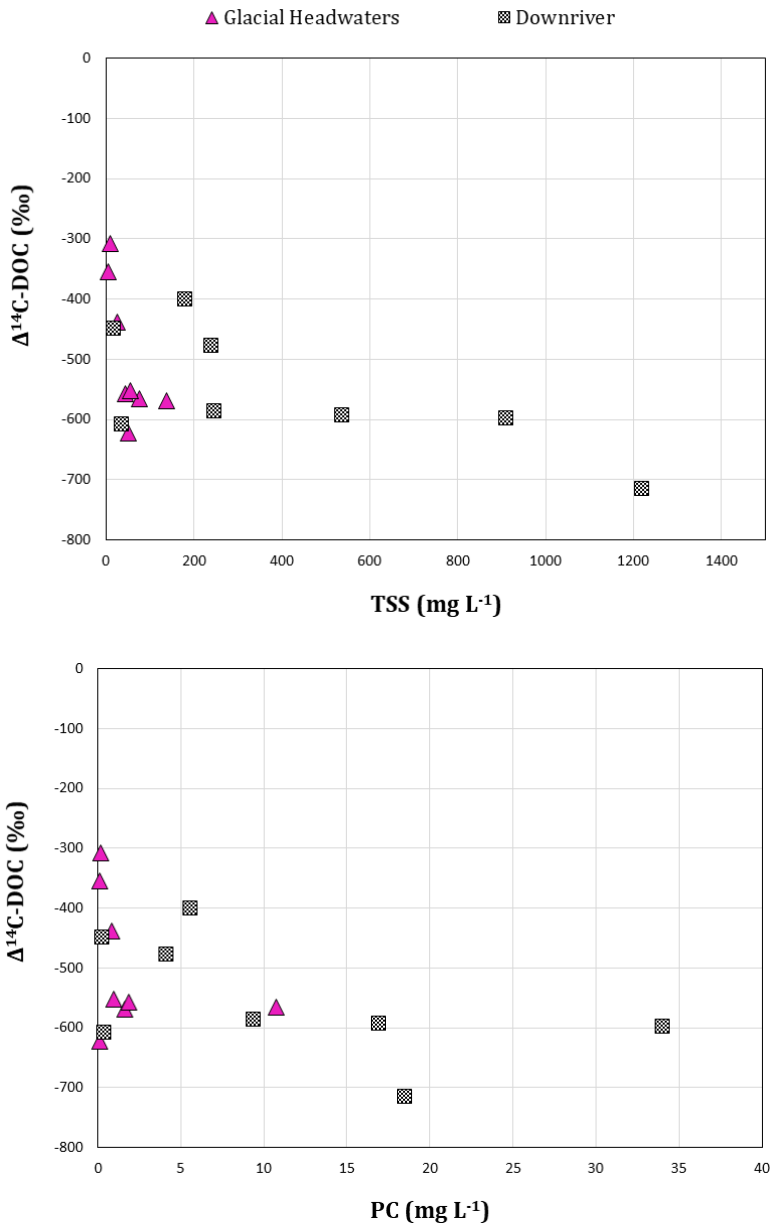

Figure S3.7: Total suspended solids (TSS) and particulate carbon (PC) concentrations versus Δ^{14}C-DOC for samples collected from glacial headwaters and downriver sites.

Appendix B

Chapter 4 – Supplementary Information

pH and DIC to define carbonate speciation and calculate theoretical δ^{13}C-DIC

Measured pH and [DIC] were used to calculate concentrations of carbonate species:

$$[CO_2] = \frac{[DIC]}{\left(1 + \frac{K_1}{H^+} + \frac{K_1 K_2}{(H^+)^2}\right)} \quad , \quad [HCO_3^-] = \frac{[DIC]}{\left(1 + \frac{H^+}{K_1} + \frac{K_2}{H^+}\right)} \quad , \quad [CO_3^{2-}] = \frac{[DIC]}{\left(1 + \frac{(H^+)^2}{K_1 K_2} + \frac{H^+}{K_2}\right)}$$

This calculation approach assumes that the carbonate system is at chemical equilibrium, and yields a pH and temperature dependent relationship that is reflected in calculations of δ^{13}C-DIC:

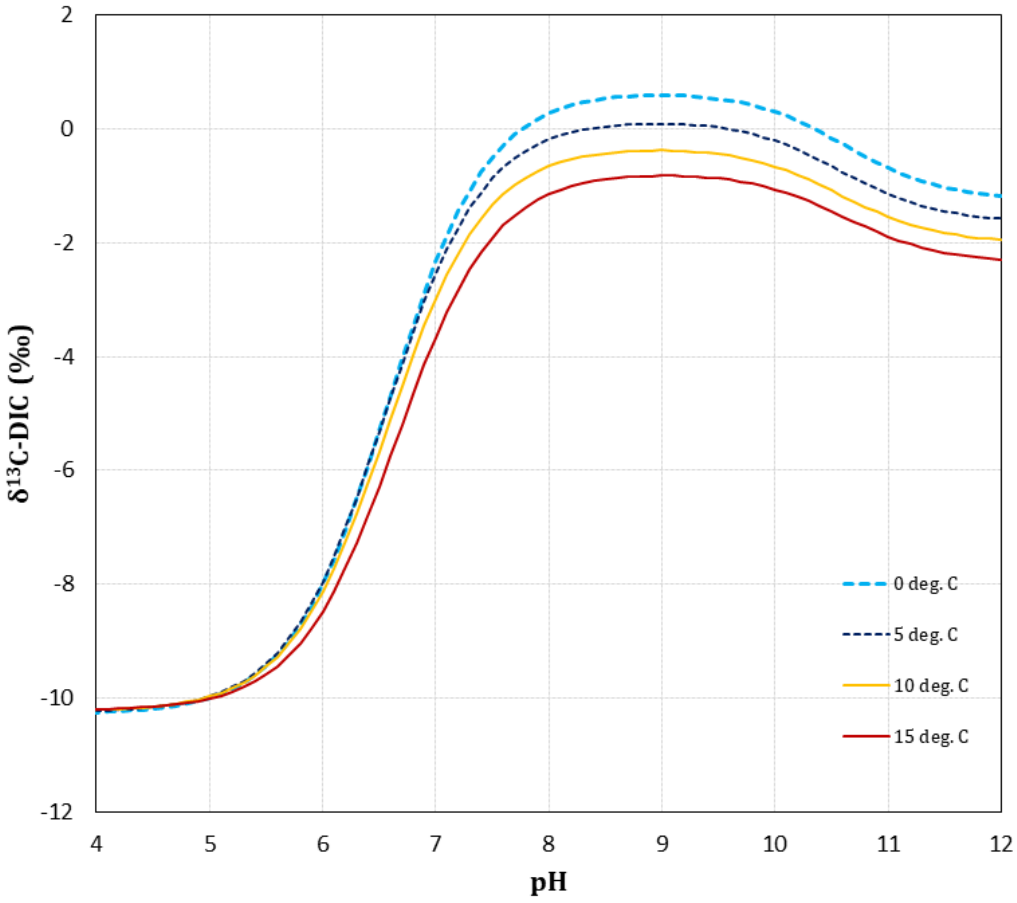

Figure S4.1: Relationship of theoretical equilibrium δ^{13}C-DIC (‰) with pH for different temperatures.

CO_2 and DIC to calculate pH, carbonate species, and theoretical $\delta^{13}C$-DIC

A scenario was tested in which the carbonate system was defined based on measured dissolved CO_2 and DIC concentrations. The following calculation of H^+ required rearrangement in the form of ($ax^2 + bx + c = 0$) prior to integration to the quadratic equation:

$$DIC\ (H^+)^2 = CO_2\ ((H^+)^2 + K_1H^+ + K_1K_2)$$

$$(CO_2 - DIC)(H^+)^2 + (CO_2K_1)H^+ + (CO_2K_1K_2) = 0$$

$$x = \frac{-b \pm \sqrt{b^2 - 4ac}}{2a} \quad , \quad H^+ = \frac{-CO_2K_1 \pm \sqrt{(CO_2K_1)^2 - 4(CO_2 - DIC)(CO_2K_1K_2)}}{2(CO_2 - DIC)}$$

Concentrations of HCO_3^- and CO_3^{2-} were then determined, which allowed for a newly defined carbonate system. At low [DIC] <100 µM changes in measured [CO_2] become more impactful to carbonate speciation and theoretical calculated pH. Such low [DIC] conditions are common in glacial headwater samples, for which the calculated pH deviate from the 1:1 line when plotted against measured pH:

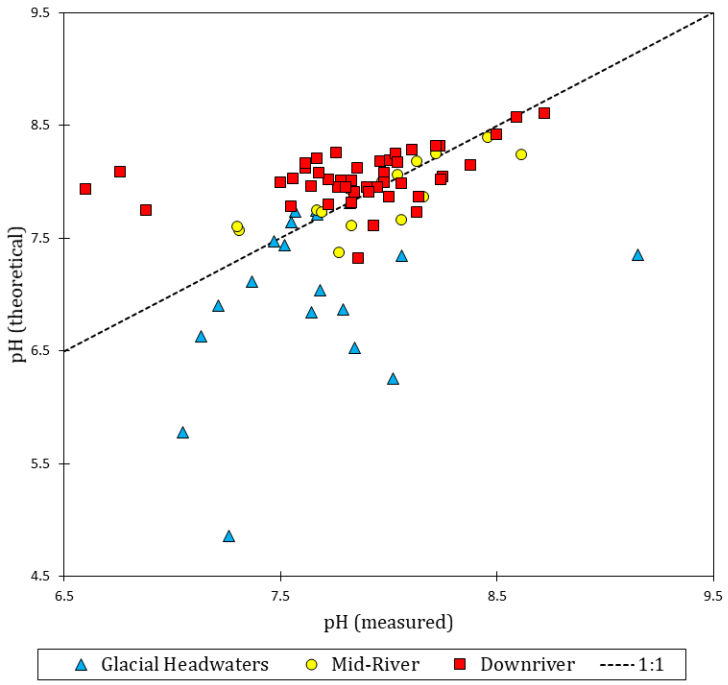

Figure S4.2: Relationship of measured pH with theoretical pH using [CO_2], [DIC], and temperature for samples taken from glacial headwater, mid-river, and downriver sites.

Accordingly, low [DIC] < 100 µM samples also show greater impact to theoretical δ^{13}C-DIC calculations spanning a range of input [CO_2], as illustrated in the following:

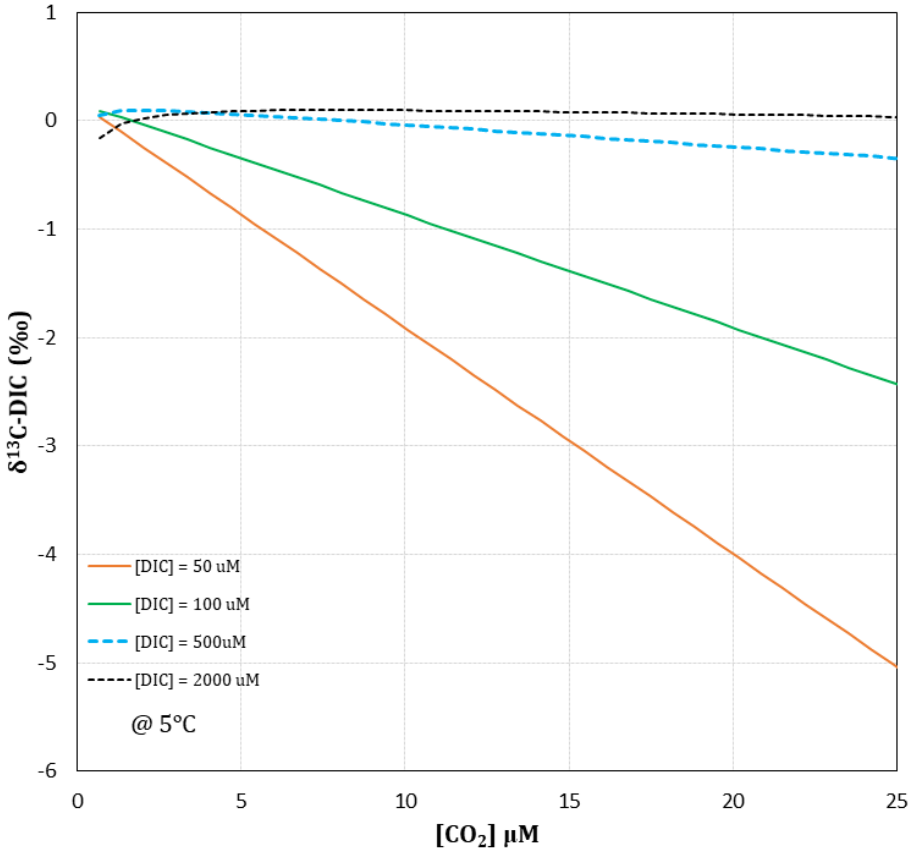

Figure S4.3: Relationship of theoretical δ^{13}C-DIC (‰) with [CO_2], derived for different [DIC] and a fixed temperature of 5ºC.

Comparison of calculation approaches for theoretical equilibrium δ^{13}C-DIC

Testing the leverage of input parameters ([DIC], [CO_2], pH) on carbonate speciation and theoretical equilibrium δ^{13}C-DIC was important to support interpretations of these values and comparisons with actual laboratory measured δ^{13}C-DIC values. Theoretical equilibrium δ^{13}C-DIC values calculated using pH were plotted against those calculated using [CO_2] and [DIC], for which observations along the 1:1 line suggested agreement between the calculation approaches (**Fig. S4.4A**). The 4 downriver samples with anomalously low pH values plotted well below the 1:1 line, as inferred equilibrium carbonate speciation from pH was not harmonious with measured [DIC] and pCO_2.

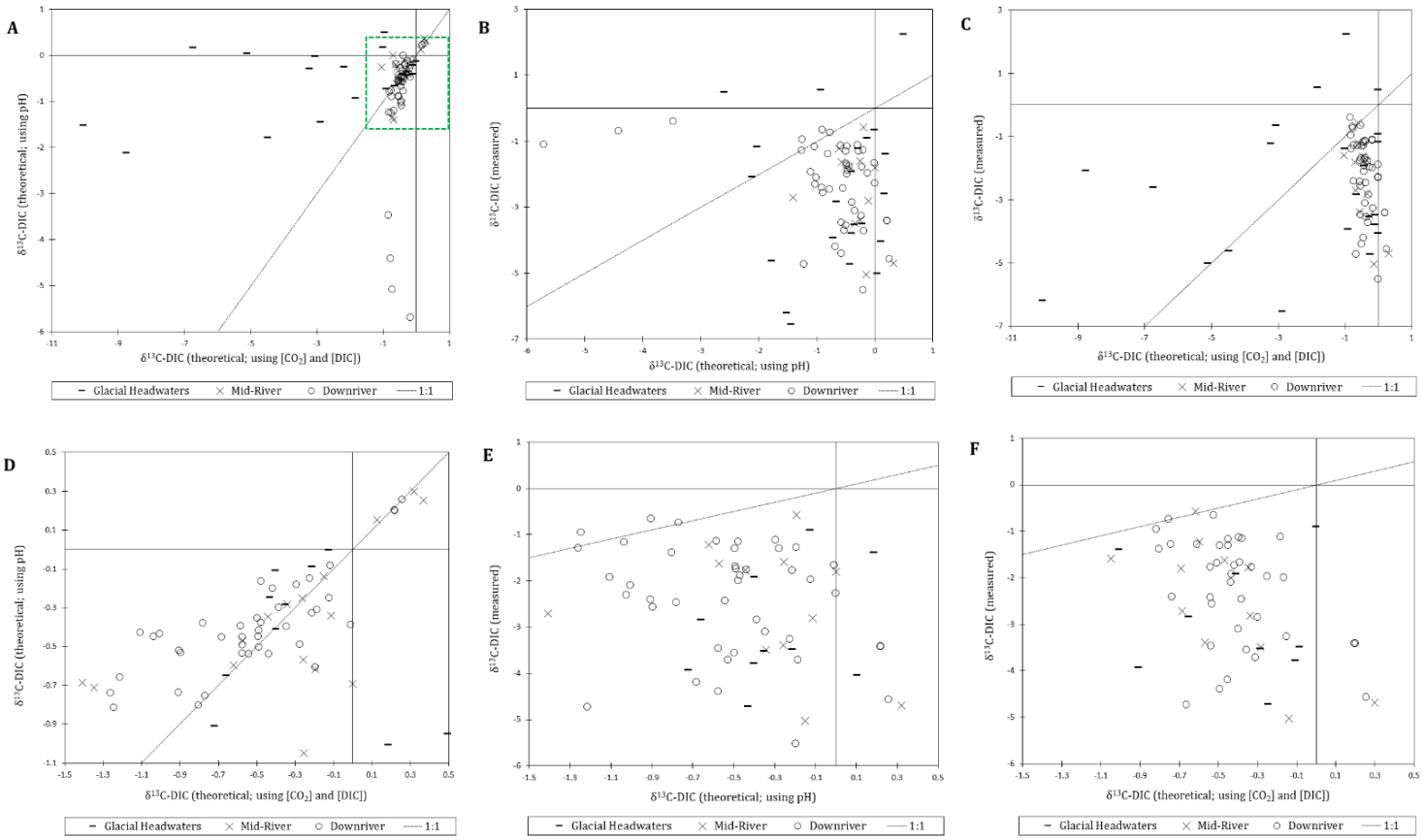

Figure S4.4: (A) Theoretical equilibrium δ^{13}C-DIC calculated using different measured components of the carbonate system (measured pH versus measured $[CO_2]$ and [DIC]). **(B-C)** Each theoretical δ^{13}C-DIC was then plotted against its corresponding measured δ^{13}C-DIC values. All δ^{13}C-DIC values were reported in per mille (‰), and were plotted alongside 1:1 lines. **(D-F)** Companion figures in which only the subset of samples that returned comparable results using either theoretical calculation approach was plotted (i.e. this data subset is highlighted within a green box in Figure 4.1A)

Many glacial headwater samples plotted above the 1:1 line based on their extremely low [DIC], which put more leverage on [CO_2] in the calculations. The remainder of samples that coincided closely with the 1:1 were more robust representations of theoretical equilibrium δ^{13}C-DIC, for which the vast majority of calculated values ranged from -1.5 to 0.5 ‰ using either calculation approach (highlighted by a green box; **Fig. S4.4A**). This subset of samples showed distinct distributions in measured δ^{13}C-DIC versus theoretical equilibrium δ^{13}C-DIC values when compared to the complete dataset (**Fig. S4.4B-C**). The subset of samples with more reproducible theoretical δ^{13}C-DIC values plotted almost exclusively below the 1:1 line for glacial headwaters, mid-river, and downriver sites, shifting towards more negative measured δ^{13}C-DIC values (**Fig. S4.4D-F**). This was indicative of a departure in measured δ^{13}C-DIC from that which would be expected under equilibrium conditions.

CO_3^{2-} and DIC to calculate pH, carbonate species, and theoretical δ^{13}C-DIC

The carbonate system could also be defined in a scenario where CO_3^{2-} was increased incrementally. The following recalculation of H^+ integrates changes to DIC concentration based on the increased molar concentrations of CO_3^{2-}:

$$CO_3^{2-}\left(1+\frac{H^+}{K_2}+\frac{(H^+)^2}{K_1K_2}\right)=DIC$$

$$CO_3^{2-}+\frac{CO_3^{2-}(H^+)}{K_2}+\frac{CO_3^{2-}(H^+)^2}{K_1K_2}-DIC=0$$

$$\left(\frac{CO_3^{2-}}{K_1K_2}\right)(H^+)^2+\frac{CO_3^{2-}}{K_2}(H^+)+\left(CO_3^{2-}-DIC\right)=0$$

$$x=\frac{-b\pm\sqrt{b^2-4ac}}{2a} \quad , \quad H^+=\frac{-\left(\frac{CO_3^{2-}}{K_2}\right)\pm\sqrt{\left(\frac{CO_3^{2-}}{K_2}\right)^2-4\left(\frac{CO_3^{2-}}{K_1K_2}\right)\left(CO_3^{2-}-DIC\right)}}{2\left(\frac{CO_3^{2-}}{K_1K_2}\right)}$$

For this scenario (at 5ºC), the theoretical equilibrium δ^{13}C-DIC was plotted for samples with initial [DIC] of 50, 100, 500, and 2000 µm across a range of [CO_3^{2-}]. This distribution spans a shift in carbonate speciation from HCO_3^- to a CO_3^{2-} dominated systems. The difference in $\varepsilon^{13}C_{HCO3\text{-}CO2(g)}$ and $\varepsilon^{13}C_{CO3\text{-}CO2(g)}$ is small and of little consequence for slightly alkaline (pH ~7 to 8.5) conditions typical

of glacial rivers in the Lake Hazen watershed where the fractional contributions of CO_3^{2-} to DIC were typically <1%. Even so, the effect of increasing CO_3^{2-} to δ^{13}C-DIC is acknowledged in the following:

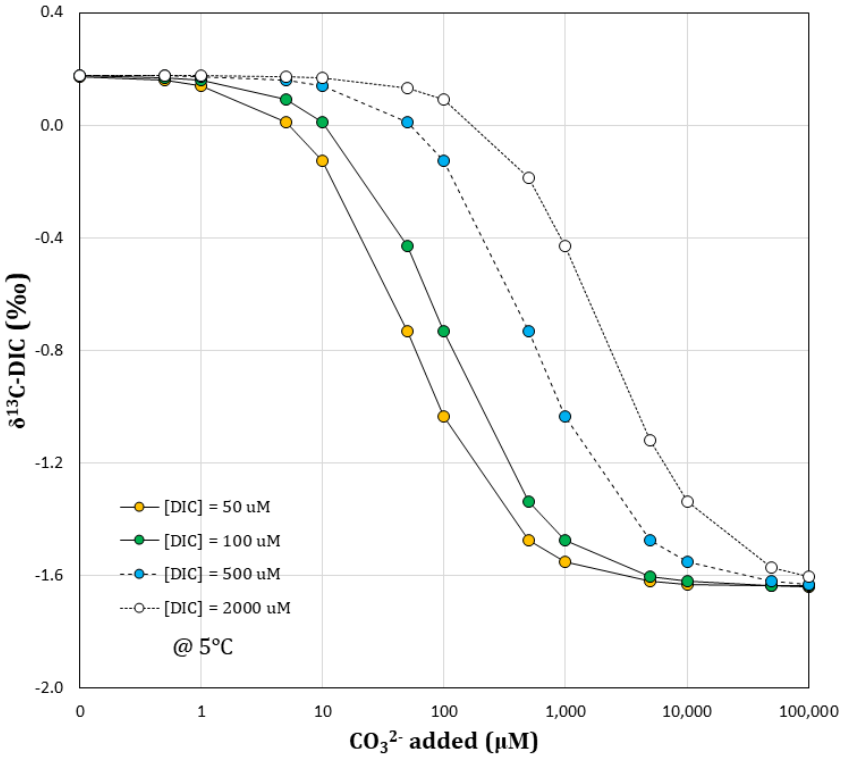

Figure S4.5: Relationship of δ^{13}C-DIC with increased CO_3^{2-} for samples with a range of initial DIC concentrations and a fixed temperature of 5ºC.

Isotopic enrichment factors for HCO_3^- relative to $CaCO_3$

The equilibrium for the precipitation and dissolution of calcite can be described by the following chemical reaction:

$$CaCO_{3(s)} + H_2O \longleftrightarrow Ca^{2+} + HCO_3^- + OH^-$$

Isotopic fractionation associated with calcite precipitation has been reported to be largely independent of temperature for experiments conducted at 10, 25, and 75ºC with a small enrichment factor relative to bicarbonate ($\varepsilon^{13}C_{CaCO3\text{-}HCO3}$ ~ 1.0 ‰) compared to that of aragonite, a polymorph of calcite, ($\varepsilon^{13}C_{CaCO3\text{-}HCO3}$ ~ 2.7 ‰)[451,452]. On the other hand, calculated $\varepsilon^{13}C_{CaCO3\text{-}HCO3}$ have also been suggested to show a slight temperature dependence, which becomes more significant at colder temperatures[111]. This relationship was used to predict the $\varepsilon^{13}C_{HCO3\text{-}CaCO3}$ for the reverse process, $CaCO_3$ dissolution, in

the following plot (approach **#1**). This is compared to an alternative approach (**#2**) in which $\varepsilon^{13}C_{CO2(g)\text{-}CaCO3}$[453] was first determined, followed by chemical fractionation to HCO_3^- ($\varepsilon^{13}C_{HCO3\text{-}CO2(g)}$)[367] to calculate net $\varepsilon^{13}C_{HCO3\text{-}CaCO3}$ (‰):

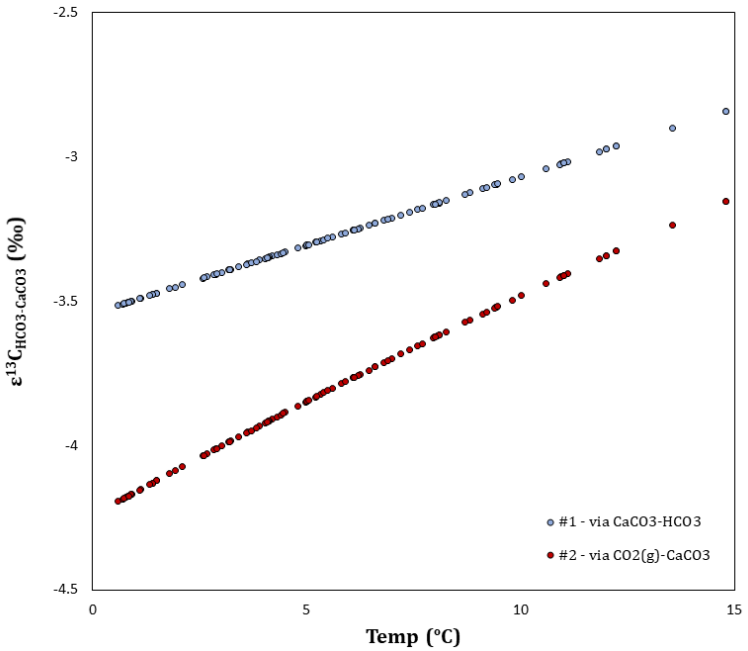

Figure S4.6: Isotopic enrichment factors for HCO_3^- relative to $CaCO_3$ ($\varepsilon^{13}C_{HCO3\text{-}CaCO3}$) spanning a range of temperatures using **(#1)** a regression of calculated values for $CaCO_3$ precipitation, and **(#2)** using $\varepsilon^{13}C_{CO2(g)\text{-}CaCO3}$ followed by $\varepsilon^{13}C_{HCO3\text{-}CO2(g)}$.

Depending on the carbonate mineral end-member (δ^{13}C-PIC), these $\varepsilon^{13}C_{HCO3\text{-}CaCO3}$ could explain some isotopic depletion in δ^{13}C-DIC. However, these effects would be greatest assuming a model closed system in which $CaCO_3$ was the sole source of DIC and there was no atmospheric exchange or mixing, which was unrealistic for proglacial meltwaters stemming from cold-based glaciers of the Lake Hazen watershed. δ^{13}C-CO_2 in equilibrium with a solid phase $CaCO_3$ of known δ^{13}C can also be calculated using the following relationship[453]:

$$CO_{2(g-water)} - CaCO_{3(s)} \rightarrow 1000 \ln \alpha = \left(-2.9880 * \frac{10^6}{T^2}\right) + \left(7.6663 * \frac{10^3}{T}\right) - 2.4612$$

Carbonation weathering reactions to carbonate minerals and kinetic isotopic fractionation effects to δ^{13}C-DIC

Kinetic isotopic fractionation effects associated with $CaCO_3$ mineral weathering is another important consideration. The carbonation of $CaCO_3$ proceeds as follows:

$$CaCO_{3(s)} + CO_{2(aq)} + H_2O \rightarrow Ca^{2+} + 2HCO_3^-$$

Fine-grain particles provide reactive surface areas for carbonate weathering reactions, but ^{12}C and ^{13}C do not necessarily react the same way on these surfaces over different time intervals. In the short term, there is thermodynamic favorability associated with the weathering of lighter $Ca^{12}CO_3$ that can result in intense isotopic depletion of the resultant δ^{13}C-DIC. As $Ca^{12}CO_3$ gets used up this effect will get less pronounced as an increasing density of $Ca^{13}CO_3$ on mineral surfaces will promote weathering of these isotopically heavier carbonates. Reaction kinetic effects of $CaCO_3$ mineral weathering thereby become particularly important in glacial rivers where meltwaters can react rapidly with freshly eroded glacial sediment. In fact, whereas experimentally determined (5ºC) isotopic fractionation of this kinetic effect has been reported as -7.8 ‰ for chemical grade $CaCO_3$, this same study presents a much more intense isotopic fractionation for fine-grain glacial till (-17.4 ‰)[360]. This effect to δ^{13}C-DIC in glacial rivers would be especially prevalent in meltwaters that have had limited time to equilibrate with the atmosphere.

Appendix C
Chapter 5 – Supplementary Information

PARAFAC component descriptions

C1 (Figure 5.2A) had a primary excitation maximum at <250 nm followed by a secondary peak at 305 nm and an emission maximum at 415 nm. C1 is comprised of 'A' and 'M' peaks[139] and has been described as humic-like organic material associated with recent biological activity[419,420]. It has been shown that a similar fluorescent component could be produced by phytoplankton and had highest fluorescence intensities in algal exudates[454]. C2 (Figure 5.2B) is similar to components that are indicative of terrigenous (or soil-derived) humic-like material. C2 contained 'A' and 'C' peaks[139] with a primary excitation maximum at 260 nm, a broad secondary peak at 345 nm, and a red-shifted emission maximum of 475 nm. Similar fluorescent components have been reported in fluvial networks[420,455] and ascribed to a high molecular weight fraction of DOM[456] associated with elevated degrees of conjugation and aromaticity[128]. This component has been thought to be a good tracer of terrestrially-derived DOM from the degradation products of higher vascular plant matter based on its strong association with lignin phenols[412,439]. C3 (Figure 5.2C) showed a 'C' peak associated with a primary excitation maximum of 345 nm as well as a minor 'A' peak residue at an excitation of <250 nm[139]. C3 had a narrow emission maximum compared to C1 and C2, centered on 450 nm, and decaying towards ~550 nm. C3 was blue shifted relative to C2, suggesting that this component was indicative of a less conjugated fluorescent fraction of DOM. PARAFAC components with spectral features resembling those of C3 have been reported previously for freshwater environments[410,419,454]. The 3 fluorescent components reported here are all representative of humic-like materials. Protein-like components were not identified via PARAFAC modeling. Similar PARAFAC results where components were exclusively humic-like have been found previously for DOM samples leached from soils of coniferous and deciduous forest stands[421] and from aquatic environments particularly rich in terrestrial DOM signature where fluorophores associated with *in situ* production were comparatively limited[454]. However, increased DOM absorption with Fe additions over the course of titration experiments was expected to have contributed to the propagation of inner filtering effects (IFEs). Accordingly, preferential IFE fluorescence quenching at shorter excitation wavelengths likely impacted the quantification of protein-like fluorescence.

Supplementary Figures

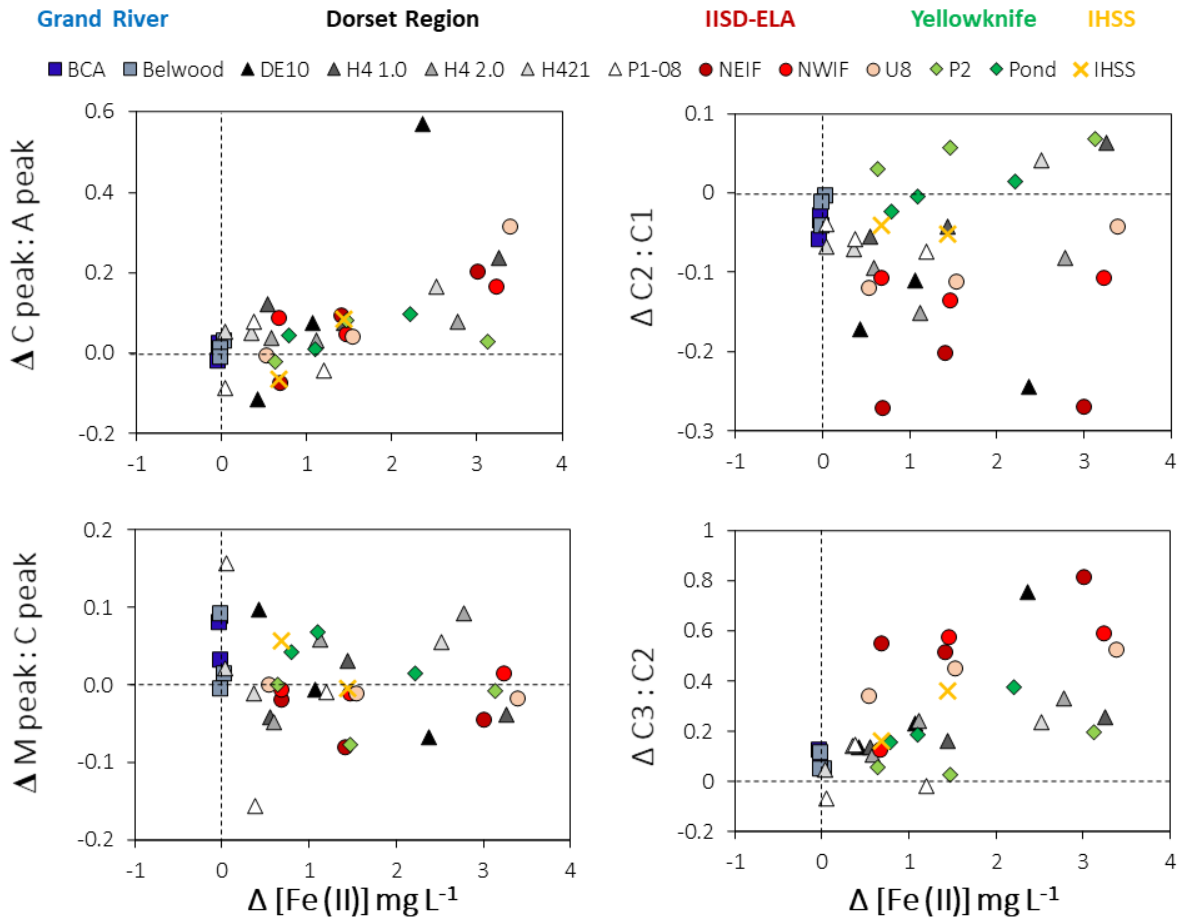

Figure S5.1: Changes in ratios of fluorescence peaks and PARAFAC components versus Fe (II) relative to initial untreated natural water samples.

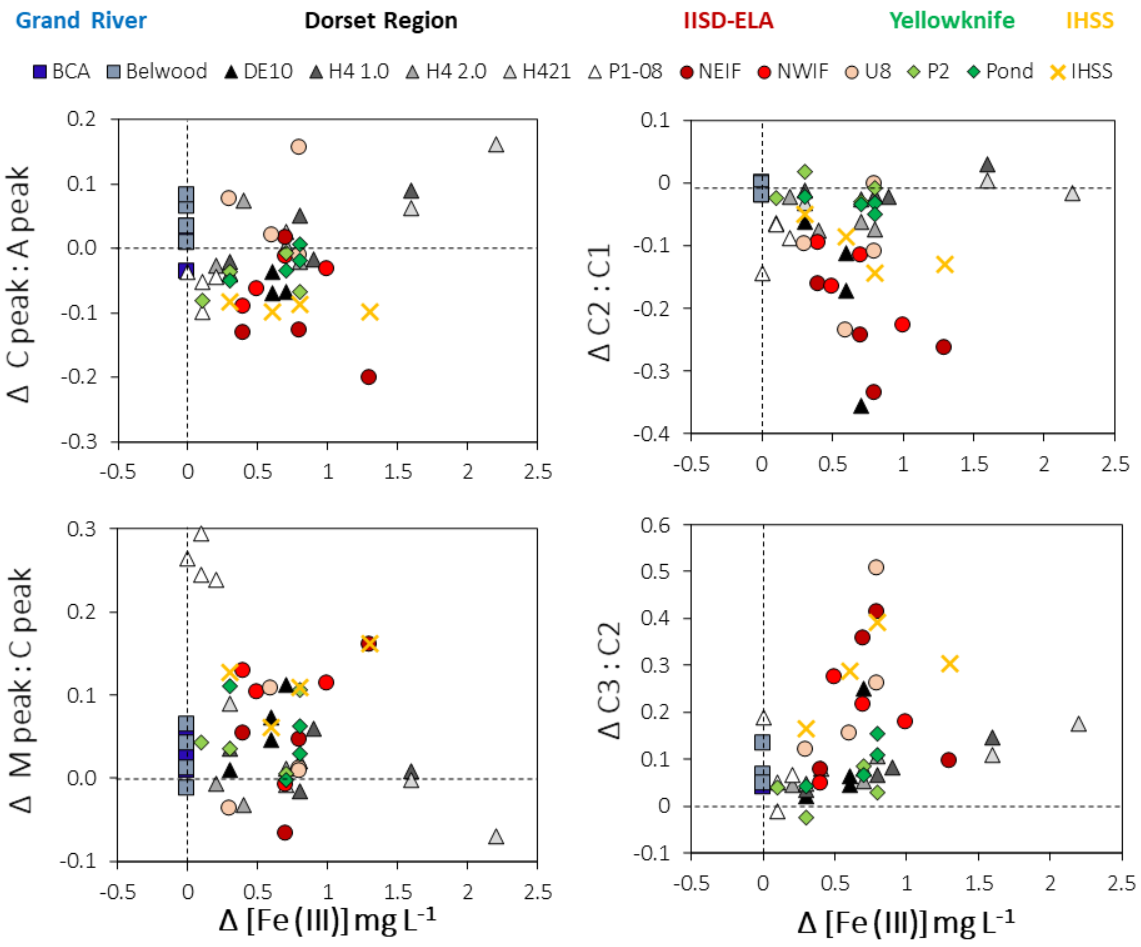

Figure S5.2: Changes in ratios of fluorescence peaks and PARAFAC components versus Fe (III) relative to initial untreated natural water samples.

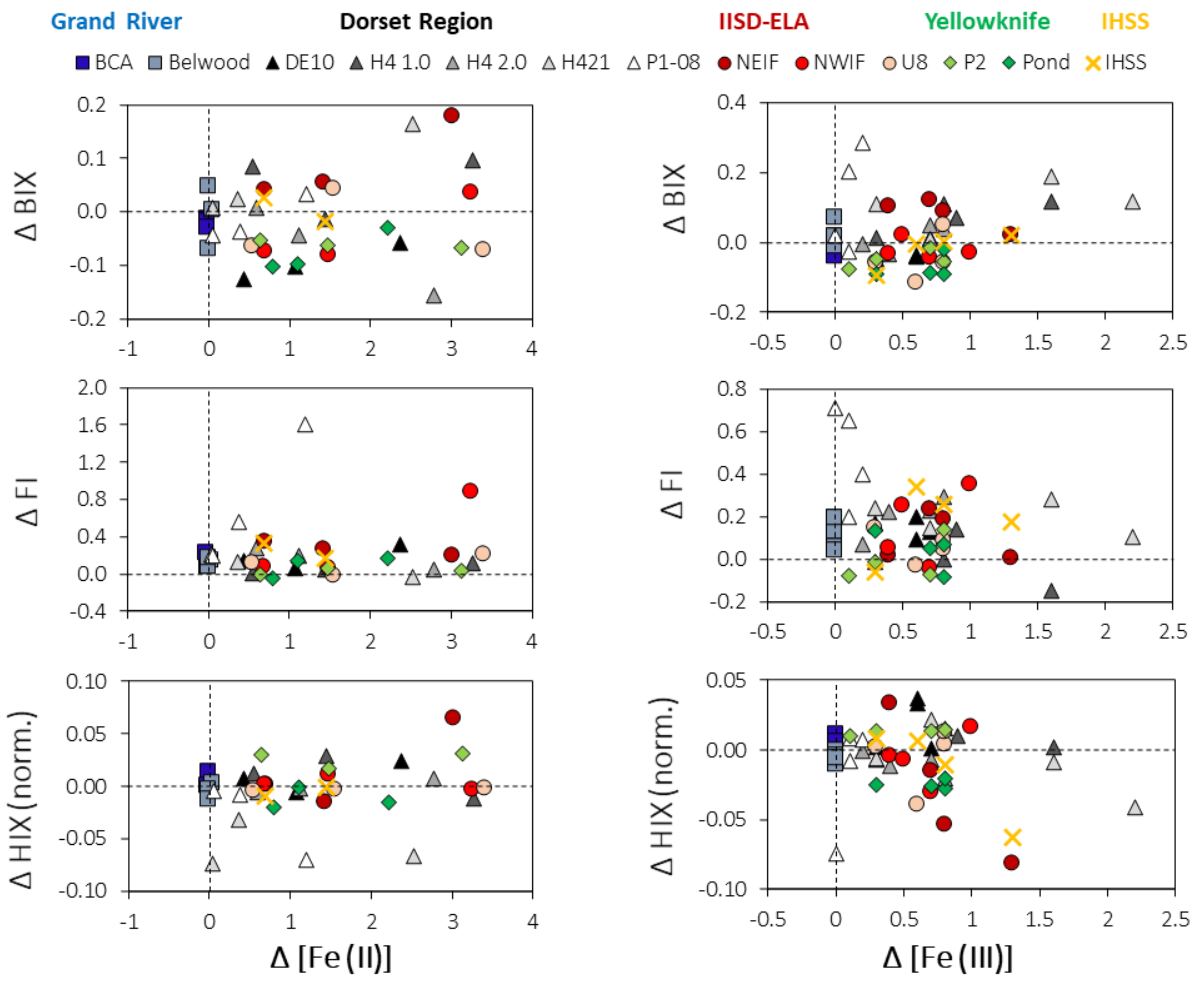

Figure S5.3: Changes in BIX, FI, and normalized HIX versus Fe (II) and Fe (III) relative to initial untreated natural water samples.

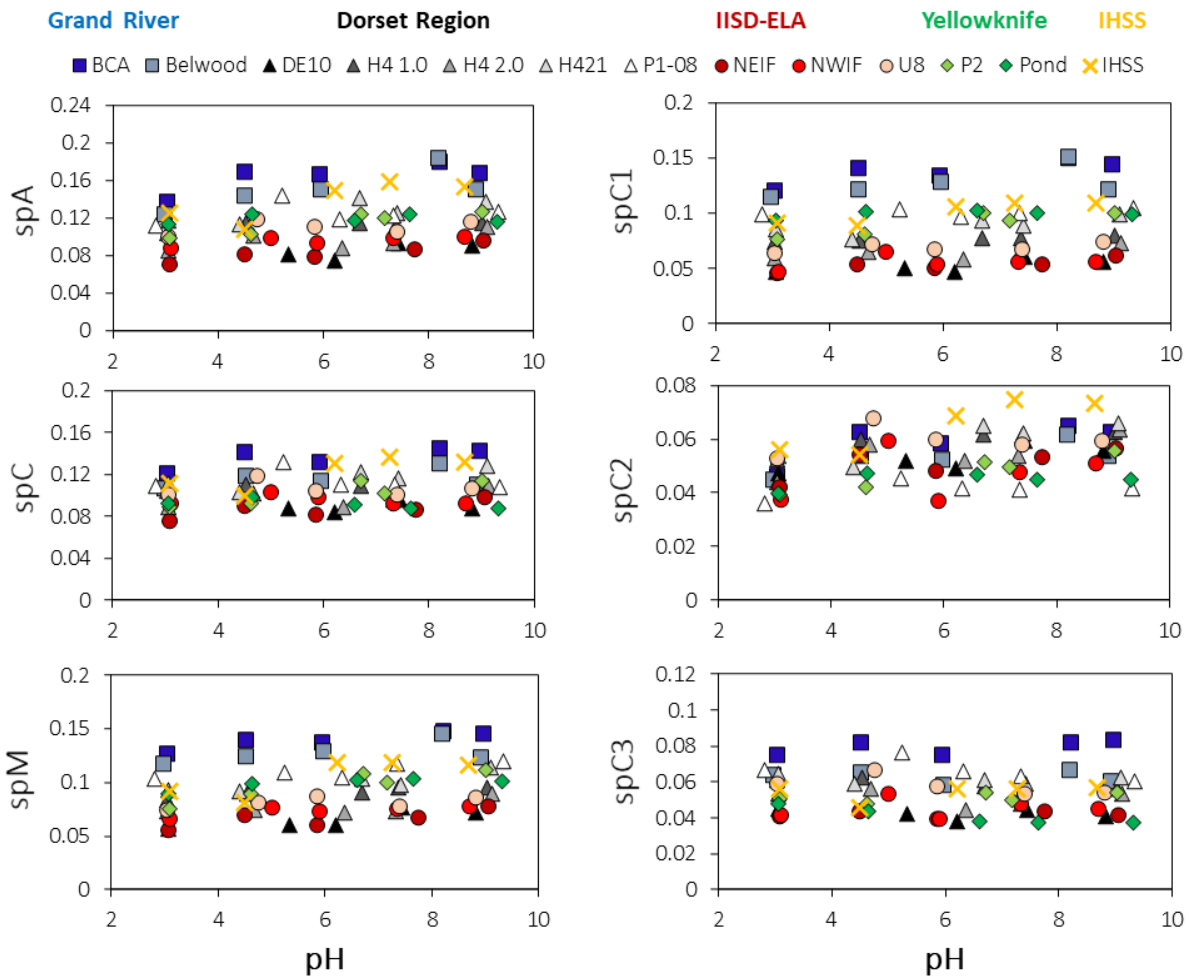

Figure S5.4: Specific (i.e., normalized to DOC concentration) fluorescence peaks and PARAFAC components across a pH gradient

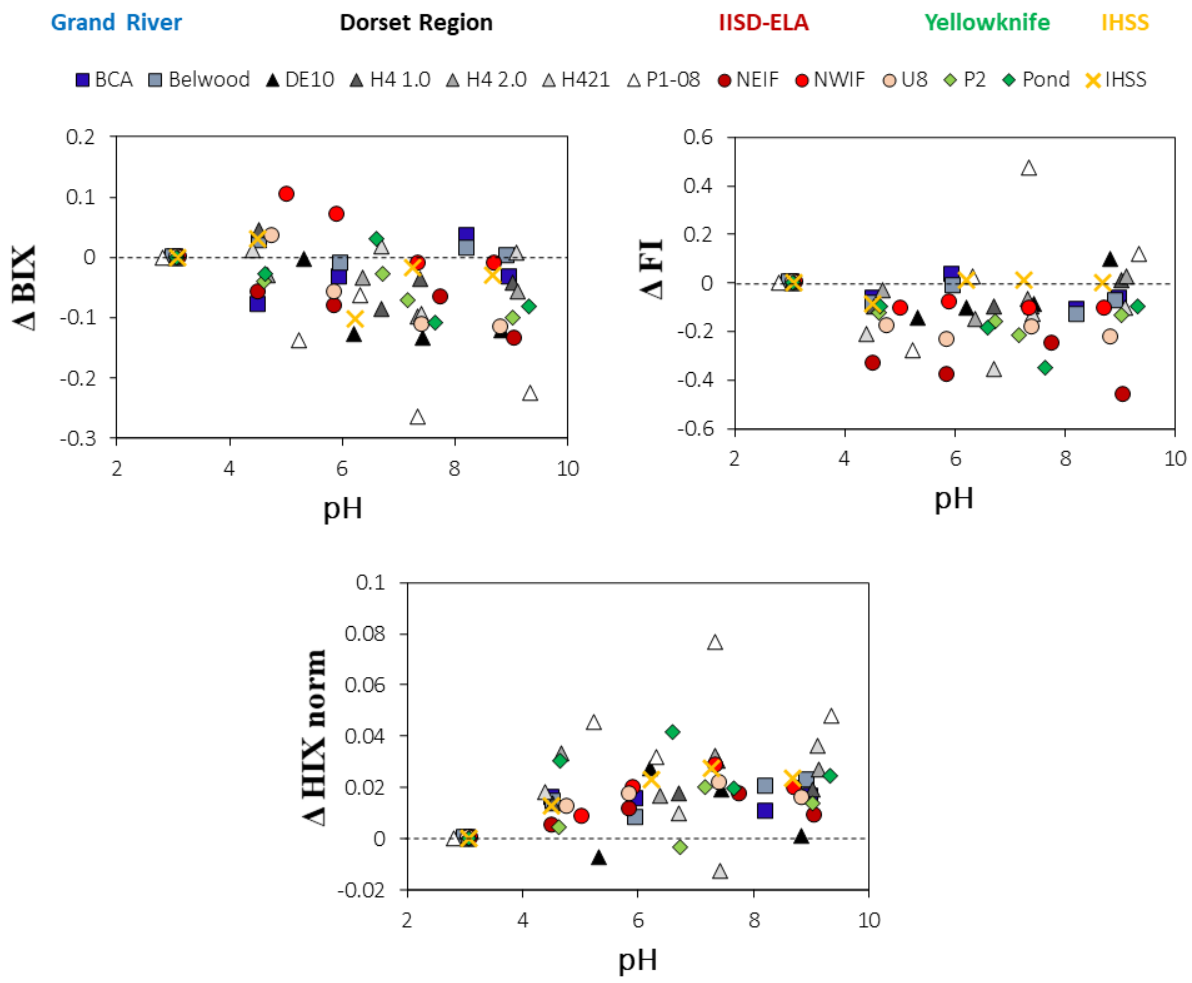

Figure S5.5: Changes in BIX, FI, and normalized HIX relative to pH ~ 3.

Appendix D

Field Photos

Lake Hazen base camp, Quttinirpaaq National Park, Nunavut, Canada:

Henrietta-Nesmith River watershed:

Meltwaters discharging from the Henrietta-Nesmith Glacier. This glacial river is short (~2.4 km) and extensively braided. Sediment-laden meltwaters are shown discharging to the ice-covered shoreline of Lake Hazen during high flow conditions (late July, 2019).

Gilman Glacier:

Supraglacial meltwater routing on the surface of the Gilman Glacier. Dark areas of glacier surface are expected to be primarily aeolian deposition of soil/mineral dust from the surrounding landscape. Ice-marginal meltwater flow can be seen along the right side of the glacier.

Gilman River:

Gilman River glacial headwaters sampled during high flow conditions (late July, 2019). The surrounding terrain is covered by rocks, with no sign of vegetation. Fine-grain suspended material gives meltwaters a cloudy appearance. Meltwaters are fast-flowing, with chunks of glacier ice floating on the surface.

Gilman River:

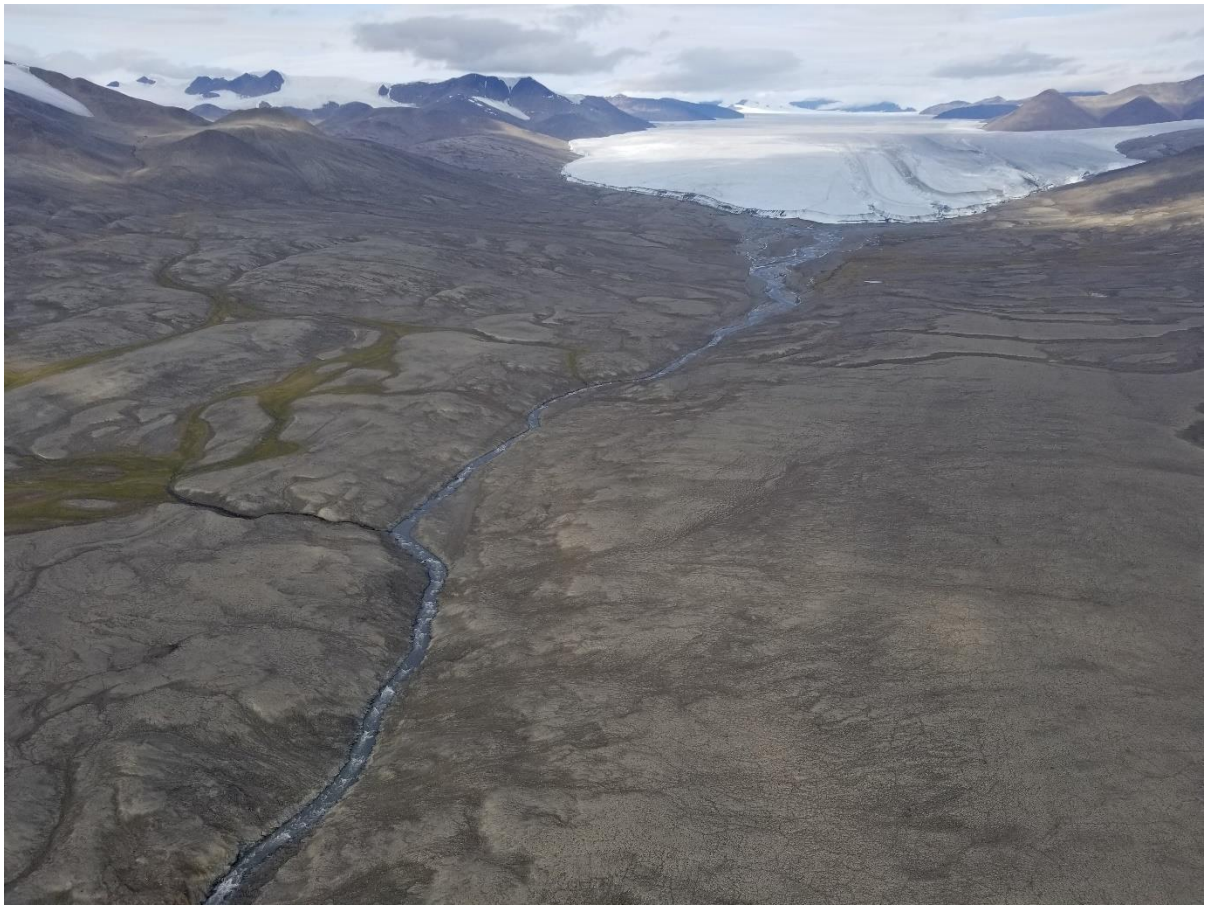

Braided channels of meltwaters converging beneath the terminus of Gilman Glacier (i.e., glacial headwaters), before flowing further downriver during low flow conditions (mid-July, 2017).

Lake Hazen:

Lake Hazen is immense, with dimensions of ~75 x 12 km and a maximum depth of ~265 m. At a distance, Snowgoose and Abbe River deltas are shown emptying into Lake Hazen (late July, 2019).